Theoretical Notes

Note 348

1 November 1983

NONLINEAR ELECTRICAL STUDIES ON BURIED CONDUCTORS

R. E. Leadon
T. M. Flanagan
C. E. Mallon
R. Denson

JAYCOR
P.O. Box 85154
San Diego, California 92138

ABSTRACT

Dielectric breakdown was measured for several standard polyethylene dielectric coaxial cables as a function of stressed volume. The results are presented in a manner which enables prediction of the breakdown voltage for other cables, with the same dielectric, as a function of length and cross sectional geometry.

The damage produced to the copper center conductor and the polyethylene jacket of a buried cable was measured for a peak drive of 200 kA, 70 Coulomb, and an action of $\sim 1.6 \times 10^6$ $A^2 \cdot s$. This drive level did not produce significant damage to the 0.69 cm diameter copper conductor or the 1.75 cm thick polyethylene jacket.

The vaporization/restrike characteristics of 40-cm long metal and graphite fiber samples were measured using pulser voltages from 40 to 210 kV. The metal samples included a helical geometry with two cross sectional areas as well as straight samples, usually tightly enclosed in 280 mils of polyethylene. The metals investigated were Fe, Aℓ, stainless steel, and Inconel. Resistivity curves are given versus time and specific action from voltage application through restrike. Enclosing the metal samples in a thick polyethylene jacket reduces the peak resistivity at burst and tends to delay and broaden the peak on a specific action scale.

Carborundum resistors (1-inch diameter) and graphite fibers (0.1-inch diameter) surrounded by soil, were pulsed with combined radial and axial voltages from 20 to 60 kV in a cylindrically symmetric geometry. The soil was contained in a metallic cylinder approximately 1-m long and 1-m diameter. Time histories of the radial and axial voltages and currents were reduced in terms of radial and axial resistances and radial electric field close to the center resistor. For pulser voltages around 40 to 60 kV, low-impedance paths, attributed to streamers through the soil, developed between the center resistor and the metal cylinder on time scales of 100 to 200 μs. With the 66-Ω carborundum resistors, an enhanced electrical conduction parallel to the center resistor was observed as a function of the radial voltage. The minimum resistance of the parallel conduction path through the soil was deduced to be more than 100 Ω up to the time of the radial attachment, but it could have gone lower if attachment had not occurred. A parallel resistance of this magnitude could not be detected with the low-resistance graphite fibers (≈ 10 Ω).

CONTENTS

CONTENTS (Concluded)

ILLUSTRATIONS

ILLUSTRATIONS (Continued)

ILLUSTRATIONS (Continued)

ILLUSTRATIONS (Continued)

ILLUSTRATIONS (Concluded)

TABLES

I. INTRODUCTION

This document presents the results of a series of experiments which addressed the nonlinear breakdown characteristics for buried conductors.

Section II presents the results of a set of experiments which measured the threshold for dielectric breakdown in coaxial cables with a polyethylene dielectric. The breakdown thresholds determined from these experiments are presented in terms of electric field (kV/cm) versus the stressed volume of dielectric so that the results can be used to predict the breakdown voltage for other cable types and lengths for the same dielectric.

Section III discusses the results of experiments performed to measure the damage produced by large current/Coulomb drive in a buried conductor with a punctured dielectric. The peak current and Coulomb drive for these tests was 200 kA and 71 C, respectively.

Section IV presents the results of a series of vaporization/restrike experiments using candidate conductors for a resistive link (R-wire). Four metals (iron, aluminum, Inconel, stainless steel) and a graphite fiber bundle were investigated. The resistivity of the conductors from ambient through burst and restrike is given as a function of time and specific action ($A^2 \times s/mm^4$) for these conductors.

Section V contains the results of a series of experiments performed to investigate the effect of large radial electric fields on the axial conductance of buried conductors. Appendix A contains time histories of currents, voltages, electric fields, and calculated axial and radial resistances used for the analysis presented in Section V.

Section VI contains an analysis of the combined drive soil breakdown experiments (Section V) by Ian Smith of Pulse Sciences, Incorporated.

The authors would like to express their thanks to the following for their contributions to the program.

We would like to thank Ian Smith of Pulse Sciences, Inc., for his assistance in the design of the dielectric breakdown experiments and analysis (Section VI) of the combined drive soil breakdown studies.

We express our appreciation to Ken Chen, Carl Baum, and Bill Kehrer of the Air Force Weapons Laboratory and Bob Carlile of the University of Arizona for their helpful discussions during planning and conduct of the experiments.

Thanks to Ed Schulte and Keith Zeisel of the McDonnell Douglas Lightning Laboratory for their assistance during the experimental phase of the program. Ed remained undaunted throughout the continued requests for changes in pulser configuration required to support the program.

II. DIELECTRIC BREAKDOWN IN COAXIAL CABLES

1. INTRODUCTION

This section of the report discusses the results of experiments designed to produce electrical breakdown in the dielectric of coaxial cables. The experiments were performed at the McDonnell Aircraft (MCAIR) lightning facility in St. Louis, Missouri, during the month of October 1981.

Section II.2 describes the experimental arrangement and design for breakdown studies of cables RG-58 and RG-217. Section II.3 discusses the results of those experiments.

In Section II.3, Figure 2-6, the mean breakdown electric field (MV/cm) is plotted versus the stressed volume (cm^3) of the cable polyethylene dielectric. This type of presentation provides a means for predicting the breakdown voltage for polyethylene dielectric cables as a function of cable geometry and length.

2. DIELECTRIC BREAKDOWN IN STANDARD RG COAXIAL CABLE

Dielectric breakdown was produced in RG-58 and RG-217 coaxial cables using MCAIR pulser #3. This pulser has a peak output voltage of ~ 400 kV and a peak current of ~ 3×10^3 A. The measured pulser rise time was about 3 kV/ns. The pulser fall time was not important for these measurements as the pulser voltage was set to a large enough value to produce dielectric breakdown during the voltage rise.

a. **Experimental Arrangement**--The experimental configuration used to produce breakdown in cable dielectrics is shown in Figure 2-1.

Ten-foot cable lengths were used during the experiments. The length of the cable to be stressed was determined by the length of the grounded cable braid and insulating cover left on the cable. The remainder of the braid and cover was removed from the cable sample. Figure 2-2 shows the geometry of the stressed portion of the cable. The approximate Rogowski profile to grade the field at each end of the grounded braid was made by forming the braid and wrapping the braid ends back over into the low field region.

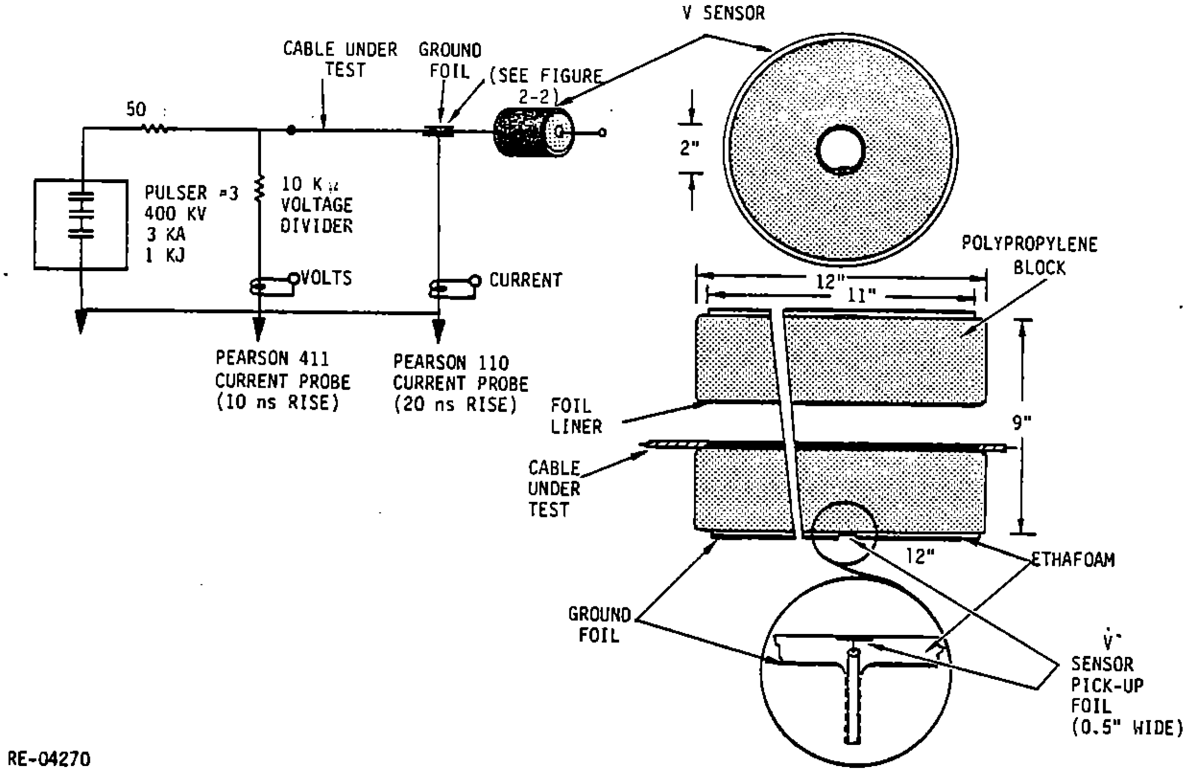

Figure 2-1. Experimental arrangement for breakdown of 10 foot long coaxial cable samples in air

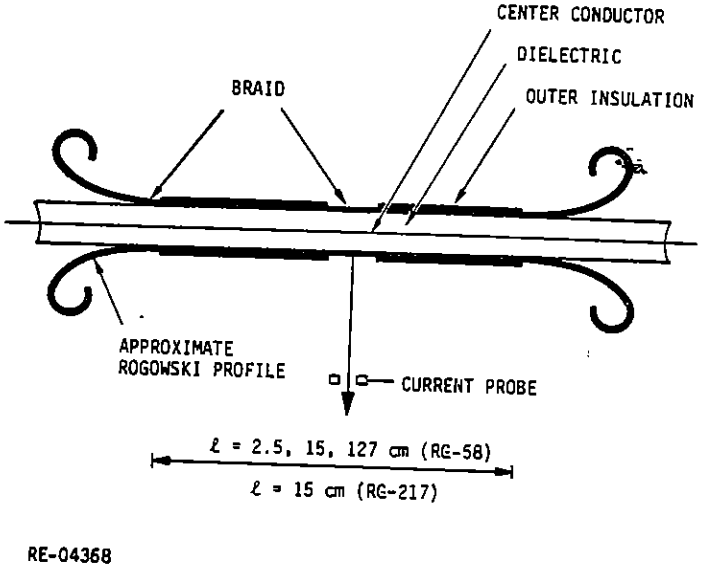

Figure 2-2. Details of the stressed region of the cable sample

The dielectric punchthrough current was measured by passing the lead that grounded the cable braid through a current probe. As shown in Figure 2-1, the test cable center conductor voltage was measured by a resistive voltage divider and a $\dot{V}$ sensor. To avoid instrumentation ground loops, a current probe was used to measure the current through the known resistance of the divider to obtain voltage. Due to the bandwidth limitation of the resistive voltage divider, it was used only to confirm the calibration of the $\dot{V}$ sensor.

The $\dot{V}$ sensor (design suggested by Dr. C. E. Baum) was constructed using a 9-inch diameter, 12-inch long polypropylene cylinder with a 2-inch diameter coaxial hole through the center. This 2-inch diameter hole was lined with metal foil 11 inches long that extended to within 1/2 inch of the ends of the polypropylene cylinder. The test cable passed through and was copper taped to this metal cylinder. The $\dot{V}$ sensor was formed by 1/2-inch wide copper tape band placed around the outer surface of the polypropylene cylinder as shown in Figure 2-1. The sensor strip was covered with several layers of electrical tape. The entire cylinder was then wrapped with approximately 0.5 inch thick ethafoam to decrease the capacitance between the $\dot{V}$ sensor and the outer ground foil. The outer ground foil and the central metal cylinder provided a uniform field in the vicinity of the $\dot{V}$ sensor, making the $\dot{V}$ sensor response more amenable to calculation. The calculated $\dot{V}$ response follows.

The capacitance between the test cable center conductor and the inner metal cylinder was 27 pF, and the capacitance between the metal cylinder and the outer ground foil was 23.7 pF (Figure 2-3), thus forming a capacitance voltage divider between the test cable center conductor, inner metal cylinder, and the outer ground foil. The voltage of the metal cylinder with respect to the test cable center conductor is therefore

$$\begin{aligned} V_{CYL} &= \frac{23.7}{23.7 + 27} \times V_{CABLE} \\ &= 0.467 \times V_{CABLE} \ . \end{aligned}$$

The calculated capacitance between the center metal cylinder and the 0.5 inch wide $\dot{V}$ sensor is 1.08 pF.

The $\dot{V}$ sensor output was integrated by a passive integrator with a time constant = 12.5 μs (Figure 2-3). The relationship between the integrator output voltage, V_{INT}, and the voltage to be measured is given by

$$V_{INT} = \frac{CR_L}{\tau} V$$

where C is the $\dot{V}$ sensor capacitance (1.08 pF), R_L is the load resistor (50 Ω), and τ is the integrator time constant, 12.5 µs.

$$V_{INT} = \frac{1.08 \times 10^{-12} \times 50}{12.5 \times 10^{-6}} \times \frac{1}{0.467} \times V$$

$$= 9.3 \times 10^{-6} \times V$$

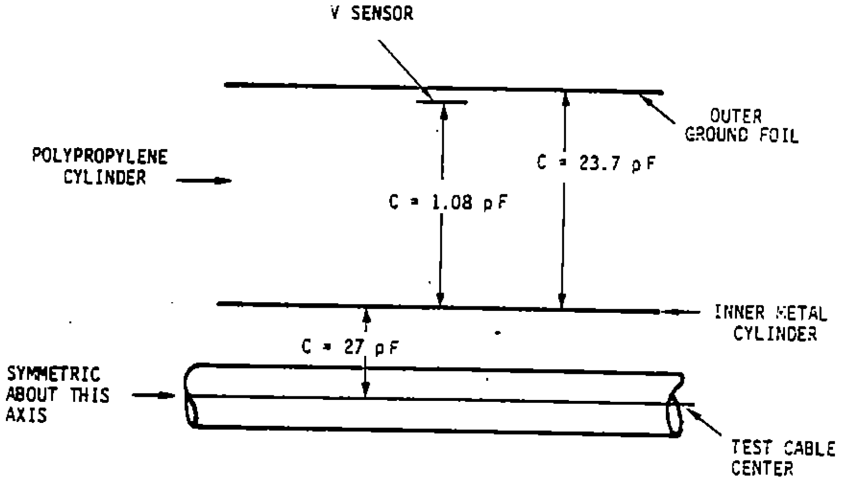

(a) $\dot{V}$ SENSOR PARAMETERS

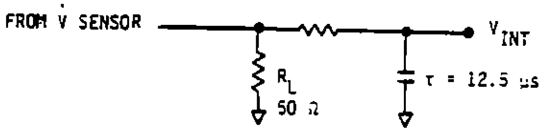

(b) PASSIVE INTEGRATOR FOR $\dot{V}$ SENSOR

RE-04369

Figure 2-3. $\dot{V}$ sensor parameters and passive integrator

The factor 0.467 accounts for the voltage division between the test cable center conductor, inner metal cylinder and the outer ground foil. Figure 2-4 is a photograph of a $\dot{V}$ sensor calibration shot. The upper trace is the voltage divider output and the lower trace is the output of the $\dot{V}$ sensor/12.5 µs passive integrator. At 0.6 µs after pulse initiation the ratio of the $\dot{V}$ integrated voltage (0.86 V) to the voltage measured by the voltage divider (94 kV) is 9.2×10^{-6}, in good agreement with the expected value. Calibration for both types of cables tested yielded the same calibration factor, which is to be expected since both were 50 ohm cables and therefore the capacitive coupling between the center conductor to the inner metal cylinder of the $\dot{V}$ probe was the same in both cases.

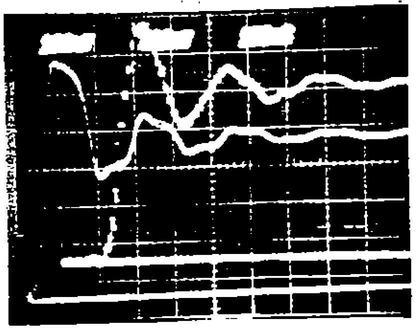

VOLTAGE DIVIDER
20 kV/cm

$\dot{V}$ SENSOR AFTER
INTEGRATION BY A
12.5 µs INTEGRATOR.
0.2 V/cm

RE-04370

Figure 2-4. $\dot{V}$ sensor calibration shot

3. EXPERIMENTAL RESULTS

a. RG-58--The ten foot long RG-58 cable samples tested were made from two 100 foot spools obtained from the same source.

RG-58/U	Belden 8240-100
$Z = 53.3\ \Omega$	
Center-conductor	20 Awg solid copper
Dielectric	0.042 inch nominal wall polyethylene
AWM STYLE	1354.

Table 2-1 summarizes the breakdown results for RG-58 samples for stressed lengths of 2.5, 15 and 127 cm. The 2.5 cm breakdown data was obtained by sliding a 1 inch long grounded braid along an RG-58 cable after successive breakdowns. To avoid flashover from previous breakdowns the ground braid was relocated at least 15 cm from a previous breakdown. The breakdown data for the 15 cm sample length was taken in a similar manner, except with a 15 cm length grounded braid. Individual 10 foot cable lengths were used for breakdown studies in the 127 cm long samples. The RG-58 data presented in Table 2-1 is summarized in Table 2-3 along with breakdown data for RG-217.

Table 2-1. Summary of Breakdown Results for RG-58

Cable No.	Stressed Length (cm)	B.D. No.	$V_{B.D.}$ (kV)	Comments
		SPOOL #1		
5	2.5	1	190	(1)
5	2.5	2	163	2-inch flashover from BD1
5	2.5	3	217	(1)
5	2.5	4	196	(1)
6	15	1	147	(1)
6	15	2	185	(1)
6	15	3	190	(1)
6	15	4	147	(1)
6	15	5	173	(1)
6	15	6	141	Punchthrough in field grading cone
7	15	1	163	(1)
7	15	2	171	(1)
7	15	3	179	(1)
7	15	4	185	(1)
7	15	5	185	(1)
7	15	6	174	(1)
8	127	1	128	(1)
		SPOOL #2		
20	15	1	223	Punchthrough in field grading cone
20	15	2	228	(1)
9	127	1	217	(1)
10	127	1	228	(1)
11	127	1	220	(1)
12	127	1	185	(1)
13	127	1	207	(1)
14	127	1	120	(1)
15	122	1	223	(1)
16	127	1	193	(1)
17	127	1	190	(1)
18	127	1	185	(1)

(1) B.D. occurred within the ground foil.

b. RG-217--A total of 18 dielectric breakdowns were produced in 15-cm length stressed regions of RG-217 cable samples. This cable (Alpha 9217) has a nominal impedance of 50 Ω, a 0.106-inch solid copper center conductor and 0.135 inch thick polyethylene dielectric.

The breakdown results for this cable are given in Table 2-2. As shown in Table 2-2, approximately 50 percent of the breakdowns occurred inside the 15-cm long grounded foil where the electric field is well-defined and the remainder occurred in the grading cone, or in some cases approximately 1 inch beyond the grounded foil. Table 2-2 also gives the average breakdown voltage and standard deviation for the total number of breakdowns, breakdowns that occurred within the ground foil, and breakdowns that occurred in the grading cone or beyond the end of the ground foil. While the average voltage differs by less than 10 percent the standard deviation is about a factor of 2 larger for breakdowns outside the ground foil.

Table 2-2. Summary of Breakdown Results for RG-217

Stressed Sample length = 15 cm Cable No.	B.D. No.	V_{BD} (kV)	Comments
1	1	223	(1)
1	2	272	(1)
1	3	293	(1)
1	4	276	(1)
3	1	152	Punchthrough occurred in grading cone
3	2	299	Punchthrough occurred ~ 2" beyond grading cone
3	3	240	(1)
3	4	278	Punchthrough in grading cone
4	1	250	Punchthrough occurred ~ 0.25" beyond grading cone
4	2	294	Punchthrough in grading cone
4	3	263	(1)
4	4	260	Punchthrough occurred ~ 2.5" beyond grounded foil
5	1	272	Punchthrough inside grading cone
5	2	261	Punchthrough occurred ~ 1.5" beyond end of ground foil
5	3	283	(1)
5	4	294	(1)
6	1	261	(1)
6	2	212	Punchthrough occurred ~ 1" beyond end of ground foil

	Total B.D. (18)	B.D. Inside Ground Foil (9)	B.D. Outside Ground Foil (9)
Average B.D. Voltage	260 kV	267 kV	253 kV
1σ	36 kV	24 kV	46 kV

(1) B.D. occurred within the ground foil.

c. **Discussion**--The breakdown data presented in Tables 2-1 and 2-2 have been analyzed in a manner which allows comparison of these results with data of J.C. Martin (Ref. 2-1), where the mean breakdown voltage is given as a function of the stressed dielectric volume. The cable parameters required for this comparison are given in Figure 2-5.

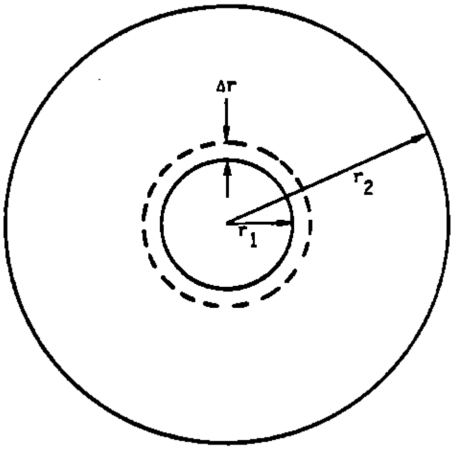

		RG 58	RG 217/RG14
RADIUS OF CENTER CONDUCTOR	r_1(cm)	4.06×10^{-2}	0.135
RADIUS OF DIELECTRIC	r_2(cm)	1.47×10^{-1}	0.47
DISTANCE FROM CONDUCTOR FOR $E = 0.9\ E_S$	Δr(cm)	4.47×10^{-3}	1.49×10^{-2}
FIELD AT SURFACE OF CONDUCTOR	E_s(V/cm)	$19 \cdot V$	$5.9 \cdot V$
STRESSED VOLUME *	$V_s(\mathrm{cm})^3$	$1.2 \times 10^{-3} \cdot \ell$	$1.34 \times 10^{-2} \cdot \ell$
	C(pf/cm)	.95	.95

* DIELECTRIC VOLUME DEFINED BY Δr AND STRESSED SAMPLE LENGTH.

RE-04272A

Figure 2-5. RG-58 and RG-217 coaxial cable geometry

Table 2-3 summarizes the cable breakdown data in terms of stressed volume, and the mean breakdown voltage and electric field.

2-1 J.C. Martin, 'Volume Effect of the Pulses Breakdown Voltage of Plastics,' Dielectric Strength Notes #3, 16 November 1965

Table 2-3. Summary of Breakdown Voltage and Electric Field for RG-58 and RG-217 Coaxial Cables

No. of B.D.	Stressed Length (cm)	Stressed Volume V_S (cm)^3	Average B.D. Voltage V_{BD} (kV)	1 σ V_{BD} (kV)	Average B.D. Field E_S (V/cm)	1 σ E_S (V/cm)	Probable Error of E_S Average (V/cm)
RG-58 SPOOL #1							
3	2.5	3×10^{-3}	201	14.2	3.8×10^6	2.7×10^5	1.1×10^5
12	15	1.8×10^{-2}	173	15	3.3×10^6	2.9×10^5	5.9×10^4
1	127	1.5×10^{-1}	128	—	2.4×10^6	—	—
RG-58 SPOOL #2							
2	15	1.8×10^{-2}	226	—	4.3×10^6	—	—
10	127	1.5×10^{-1}	197	31.5	3.7×10^6	6×10^5	1.3×10^5
RG-217							
9*	15	0.2	267	23.7	1.6×10^6	1.4×10^5	3.2×10^4
9**	15	0.2	253	46	1.5×10^6	2.7×10^5	6.1×10^4

*9 Breakdown within ground foil.
**9 Breakdown near end of ground foil (see Table 2-2)

In Table 2-3 the stressed volume (V_S) is defined by a distance Δr from the center conductor where the electric field has decreased to 90 percent of the maximum value at the surface of the center conductor, multiplied by the length of the stressed region.

The breakdown data summarized in Table 2-3 is shown in Figure 2-6 where the mean breakdown field in MV/cm is plotted versus the stressed dielectric volume. Figure 2-6 also includes breakdown data of J.C. Martin for comparison. The measured breakdown electric field versus stressed volume for RG-58 agrees fairly well with the data of Martin. The RG-58 data shown in Figure 2-6 was obtained from samples taken from different 100 foot spools. The breakdown threshold for samples taken from spool #1 was approximately 25% greater than that measured for spool #2. Post breakdown inspection of these samples revealed no apparent reason for the observed difference in thresholds.

The measured breakdown threshold for RG-217 was approximately a factor of 1.5 lower than expected from Martin's data. A post-test examination of the RG-217 cable samples however, revealed many small approximately hemispherical voids in the dielectric at the dielectric/center conductor interface. A photograph of these voides is shown in Figure 2-7. The average width of the voids at the center conductor interface was ~ 2.5 mm with depths ranging from ~ 0.25 to 0.5 mm. The electric field inside the dielectric of the RG-217 cable adjacent to the center conductor is about (6 V)/cm where V is the voltage applied between the center conductor and the cable shield. For a dielectric constant of 1.41, the electric field across an air gap adjacent to the center conductor would be about (8.5 V)/cm. For the average observed breakdown voltage of ~ 260 kV for RG-217, the stress in the air-gap was ~ 2.2 x 10^6 V/cm which is more than adequate to produce breakdown across the air gap. A possible explanation* for the lower than expected threshold in the RG-217 is that the highly conductive-ionized air in these voids essentially forms a sphere-to-plane geometry (center conductor to shield) which can result in approximately a factor of 3 field enhancement in the dielectric and thus lead to dielectric breakdown.

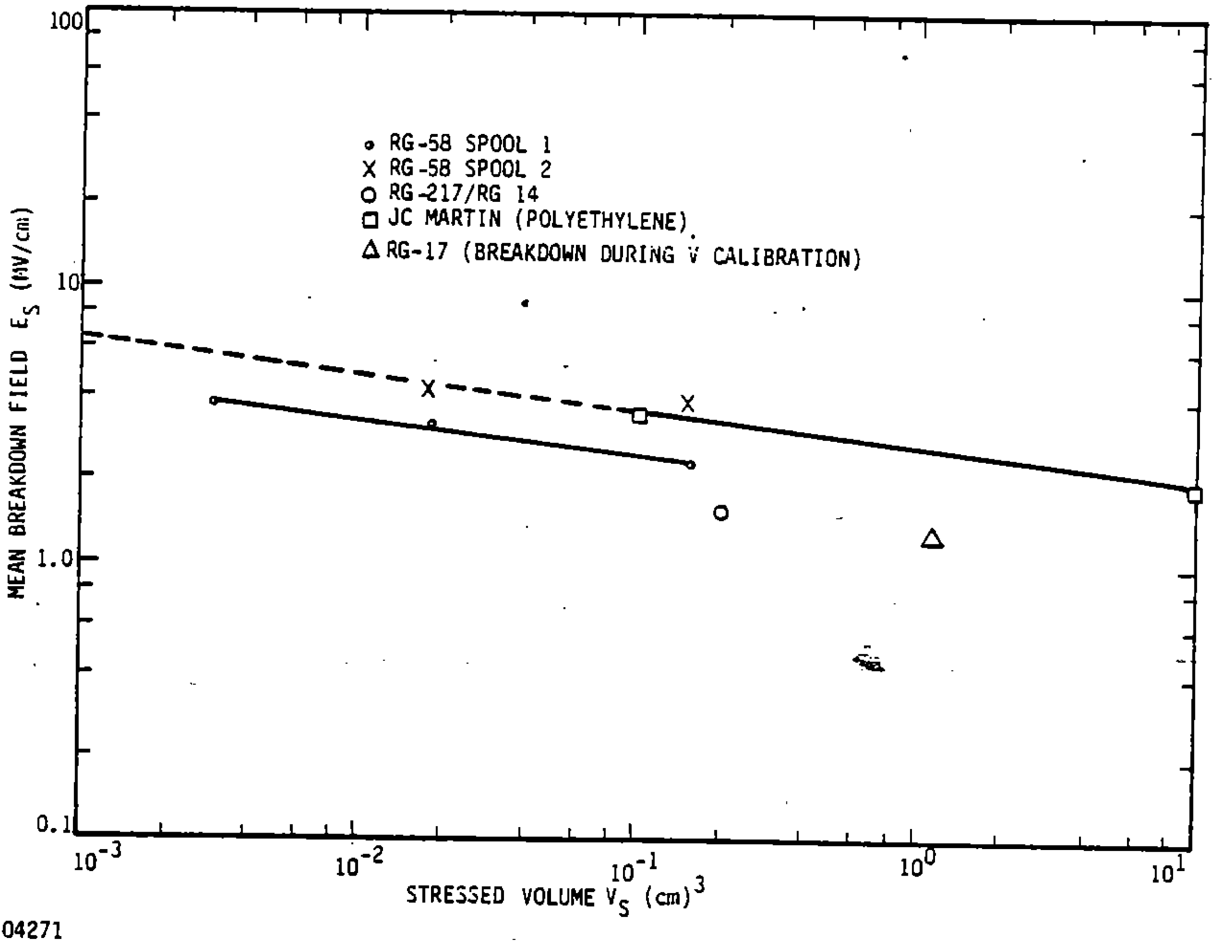

RE-04271

Figure 2-6. Mean breakdown field versus stressed volume for RG-58 and RG-217

---

* Ian Smith, private communication.

Figure 2-7. **Photograph of the voids in the dielectric at the dielectric/center conductor interface of the RG-217 cable tested. Voids decorated with black dye. Scale = 1 mm/div**

If one assumes a factor of 3 field enhancement as a result of the voids and a factor of 10 reduced stressed volume (10 percent of the center conductor/dielectric interface area contains voids) a breakdown field of 4.8×10^6 V/cm at a stressed volume of $2 \times 10^{-2} cm^3$ is obtained, which lies on the curve of Martin. Thus, the consideration of voids in the dielectric of RG-217 appears to be a plausible explanation for the observed lower than expected breakdown threshold.

In comparison, the dielectric of the RG-58 cable was free of these types of voids. Breakdown for a single sample of RG-17 (triangular data point in Figure 2-6) was observed during calibration of the voltage monitoring system. This breakdown occurred at a voltage well below the expected threshold, and as with the RG-217, many voids were found in the dielectric. While breakdowns were not produced in the MF antenna, inspection of samples used in the current drive tests revealed the presence of many voids in the dielectric at the center conductor/dielectric interface. Inspection of RG-220, which presumably forms the central portion of the MF antenna, obtained from another source was completely free of similar voids.

The presence of voids, at least in 100 foot spools of cables, does not appear to be random along the cable length. That is, inspection of a short length taken at random would reveal the presence of voids.

The breakdown data of Figure 2-6, where the mean breakdown electric field is plotted versus the stressed volume of the dielectric, provides a means of estimating the breakdown voltage for longer more realistic cable lengths. For example, the breakdown data for RG-58 in Figure 2-6 fits a power law given by:

$$E_S\ (\mathrm{V/cm}) = 2 \times 10^6\ [V_S\ (\mathrm{cm}^3)]^{-0.12}$$

where E_S is the electric field at the surface of the center conductor and V_S is the stressed volume of the dielectric (Figure 2-5).

For a 100 meter length of RG-58 the stressed volume is:

$$\begin{aligned} V_S &= 1.2 \times 10^{-3} \times 10^4 \\ &= 12\ \mathrm{cm}^3 \quad . \end{aligned}$$

The factor 1.2×10^{-3} is defined in Figure 2-5. Inserting the stressed volume of 12 cm^3 for a 100 meter length of RG-58 in the above equation yields a value of E_S for dielectric breakdown of 1.5×10^6 V/cm, which is equivalent to an applied voltage of 7.8×10^4 V between the center conductor and shield using a field enhancement factor of 19 for RG-58 (see Figure 2-5).

III. DAMAGE PRODUCED BY LARGE CURRENT/COULOMB DRIVE IN MF ANTENNA WITH PUNCTURED DIELECTRIC

1. INTRODUCTION

Sections of the (medium frequency) MF antenna and RG 220, which forms the central portion of the MF antenna, were subjected to high current pulses (170 to 200 kA) where the current was forced to flow to ground via an arc from the center conductor through a puncture in the dielectric. These tests were performed to determine the current drive threshold that would produce significant damage to the copper center conductor and/or the polyethylene dielectric. Failure of the antennas would result from complete vaporization of the conductor at the puncture site or sufficient dielectric erosion to provide a low impedance shunt from the center conductor to the surrounding earth.

2. EXPERIMENTAL ARRANGEMENT

The experimental configuration used for the MF antenna current drive experiment is shown in Figure 3-1. Figure 3-1 shows the cable under test connected to MCAIR pulser #4 in its normal 10 stage configuration. During current drive, the test cable was placed in a metal cylinder 0.36 meter tall and 1 meter diameter. The cylinder was filled with soil type DWP-25 (Ref. 3-1) with a water content of ~2.6 weight percent. The electrical conductivity and relative dielectric constant for this soil type and water content are shown in Figure 3-2. At 10^5 Hz the dielectric relaxation time is $\sim 3.5 \times 10^{-8}$ s. This soil type, with a relatively short relaxation time constant, was chosen to insure that the pulser voltage applied between the test cable center conductor and the grounded metal cylinder would appear across the punctured cable dielectric to initiate the discharge.

The discharge current flow from the metal cylinder to ground was measured by a Pearson 1049 current probe. ($I = 250$ kA, $\tau_r \sim 250$ ns). The voltage across the discharge was monitored by a calibrated resistive voltage divider. The inset of Figure 3-1 shows the details of the puncture in the dielectric. The puncture (0.16 cm diameter) was made by drilling through the dielectric to the center conductor of the test cable.

3-1 C. Mallon, R. Denson, T. M. Flanagan, and R. E. Leadon, 'Electrical Breakdown Characteristics in 0.8 to 1.0 meter Soil Samples,' Theoretical Note 318, 19 April 1982.

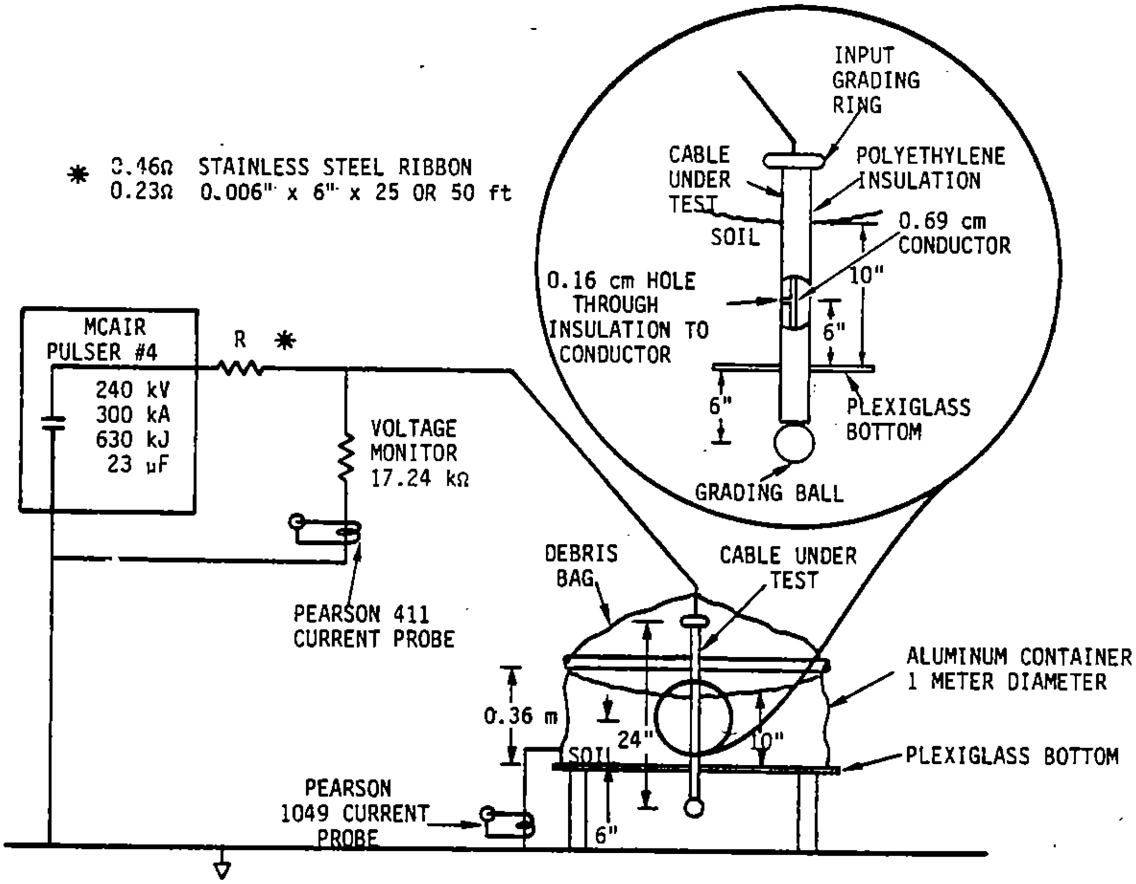

RE-04728

Figure 3-1. MF antenna current drive experiment using MCAIR pulser #4.

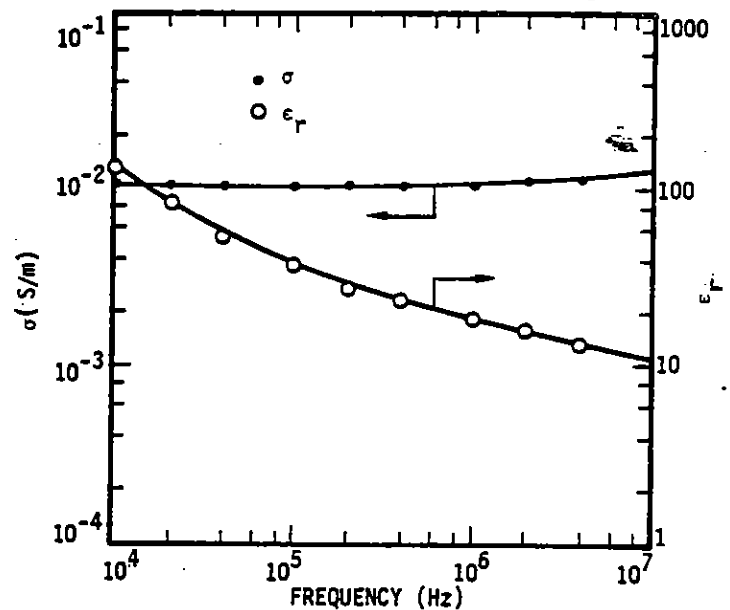

RE-04012

Figure 3-2. Low-field electrical conductivity and relative dielectric constant versus frequency (DWP-25-2.6%)

Figures 3-3, 3-4, and 3-5 are photographs of a cable sample in place for a current drive test. Figure 3-3 shows the cable sample installed in the soil filled cylinder supported by a dielectric stand. In Figure 3-4, a 3-inch diameter metal pipe is installed over the input electrode to reduce the radial fields which could produce arcing to the grounded metal cylinder. Grading rings at the cable sample ends and conductive-rubber-foam tubing at each end of the metal cylinder were also used to lessen the probability of unwanted arcs. Figure 3-5 shows the completed installation, which incorporated a plastic bag cover for the cylinder to contain the soil during current drive experiments and to maintain the water content of the soil.

In the normal 10 stage configuration pulser #4 has the following parameters:

$V = 220$ kV
$C = 23\ \mu$F
$Q \sim 5$ C.

To compare the damage produced in the antenna as a function of pulse width, peak current, and total coulombs, MCAIR pulsers 4 and 5 (Figure 3-6) were configured to discharge simultaneously into the test cable. For this test, pulser #4 was configured in a parallel mode (two-parallel-5 stage-sections) to increase its pulse width and coulomb drive. For this configuration, pulser #4 parameters were:

$V = 110$ kV
$C = 92\ \mu$F
$Q = 10$ C.

Pulser #5, shown schematically in Figure 3-6, used a series 3 mH inductor and 0.8 ohm resistor in its output to isolate the two pulsers during the relatively short pulse (~70 μs FWHM) from pulser #4. For this configuration the parameters of pulser #5 were:

$V = 12$ kV
$I \sim 12$ kA
$C = 6600\ \mu$F
$Q = 80$ C.

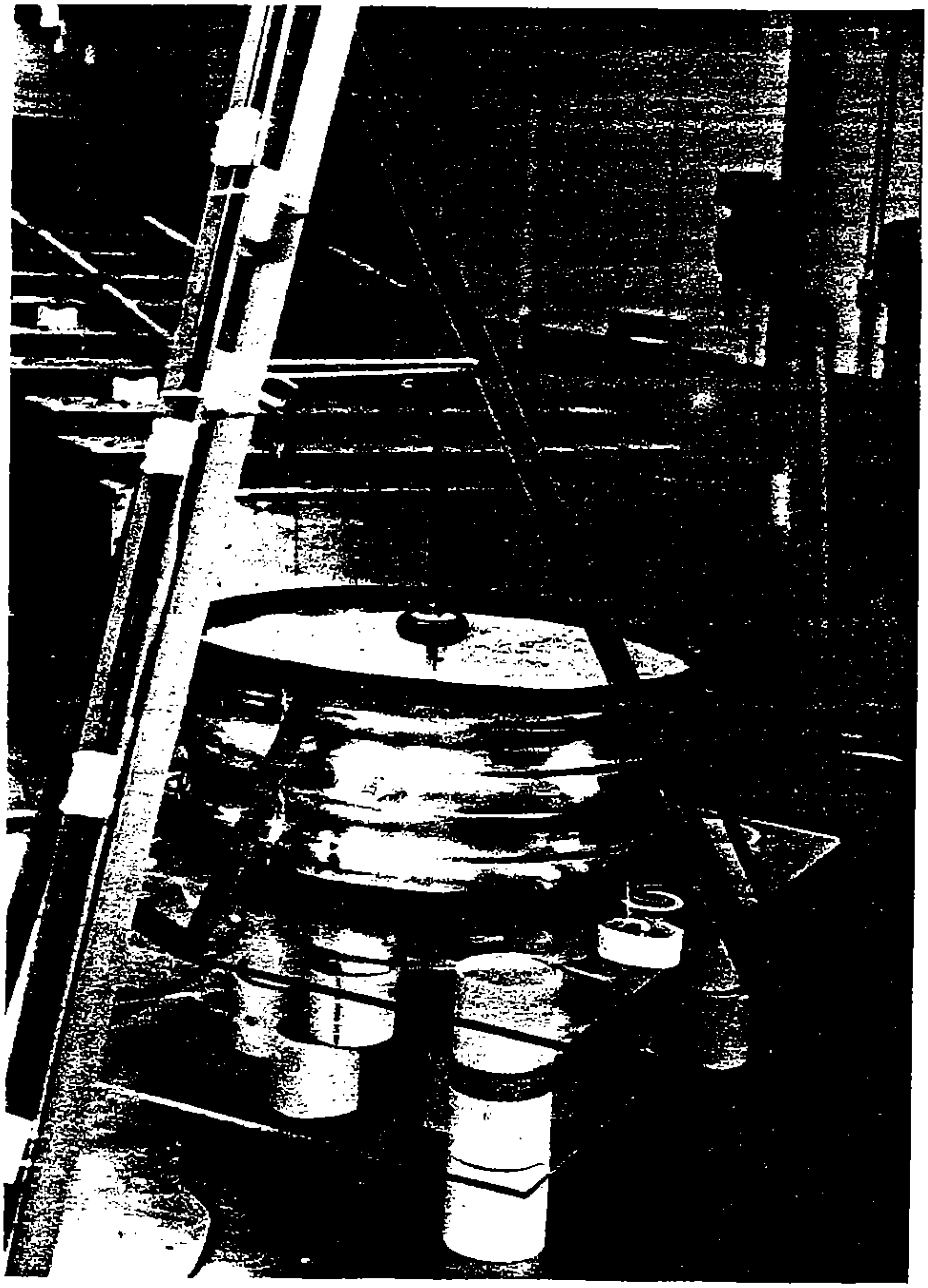

RE-04729

Figure 3-3. RG 220 (6) installed in soil-filled 1-m diameter, 0.36 m tall metal cylinder for current drive through punctured dielectric.

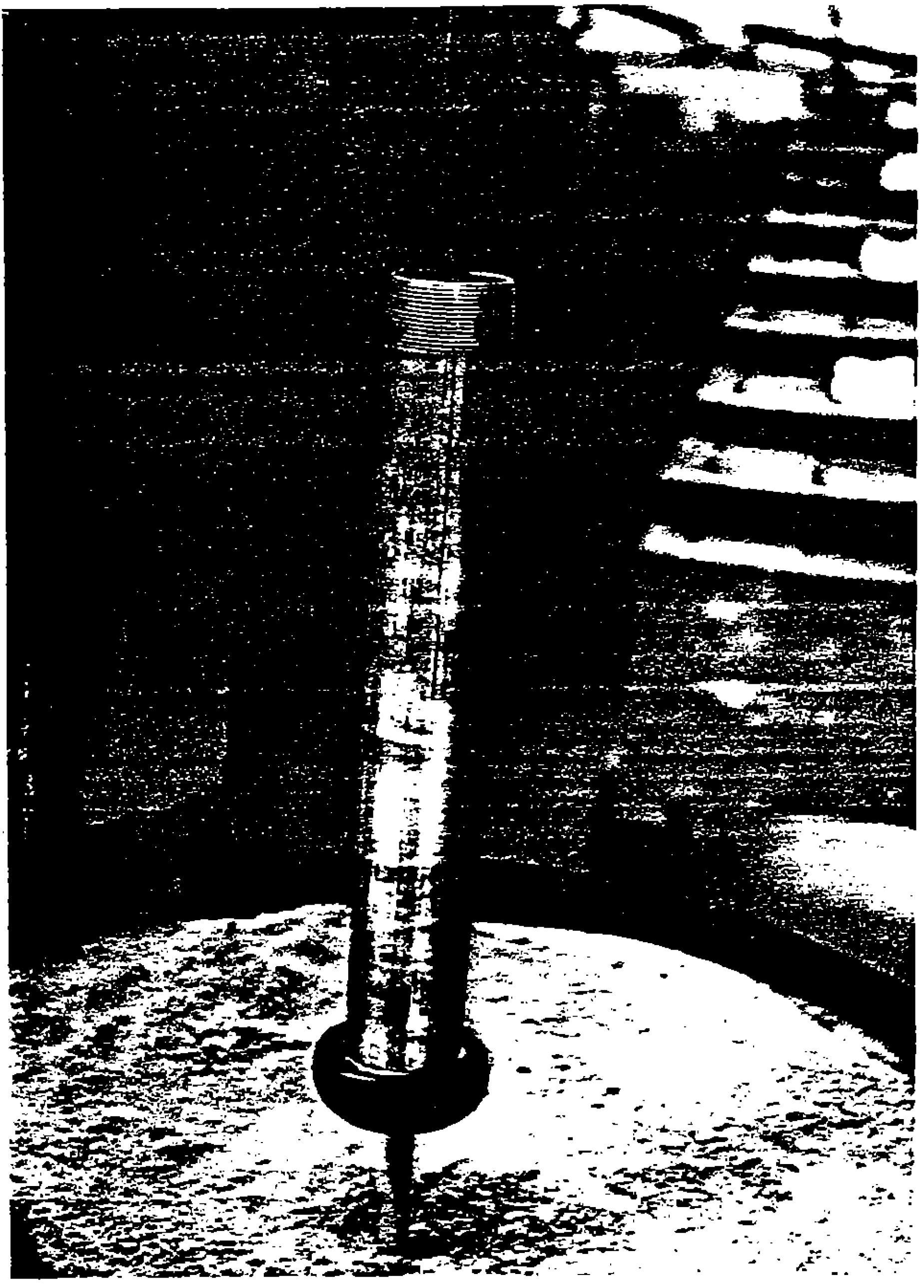

RE-04730

Figure 3-4. RG 220 (6) shown with grading ring and metal cylinder around input electrode to reduce radial electric fields.

RE-04731

Figure 3-5. RG 220 (6) installed in metal cylinder with debris bag in place.

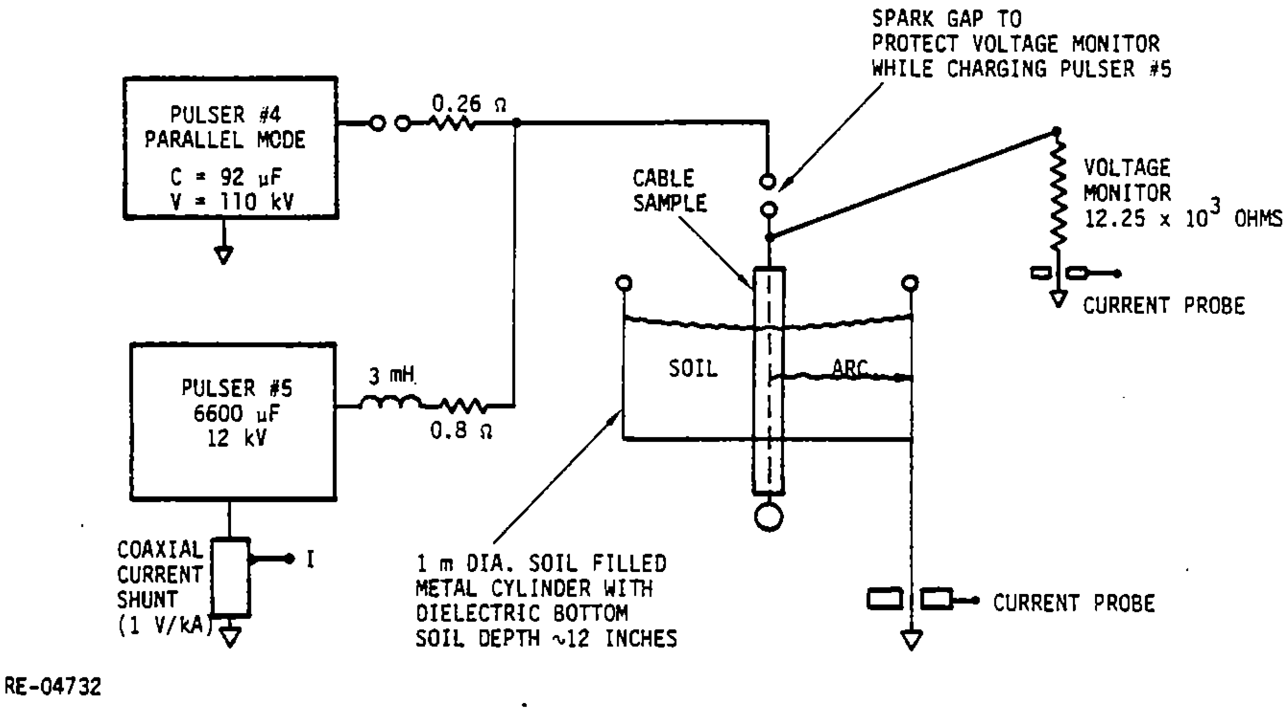

Figure 3-6. Pulsers 4 and 5 connection during current drive in MF antenna sample #19.

3. EXPERIMENTAL RESULTS

The current drive parameters for the two RG 220 samples and the two MF antenna samples tested are summarized in Table 3-1. RG 220 samples 6 and 14 and MF antenna sample 15 were driven by pulser 4 only with peak current ranging from 170 kA to 200 kA with a total charge of ~5 C. MF antenna sample 19 was driven by two pulsers to obtain a longer current pulse width and a higher coulomb level for damage comparison. Note that the action integral is only approximately 30 percent larger for the two pulser configurations (MF antenna 19) while the total charge is increased approximately by a factor of 14.

Table 3-1. Current Drive Parameters for RG 220 and MF Antenna Samples

	I_{PEAK} (kA)	FWHM	Action ($A^2 \cdot s$)	Coulombs
RG 220 (6)	170.0	38 μs	0.8×10^6	5.0
RG 220 (14)	183.0	38 μs	1.1×10^6	5.0
MF Antenna (15)	200.0	38 μs	1.2×10^6	5.0
MF Antenna (19)				
Pulser #4	150.0	75 μs	1.2×10^6	11.4
Pulser #5	8.5	6.5 ms	3.9×10^5	60.0
			1.6×10^6 Total	71.4 Total

a. RG 220(6) and RG 220(14)--Figures 3-7 and 3-8 show the current pulses used to drive RG 220 samples 6 and 14, respectively. Figure 3-9 is a photograph of RG 220(6) after a peak current drive of 170 kA, where the soil has been removed to show the damaged region. The action integral for this current drive was 8×10^5 $A^2 \cdot s$. This current drive level enlarged the diameter of the puncture in the polyethylene dielectric from ~0.16 cm to 0.35 cm and resulted in an insignificant copper loss from the center conductor.

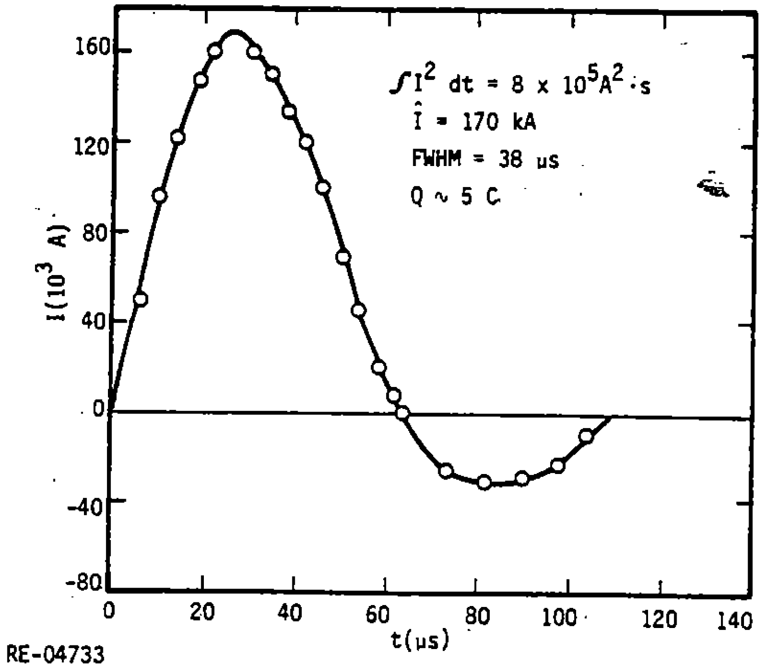

Figure 3-7. Current drive pulse for sample RG 220 (6).

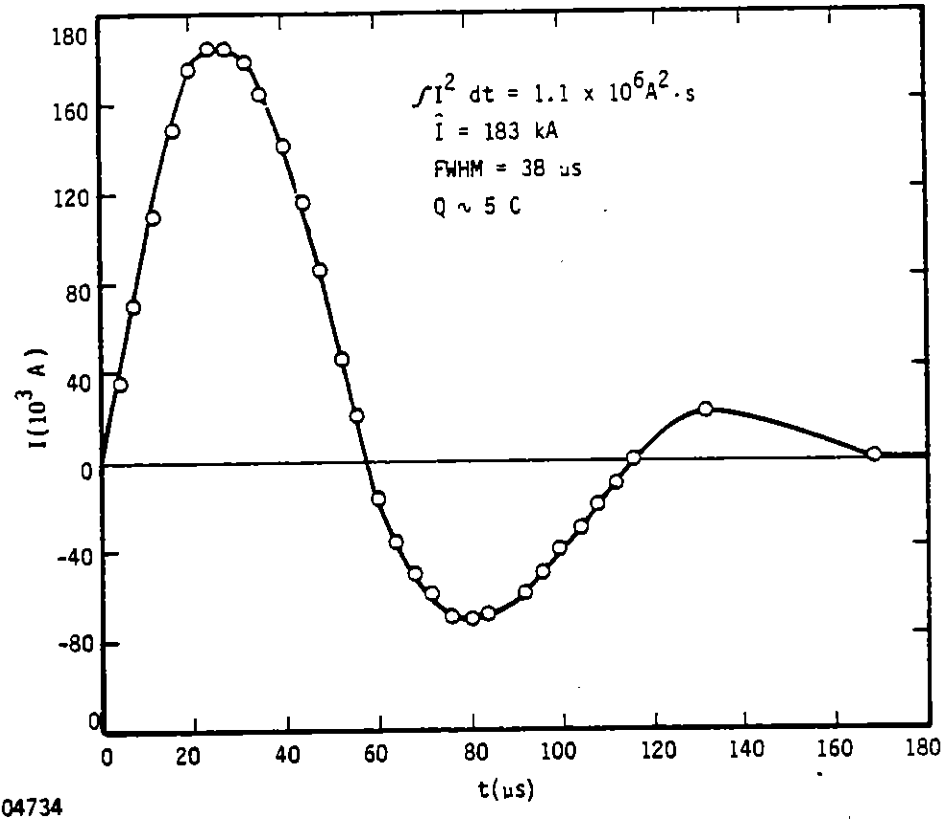

RE-04734

Figure 3-8. Current drive pulse for sample RG 220 (14)

Figures 3-10 and 3-11 are photographs of sample RG 220(14) after a peak current drive of 183 kA and an action integral of 1.1 x 10^6 A^2·s. This current drive level produced an approximate 18° bend in the cable at the dielectric puncture location. The pre-shot 0.16 cm diameter puncture enlarged to an approximate oval hole 0.9 cm by 0.38 cm. A rather uniform 10 mil decrease in the center conductor (0.69 to 0.66 cm) diameter occurred at the puncture site during the current drive. During the pulse, the pressure build-up between the center conductor and the dielectric was sufficient to force vaporized/carburized polyethylene out of the upper end of the cable sample after traversing the 12-inch long center conductor/polyethylene interface. Figure 3-12 is an x-ray of RG 220(14) after the current drive test. Note in Figure 3-12 that most of the cable deformation occurred in a plane 90° with respect to the puncture channel.

The leakage resistance from the center conductor to ground after the current drive tests for both RG 220 samples was ~ 6 x 10^5 ohms.

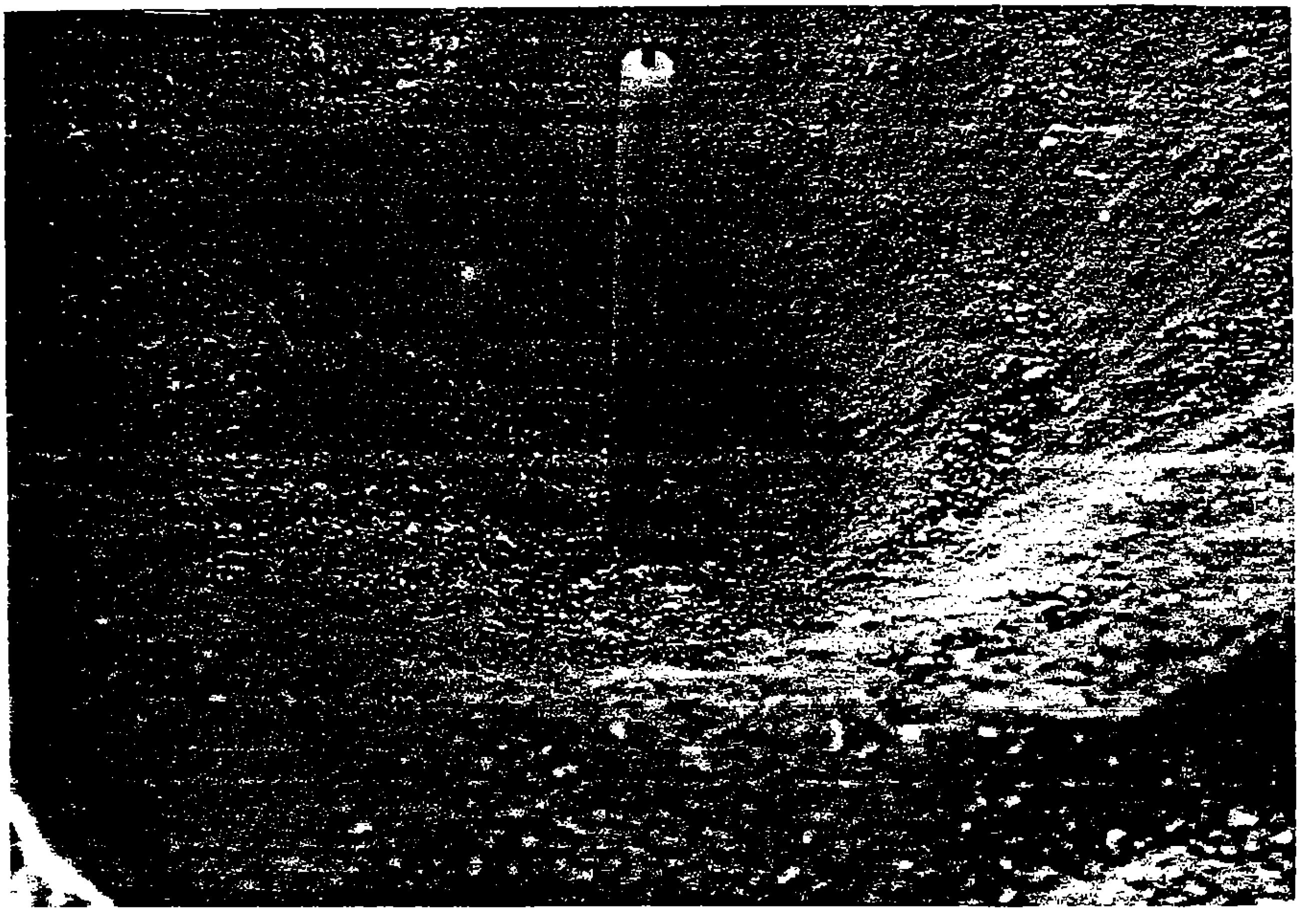

RE-04735

Figure 3-9. RG 220 (6) post current drive. $I_{PEAK} = 170$ kA. Soil removed to show damaged region.

b. **MF Antenna (15)**—This sample of MF antenna was subjected to a peak current drive of 200 kA with an action integral of 1.2×10^6 $A^2 \cdot s$. The current drive pulse is shown in Figure 3-13. Figure 3-14 is a post current drive photograph of this sample. The current drive level enlarged the 0.16 cm diameter dielectric puncture to an oval hole ~0.5 by 0.7 cm at the outer surface of the dielectric and a circular hole of 0.56 cm diameter at the center conductor/dielectric interface. A 0.025 cm decrease of the 0.69 cm diameter center conductor occurred at the puncture site during the current drive pulse. Vaporized/carburized polyethylene and/or copper was forced out of both ends of the 2 foot long cable sample as shown in Figure 3-15, which is a photograph of the lower end of the sample with the grading sphere removed. This material flowed both along the center conductor/dielectric interface and also between the two layers of polyethylene dielectric.

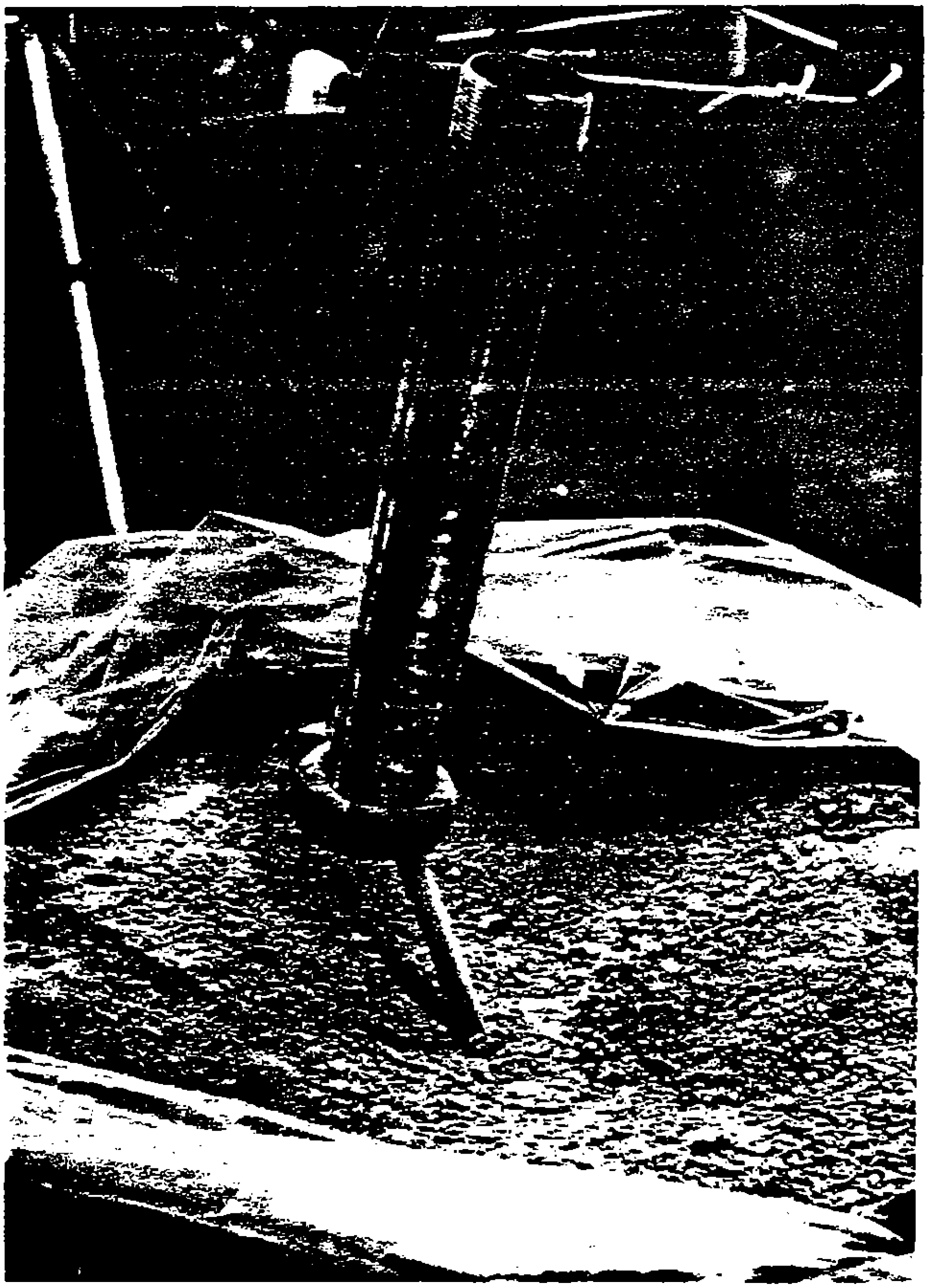

RE-04736

Figure 3-10. RG 220 (14) post 183 kA current drive.

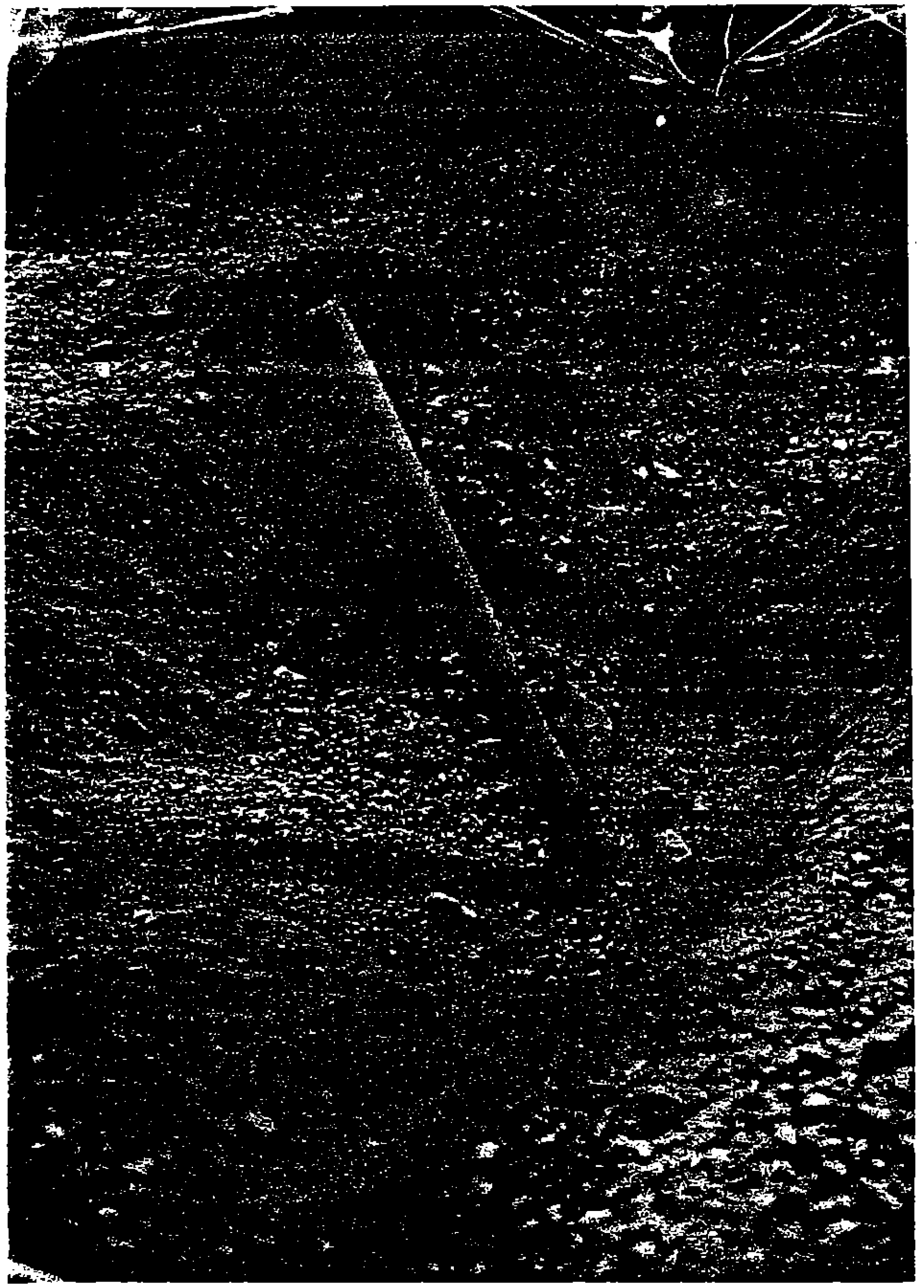

RE-04737

Figure 3-11. RG 220 (14) post 183 kA current drive. Soil removed to show damaged region.

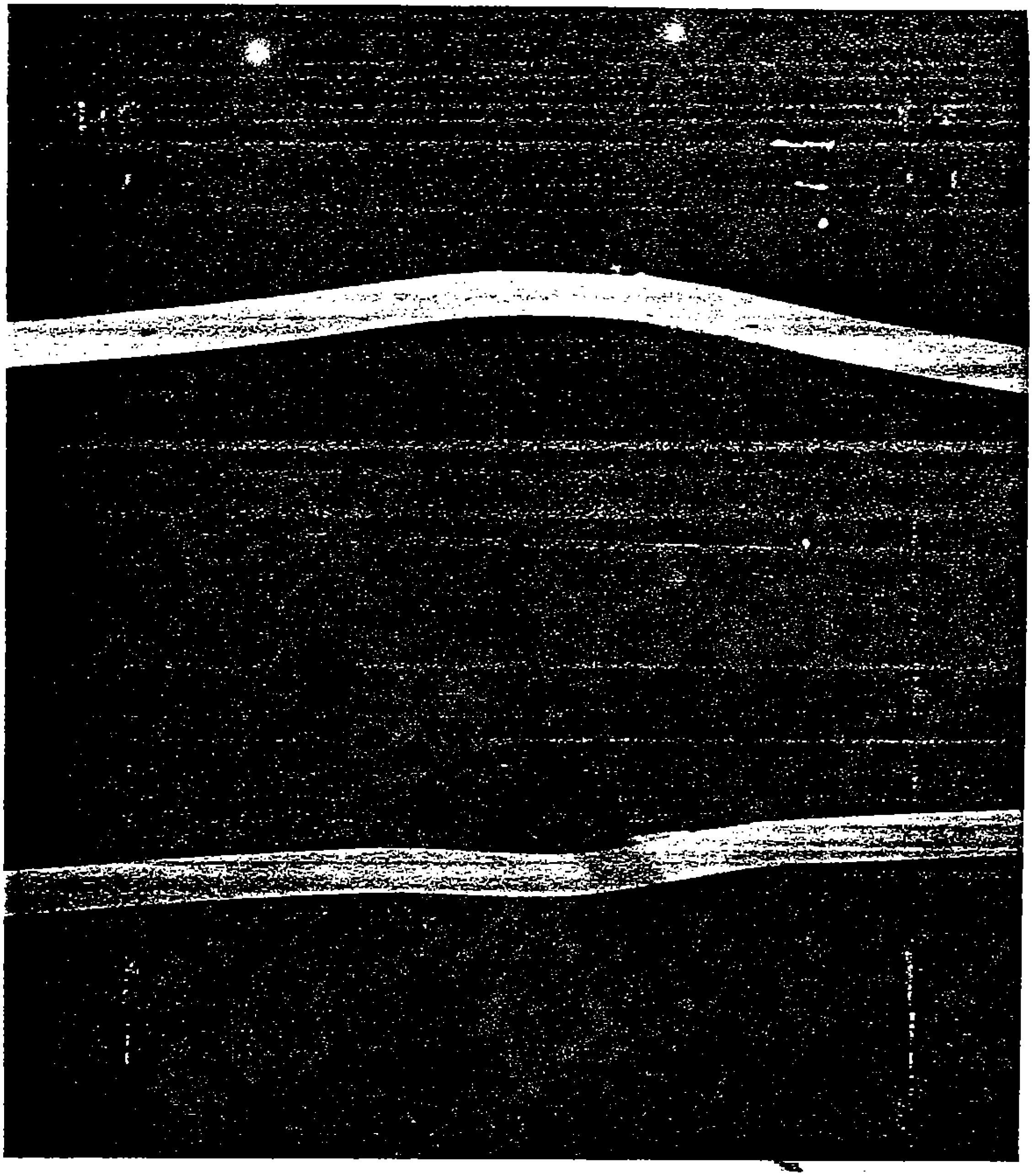

RE-04738

Figure 3-12. X-ray of RG 220 (14) after current drive test. The lower x-ray is a view at 90° to the dielectric puncture. The upper x-ray is a view at 0° looking down the puncture channel.

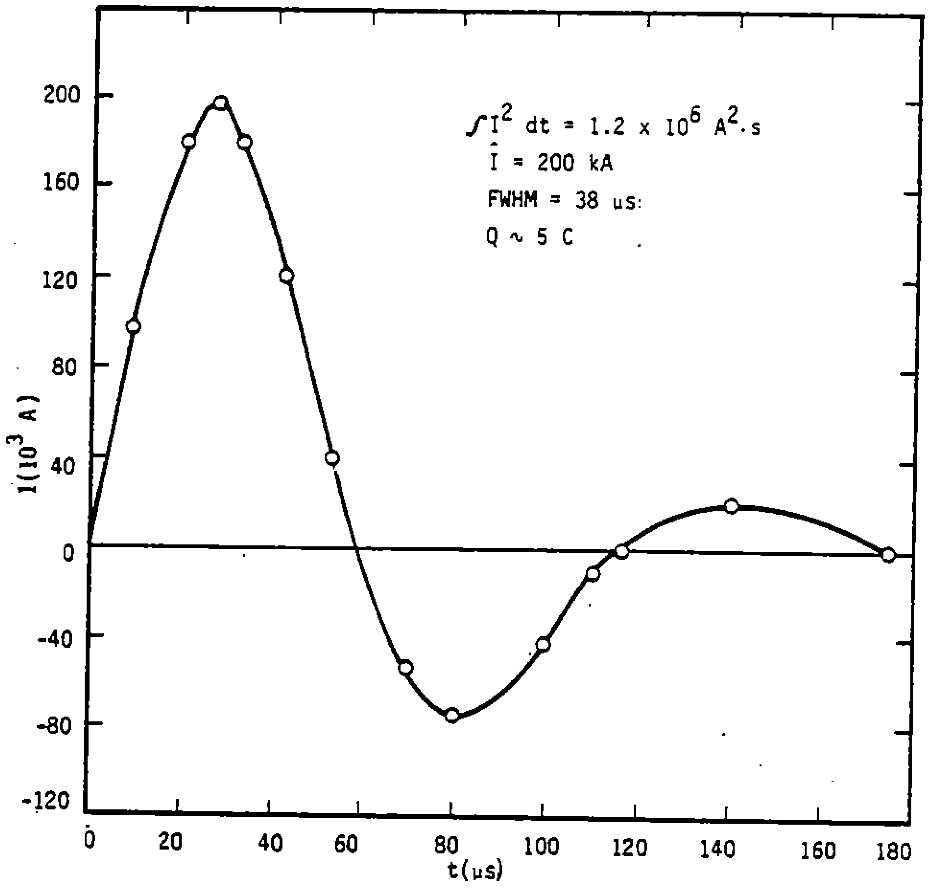

RE-04739

Figure 3-13. Current drive pulse for MF antenna (15)

The peak current drive level of 200 kA produced damage to the aluminum cylinder containing the MF antenna sample and soil. Figure 3-16 is a photograph of the experiment during the 200 kA current drive on MF antenna (15). The large light flash exiting the far side of the cylinder resulted from a hole being blown in the cylinder wall. This hole was approximately 4 inches vertical and 2 inches wide. While a rigorous calculation of the magnetic forces was not made, it appears these forces may have been adequate to produce the observed damage. The force between two parallel wires is:

$$F(\text{lbs}) = \frac{4.5\ I_1 \times I_2 \times 10^{-8} \cdot \ell}{d} \qquad (3\text{-}1)$$

RE-04740

Figure 3-14. MF antenna (15) after 200 kA peak current driver. Soil removed to show damaged region.

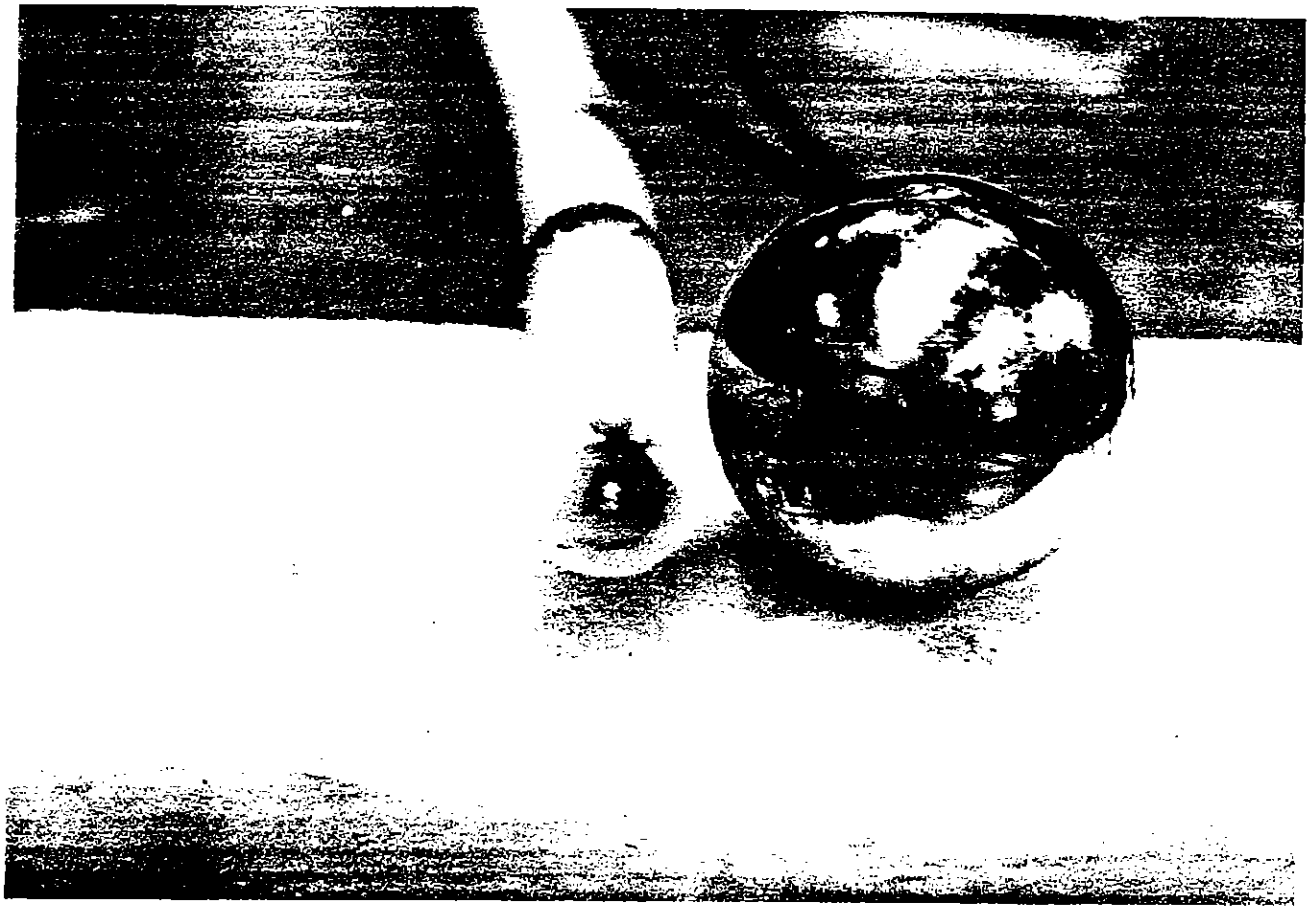

RE-04741

Figure 3-15. View of lower end of MF antenna (15) post current drive, showing the presence vaporized/carburized polyethylene at the cable end.

where ℓ is the wire length (in.) and d is the separation (in.). For I_1 and I_2 equal 200 kA the force is:

$$\begin{aligned} F &= 4.5 \times (2 \times 10^5)^2 \times 10^{-8} \frac{\ell}{d} \\ &= 1.8 \times 10^3 \frac{\ell}{d} \text{ lbs} \end{aligned} \tag{3-2}$$

assuming an ℓ/d ratio of unity yields a force of 1.8×10^3 pounds. It is not unreasonable that the outward force on the metal cylinder wall equaled or exceeded this value where the arc attached (Figure 3-17). At this point magnetic field crowding occurs to exert an outward force on the cylinder wall.

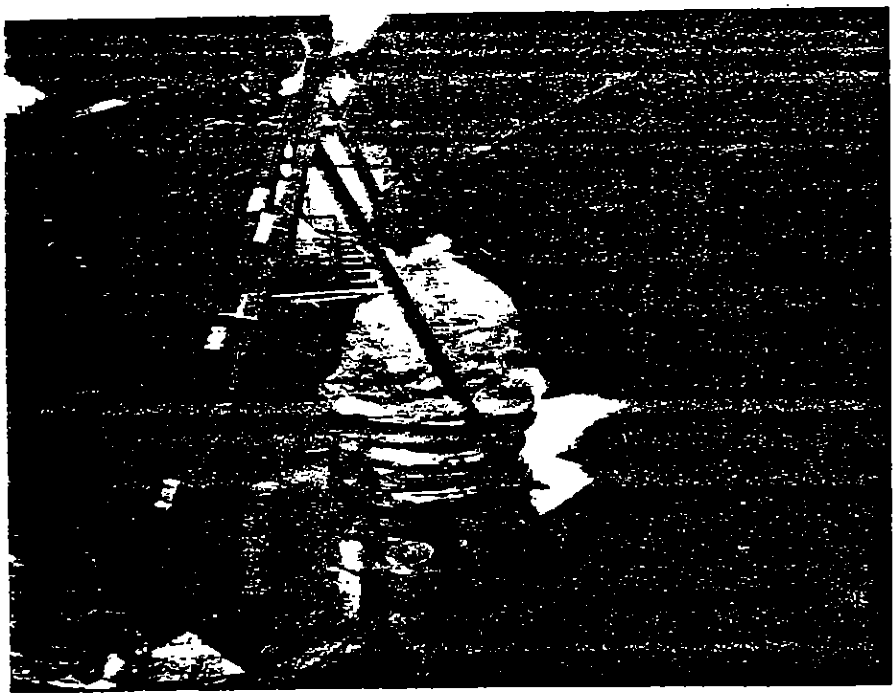

RE-04742

Figure 3-16. Photograph of current drive experiment during 200 kA peak current drive on MF antenna (15) sample. Light flash at right exits through hole blown in metal cylinder.

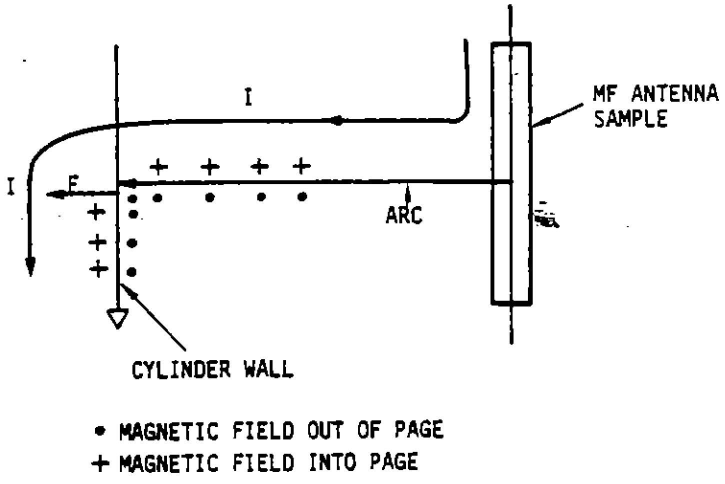

RE-04743

Figure 3-17. Schematic to estimate the magnetic forces at cylinder wall due to discharge current.

c. **MF Antenna (19)**--MCAIR pulsers #4 and #5 were used to drive current in this MF antenna sample to compare the damage produced by a longer-pulse-width-higher-coulomb drive with that produced by a shorter pulse width higher peak current drive for MF antenna (15). The pulser configuration for this current drive was shown in Figure 3-6 and the current drive parameters for the two MF antenna samples were compared in Table 3-1.

The combined pulser current drive for MF antenna 19 resulted in a peak current of 150 kA with a FWHM of 75 μs and a longer current pulse of 8.5 kA with a 6.5 ms FWHM (Figure 3-18). The total action and charge for the combined pulsers was $1.6 \times 10^6\ A^2 \cdot s$ and 71.4 C, respectively. This drive level resulted in an enlargement of the 0.16 cm diameter dielectric puncture to ~0.33 cm diameter at the outer dielectric surface and ~0.56 cm diameter at the center conductor/dielectric interface. At the dielectric puncture site the center conductor diameter was decreased from 0.69 cm to ~0.51 cm over a length of ~1.27 cm, and resulted in approximately a 1 gram copper loss. This amount of copper loss would not impair MF antenna operation.

Figure 3-19 is a photograph of the damaged region of the copper center conductor of MF antenna (19) after the combined pulser current drive.

4. ARC RESISTANCE DURING CURRENT DRIVE

The resistance of the arc through the 0.5 meter of soil between the driven cable sample with a punctured dielectric and the grounded metal cylinder was determined from current and voltage measurements during the current drive pulse. The small output resistor (~0.25 ohm) used in series with pulser 4 output and the small arc resistance (~0.2 ohms) caused the pulser to ring with a period of about 200 μs. The large time-rate-of-change of current, coupled with the inductance of the connecting leads to the cable sample plus the inductance of the arc itself, required a relatively large voltage correction [$V = L \times (dI/dt)$] to accurately determine the arc resistance. No attempt was made to determine this voltage correction, which requires knowing the inductance of the leads to the cable sample and the 0.5 meter long arc. The arc resistance, however, was calculated at the first positive and negative peaks of the current pulse where dI/dt is zero and no voltage correction is required. These arc resistance values are given in Table 3-2 along with the time of the measurement and value of current at that time. As can be seen in Table 3-2, the resistance of the 0.5 meter long arc decreased to ~0.1 to 0.2 ohms at current levels between 70 kA and 200 kA.

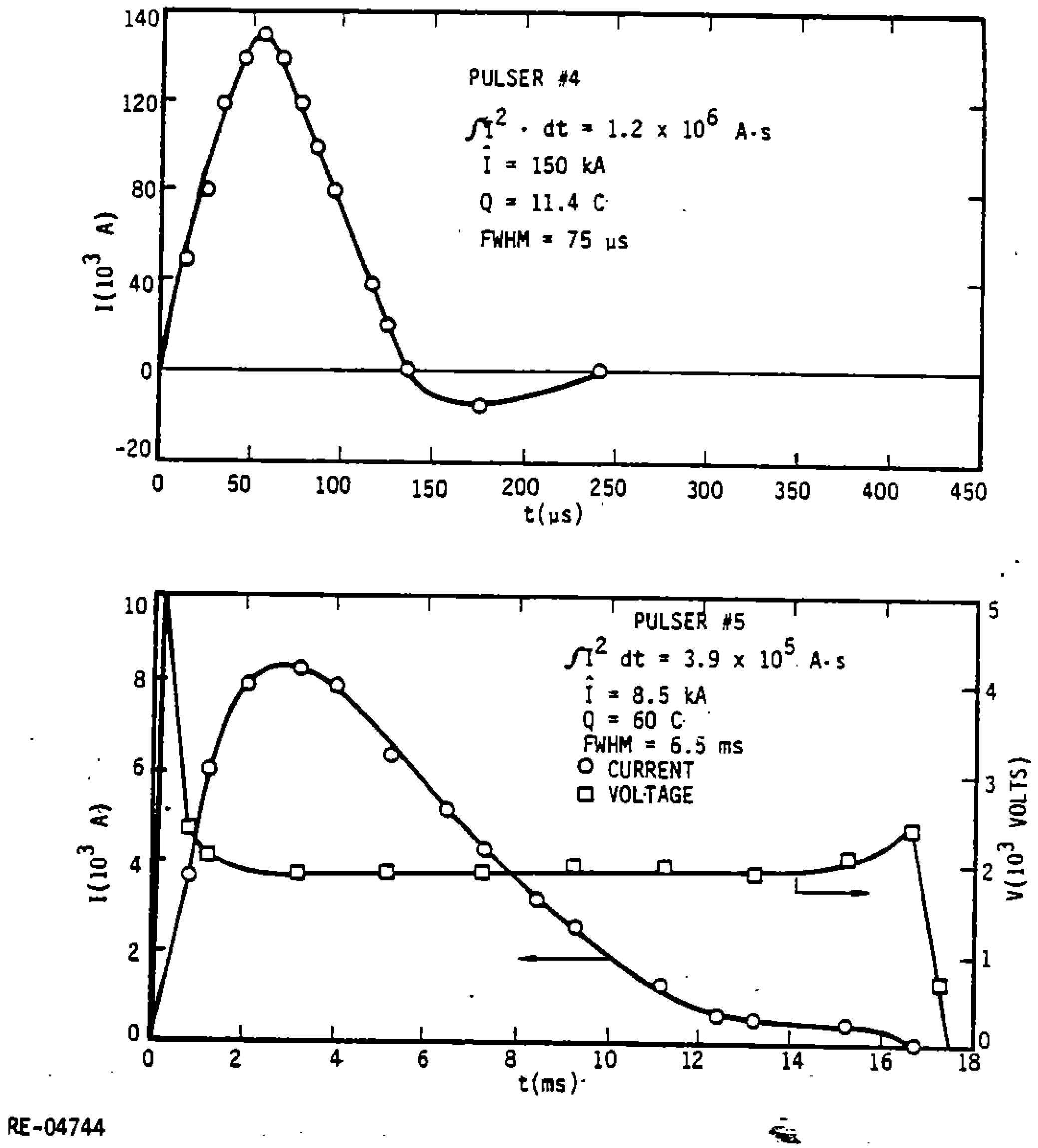

Figure 3-18. Voltage and current waveform for combined pulser current drive on MF antenna (19). Upper - Pulser 4, Lower - Pulser 5.

In Table 3-2, the arc resistances given for sample MF antenna (19) are those measured during the 75 μs FWHM, 150 kA current pulse produced by pulser 4. Pulser 5, which fired simultaneously with pulser 4, had a peak current of ~8.5 kA with a FWHM time of ~6.5 ms. For this lower value current and longer pulse width, no L·dI/dt voltage correction was required to accurately determine the time dependent arc resistance, which is shown in Figure 3-20. Between ~3 and 16 ms the arc resistance increased from ~0.2 ohms to 9 ohms. At 16 ms the measured voltage across the 0.5 meter arc was 2.4 kV at which point the arc appears to extinguish.

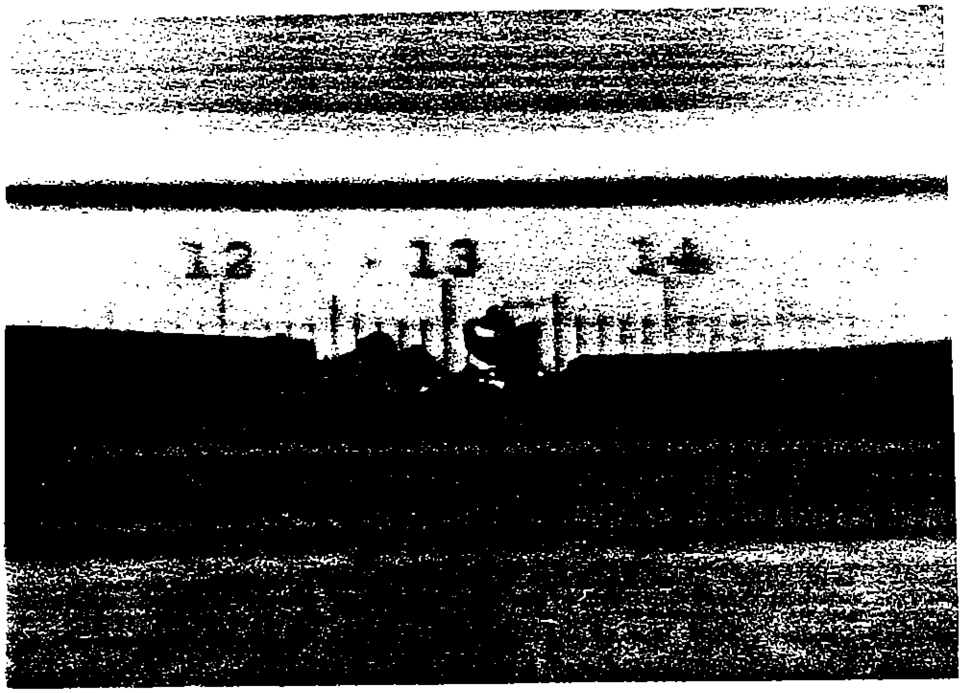

RE-04745

Figure 3-19. Photograph of the copper center conductor of MF antenna (19) after current drive. Small divisions on scale equal 1 mm.

Table 3-2. Resistance of Arc Through 0.5 Meters of Soil Between Test Cable With Punctured Dielectric and Grounded Metal Cylinder

	1st Positive Current Peak			1st Negative Current Peak		
Sample	t (μs)	I (kA)	R (ohms)	t (μs)	I (kA)	R (ohms)
RG 220 (14)	26	190	0.15	80	70	0.20
MF Antenna (15)	27	200	0.14	80	78	0.18
MF Antenna (19)	48	150	0.21	175	15	0.58

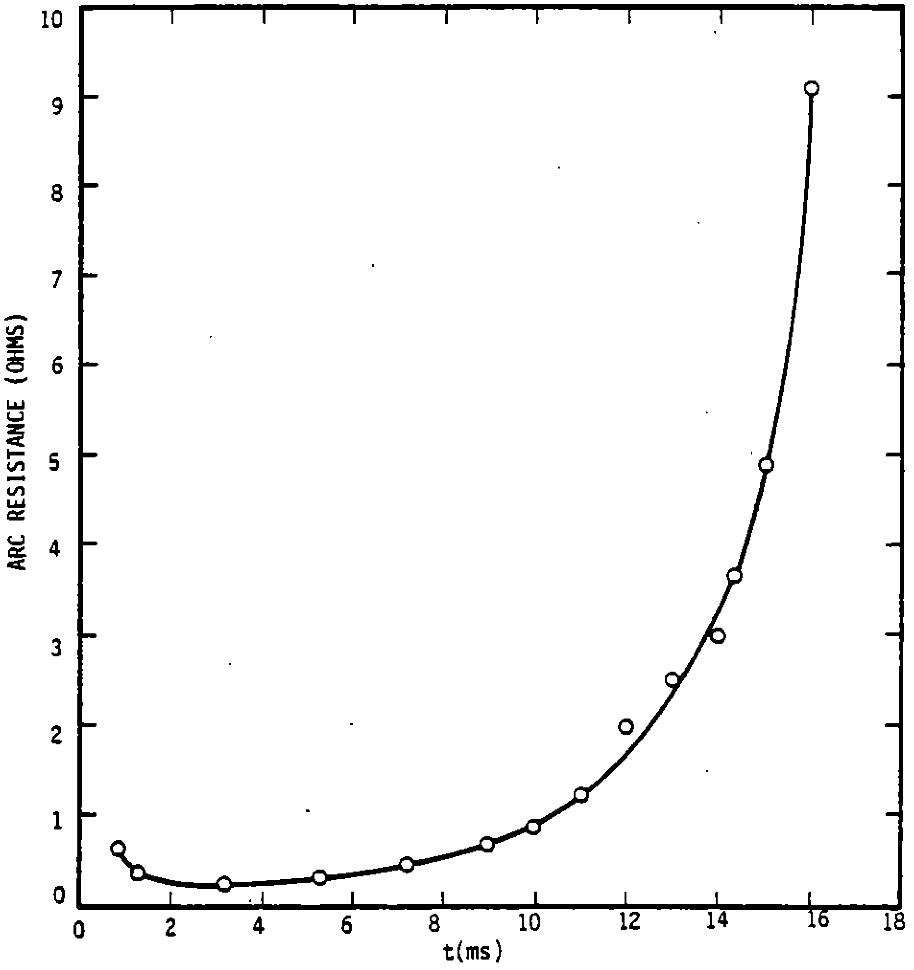

RE-04746

Figure 3-20. Arc resistance versus time during the 6.5 ms FWHM current pulse produced by pulser 5; MF antenna (19).

5. SUMMARY

Samples of the MF antenna and RG 220 with punctured dielectrics were driven with high-current-high-coulomb pulses up to 200 kA and ~70 C to investigate failure threshold. Antenna failure would result from complete vaporization of the copper center conductor, which would open-circuit the antenna, and/or sufficient dielectric erosion to provide a low impedance shunt between the center conductor and the surrounding earth.

The largest combined current/coulomb drive of 150 kA (75 μs FWHM) and 71 C (6.5 ms FWHM) resulted in approximately a 1 gram copper loss from the center conductor, which reduced the diameter of the copper center conductor from ~0.69 cm to 0.51 cm at the puncture site. The post shot shunt resistance from the antenna center conductor to the 1 meter diameter soil filled metal cylinder ($\sigma = 2 \times 10^{-2}$ S/m) was about 6×10^5 ohms. This degree of copper loss and shunt resistance would not impair operation of the MF antenna.

IV. WIRE VAPORIZATION/RESTRIKE EXPERIMENTS

1. INTRODUCTION

This section of the report presents the results of a series of experiments whose objective was to measure the vaporization/restrike characteristics of short sections of resistive (metal and graphite) cables using materials that were candidates for a resistive power link (R-wire) to a missile shelter.

The experiments were performed at the McDonnell Douglas (MCAIR) Lightning Facility in St. Louis, Missouri.

The information obtained from the series of experiments was (1) resistance of the different material types from ambient temperature through vaporization, (2) the voltage/electric field required to produce restrike after vaporization occurs, and (3) the effects of the surrounding medium (insulation, soil) on the vaporization and restrike characteristics. In addition, considerable experience was gained pertaining to confining the debris produced by the violent explosion (equivalent to ~150 grams of TNT) that accompanied vaporization/restrike.

a. Background--Current missile systems may incorporate several buried conductors that extend considerable distances away from the missile shelter. One possible buried conductor is a power line that provides electrical power to the shelter. Without some protection system, the EMP environment in the vicinity of the shelter would drive excessively large currents into the electrical equipment inside the shelter. One method to limit excessive currents is to include a section of resistive wire (R-wire) which can transmit the required power under normal operating conditions, but which will not permit excessive currents to reach the shelter during the EMP pulse. This resistive link does not have to survive the EMP environment, but must maintain isolation even if the wire vaporizes. Unfortunately for this purpose, it is well known that exploding wires will often restrike after vaporization; that is, when certain conditions are reached in the ionized vapor, avalanche ionization can occur and produce a highly conductive path through the plasma. If such a restrike should occur along the R-wire, it would negate the purpose of the R-wire, even though it had been vaporized, and destructive currents could reach the shelter.

Although exploding wires have been studied and used for many years, little was known about the vaporization and restrike characteristics in the microsecond time regime and of some of the materials proposed for the resistive wire, such as carbon fibers, Inconel, aluminum, and stainless steel. Perhaps a more important unknown was the effect of tightly confining the vaporized material by the cable jacket, and then the surrounding soil.

The purpose of the present experiments was to resolve some of these uncertainties for several candidate resistive cable materials and to provide data for coupling calculations. Although the actual R-cable would be many meters long, the present experiments were performed on short (0.4 m) sections of cable, mainly due to the limitations of the available pulsers, but also to provide better experimental control of the tests.

2. PRETEST ANALYSIS

A pretest analysis was performed to ensure compatibility between the pulser chosen for the vaporization/restrike experiments and the design of the resistive cable samples. That is, the pulser must be capable of supplying the required specific action to produce vaporization, and still have sufficient voltage to supply the required restrike electric field. The available specific action and the pulser voltage remaining at that time, therefore, dictated the sample cross-sectional area and its physical length.

The pretest analysis included:

a. Derivation of the pulser/return circuit resistance and inductance from previously measured short circuit I-V characteristics.

b. Calculation of the specific action that the above pulser can generate in iron samples with various cross-sectional areas and lengths.

a. __LCR Characteristics of Pulser__--For making realistic predictions of the pulser/sample responses, as an aid in analyzing the data, it was important to have a reasonably accurate estimate of the LCR characteristics of the pulser/return-circuit in the absence of the sample, that is, with the sample shorted. On a previous series of tests, the current out of the pulser and the voltage from the top of the load resistor (R_L, Figure 4-12) to ground were measured for a shorted sample for two values of R_L (0.23 ohms and 0.46 ohms). These results are shown in Figures 4-1 and 4-2. Assuming that R_L does not change significantly during the pulse, and knowing the pulser capacitance (22.6 μF) and the initial voltage (≈220 kV), it is straightforward to deduce the total effective inductance and resistance of the loop by trial-and-error fitting of the

I curve. Once the total L and R in the circuit are determined,, the curve of voltage across the load resistance can be used to determine the division of L and R between the pulser/return-line and the load resistor. Actually, this division is not required for predicting the responses of the circuit with non-shorted samples, but the fit to the curve gives further confidence in the derived circuit parameters. The derived circuit parameters are summarized in Table 4-1. The inductance in Table 4-1 for the pulser/return is much larger than the internal inductance of the pulser alone because it includes the inductance of a considerable length of ground path. Since the load resistor consists of a 6-inch wide metal tape looped back and forth to reduce the inductance, it is reasonable that its inductance should increase with its length, and, therefore, with its resistance. The calculated fits to the experimental curves using these parameters are also shown in Figures 4-2 and 4-3, and are quite satisfactory.

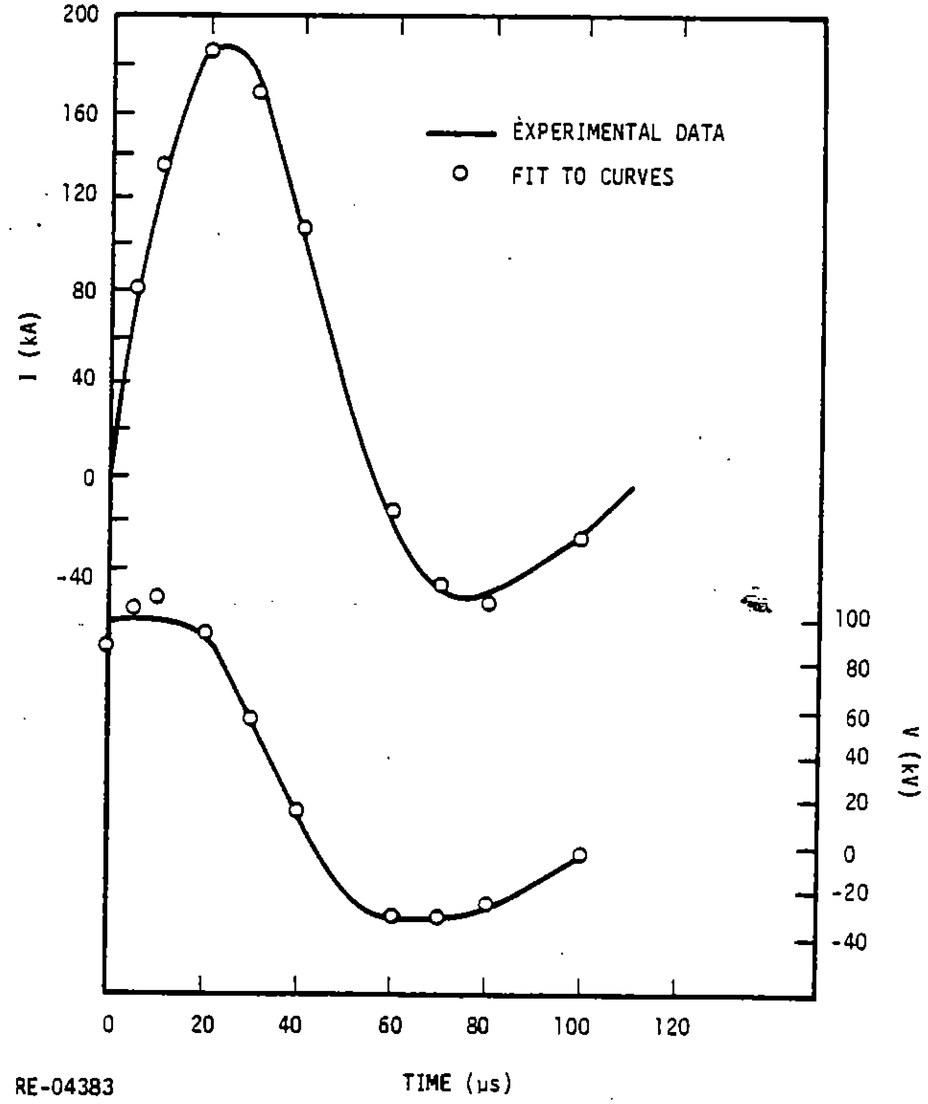

Figure 4-1. Current and voltage from pulser for shorted sample (R_L = 0.46 Ω)

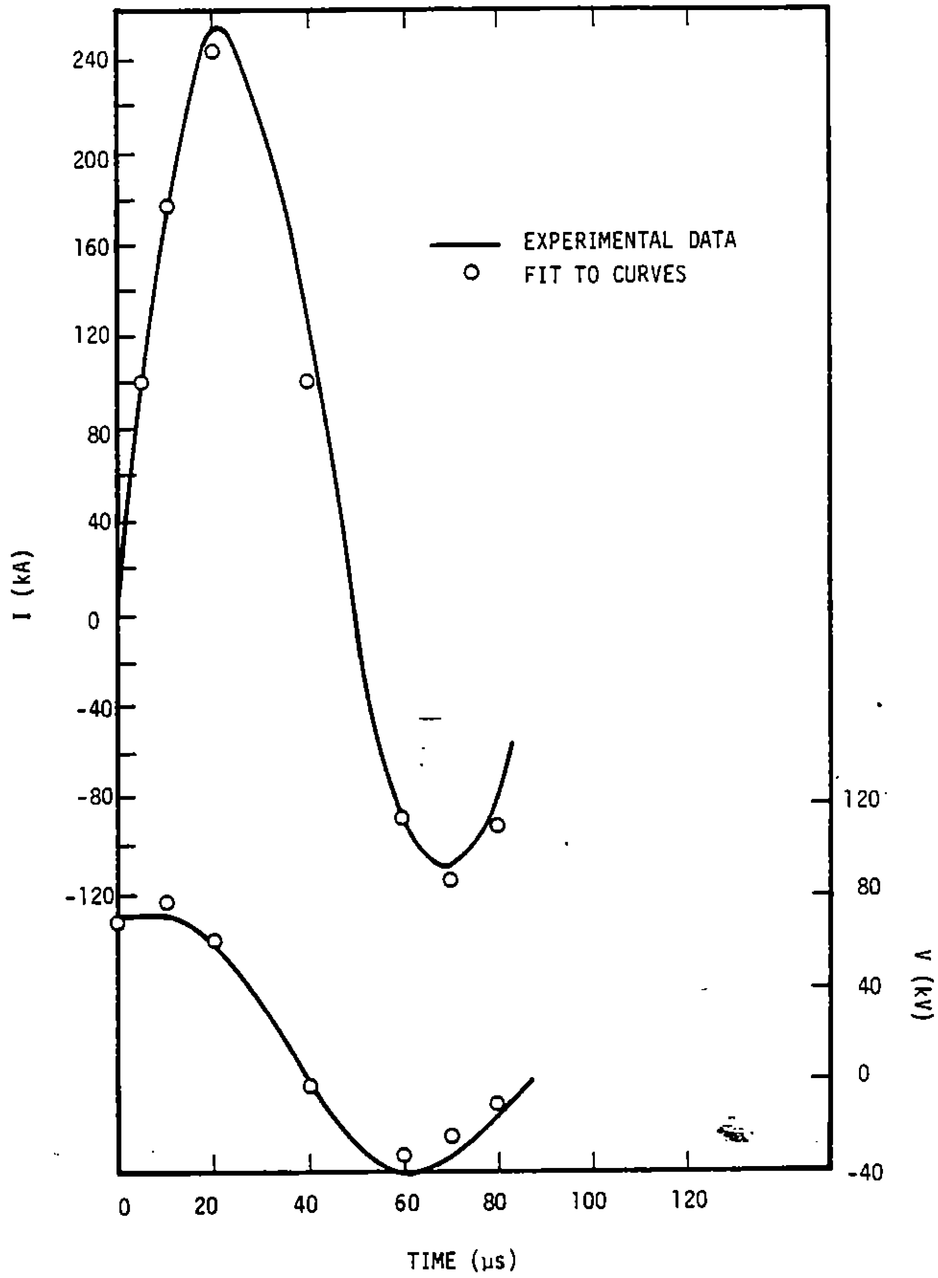

RE-04383

Figure 4-2. Current and voltage from pulser with shorted sample (R_L = 0.23 Ω).

Table 4-1. Derived circuit resistance and inductance for shorted samples

R_L (ohms)	0.23	0.46
Resistance of pulser/return (ohms)	0.075	0.075
Total circuit resistance (ohms)	0.305	0.535
Inductance of pulser/return (μ H)	7.5	7.5
Inductance of load resistor (μ H)	2.5	5.0
Total circuit inductance, L_C, (μ H)	10.0	12.5

b. Calculated Specific Action for Iron Cables--Using the pulser characteristics described in Section IV.2b and the curve of resistivity versus specific action for iron shown in Figure 4-3, the I-V response time histories of the circuit were calculated using a simple computer code to integrate the circuit equations for a time-varying resistivity and different sample cross-sectional areas and lengths. Some of these results are shown in Figures 4-4 through 4-8.

Figures 4-4 and 4-5 are for a 1/2-inch wide Fe ribbon for two pulser output resistances (R_L = 0.23 and 0.46 ohms), while Figures 4-6 and 4-7 give similar results for a 1/4-inch wide ribbon. For these calculations, the inductance of the sample (L_W) was assumed to be zero, so the voltage across the sample is purely resistive (IR_W). Figure 4-8 shows similar calculations for a 60 cm long, 1/2-inch wide ribbon, and R_L = 0.46 ohms, but with a sample inductance of 1 μ H. The purpose of this figure is to illustrate how much the sample inductance will change the measured voltage across the sample ($IR_W + L_W \dot{I}$ compared to IR_W). Also shown in Figure 4-8 is the calculated time history of $\dot{I}$.

Before discussing these curves, a word of caution about them is in order, especially regarding the voltage peak. This peak is a direct consequence of the assumed resistivity curve in Figure 4-3, which was obtained in exploding wire experiments in air. The fact that the present samples are enclosed by 280 mils of polyethylene, is very apt to significantly affect the resistivity curve after the point of vaporization (indicated in Figure 4-3). If the increase in resistivity after the vaporization point is due to expansion of the ionized vapor, this increase might not occur in the present samples if the polyethylene remains intact and continues to confine the vapor. In that case, the voltage curve would probably remain relatively flat after vaporization occurs, at a level corresponding to the resistivity of a tightly-confined ionized vapor. On the other hand, if the polyethylene ruptures and the vapor escapes to the surrounding soil, restrike might occur through the dilute vapor outside the cable jacket or through the residual vapor inside the polyethylene jacket when the vapor density decreases to a level that is conducive for a restrike. In this case, the voltage curve might be reasonably similar to the calculated curves in Figures 4-4 through 4-8. A third possibility is that the polyethylene will rupture and the vapor will escape from the jacket, but a restrike will never occur. In that case, the voltage curve would rise to the voltage still available in the pulser and it would remain there until the pulser voltage slowly decayed away via the internal resistance of the pulser.

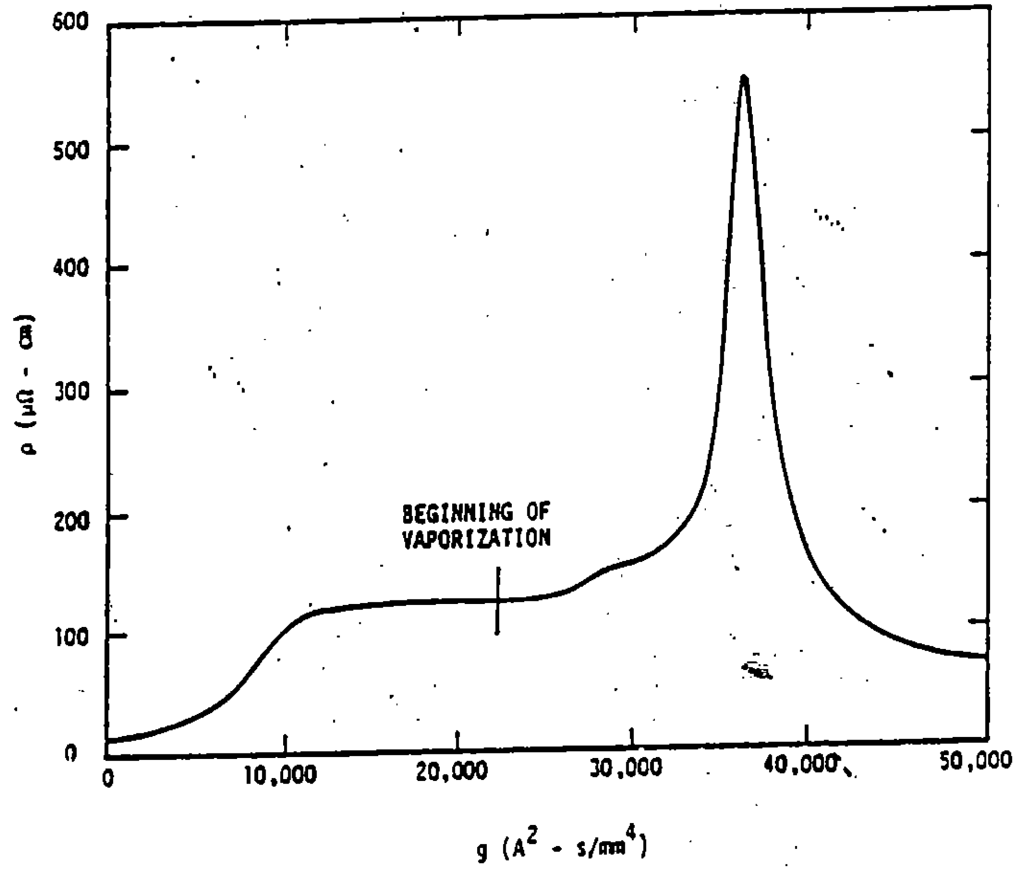

RE-04382

Figure 4-3. Resistivity versus action for iron (Ref. 4-1)

4-1 T. J. Tucker and R. P. Toth, 'EBWI: A Computer Code for the Prediction of the Behavior of Electrical Circuits Containing Exploding Wire Elements,' Sandia Laboratories Report SAND-75-0041, April 1975.

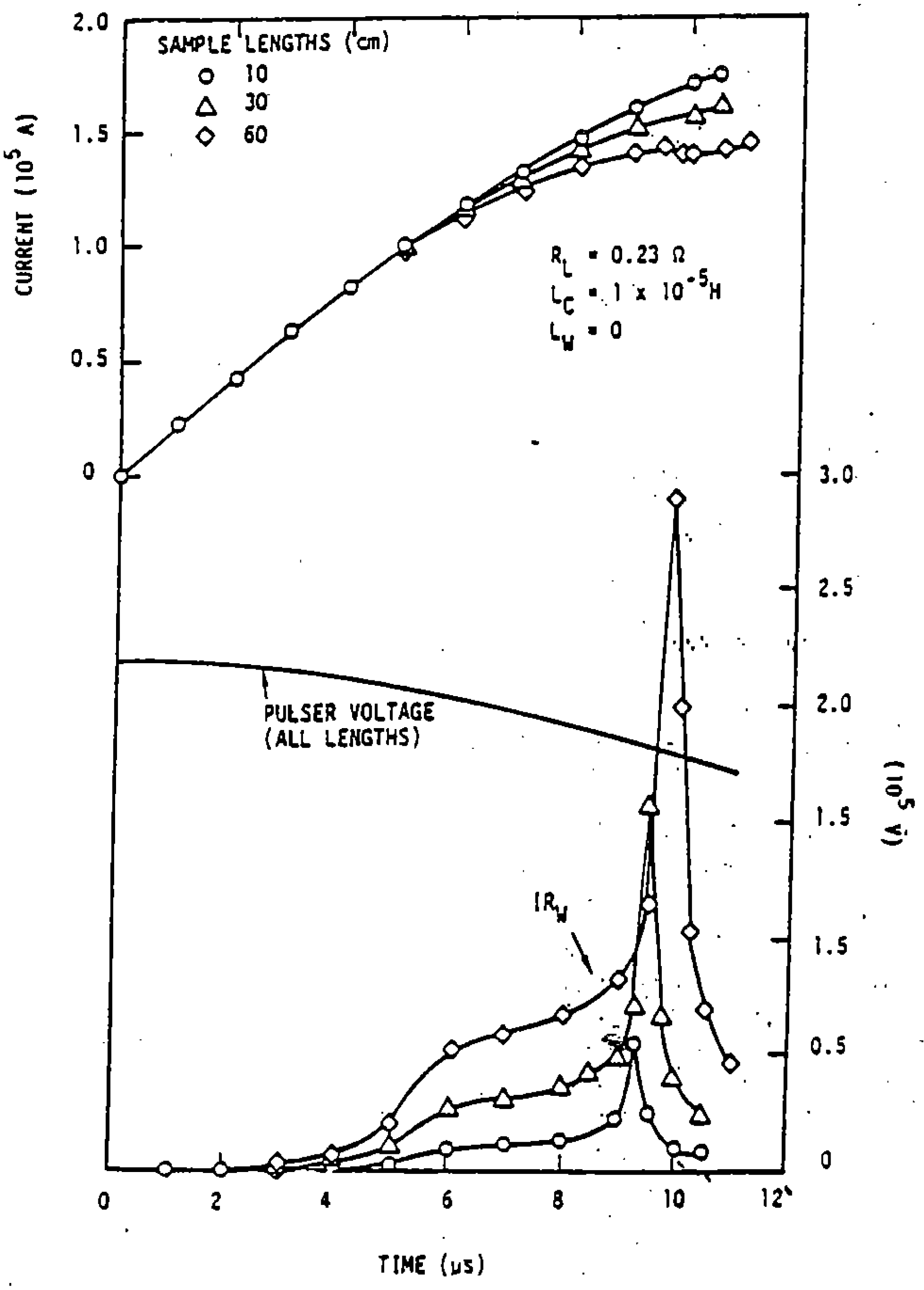

RE-04381

Figure 4-4. Current and IR voltage across sample for 1/2-inch Fe ribbon.

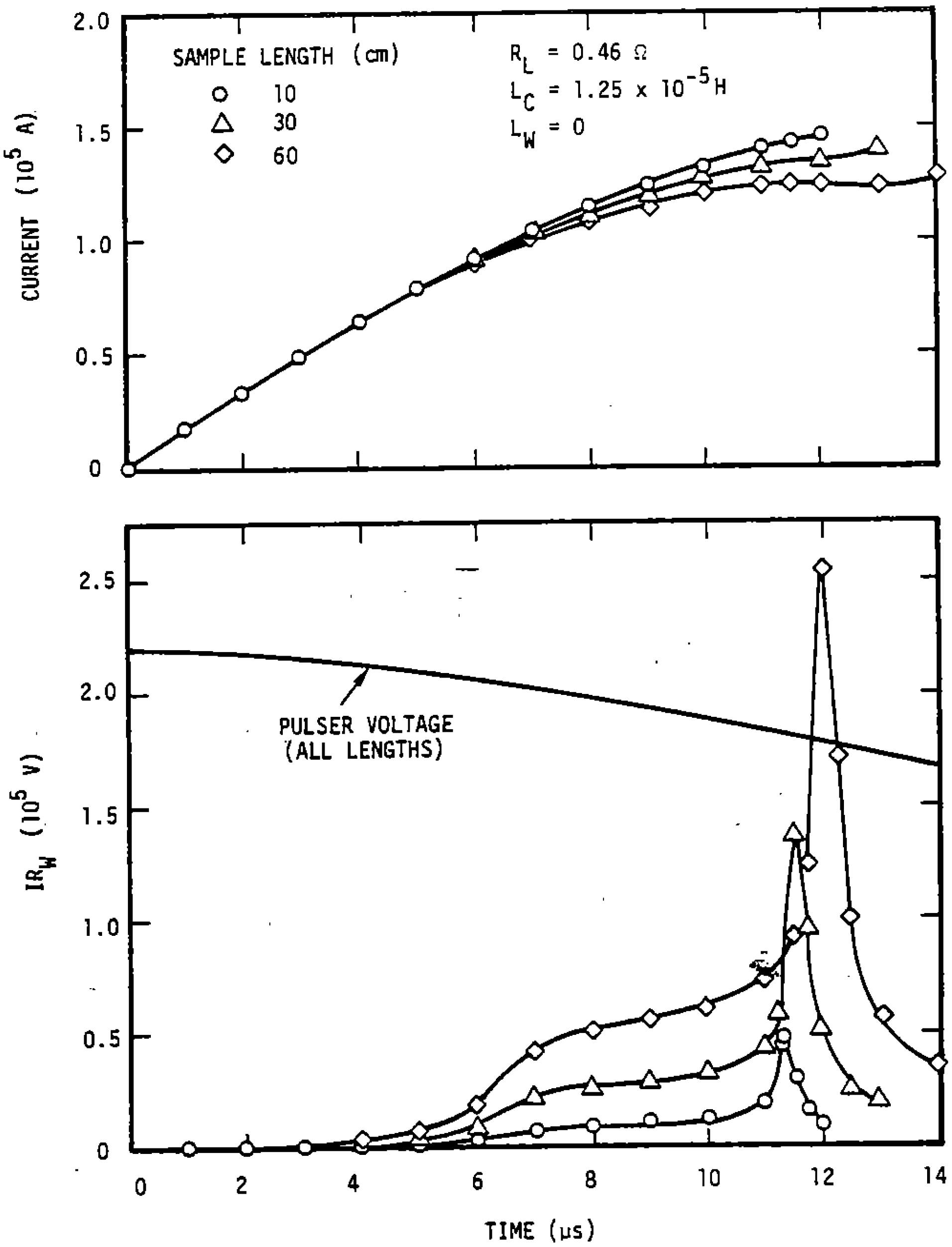

RE-04380

Figure 4-5. Current and IR voltage across sample for 1/2-inch Fe ribbon.

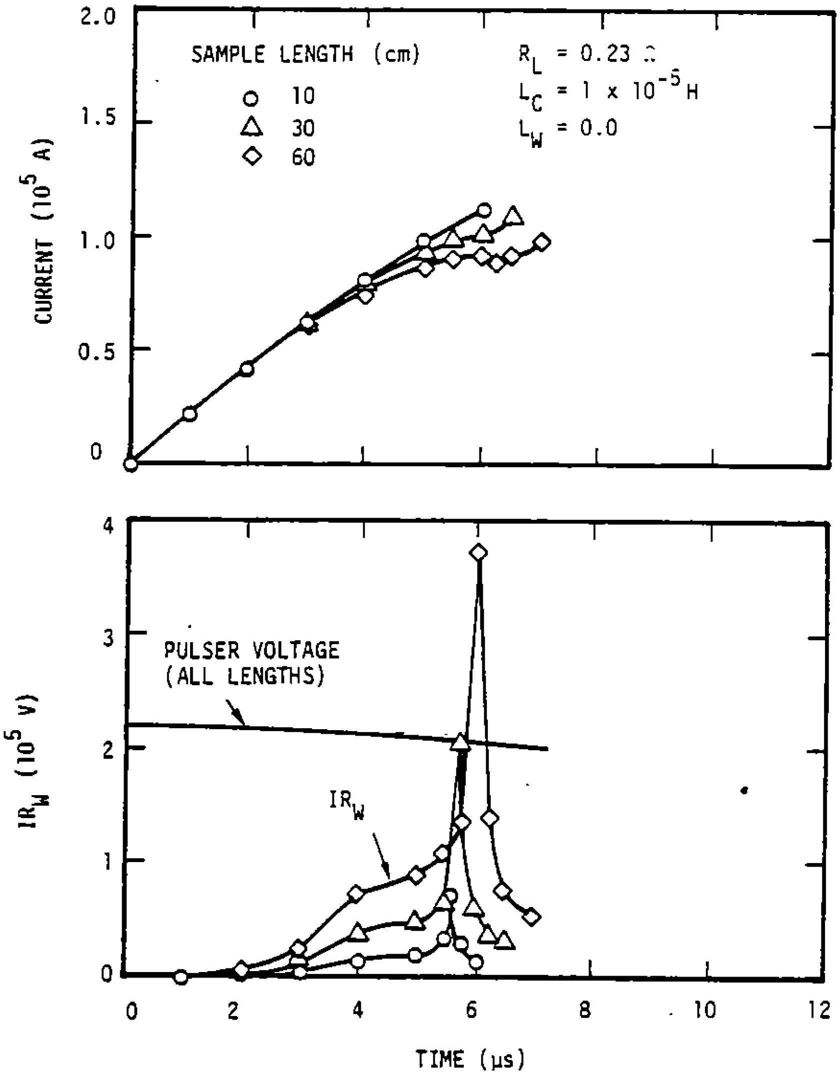

RE-04379

Figure 4-6. Current and IR voltage across sample for 1/4-inch Fe ribbon.

Keeping the above caveats in mind, several conclusions were drawn from the results of Figures 4-4 through 4-8.

(1) For 1/4-inch Fe ribbons, the burst condition (peak resistance) can be reached when the remaining pulser voltage is about 200 kV. For 1/2-inch ribbons, the corresponding condition is reached when the pulser voltage is about 175 kV. Since action varies as (cross-sectional area)$^{-2}$, the ribbon width could not be much greater than 1/2 inch and still reach the burst condition with this pulser. This conclusion is not sensitive to the details of the resistivity curve after vaporization.

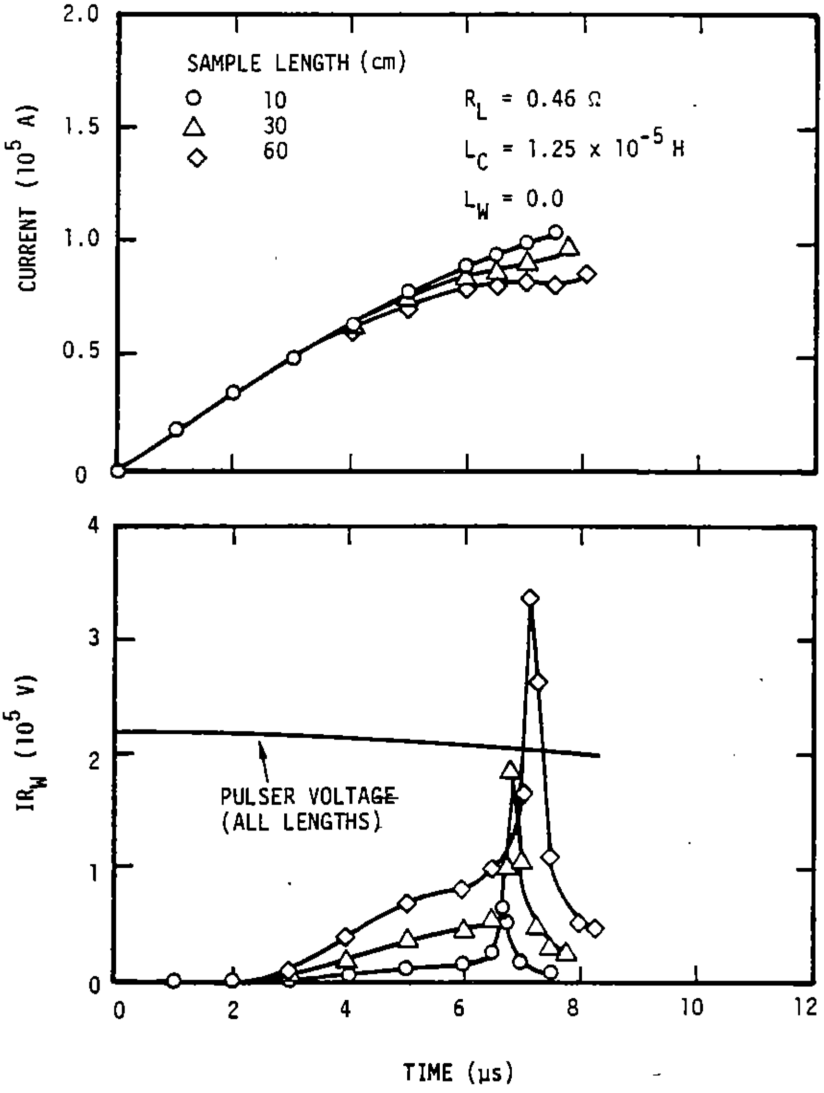

RE-04378

Figure 4-7. Current and IR voltage drop across sample for 1/4-inch Fe ribbon.

(2) The peak voltage across the sample increases approximately linearly with sample length. This result is a direct consequence of assuming a peak resistivity of 550 microhms-centimeter for the vaporized iron. If an open circuit actually occurs, the voltage across the sample would rise to essentially the remaining pulser voltage, independent of the sample length.

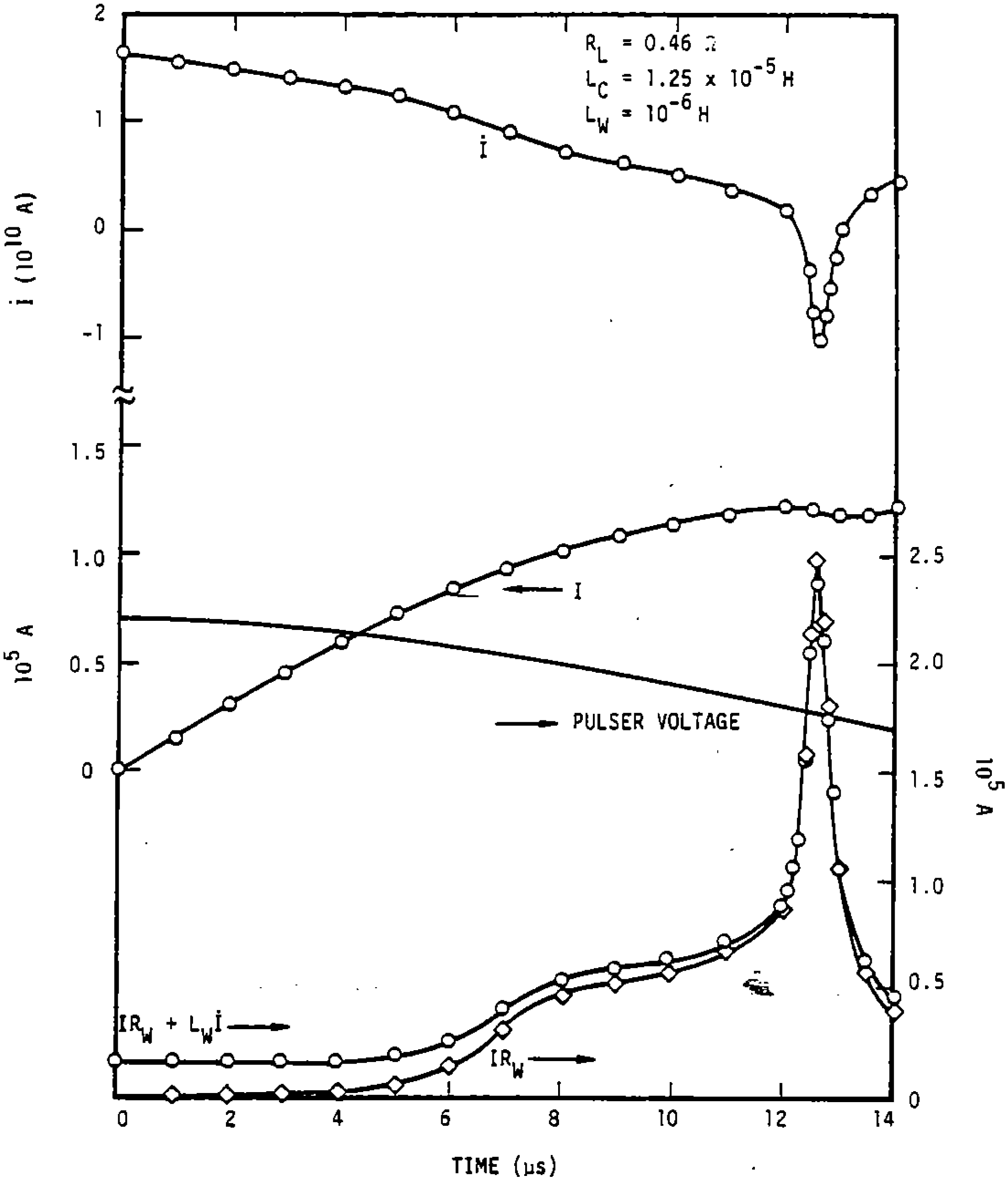

RE-04377

Figure 4-8. Current and voltage for 1/2-inch wide, 60 cm long Fe ribbon including inductance in sample.

(3) For the longer samples, the voltage across the sample considerably exceeds the residual pulser voltage. The extra voltage comes from the $L\dot{I}$ term in the circuit equation. The amount that the peak voltage exceeds the pulser voltage is sensitive to the assumed shape of the resistivity versus action curve (Figure 4-3) above the vaporization point.

(4) If necessary to avoid breakdown through air or soil, the sample (ribbon) length could probably be as much as 1 meter for Fe conductors and still achieve vaporization, at least with the 1/4-inch ribbon.

(5) The sample inductance has a relatively large effect on the measured sample voltage at early times in Fe samples, but it has a relatively small effect near the peak voltage.

3. EXPERIMENT DESCRIPTION

a. Sample Materials and Fabrication

(1) R-Wire Types—Five types of resistive conductors were examined during the R-wire vaporization/restrike tests:

(a) Low carbon steel - C1010.

(b) Inconel 600 (Inconel has been abbreviated IN in the report and should not be confused with In, Indium).

(c) 302 stainless steel.

(d) 2024 aluminum.

(e) Graphite fiber.

(2) R-Wire Geometry—Three types of cable were used during the tests: twisted graphite fiber, linear metallic, and helical metallic. Figure 4-9 shows the linear and helical cables in progressive stages of assembly.

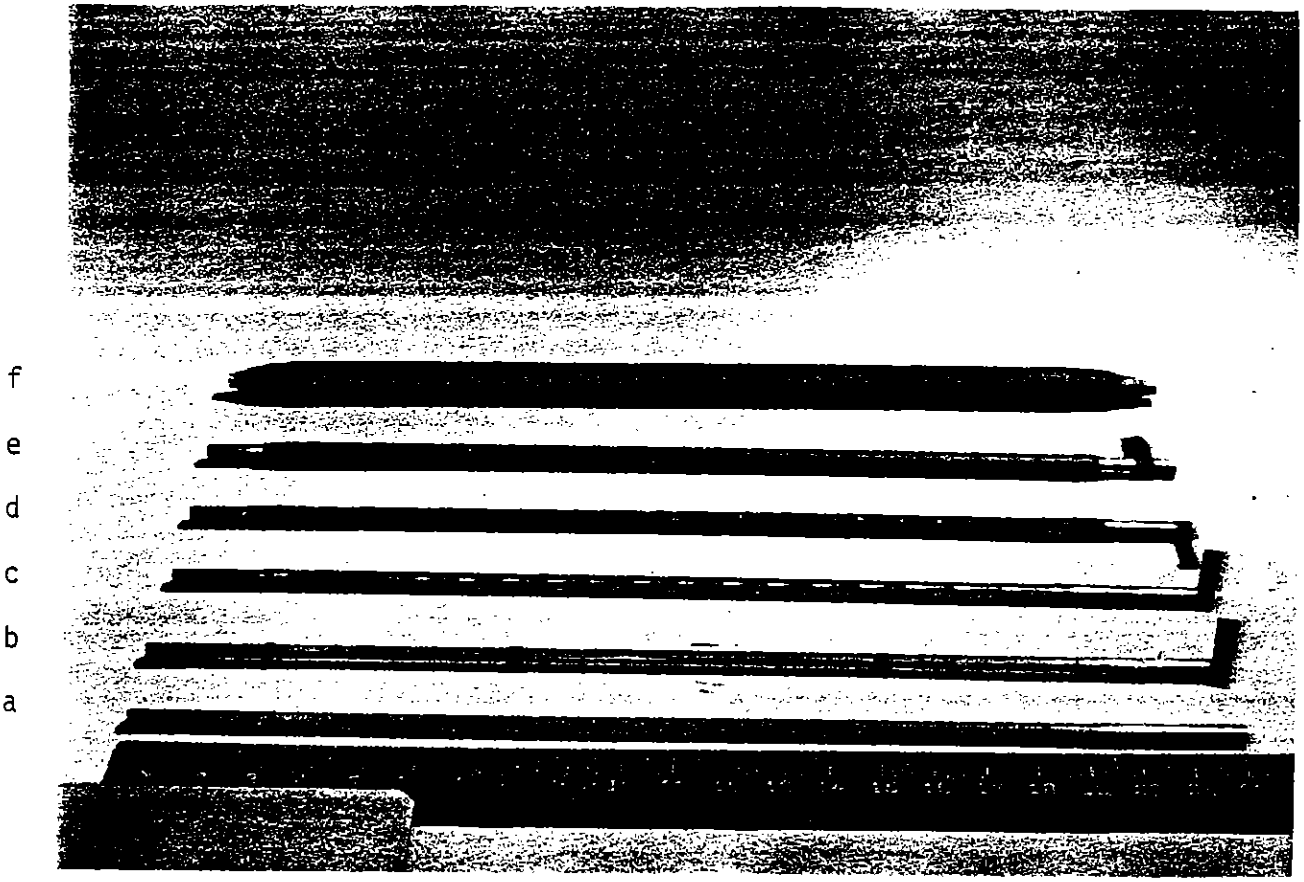

SCALE = INCHES

a. G10 FIBERGLASS ROD WITH BRASS TERMINATIONS
b. 1/4-INCH LINEAR RIBBON
c. 1/4-INCH HELICAL RIBBON
d. XLP SEMICON WRAP
e. 1st LAYERS OF POLYETHYLENE INSULATION
f. COMPLETED CABLE

Figure 4-9. Photograph of linear and helical cable models at various stages of construction.

Twisted Graphite Fiber--The basic element for this cable is a 12,000 fiber tow of Hercules AS-4 uncoated graphite fiber which was fabricated into a cable by Phelps Dodge Cable and Wire Company with a thin (0.03 inch thick) polymer exterior insulation. Data supplied by Hercules, Inc. indicates that the graphite conductor in the cable has a density of 1.76 gram/cm^3, and a resistivity of 1.54×10^{-3} Ω-cm. The outside dimension of the cable is approximately 0.140-inch with a center core of graphite fibers of approximately 0.80 inch.

For the vaporization/restrike tests, three of the fiber units were twisted into a single rope type cable as illustrated in Figure 4-10, with a brass electrical attachment at each end. There was no additional outside dielectric jacket around the three strand cable assembly.

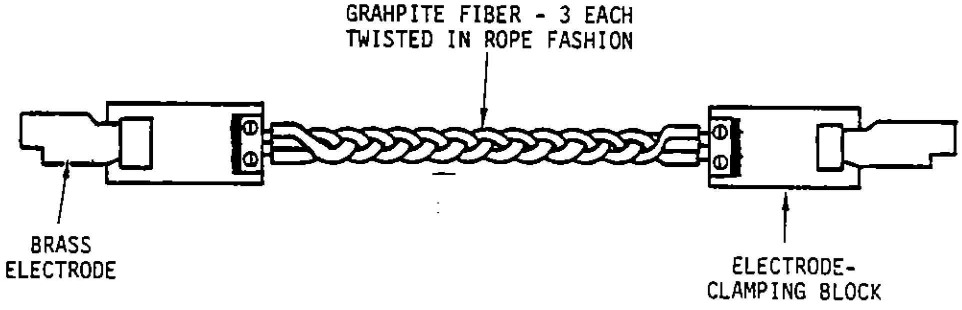

RE-04754

Figure 4-10. Graphite fiber cable (3 strands).

Linear Metallic Models--For each of the four metals listed, two different linear geometry models were fabricated. For one of these linear geometries, a single 0.5-inch wide by 0.005-inch thick ribbon of the metal was formed on a 3/8-inch diameter G-10 fiberglass rod, with the axes of the ribbon and the rod being parallel. The 0.5-inch wide ribbon covered roughly half of the circumference of the 3/8-inch rod. Each end of the fiberglass rod was terminated with a 3/8-inch by 2-inch brass rod onto which the metal ribbon was soldered and served as the attachment points for the pulser electrodes. The outer insulation of this cable followed a proposed Alcoa R-cable design, i.e., 0.015-inch of semicon XLP wrap (Scotch #13 tape) over the metal ribbon, followed by 0.280-inch of polyethylene. The thickness of polyethylene was obtained by using multiple layers of polyethylene heat shrinkable tubing. The fiberglass rod was used in place of Kevlar, which is expected to be used in the R-cable, because its thermal properties were known and are similar to those of Kevlar. However, because it is rigid, it was more convenient to use for fabricating these cable models by hand than the flexible Kevlar.

The second linear model is essentially the same as the above model except that the single 0.5-inch ribbon is replaced by two 0.25-inch wide ribbons of the same thickness (0.005 inch). The two 0.25-inch ribbons were formed to the fiberglass rod on opposite sides of the rod, leaving roughly a 0.25-inch gap between adjacent edges of the 0.25-inch metal strips. The exterior insulation was the same as for the 0.5-inch ribbon. The rationale for this design was to investigate possible geometry effects on a cable with the same cross-sectional area, and therefore, the same current density and specific action, as the 0.5-inch wide ribbon.

The 0.5-inch wide ribbon was the widest ribbon used in order that specific actions necessary to vaporize the metal conductors could be achieved with the MCAIR #4 pulser.

Helical Metallic Models--For each of the four metals listed in Section IV.3a(1), two helical cable models were fabricated. For one helical model, a 0.5-inch wide by 0.005-inch thick metal ribbon was wound helically on a 3/8-inch diameter G-10 fiberglass rod with 0.25-inch spacing between turns. For the second helical model, a 0.25-inch wide by 0.005-inch thick ribbon was wound helically on the 3/8-inch fiberglass rod with 0.5-inch spacing between turns. With ~~this~~ arrangement, the ratio of ribbon length to axial cable length is the same (≈1.6) for the two cables. However, their specific actions, for a given current time history, differ by a factor of four because the cross-sectional areas of the ribbons differ by a factor of two.

The termination and exterior insulation for these cables was the same as for the linear metallic cables. All of the cables were fabricated by JAYCOR.

Cable Lengths--There were three factors that dictated the length of the cable samples. First, the length had to be short enough so that the resistance of the cable did not overly reduce the current that the pulser could drive through the sample and thus the specific action that would be generated. Secondly, the sample should be short enough so that when the conductor vaporized, there was sufficient electric field across the vapor-filled gap to initiate a restrike when the other necessary conditions for restrike occurred. It was not known before the test how large this required field was, but a value of 5 kV/cm was assumed for purposes of selecting the cable lengths. Finally, the sample length had to be long enough so that breakdown would not occur between the electrodes through the soil, or air before vaporization occurred. From previous work, Reference 4-2, the threshold field for breakdown of soil with pulse lengths of about 100 μs was about 1 to 2 MV/m, including field enhancement near the electrodes.

4-2 C. Mallon, et al., "Electrical Breakdown Characteristics in 0.8 to 1.0 meter Soil Samples," Theoretical Note 318, 19 April 1982.

The subject of the specific action and voltage remaining at the time of vaporization was discussed in Section IV.2(c). In general, at the time of vaporization, the voltage from the pulser was still on the order of 200 kV. Therefore, to prevent soil breakdown, the sample lengths should not be less than about 20 cm. To meet the estimated requirement of 5 kV/cm for restrike with 200 kV from the pulser, the sample lengths could be 40 cm long. For these reasons, the test cables were constructed with a 40 cm axial length. (The length of the metal ribbons for the helical cables was about 64 cm.)

b. Sample Resistances and Inductances--To aid in extracting the sample resistivity from the voltage measurements, the resistance and inductance of the 40 cm long samples of each cable type were measured at room temperature. These results are summarized in Table 4-2.

Table 4-2. Measured Resistance and Inductance of Cable Types at Room Temperature
(Axial length of all cables = 40 cm. Ribbon length for helixes ≈ 64 cm)

Material	Ribbon Width (in.)	Configuration	R_W (ohms)	L_W (μH)	Resistivity (μ Ω-cm)
SS	1/2	helix	0.30	0.53	68
SS	1/4	helix	0.58	0.59	
SS	1/2	linear	0.163	0.54	
SS	(two 1/4)	linear	0.193	0.50	
Inconel	1/2	helix	0.43	0.57	103
Inconel	1/4	helix	0.85	0.60	
Inconel	1/2	linear	0.27	0.53	
Inconel	(two 1/4)	linear			
Iron	1/2	helix	0.033	0.57	10.1
Iron	1/4	helix	0.093	0.67	
Iron	1/2	linear	0.023	0.57	
Iron	(two 1/4)	linear			
Aluminum	1/2	helix	0.015		3.75
Aluminum	1/4	helix	0.03		
Aluminum	1/2	linear	0.0093		
Aluminum	(two 1/4)	linear	0.0093		
Graphite Fiber	—	three twisted cables	≈1.5	0.30	2000
Aluminum calibration rod	—	3/8 inch diameter rod, 40 cm long	—	0.36	

It is interesting to note that the inductance of the 1/2-inch wide helical samples is approximately equal to the inductance of the 1/2-inch wide linear samples even though the helical samples are 60 percent longer. The reduced inductance results from an effective overlap of successive turns on opposite sides of the cable which produces field cancellation (Figure 4-11).

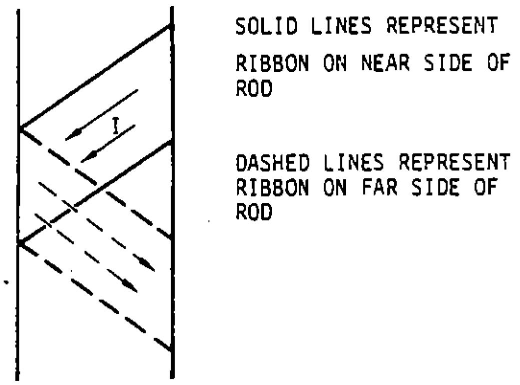

RE-04753

Figure 4-11. Diagram to illustrate reduced inductions in helical samples.

c. Pulser/Sample Configuration--MCAIR pulser #4 was used during the wire vaporization/restrike experiments. This pulser is a 10-stage Marx bank at 230 μF/stage. Each stage is capable of a 24 kV charge. Therefore, when all 10 stages are used, and fully charged, the maximum output voltage is 240 kV with a pulser capacitance of 23 μF (230 μF/10). The pulser is configured such that any number of the 10 stages may be selected to obtain a wide variation of pulser output voltages. During the series of tests as few as two stages (~40 kV) were used during investigations of vaporization/restrike thresholds.

Figure 4-12 shows the experimental arrangement used during the wire vaporization/restrike experiments.

A fiberglass angle/plywood stand (Figure 4-12) was used to support the R-cable samples, pulser electrodes, and associated instrumentation during the series of tests.

A stainless steel ribbon 6 mils thick by 6 inches wide served as an output resistor (R_L) for the pulser, and connected the pulser output spark gap to the 1-inch diameter copper pipe/R-cable samples. During the series of experiments the length of this resistor was varied between approximately 10 feet and 60 feet (~0.1 Ω to 0.5 Ω) to vary the level of current drive to the R-cable samples.

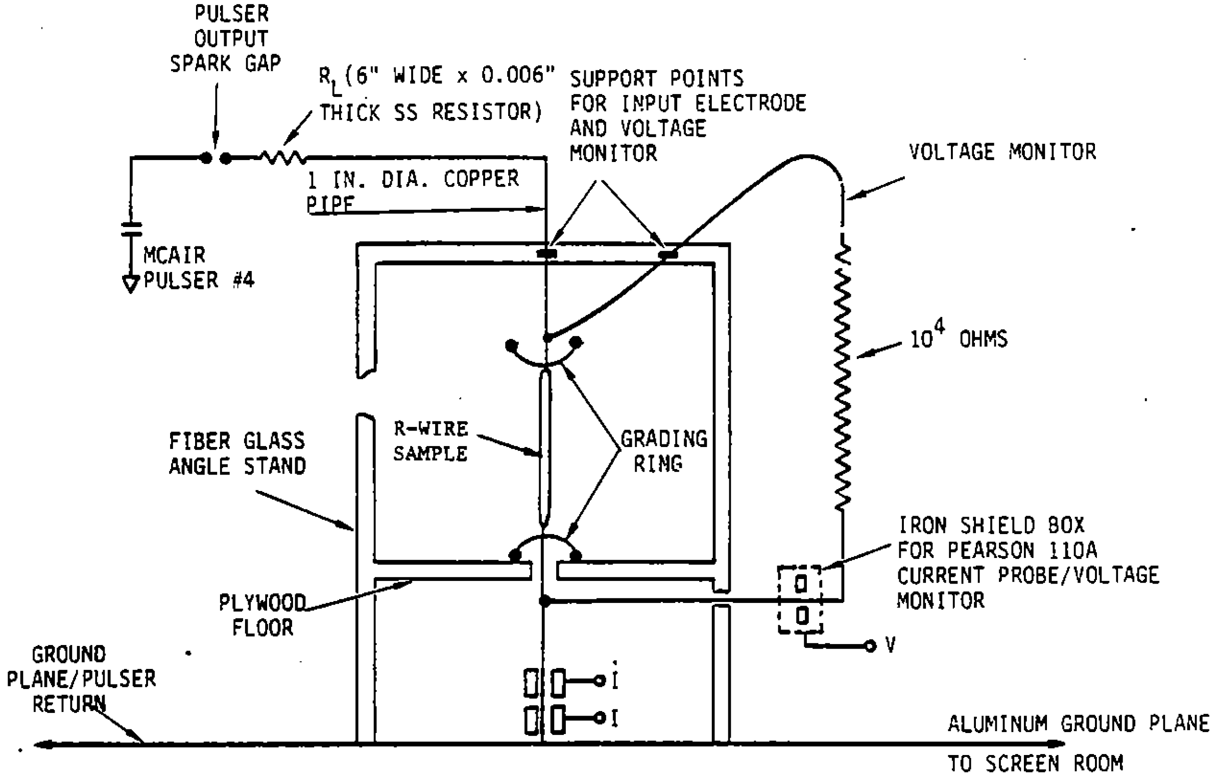

RE-04755

Figure 4-12. Experimental arrangement used for wire vaporization/restrike experiments.

Figure 4-13 is a photograph of the experiment with an R-cable sample installed for vaporization/restrike.

The debris produced by the explosion accompanying R-cable vaporization was successfully contained by wrapping the test stand with approximately three layers of heavy-tightly-woven nylon cloth used for bullet-proof enclosures.

d. **Instrumentation**—The data of interest during the R-cable vaporization/restrike experiments was the time-dependent R-cable resistance (resistivity) from ambient through vaporization and restrike. The time-dependent measurements required to determine the resistivity is (1) voltage across the R-cable sample, (2) current through the sample, and (3) $\dot{I}$, the time rate of change of current required to correct the voltage appearing across the sample for $L\dot{I}$.

(1) **Current Measurements**—The current through the R-cable sample was measured by a Pearson Model 1049 current probe. This probe has a peak current capacity of 250 kA and a rise time of 0.25 μs.

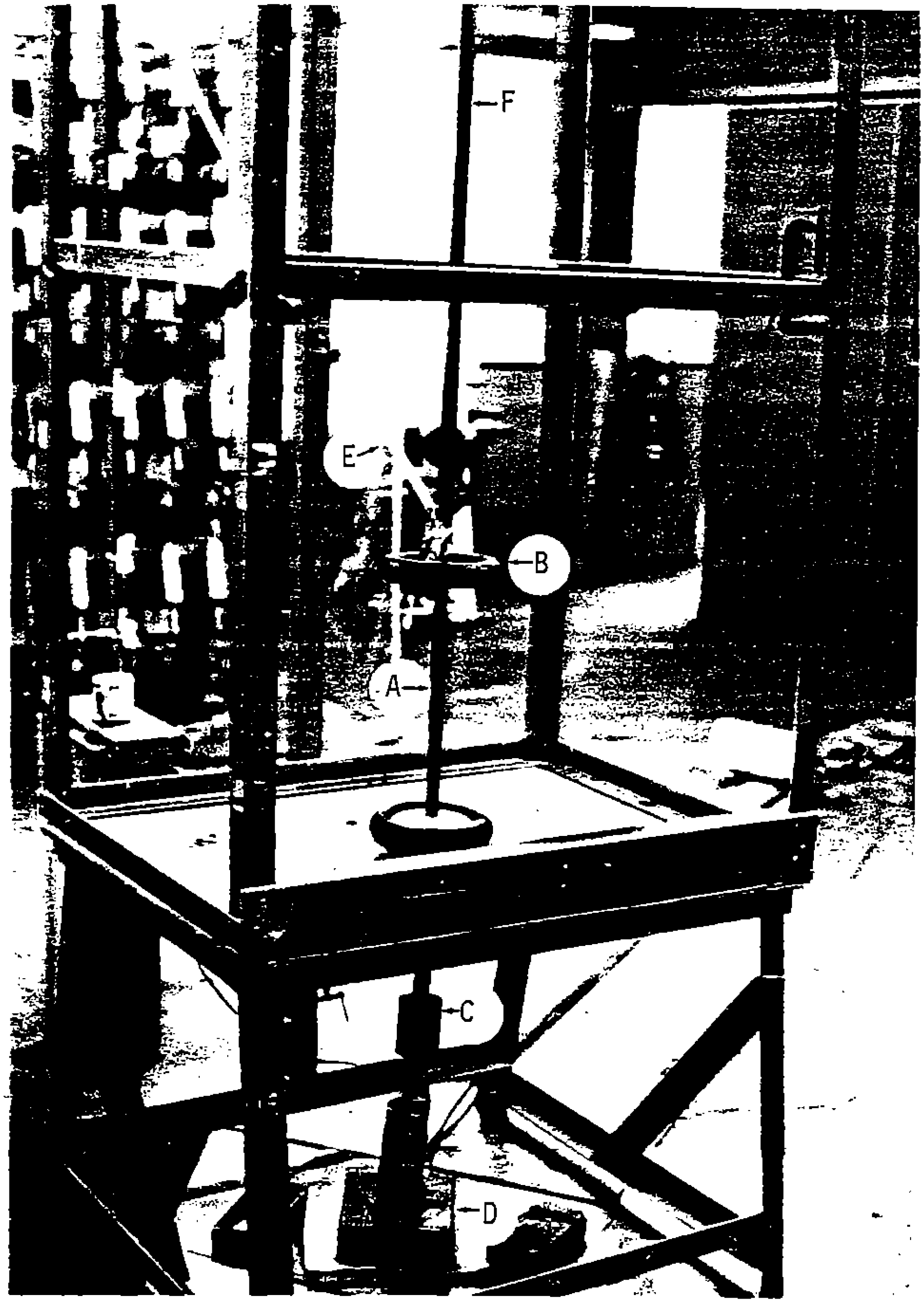

A - R-CABLE SAMPLE
B - FIELD GRADING RING
C - $\dot{I}$ PROBE

D - CURRENT PROBE
E - VOLTAGE MONITOR CABLE
F - 1 INCH DIAMETER COPPER PIPE INPUT ELECTRODE

Figure 4-13. Photograph of experiment with R-cable sample installed.

(2) **I-Dot Measurement**--The time rate of change of current ($\dot{I}$) through the R-cable sample was measured by a toroidal $\dot{I}$ sensor fabricated by JAYCOR. The output voltage of this sensor is given by $V_{OUT} = M\dot{I}$ where $\dot{I}$ is the time rate of change of current in a conductor threading the sensor and M is the mutual inductance.

$$M = \frac{\mu_o}{2\pi} W \ell n \frac{r_o}{r_i}$$

$$= 1.13 \times 10^{-8} \text{ H}$$

for the geometry of the sensor. A value of 1.18×10^{-8} H was obtained from calibration of the sensor. The rise time for this sensor is approximately:

$$\tau_r = \frac{L}{R} \sim \frac{1.1 \times 10^{-8} \text{ H}}{50 \ \Omega} \sim 2.2 \times 10^{-10} \text{ s}$$

(3) **Data Recording**--The output signals from the voltage and current monitors and the $\dot{I}$ sensor were recorded on time correlated oscilloscope channels. In general, each signal was recorded on more than one channel with different gains and sweep-speeds to obtain both early- and late-time data.

Figures 4-14 through 4-16 are typical data sets for several shots.

Figures 4-14 and 4-15 compares the voltage, current, and $\dot{I}$ time histories for 1/4-inch linear stainless steel samples with and without the 280 mil polyethylene jacket for a pulser voltage of 200 kV. Note the rapid restrike for the bare sample (Figure 4-15) shown by the abrupt decrease in voltage after burst, compared to the slowly decreasing voltage/resistivity when the vapor is confined (Figure 4-14) by the polyethylene jacket. For these samples at a pulser voltage of 200 kV vaporization/restrike is complete within 50 μs and therefore only the fast sweep data is shown.

Figure 4-16 is a data set for an Inconel, 0.5 inch, Helical sample for a pulser voltage of 54 kV. This drive level for this sample was near the threshold value and only a 'partial' restrike occurs at ~175 μs after pulse initiation. This is shown by the slight current increase (lower trace of photo at 50 μs/division sweep) at about 175 μs.

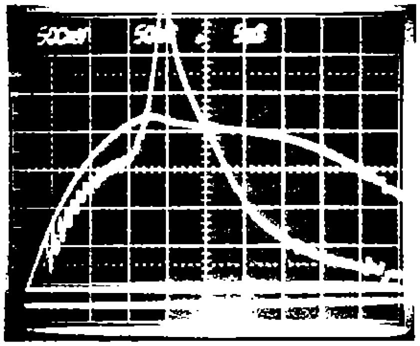

I = 25 kA/DIV.

5 µs/DIV.

V = 10 kV/DIV.

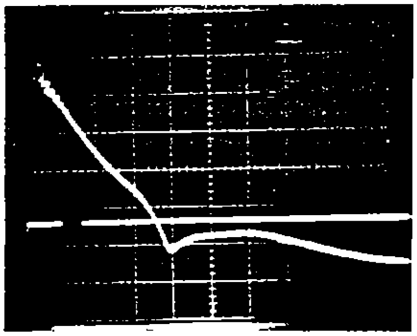

$\dot{I} = 3.4 \times 10^9$ A/s/DIV.

5 µs/DIV.

Figure 4-14. Shot 47; SS, 1/4 inch, linear with 280 mil polyethylene jacket. Pulser V_o = 200 kV.

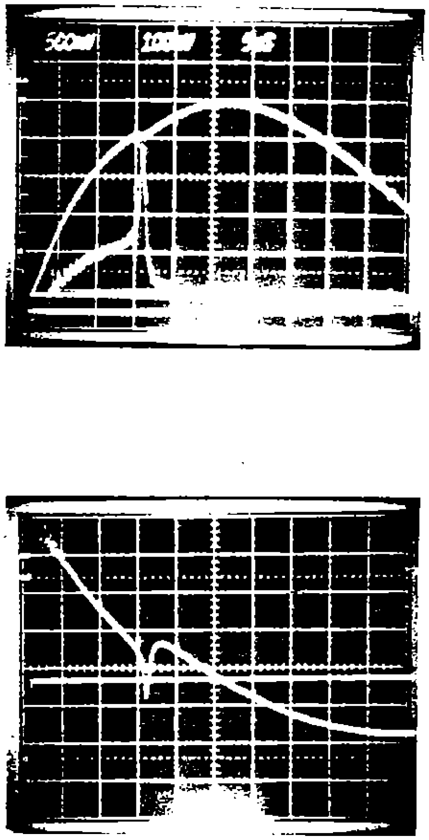

I = 25 kA/DIV.

5 μs/DIV.

V = 20 kV/DIV.

$\dot{I} = 3.4 \times 10^9$ A/s/DIV.

5 μs/DIV.

Figure 4-15. Shot 60; SS, 1/4 inch, linear, bare. This sample was vaporized without the 280 mil polyethylene jacket. Pulser $V_o = 200$ kV.

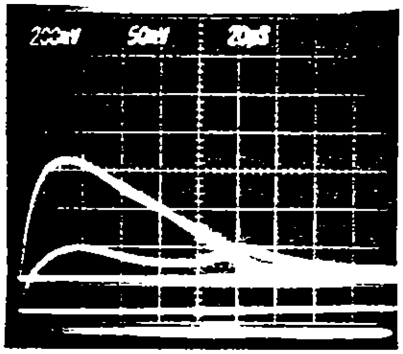

I = 10.9 kA/DIV.

20 µs/DIV.

V = 10 kV/DIV.

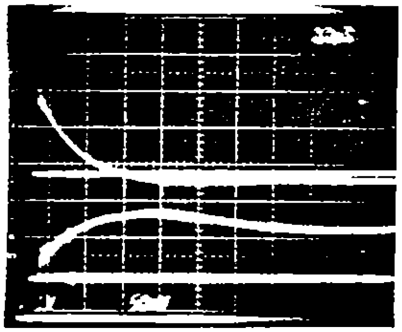

$\dot{I}$ = 1.7 x 10^9A/s/DIV.

10 µs/DIV.

V = 9.4 kV/DIV.

Figure 4-16. Shot 77; Inconel, 0.5 inch, helix, low voltage shot. Pulser V_o = 54 kV.

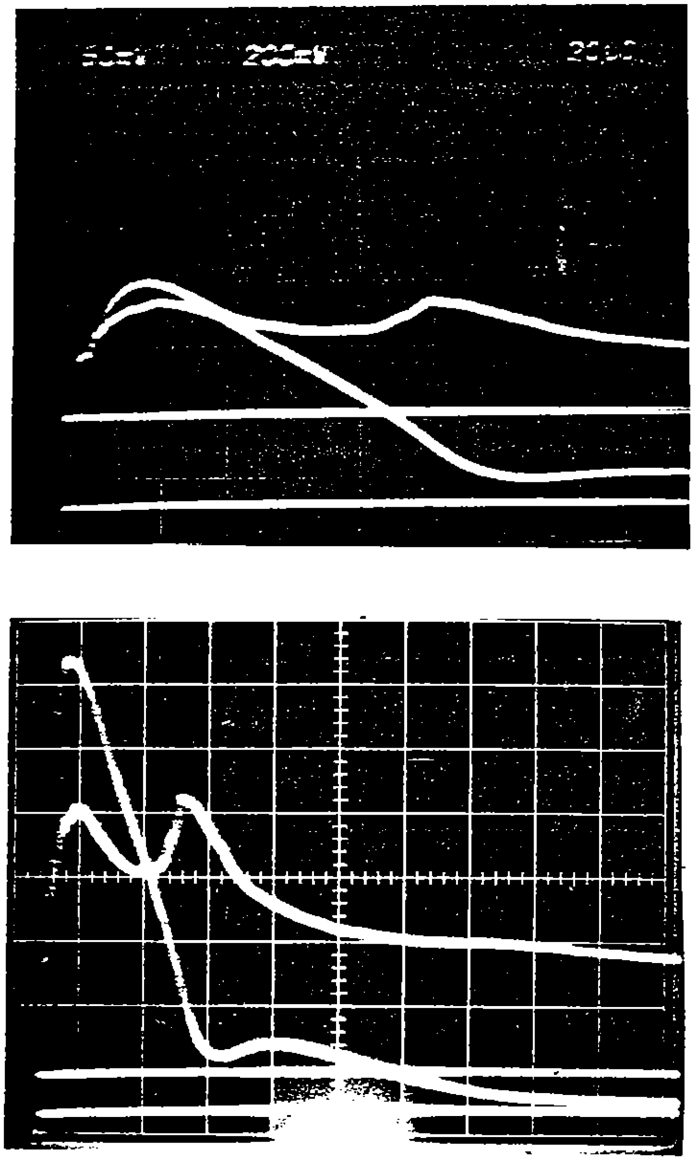

V = 10 kV/DIV.

20 μs/DIV.

I = 10 kA/DIV.

V = 4.2 kV/DIV.

50 μs/DIV.

I = 4.9 kA/DIV.

Figure 4-16. (Continued).

e. **Pre- and Post-Shot Photographs of Test Stand**--Figures 4-17 through 4-21 are photographs taken before and after R-cable vaporization/restrike shots.

Figure 4-17 shows a sample installed for a vaporization shot. Figure 4-18 is a photograph of the test stand after a low level shot near threshold for vaporization/restrike. At this drive level the polyethylene jacket and metal sample are completely removed from the fiberglass rod, however, the rod is still attached to the upper electrode. Figure 4-19 is a similar photograph after a high level drive (V pulser = 200 kV). At this level the fiberglass rod is completely broken away from the pulser electrodes.

Figures 4-20 and 4-21 are pre- and post-shot photographs of a low level (80 kV) R-cable vaporization shot in sand. The sand was contained in a non-rigid cylinder of ethafoam so that expansion could take place and allow the sand to absorb the shock. The shock accompanying vaporization ruptured the ethafoam container as shown in Figure 4-21.

4. PRESENTATION OF DATA

The time-history curves for the voltage across the sample (V), the current (I), and the time derivative of the current ($\dot{I}$) have been used to calculate resistivity versus time and action using the formula:

$$\rho = \frac{RA}{\ell} = \frac{\left(V - L_w \dot{I}\right)}{I} \frac{A}{\ell} \tag{4-1}$$

where L_w is the inductance of the sample itself, and A and ℓ are respectively the pre-melt cross-sectional area and length of the samples. For the helically wrapped metal samples, ℓ is the length along the helix—that is, ℓ is about 1.6 times the axial length of the sample. Admittedly, after vaporization occurs, the pre-melt cross-sectional area of the metal has little relationship to the cross-sectional area of the arc. In addition, after vaporization, the length of the arc for the helical samples is probably closer to the axial length rather than the helical length. However, the present system is used to avoid confusion in changing A/ℓ during a shot. L_w was measured for several samples and was around 6×10^{-7} H for all metal samples. At times close to zero, I is fairly small and $L_w \dot{I}$ is approximately equal to V. Hence, in this time regime, the calculated values for ρ can be somewhat inaccurate. Thus, one should not attach too much significance to the detailed shapes or magnitudes of the curves at very early times, say, $t \lesssim 1\,\mu s$. The

(Text continues on page 74)

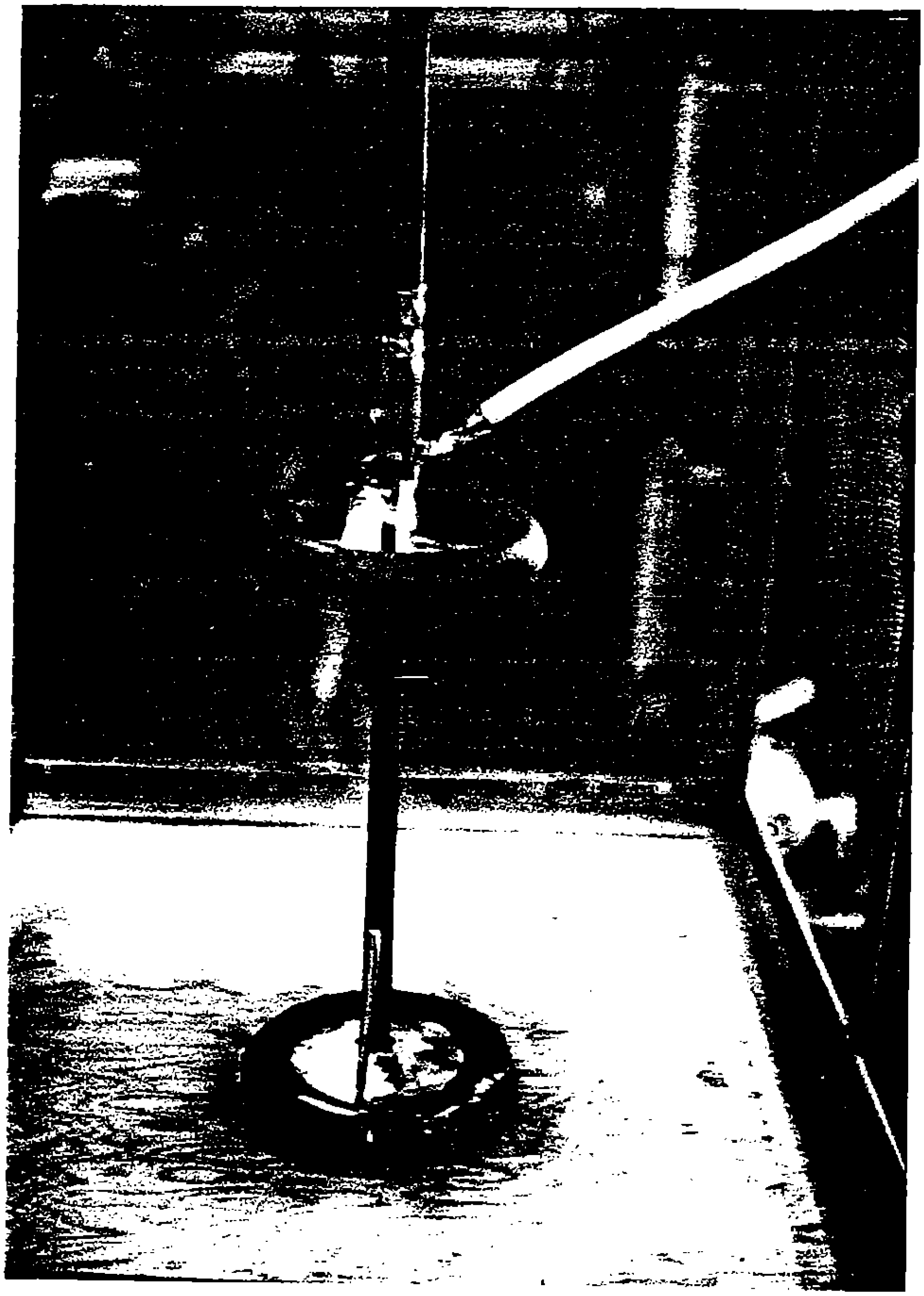

Figure 4-17. R-cable sample installed for vaporization/restrike shot.

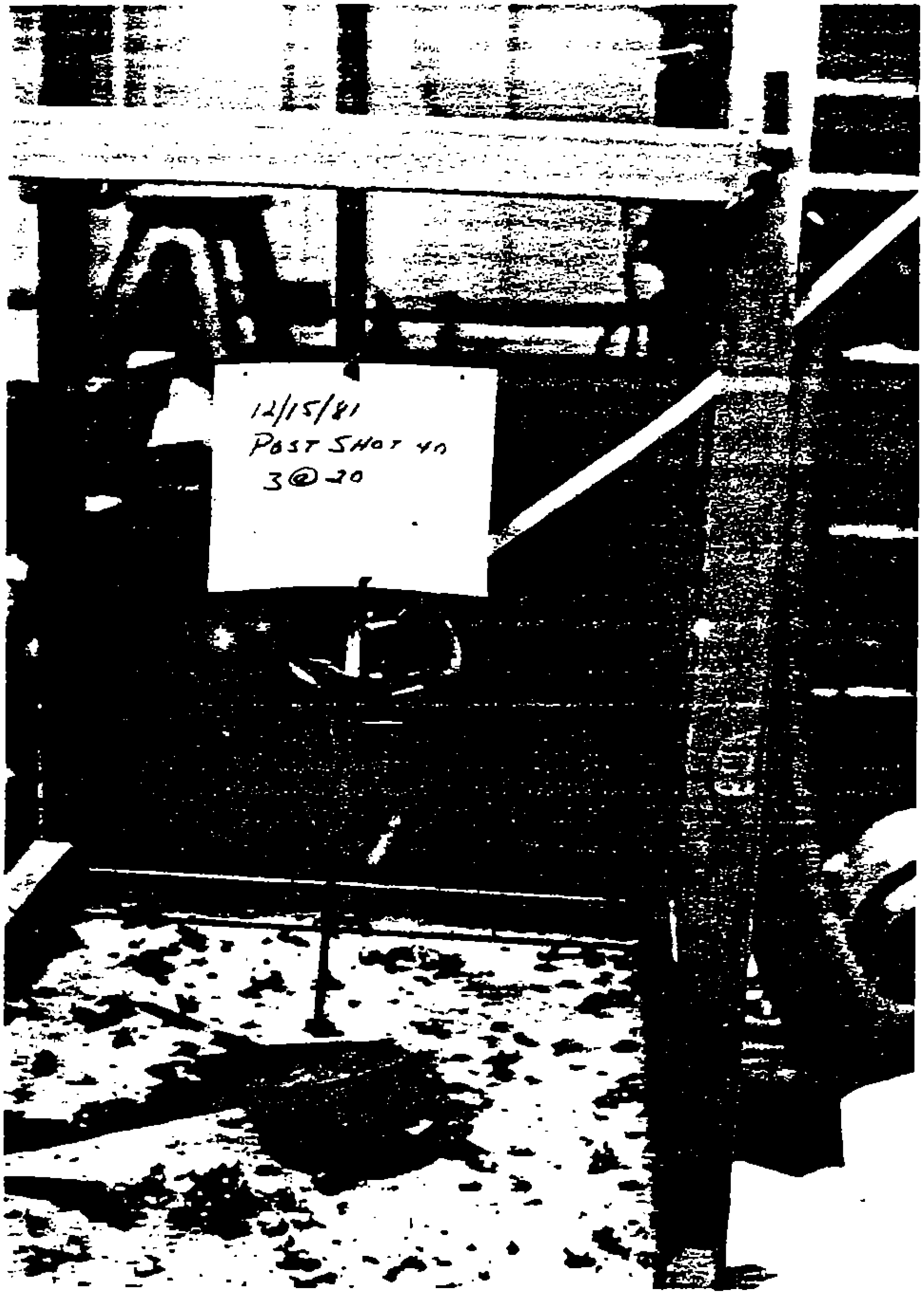

Figure 4-18. R-cable sample (shot 40) after low-drive-near-vaporization/restrike threshold. The G-10 fiberglass rod remains but the metal ribbon and 280 mil polyethylene jacket have been blown away.

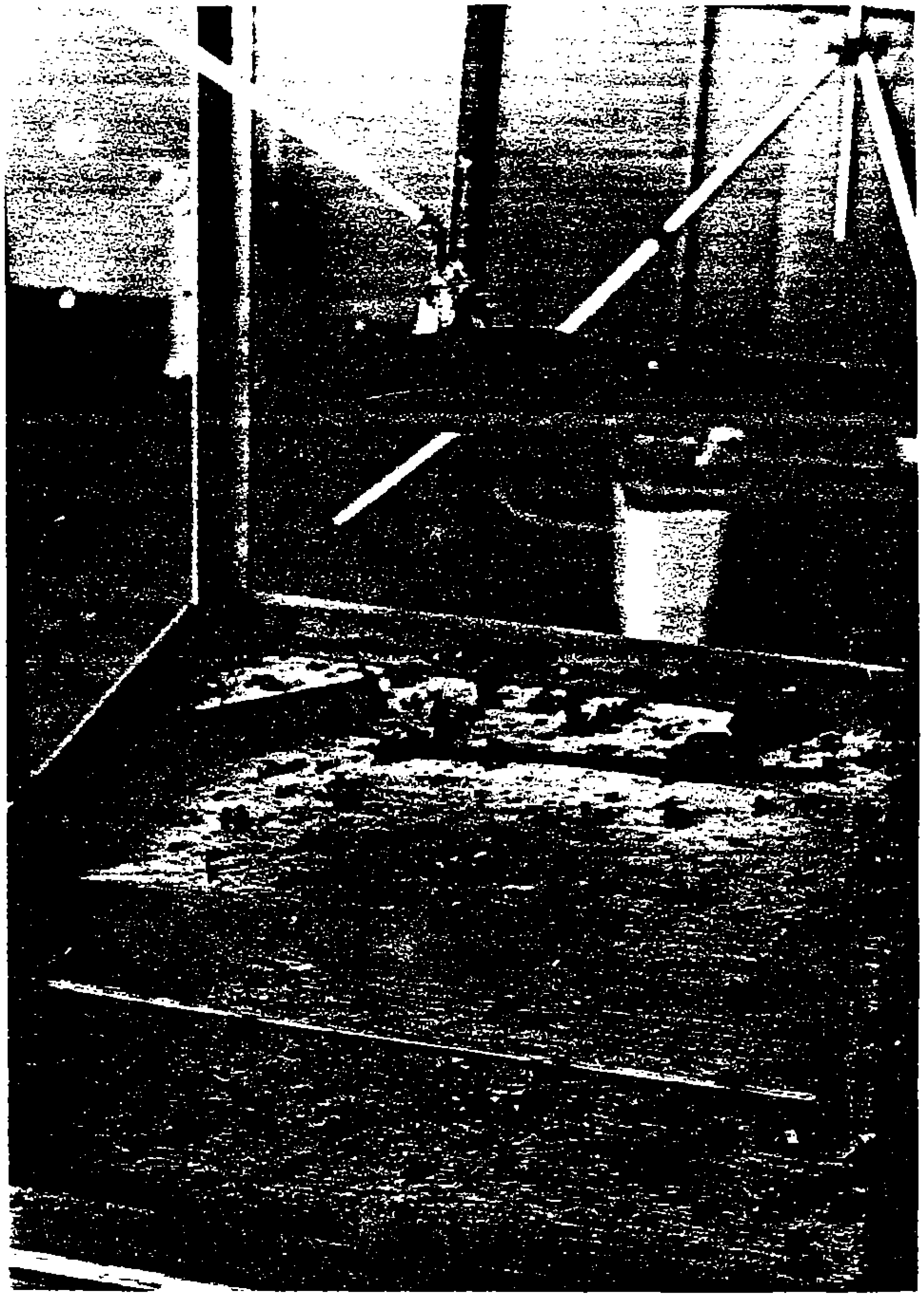

Figure 4-19. Test stand after high-level drive (200 kV).

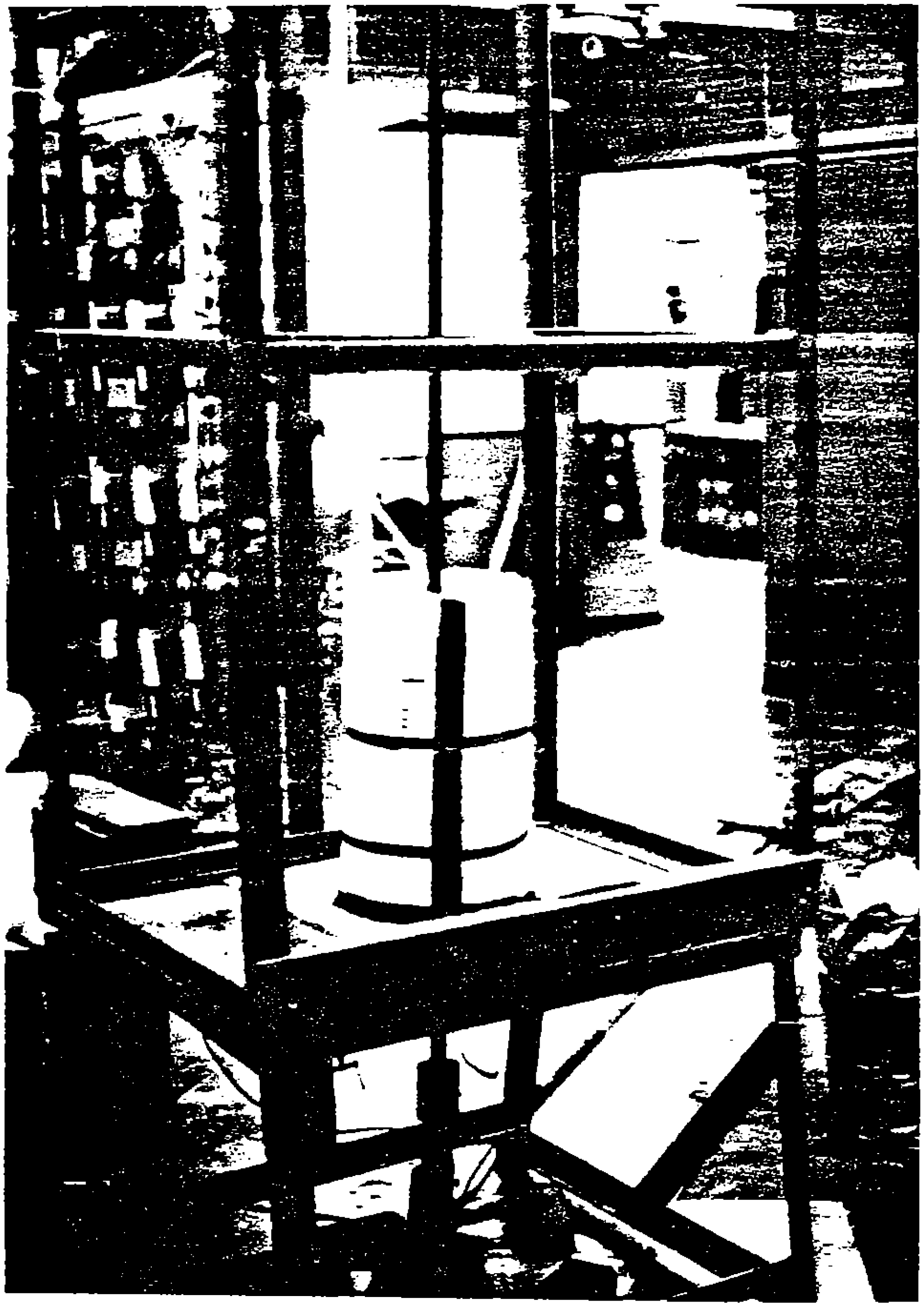

Figure 4-20. Set-up for R-cable vaporization in sand. Sand contained in break-away ethafoam cylinder.

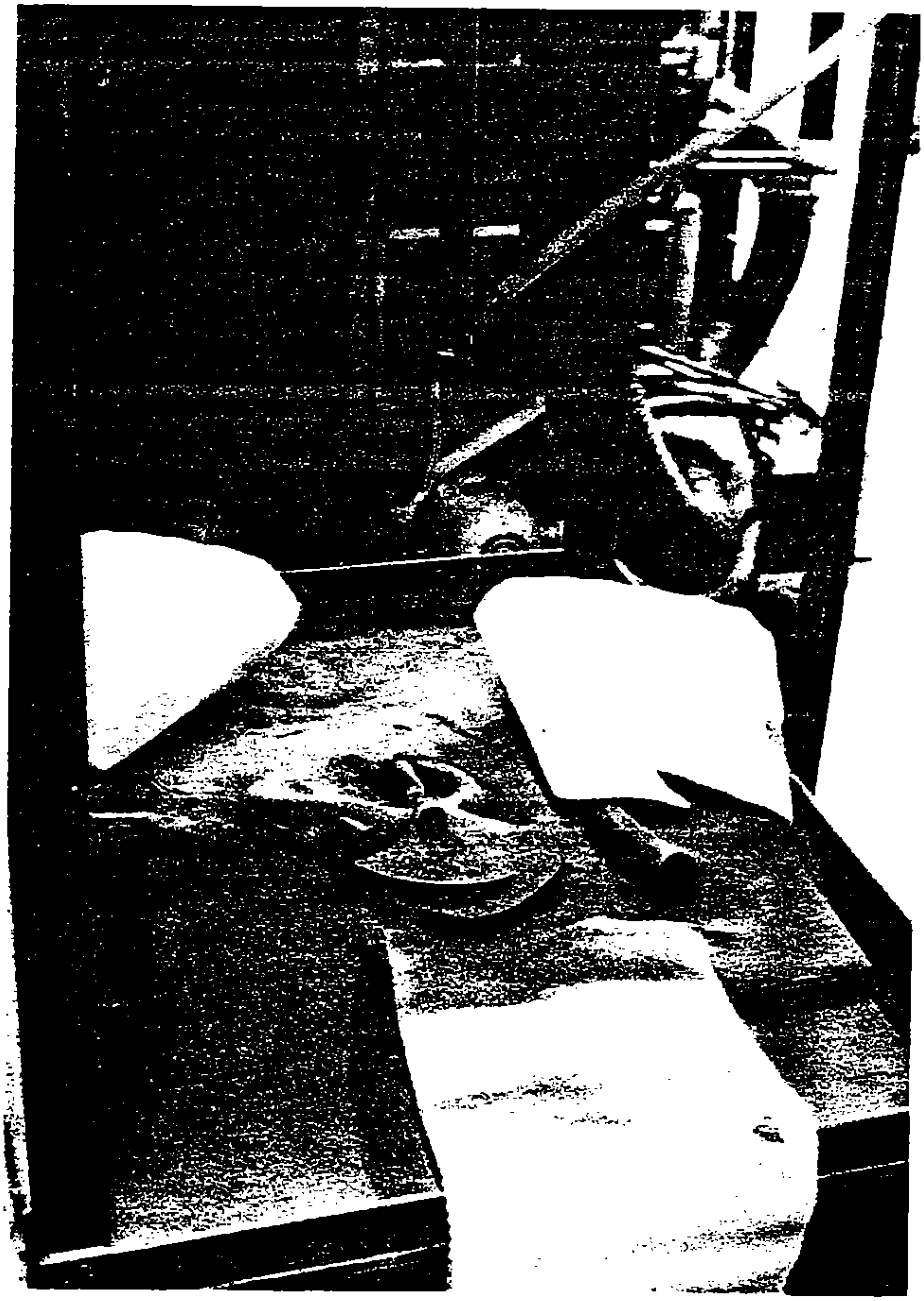

Figure 4-21. Post R-cable vaporization in sand.

resistivities are plotted versus specific action (A^2-s/mm^4) and versus time because the present data indicate that resistivity is not a unique function of action for these geometries. In particular, the curves of resistivity versus action vary significantly for different pulser voltages. The data are grouped together to illustrate the effects of (1) sand versus no sand around the sample, (2) the four geometries for the metal samples for each metal type and the same peak pulser voltage, (3) different pulser voltages for the same geometry and material (including the graphite fiber samples), (4) different materials for the same geometry and pulser voltage, and (5) bare metal versus enclosing the metal conductors in 280 mils of polyethylene.

The shot numbers and the test parameters for the wire vaporization/restrike experiments are summarized in Table 4-3. Also shown in the table are (1) the resistivity at burst, (2) the time of occurrence of the burst, (3) the voltage across the sample at the time of the burst, (4) the action and energy deposited in the resistor up to burst, and (5) the minimum resistivity after burst. For this discussion, burst is defined as the time of the peak in the resistivity curve before restrike. On the time scale of the present experiments, this burst resistivity is usually the peak resistivity observed, although the resistivity always eventually goes to the open-circuit condition (if vaporization has occurred) when the pulser voltage decays away and the arc turns off. However, in a few shots with pulser voltages just above the burnout threshold, the resistivity at the end of the scope picture was larger than at burst. In comparing and interpreting the values of minimum resistance after restrike, it is important to remember that the resistivities are calculated using the pre-melt cross-sectional area and length, not the actual area and length of the arc.

For all of the materials tested, with the exception of aluminum, the resistivity exhibits a leveling off or plateau region just prior to burst. This plateau is interpreted as the melt region prior to the start of vaporization. Table 4-4 compares the resistance and resistivity in the melt region with that measured at 300° K. Inconel, which had the largest 300° K resistivity, shows little change between 300° K and melt, while the resistivity of iron increases by a factor of 14.5 to achieve a resistivity at melt that is comparable to Inconel.

The resistivity of graphite fiber increases from 2030 μ Ω-cm to ~ 3000 μ Ω-cm early in the pulse, then decreases to ~ 50 percent of its 300° K value just prior to burst.

Table 4-3. Summary of Shot Parameters

Shot No.	Material*	Geometry**	Pulser Voltage (kV)	Values At Burst						ρ_{min} After ρ_{peak} ($\mu\Omega$-cm)†	Comments
				ρ ($\mu\ \Omega$-cm)	V (kV)	E (kV/cm)‡	Action (10^4 A^2-s/mm^4)	Time (μs)	Energy (kJ/cm^3)		
28	IN	1/4 WR	210	265	170	4.3	6.3	10.7	74	10	
29	SS	1/4 WR	210	248	156	3.9	5.9	10.8	78	9	
31	FE	1/4 WR	205	248	153	3.8	6.7	11.8	85	17	
32	FE	1/4 WR	147	276	140	3.5	6.1	13.0	81	18	
33	Same as 32, in sand		147	284	139	3.5	6.4	13.5	84	21	
34	FE	1/4 WR	120	303	130	3.3	5.4	14.3	74	<29	
35	FE	1/4 WR	80	529	74	1.9	5.9	26.8	100	<29	
36	SS	1/4 WR	80	487	71	1.8	4.3	27.3	88	<38	
37	Same as 36, in sand		80	486	71	1.8	4.6	27.3	82	<49	
40	IN	1/4 WR	60	806	57	1.4	4.5	34.3	82	<120	
41	IN	1/4 WR	40	No restrike							
43	FE	1/2 ST	200	243	68	1.7	5.4	18.0	74	60	
44	SS	1/2 ST	200	208	59	1.5	5.4	18.5	76	65	
45	RE	1/4 ST	200	273	72	1.8	5.7	19.5	76	63	
46	IN	1/4 ST	200	293	78	2.0	5.2	19.0	81	54	
47	SS	1/4 ST	200	295	81	2.0	5.1	17.8	76	57	
48	IN	1/2 ST	200	230	64	1.6	5.2	18.5	74	51	
49	FE	1/2 WR	200	267	104	2.6	4.9	18.8	61	55	
50	SS	1/2 WR	200	289	113	2.8	4.8	19.0	69	61	
51	IN	1/2 WR	200	285	116	2.9	4.6	18.0	57	56	
53	Graphite fiber		200	5950	335	8.4	0.177	14.0	27	110	
60	SS	1/4 ST, bare	200	290	79	2.0	3.5	14.5	47	22	
66	Aℓ	1/4 WR	200	343	225	5.6	8.1	11.5	61	24	
67	Aℓ	1/2 WR	200	378	171	4.3	7.3	20.3	44	72	
68	Aℓ	1/4 ST	200	296	90	2.3	7.0	19.5	35	66	
69	Aℓ	1/2 ST	200	311	92	2.3	7.6	20.3	45	58	
71	IN	1/4 WR	60	1110	44	1.1	3.9	4.9	71	29	
72	IN	1/2 WR	60	900	22	0.55	2.6	92	40	176	Final $\rho > \rho_{burst}$
73	SS	1/2 WR	60	731	22	0.55	2.8	92	40	220	.
77	IN	1/2 WR	54	870	15.0	0.38	2.7	132	45	492	.
78	FE	1/2 WR	54	371	10.8	0.27	3.2	135	34	320	.
79	SS	1/2 WR	54	947	16.7	0.42	2.6	125	38	432	.
80	IN	1/4 ST	54	665	12.7	0.32	3.0	138	57	322	
81	IN	1/2 ST	54	694	10.7	0.27	2.5	125	47	<328	
82	SS	1/4 WR	54	1050	38.3	0.96	3.4	52	59	31	
83	Aℓ	1/4 WR	54	302	30.2	0.76	6.8	46	39	44	
84A	Graphite fiber		54	6070	21.0	0.53	0.16	126	22	<400	
85	Aℓ	1/2 WR	54		No restrike						
86	Aℓ	1/2 WR	60		No restrike						

*'IN' = Inconel; 'SS' = stainless steel, 'FE' = iron; 'Aℓ' = aluminum; 'graphite' = three-strand graphite fiber.

**'WR' = helical wrap; 'ST' = straight; '1/4' and '1/2' are widths of 5-mil metals.

†< indicates resistivity was still decreasing at end of trace.

‡Electric field calculated using axial length of 40 cm for all samples.

Table 4-4. Comparison of Measured Resistance/Resistivity at Ambient With the Values at the Plateau (Melt) Region Just Prior to Burst.

	Resistance (Ω)		Resistivity (μ Ω-cm)		Ratio R(melt)/R(300°K)
Inconel	300°K	Melt	300°K	Melt	
0.5 Linear	0.27	0.32	108	128	1.19
0.25 Linear	0.27	0.31	108	124	1.15
0.5 Helix	0.43	0.43	108	108	1.0
0.25 Helix	0.85	0.80	108	101	0.94
				AVG =	1.07
Stainless Steel					
0.5 Linear	0.16	0.36	64	144	2.25
0.25 Linear	0.19	0.37	76	148	1.95
0.5 Helix	0.30	0.51	75	128	1.70
0.25 Helix	0.58	0.91	73	115	1.57
				AVG =	1.9
Iron					
0.5 Linear	0.023	0.36	9.2	144	15.7
0.25 Linear	0.023	0.36	9.2	144	15.7
0.5 Helix	0.033	0.51	–8.3	128	15.5
0.25 Helix	0.093	1.0	11.8	127	11.0
				AVG =	14.5

Aluminum

300°K resistivity = 3.75 μ Ω-cm

No well-defined plateau observed.

Graphite Fiber

	Resistance (Ω)		Resistivity* (μ Ω-cm)		Ratio R (300°K) / R (Plateau)
	300°K	Plateau	300°K	Plateau	
Shot 53 (200 kV)	1.5	0.75	2030	1010	0.5
Shot 84 (54 kV)	1.5	0.70	2030	950	0.47
				AVG =	0.49

*Graphite resistivity increases approximately 50 percent (2030 μ Ω-cm to 3000 μ Ω-cm) early in the pulse before decreasing to the value shown above just before burst.

Figures 4-22 and 4-23 show the ρ versus action and ρ versus time curves for 1/4-inch helically wrapped samples for Fe with a pulser voltage of 147 kV and for SS with a pulser voltage of 80 kV, in both cases with and without sand around the sample. For both sets of data, there is little effect due to the sand, which indicates that most of the restrike current probably flows inside the expanded shell of the polyethylene jacket rather than through the vapor after it has escaped from the jacket. These comparisons were made early in the test sequence and, since little effect was noticed due to the sand, the subsequent tests were made without the sand to simplify the test procedure.

Figures 4-24 through 4-27 show the effect of the four geometries for the four metal materials (Fe, Inconel, stainless steel, and aluminum) for a peak pulser voltage of about 200 kV. The geometry effects that are compared in these samples are (1) helical versus straight conductors, (2) two separated 1/4-inch wide straight conductors versus one 1/2-inch wide straight conductor, and (3) one-half the cross sectional area for the helical samples. For a given voltage the electric field along the wire is 60 percent larger for the straight samples than the helical samples. From the curves of ρ versus action, there appears to be some effect of geometry, especially for the 1/4-inch helically wrapped samples. Since these samples had only half the cross-sectional area of the other three samples, their current densities are twice as large as in the other samples, for a given pulser voltage (and approximately the same current through each sample). Therefore, the 1/4-inch helical samples reached the vaporization and burst condition at much earlier times than the other samples. This difference is clearly illustrated in the plots of ρ versus time in those figures. Since the post-vaporization resistivities are undoubtedly a function of how fast the ionized vapor can escape from the polyethylene jacket, the difference in the ρ versus action curves for the 1/4-inch helical samples compared to the other samples must be at least partially due to this difference in time. Thus, the differences observed for this sample are probably due more to its smaller area than to its helical wind. If a straight sample had been run with the same smaller cross-sectional area, a similar effect probably would have been observed--that is, the ρ versus action curve for a straight sample with a smaller cross-sectional area probably would have been closer to the results for the 1/4-inch helical sample than for the present straight samples with twice the area.

For the Fe, Inconel, and SS samples at this voltage, there is a consistency in that the largest peak resistivity always occurred with the 1/4-inch ST samples, the lowest peak resistivity was with the 1/2-inch ST samples, and the earliest peak versus action occurred with the 1/2-inch WR samples. This trend was not borne out with Aℓ, although the

(Text continues on page 90)

Figure 4-22a.

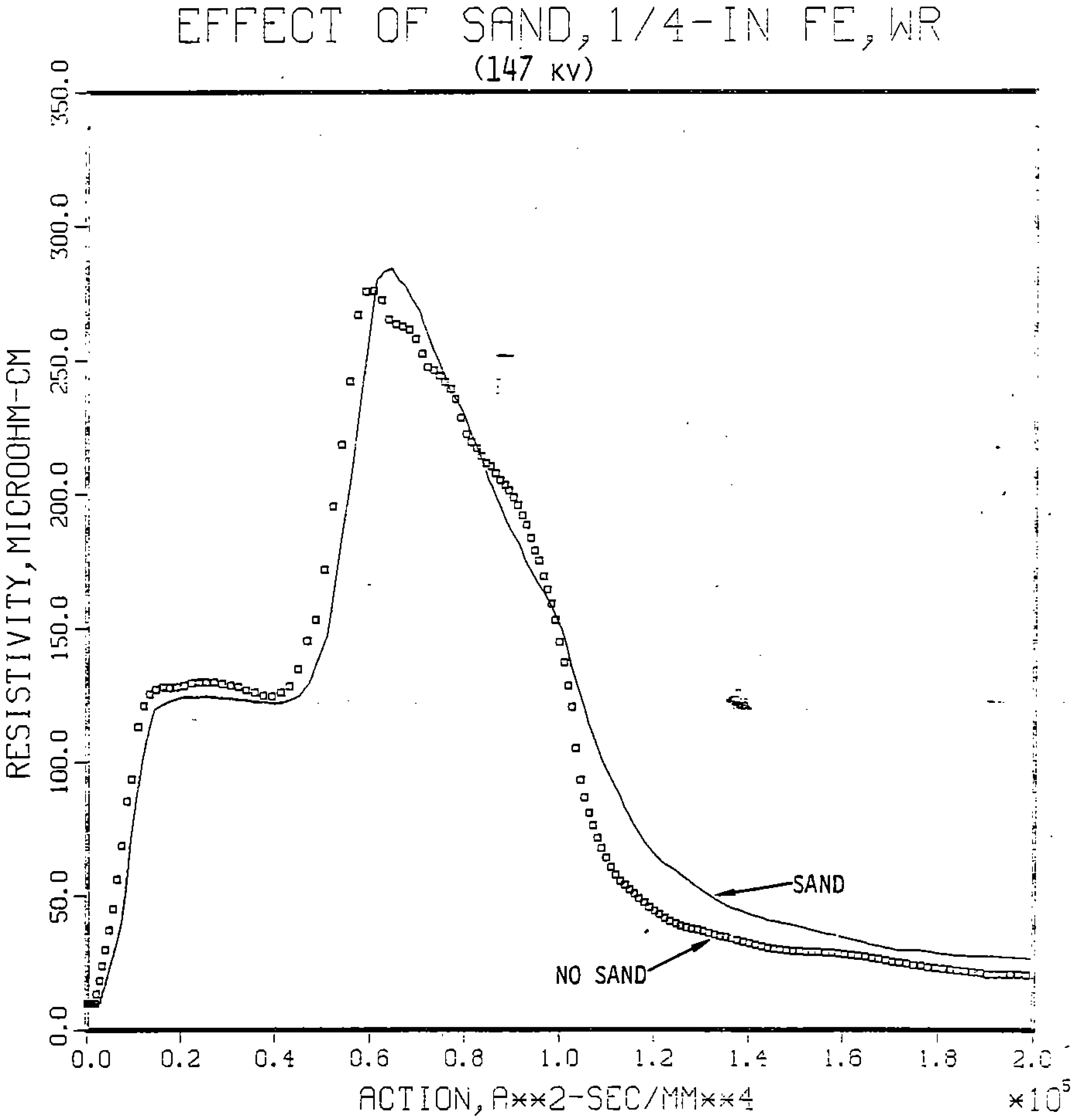
EFFECT OF SAND, 1/4-IN FE, WR
(147 KV)
RESISTIVITY, MICROOHM-CM
0.0
50.0
100.0
150.0
200.0
250.0
300.0
350.0
0.0
0.2
0.4
0.6
0.8
1.0
1.2
1.4
1.6
1.8
2.0
ACTION, A**2-SEC/MM**4
$\times 10^5$
SAND
NO SAND

Figure 4-22b.

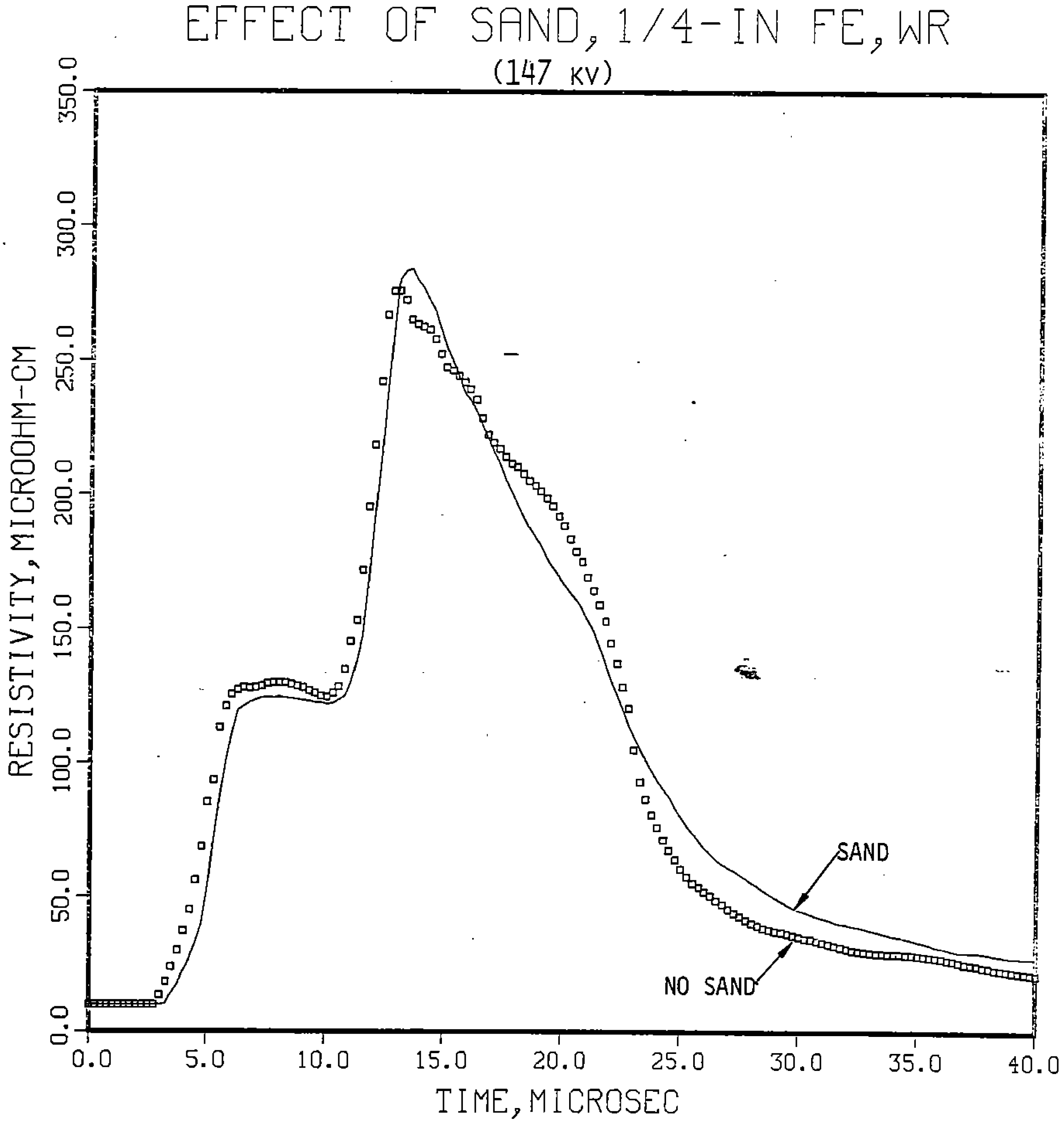
EFFECT OF SAND, 1/4-IN FE, WR
(147 KV)
RESISTIVITY, MICROOHM-CM
0.0
50.0
100.0
150.0
200.0
250.0
300.0
350.0
TIME, MICROSEC
0.0
5.0
10.0
15.0
20.0
25.0
30.0
35.0
40.0
SAND
NO SAND

Figure 4-23a.

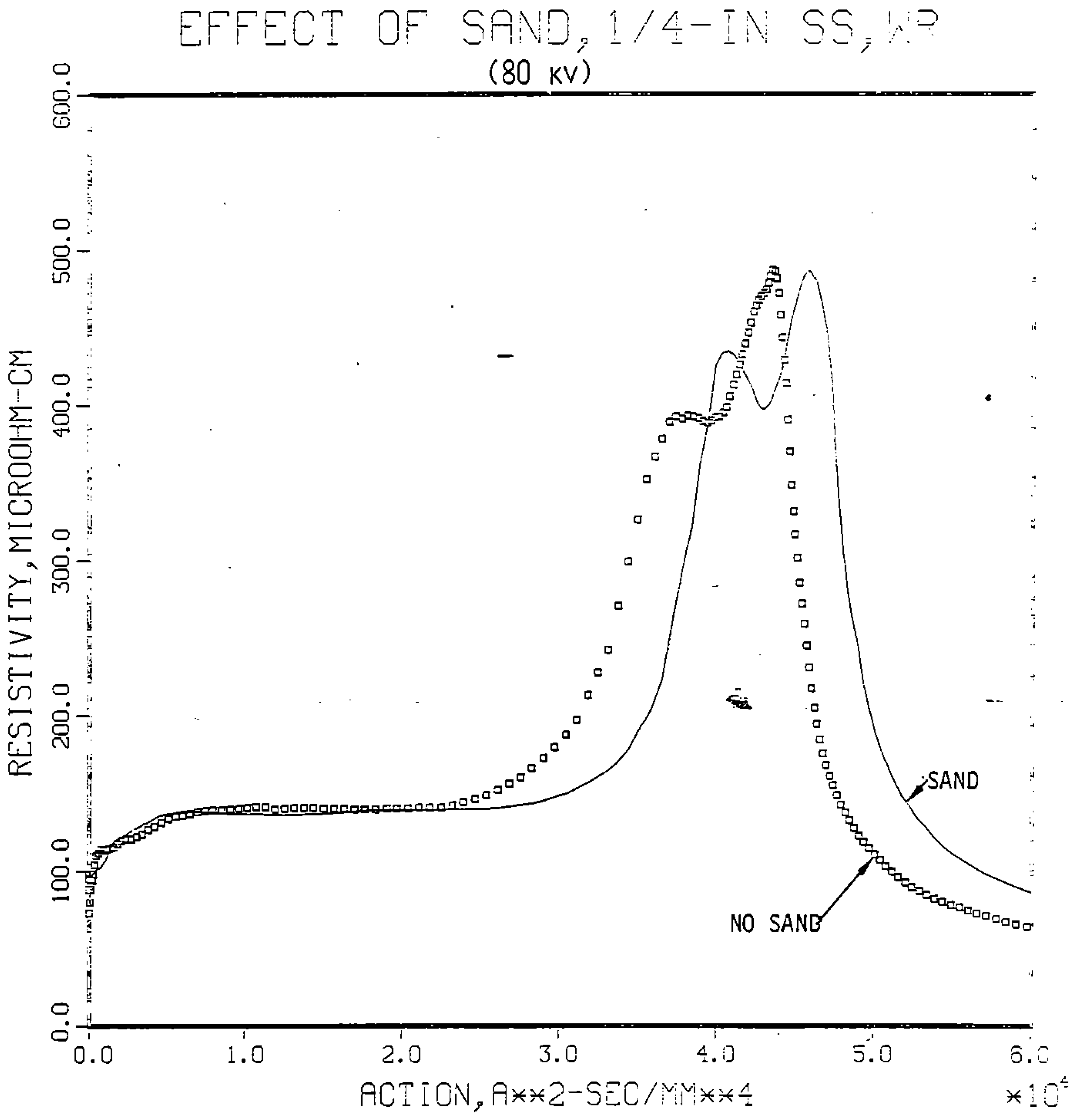
EFFECT OF SAND, 1/4-IN SS, WR
(80 KV)
RESISTIVITY, MICROOHM-CM
600.0
500.0
400.0
300.0
200.0
100.0
0.0
0.0
1.0
2.0
3.0
4.0
5.0
6.0
ACTION, A**2-SEC/MM**4
*10^4
SAND
NO SAND

Figure 4-23b.

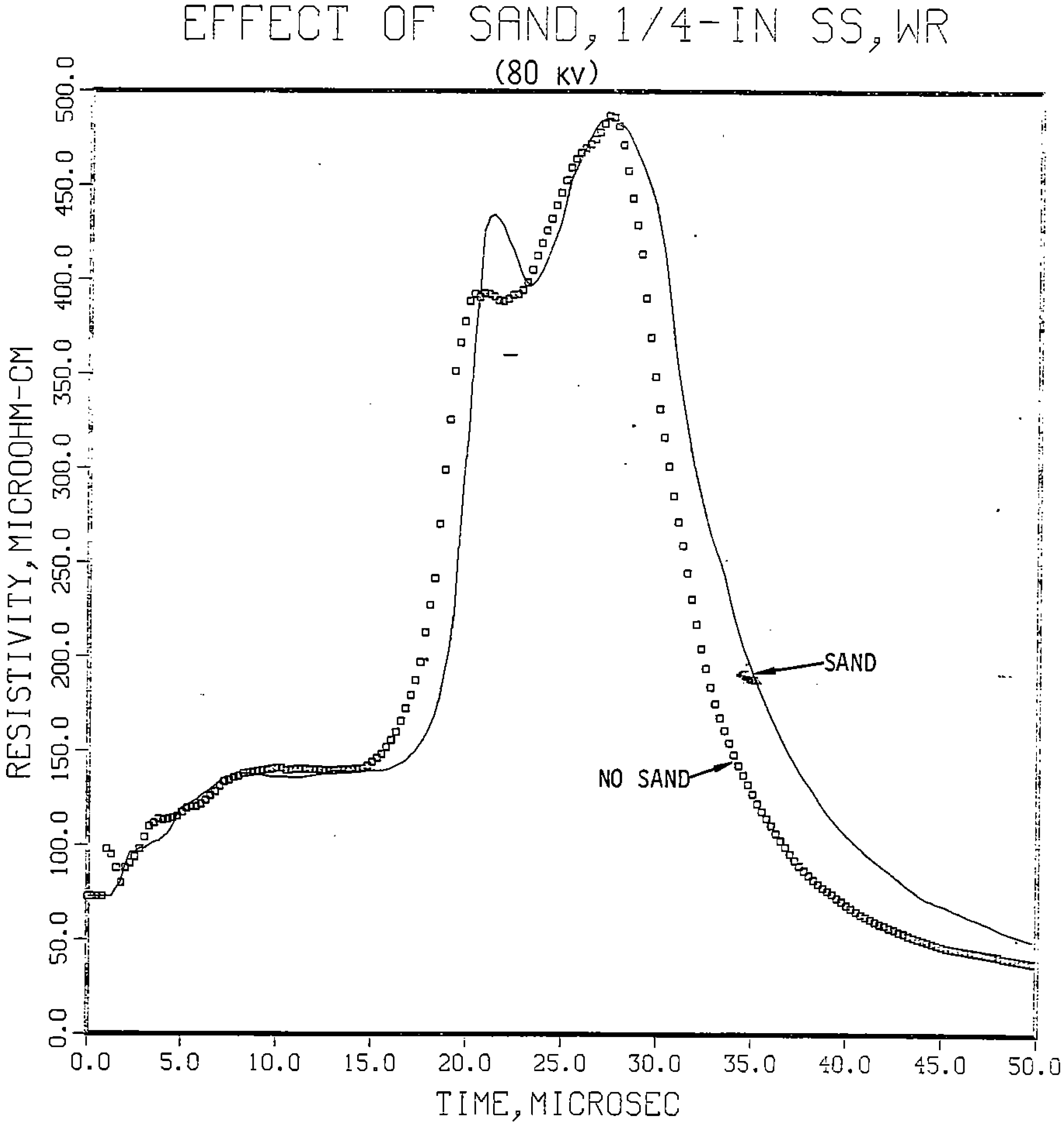

EFFECT OF SAND, 1/4-IN SS, WR
(80 KV)
RESISTIVITY, MICROOHM-CM
0.0
50.0
100.0
150.0
200.0
250.0
300.0
350.0
400.0
450.0
500.0
TIME, MICROSEC
0.0
5.0
10.0
15.0
20.0
25.0
30.0
35.0
40.0
45.0
50.0
SAND
NO SAND

Figure 4-24a.

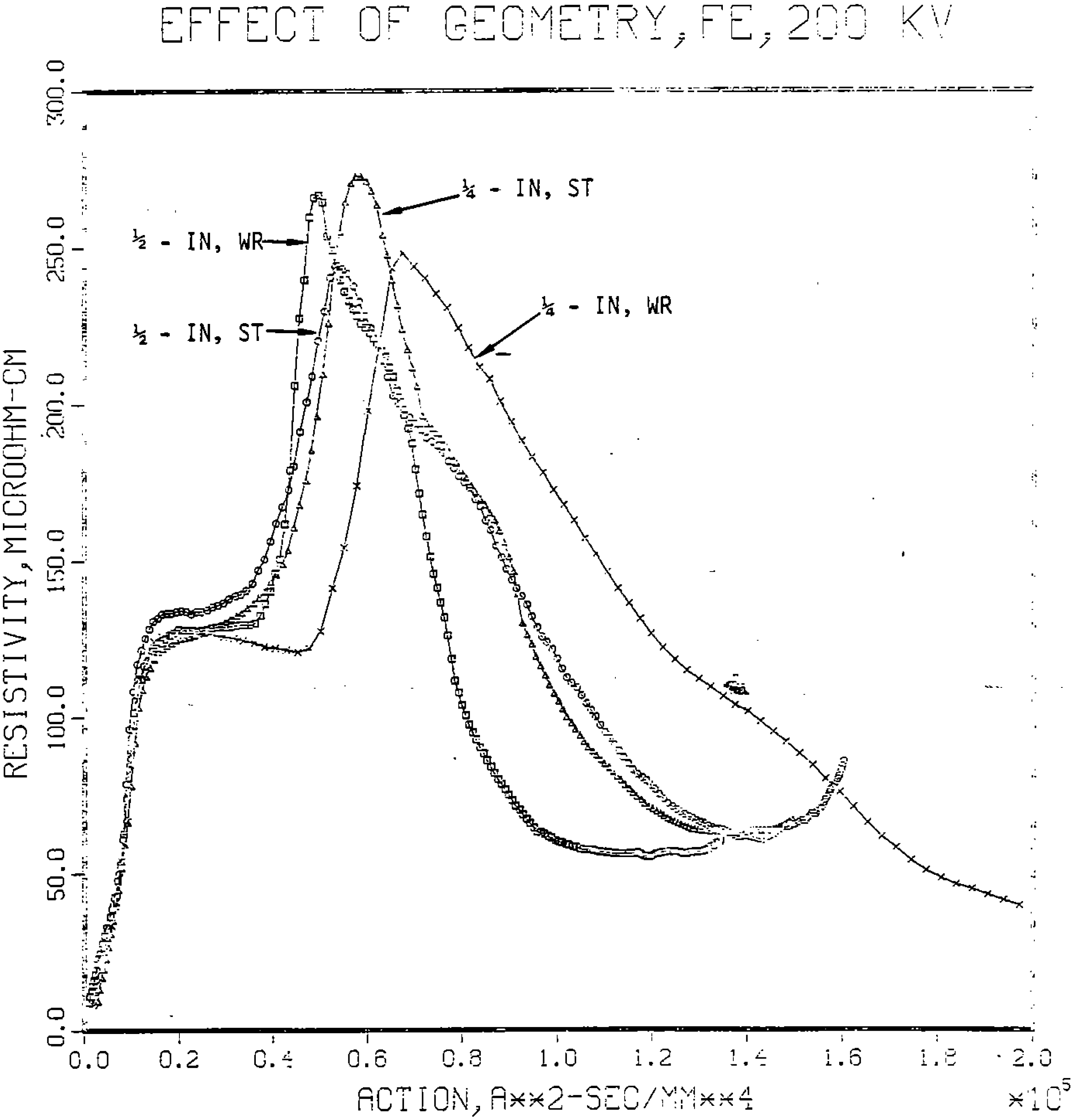
EFFECT OF GEOMETRY, FE, 200 KV
RESISTIVITY, MICROOHM-CM
ACTION, A**2-SEC/MM**4
×10^5
0.0
50.0
100.0
150.0
200.0
250.0
300.0
0.0
0.2
0.4
0.6
0.8
1.0
1.2
1.4
1.6
1.8
2.0
¼ - IN, ST
½ - IN, WR
½ - IN, ST
¼ - IN, WR

Figure 4-24b.

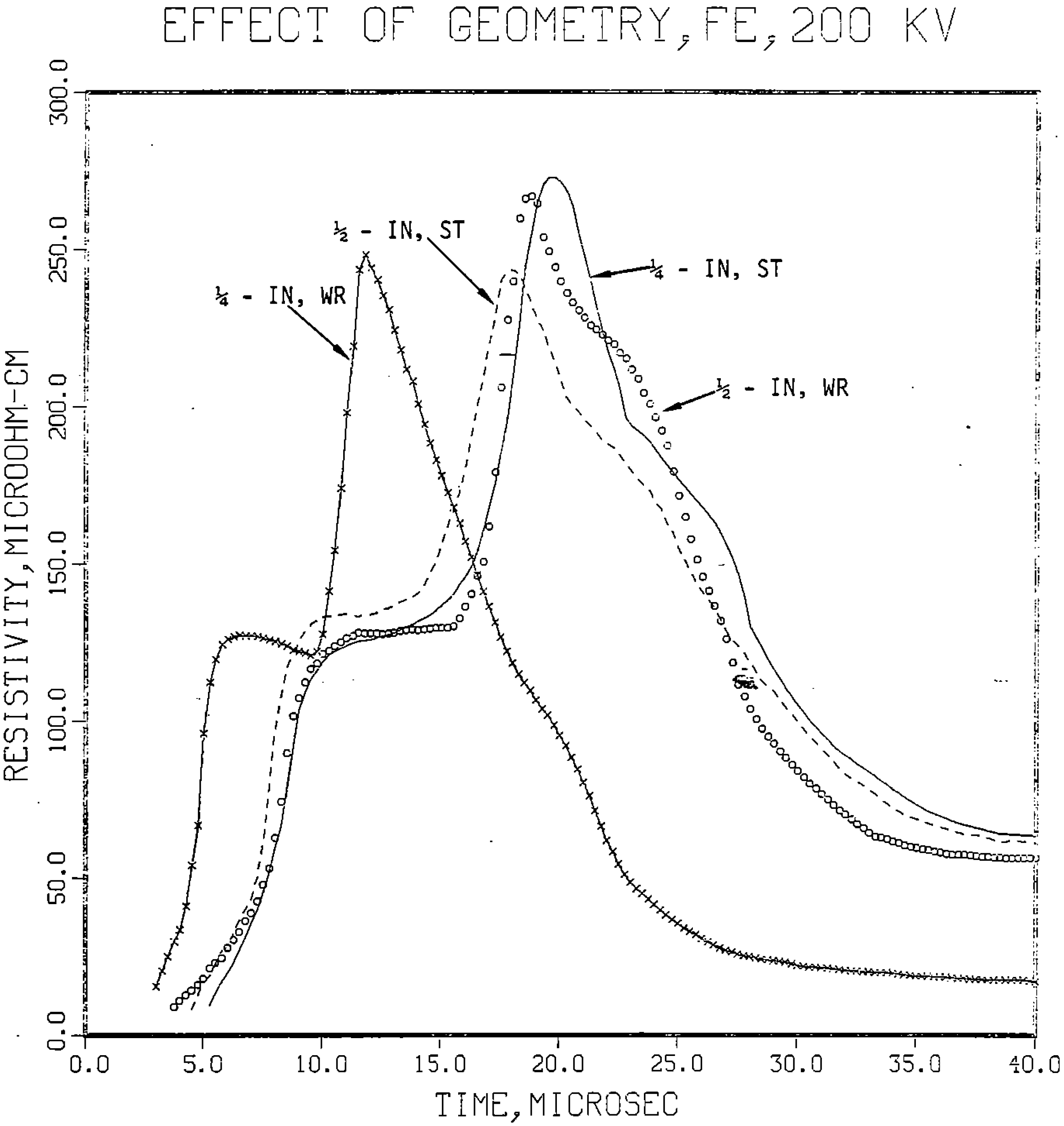
EFFECT OF GEOMETRY, FE, 200 KV
RESISTIVITY, MICROOHM-CM
TIME, MICROSEC
0.0
50.0
100.0
150.0
200.0
250.0
300.0
0.0
5.0
10.0
15.0
20.0
25.0
30.0
35.0
40.0
½ - IN, ST
¼ - IN, WR
¼ - IN, ST
½ - IN, WR

Figure 4-25a.

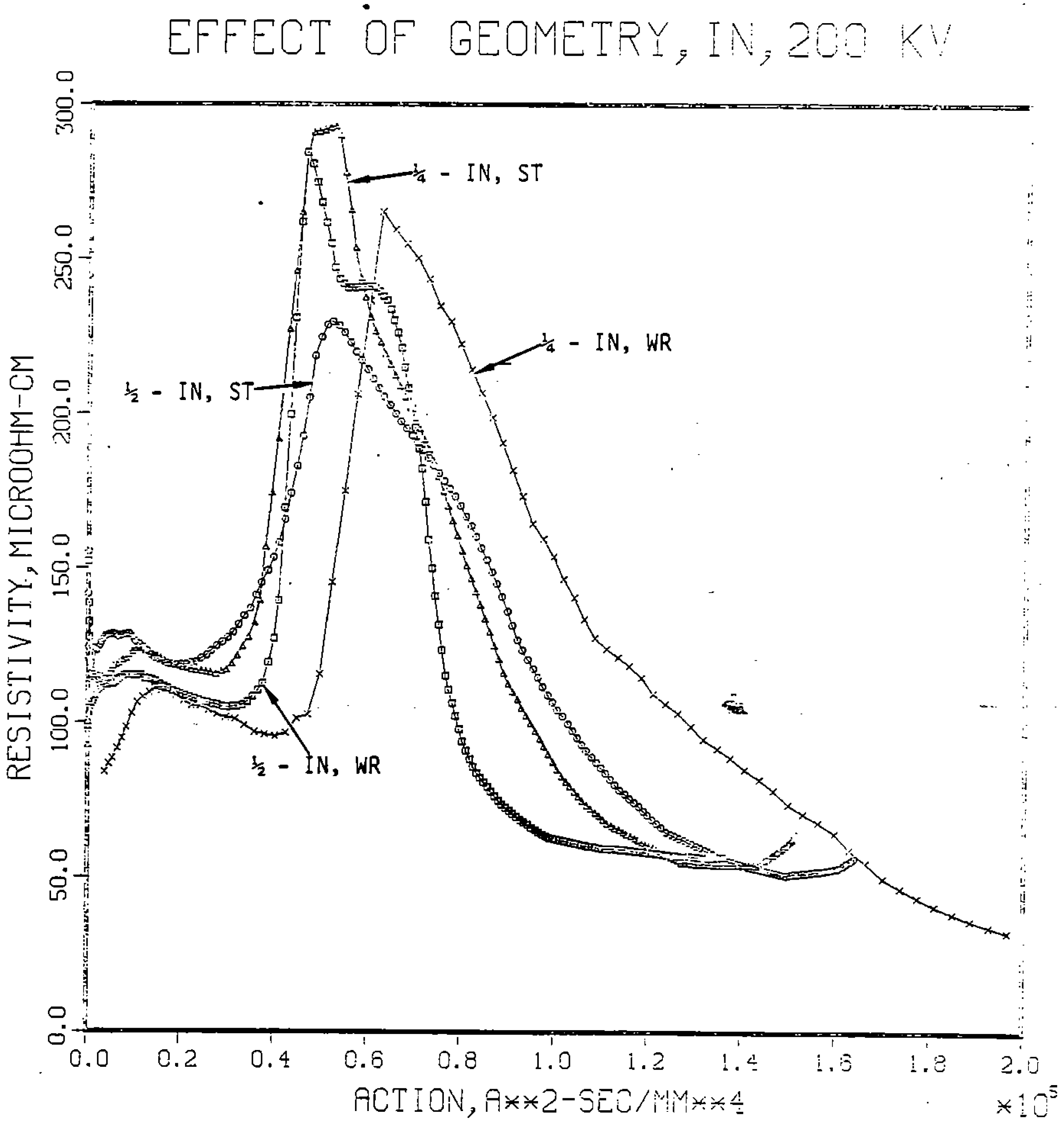

EFFECT OF GEOMETRY, IN, 200 KV
RESISTIVITY, MICROOHM-CM
ACTION, A**2-SEC/MM**4
*10^5
300.0
250.0
200.0
150.0
100.0
50.0
0.0
0.0
0.2
0.4
0.6
0.8
1.0
1.2
1.4
1.6
1.8
2.0
¼ - IN, ST
¼ - IN, WR
½ - IN, ST
½ - IN, WR

Figure 4-25b.

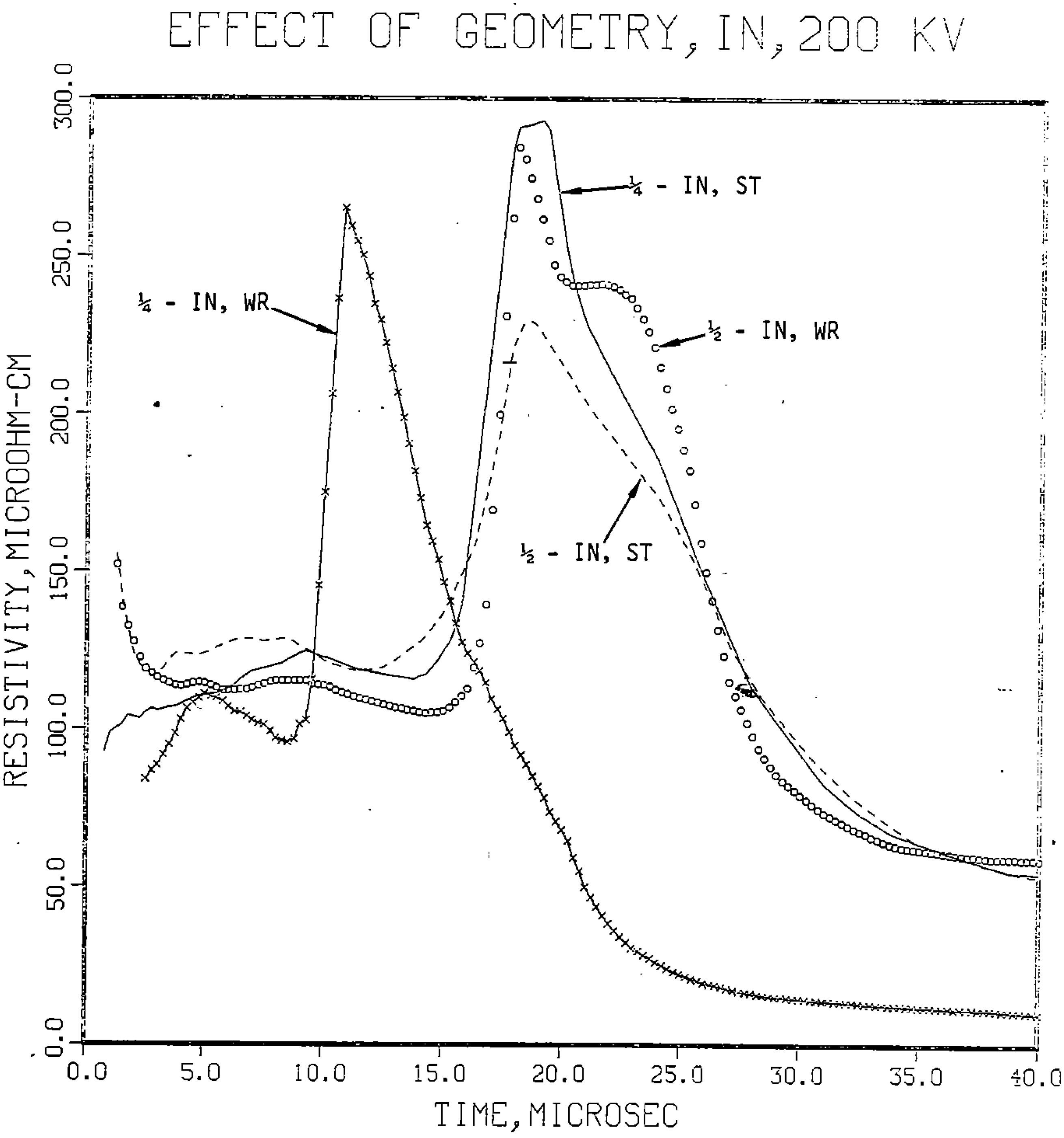
EFFECT OF GEOMETRY, IN, 200 KV
RESISTIVITY, MICROOHM-CM
TIME, MICROSEC
0.0
50.0
100.0
150.0
200.0
250.0
300.0
0.0
5.0
10.0
15.0
20.0
25.0
30.0
35.0
40.0
¼ - IN, ST
¼ - IN, WR
½ - IN, WR
½ - IN, ST

Figure 4-26a.

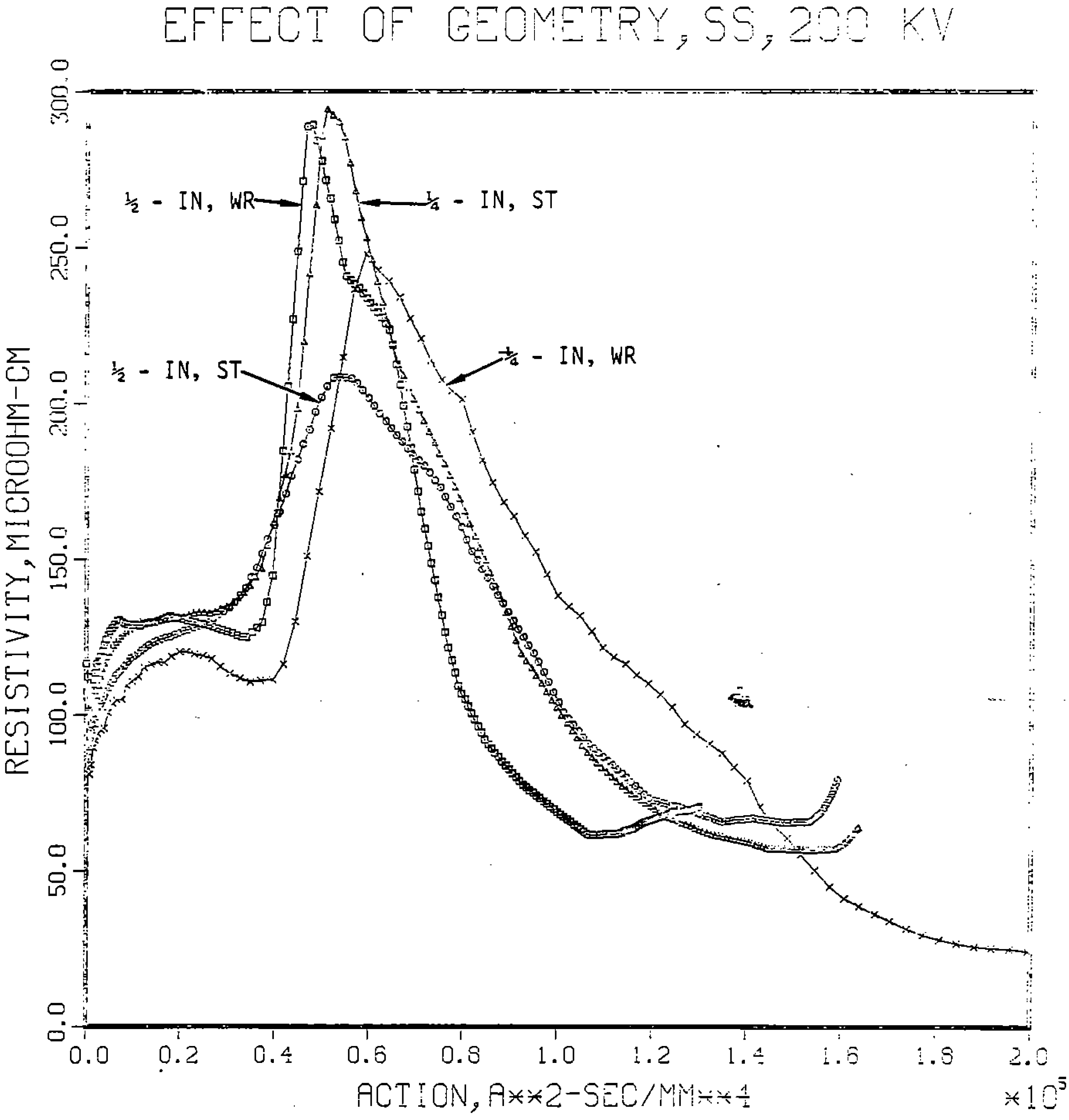
EFFECT OF GEOMETRY, SS, 200 KV
RESISTIVITY, MICROOHM-CM
ACTION, A**2-SEC/MM**4
*10^5
0.0
50.0
100.0
150.0
200.0
250.0
300.0
0.0
0.2
0.4
0.6
0.8
1.0
1.2
1.4
1.6
1.8
2.0
½ - IN, WR
¼ - IN, ST
½ - IN, ST
¼ - IN, WR

Figure 4-26b.

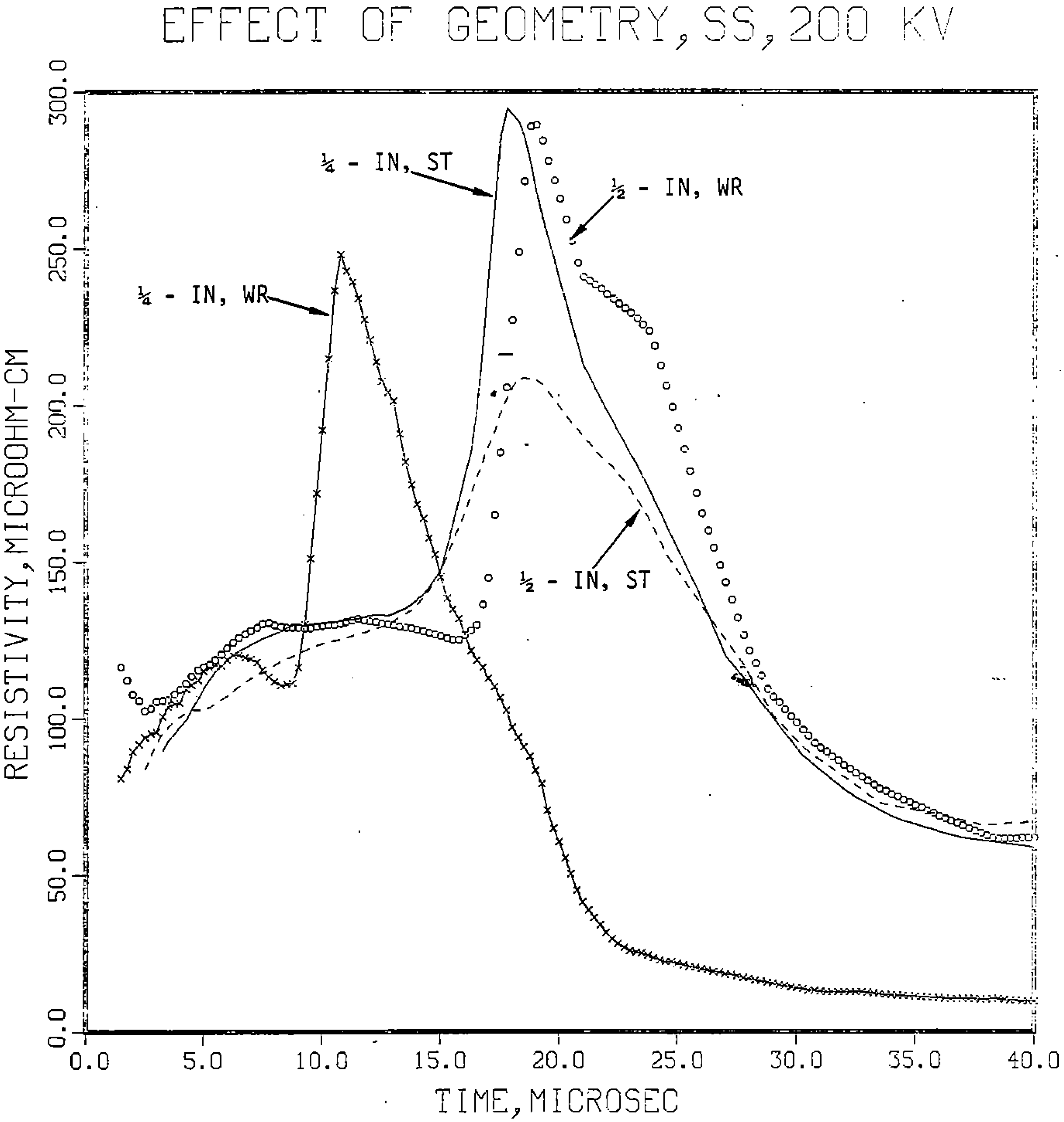
EFFECT OF GEOMETRY, SS, 200 KV
RESISTIVITY, MICROOHM-CM
TIME, MICROSEC
0.0
50.0
100.0
150.0
200.0
250.0
300.0
0.0
5.0
10.0
15.0
20.0
25.0
30.0
35.0
40.0
¼ - IN, ST
½ - IN, WR
¼ - IN, WR
½ - IN, ST

Figure 4-27a.

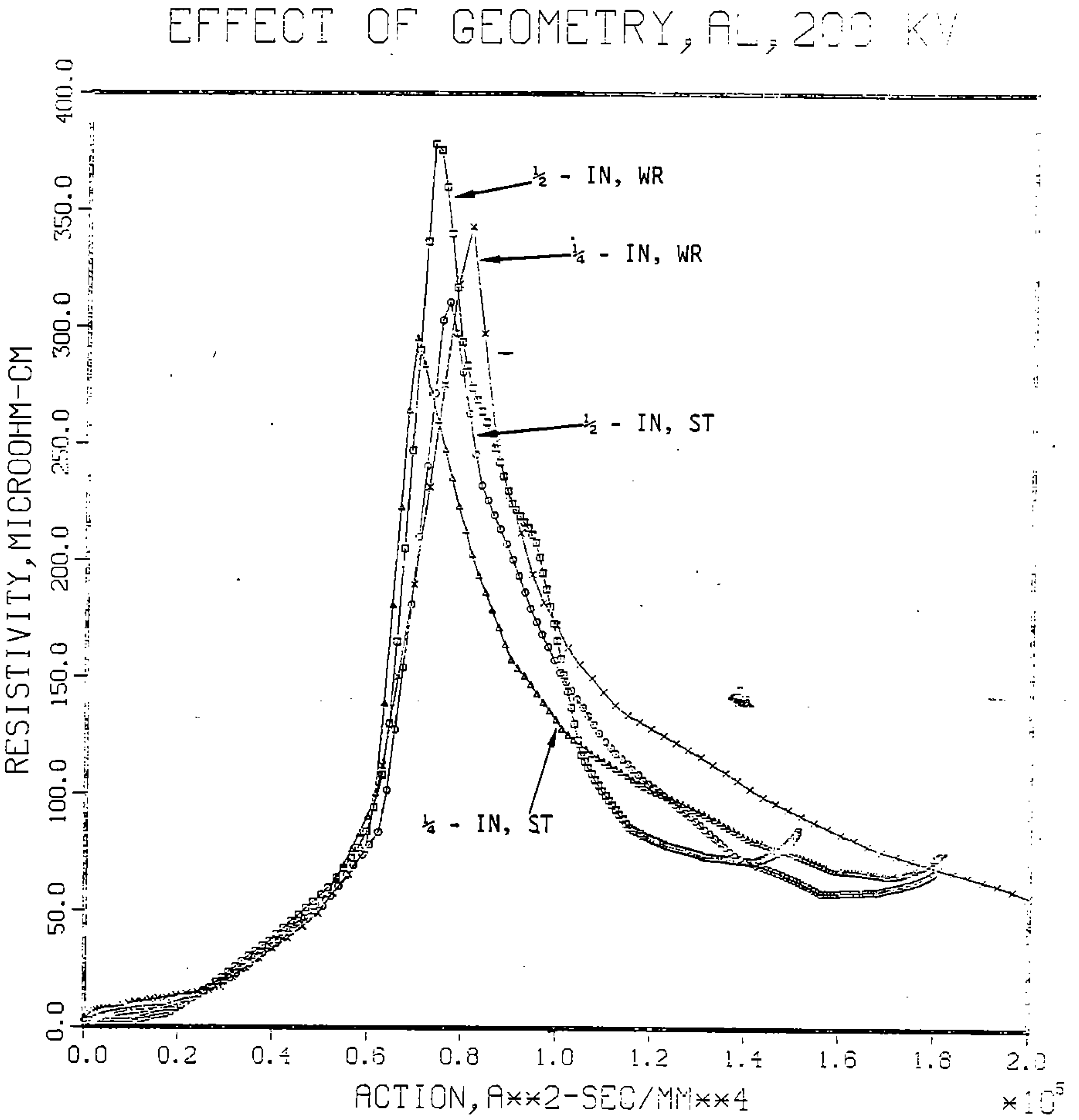
EFFECT OF GEOMETRY, AL, 200 KV
RESISTIVITY, MICROOHM-CM
400.0
350.0
300.0
250.0
200.0
150.0
100.0
50.0
0.0
0.0
0.2
0.4
0.6
0.8
1.0
1.2
1.4
1.6
1.8
2.0
ACTION, A**2-SEC/MM**4
*10^5
½ - IN, WR
¼ - IN, WR
½ - IN, ST
¼ - IN, ST

Figure 4-27b.

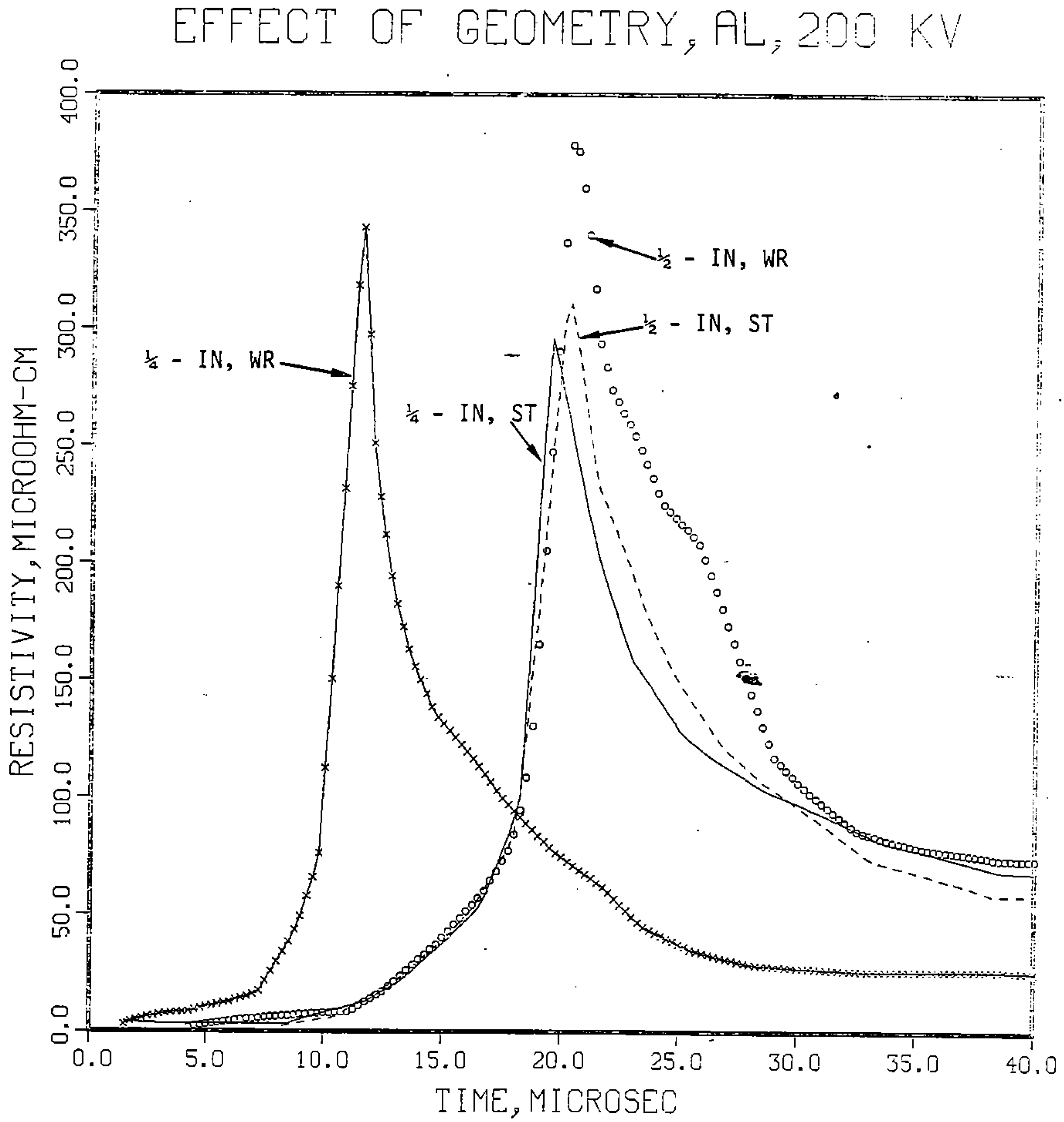
EFFECT OF GEOMETRY, AL, 200 KV
RESISTIVITY, MICROOHM-CM
TIME, MICROSEC
0.0
50.0
100.0
150.0
200.0
250.0
300.0
350.0
400.0
0.0
5.0
10.0
15.0
20.0
25.0
30.0
35.0
40.0
¼ - IN, WR
¼ - IN, ST
½ - IN, WR
½ - IN, ST

1/2-inch ST Aℓ samples had almost the smallest peak resistivity for Aℓ, nearly in agreement with the other metals.

In summary, for a pulser voltage of 200 kV, the major geometry effect appears to be the smaller cross-sectional area for the 1/4-inch WR samples.

A complete comparison of geometry effects was not made for other voltages for all metal types. However, at least for Inconel, all geometries were tested with large and small voltage drives. Figure 4-28 shows ρ versus action and ρ versus time for the four geometries for Inconel with a pulser voltage of 54 to 60 kV. Figures 4-29 and 4-30 compare the resistivity curves for the 1/4-inch and 1/2-inch helical geometries for stainless steel and aluminum with the same range of pulser voltages. These figures show the same general effect of the smaller cross-sectional area for the 1/4-inch WR samples as the 200 kV data in Figures 4-24 through 4-27 in that the 1/4-inch WR samples go through their peak resistivities at earlier times but at larger values of action than the other geometries. However, one should note that some of these curves are for pulser voltages of 54 kV and others for 60 kV. Since these voltages are close to the threshold voltage for vaporization and restrike in these samples, the relatively small voltage difference between 54 and 60 kV could make a sizable difference in the resistivity curves. In other words, some of the difference between the curves could be a voltage effect rather than a geometry effect.

It can be seen in Figures 4-28b and 4-29b that the 1/2-inch WR samples go through an initial resistivity peak and then the resistivities are increasing again at the end of the graphs. By comparison, for Aℓ (Figure 4-30b), the 1/2-inch WR samples apparently do not restrike with a voltage of 54 kV. Thus, the threshold voltage for restrike for these metals with cross-sectional areas corresponding to the 1/2-inch WR samples is around 54 to 60 kV, that is, 0.84 to 0.94 kV/cm based on the helical length of the samples. On the other hand, the 1/4-inch WR samples, because of their smaller areas, restrike at 54 kV (0.84 kV/cm) and show no indication of turning off on the time scale of the graphs. An Inconel sample with this geometry did not restrike with a pulser voltage of 40 kV (0.63 kV/cm) (shot #41).

Figures 4-31 through 4-36 illustrate the effect of pulser voltage (ρ versus action and ρ versus time) for several geometries and metals. In general, the resistivity versus action curves are independent of voltage (within the accuracy of the data reduction) up to the vaporization point (start of large increase in resistivity), as would be expected since there is little heat loss from the metal in the time that it takes to reach the vaporization point in these experiments (usually less than ≈200 μs). Of course, one would

(Text continues on page 109)

Figure 4-28a.

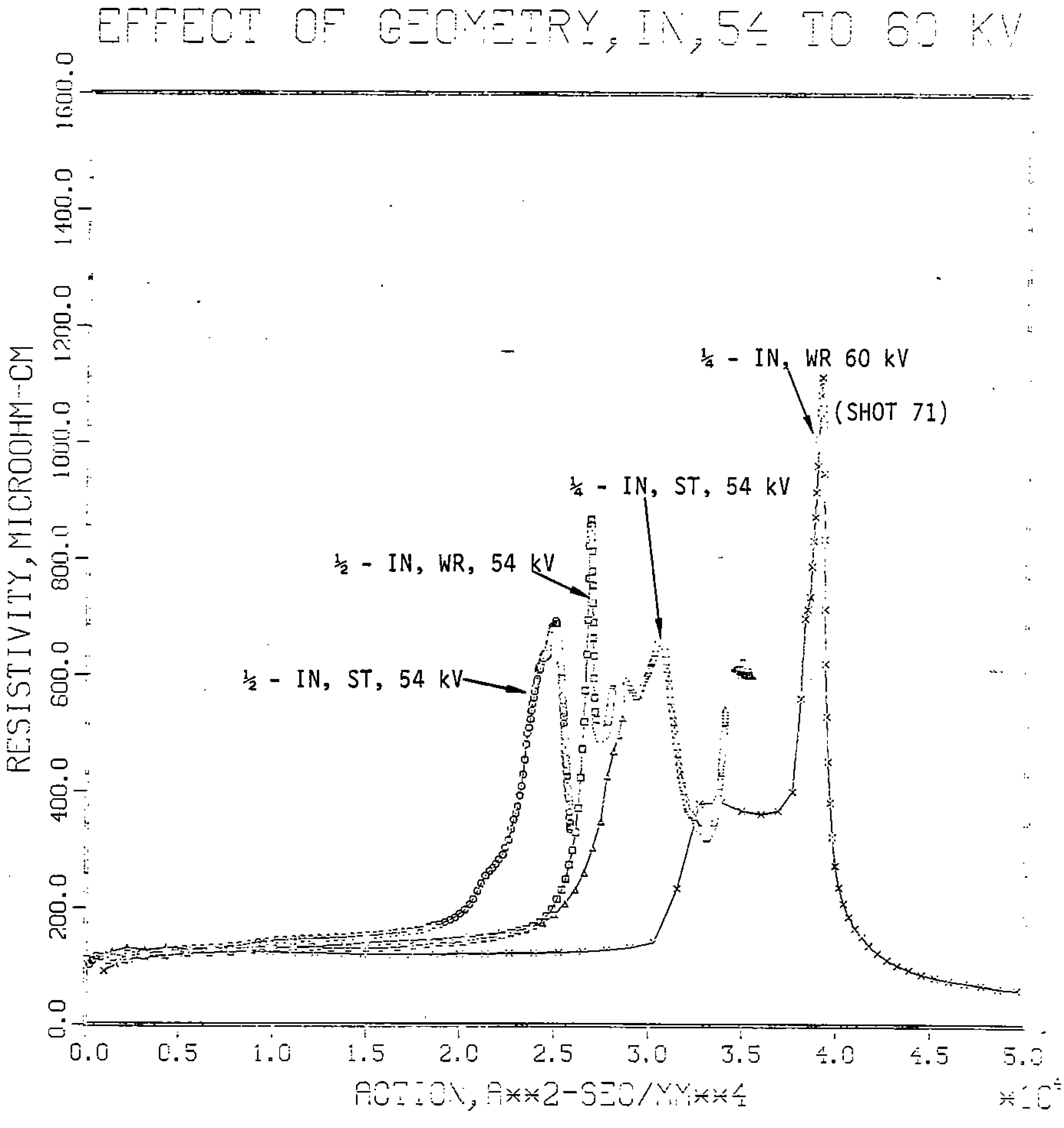

EFFECT OF GEOMETRY, IN, 54 TO 60 KV
RESISTIVITY, MICROOHM-CM
0.0
200.0
400.0
600.0
800.0
1000.0
1200.0
1400.0
1600.0
0.0
0.5
1.0
1.5
2.0
2.5
3.0
3.5
4.0
4.5
5.0
ACTION, A**2-SEC/MM**4
*10⁴
¼ - IN, WR 60 kV
(SHOT 71)
¼ - IN, ST, 54 kV
½ - IN, WR, 54 kV
½ - IN, ST, 54 kV

Figure 4-28b.

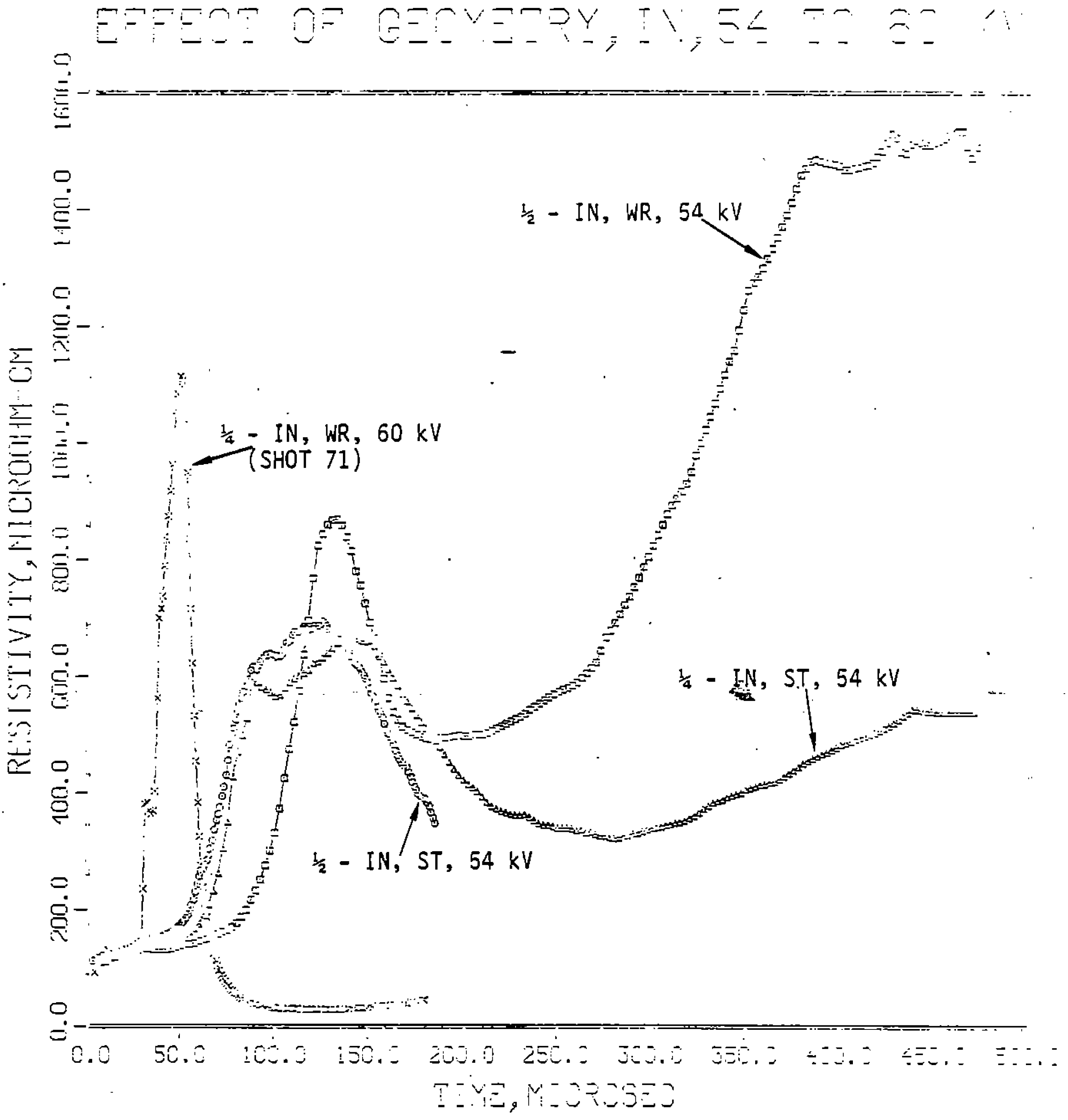
EFFECT OF GEOMETRY, IN, 54 TO 60 KV
RESISTIVITY, MICROOHM-CM
TIME, MICROSEC
0.0
200.0
400.0
600.0
800.0
1000.0
1200.0
1400.0
1600.0
0.0
50.0
100.0
150.0
200.0
250.0
300.0
350.0
400.0
450.0
500.0
½ - IN, WR, 54 kV
¼ - IN, WR, 60 kV (SHOT 71)
¼ - IN, ST, 54 kV
½ - IN, ST, 54 kV

Figure 4-29a.

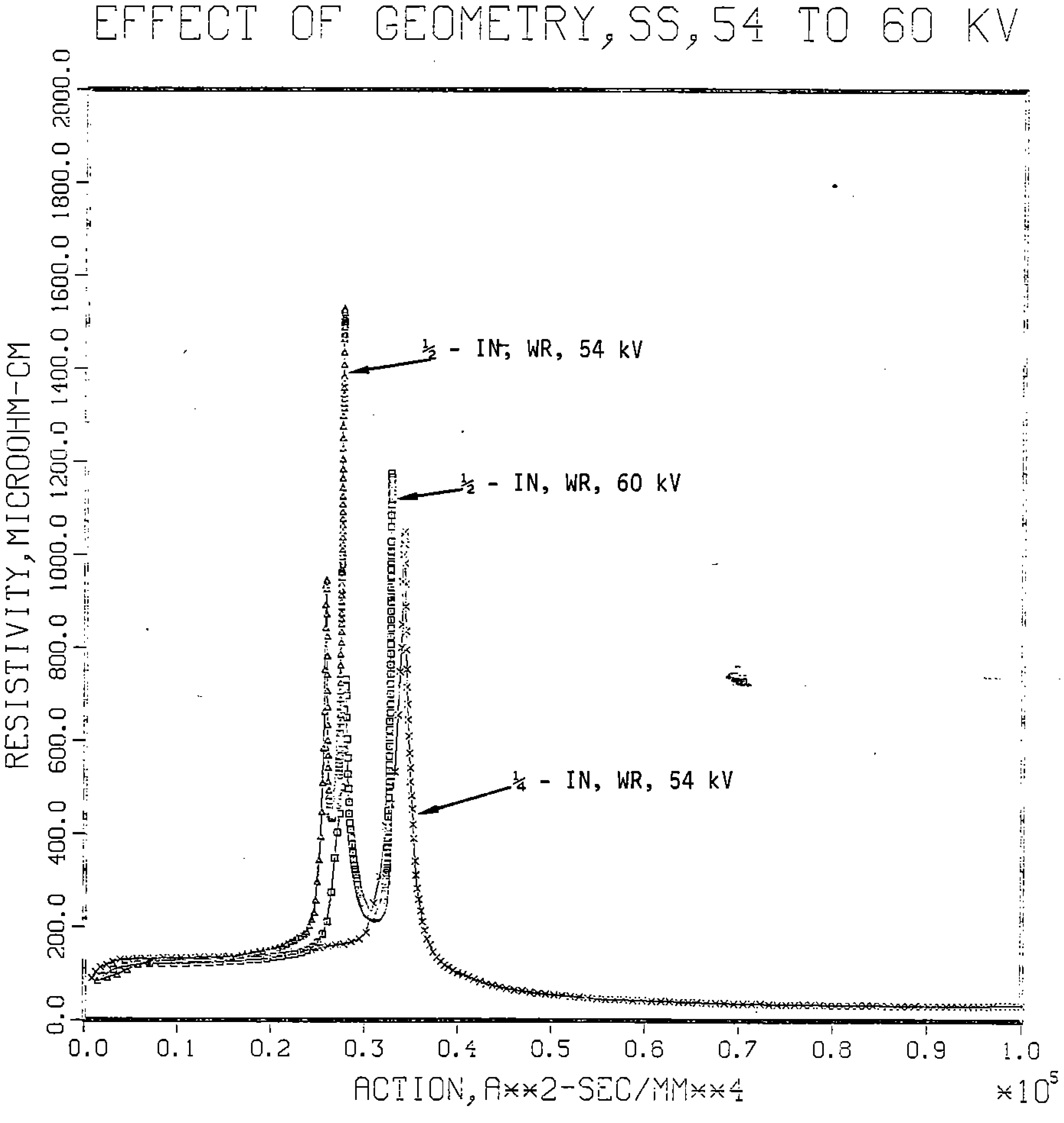
EFFECT OF GEOMETRY, SS, 54 TO 60 KV
RESISTIVITY, MICROOHM-CM
0.0
200.0
400.0
600.0
800.0
1000.0
1200.0
1400.0
1600.0
1800.0
2000.0
½ - IN, WR, 54 kV
½ - IN, WR, 60 kV
¼ - IN, WR, 54 kV
0.0
0.1
0.2
0.3
0.4
0.5
0.6
0.7
0.8
0.9
1.0
ACTION, A**2-SEC/MM**4
$*10^5$

Figure 4-29b.

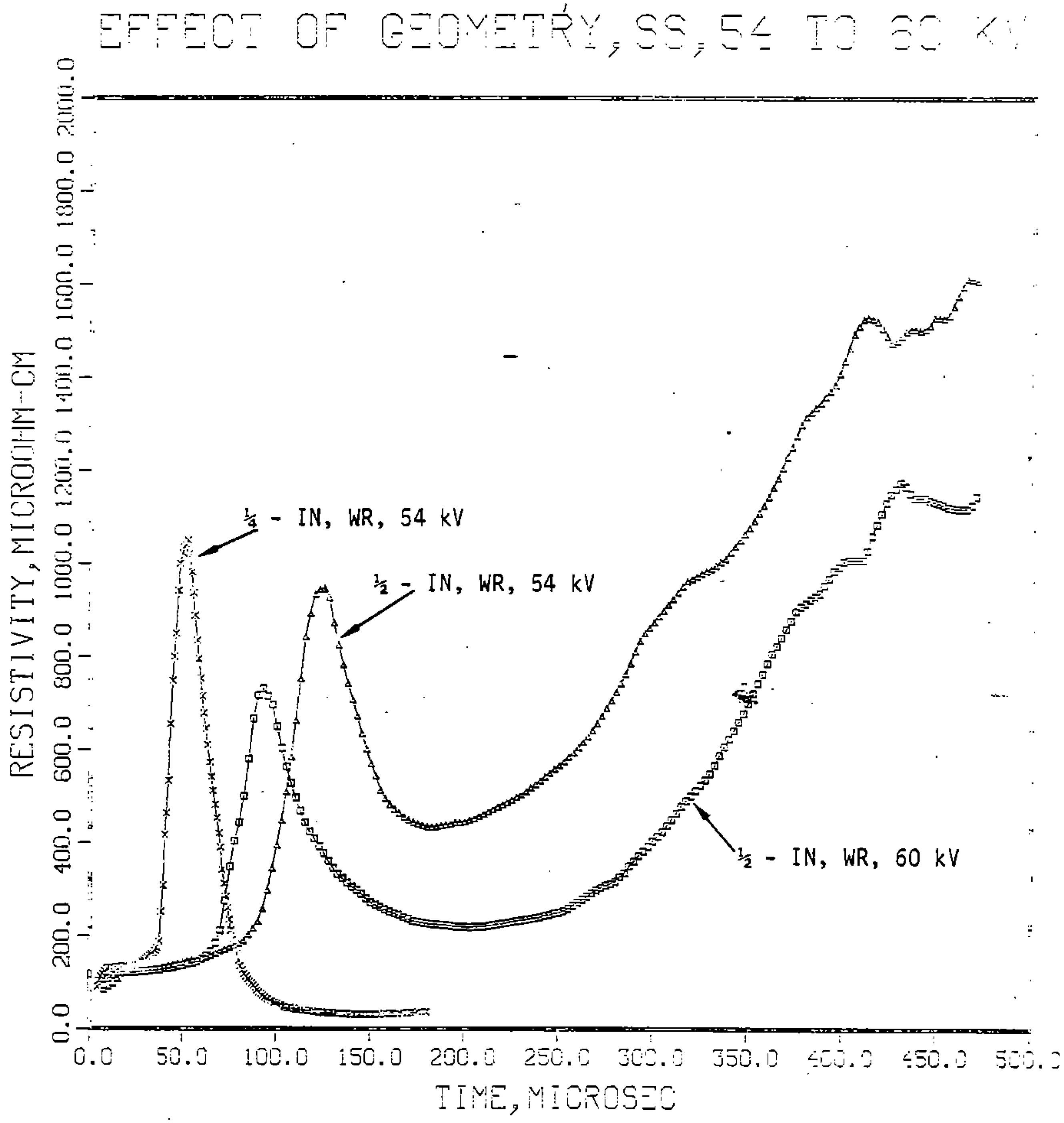
EFFECT OF GEOMETRY, SS, 54 TO 60 KV
RESISTIVITY, MICROOHM-CM
0.0
200.0
400.0
600.0
800.0
1000.0
1200.0
1400.0
1600.0
1800.0
2000.0
TIME, MICROSEC
0.0
50.0
100.0
150.0
200.0
250.0
300.0
350.0
400.0
450.0
500.0
¼ - IN, WR, 54 kV
½ - IN, WR, 54 kV
½ - IN, WR, 60 kV

Figure 4-30a.

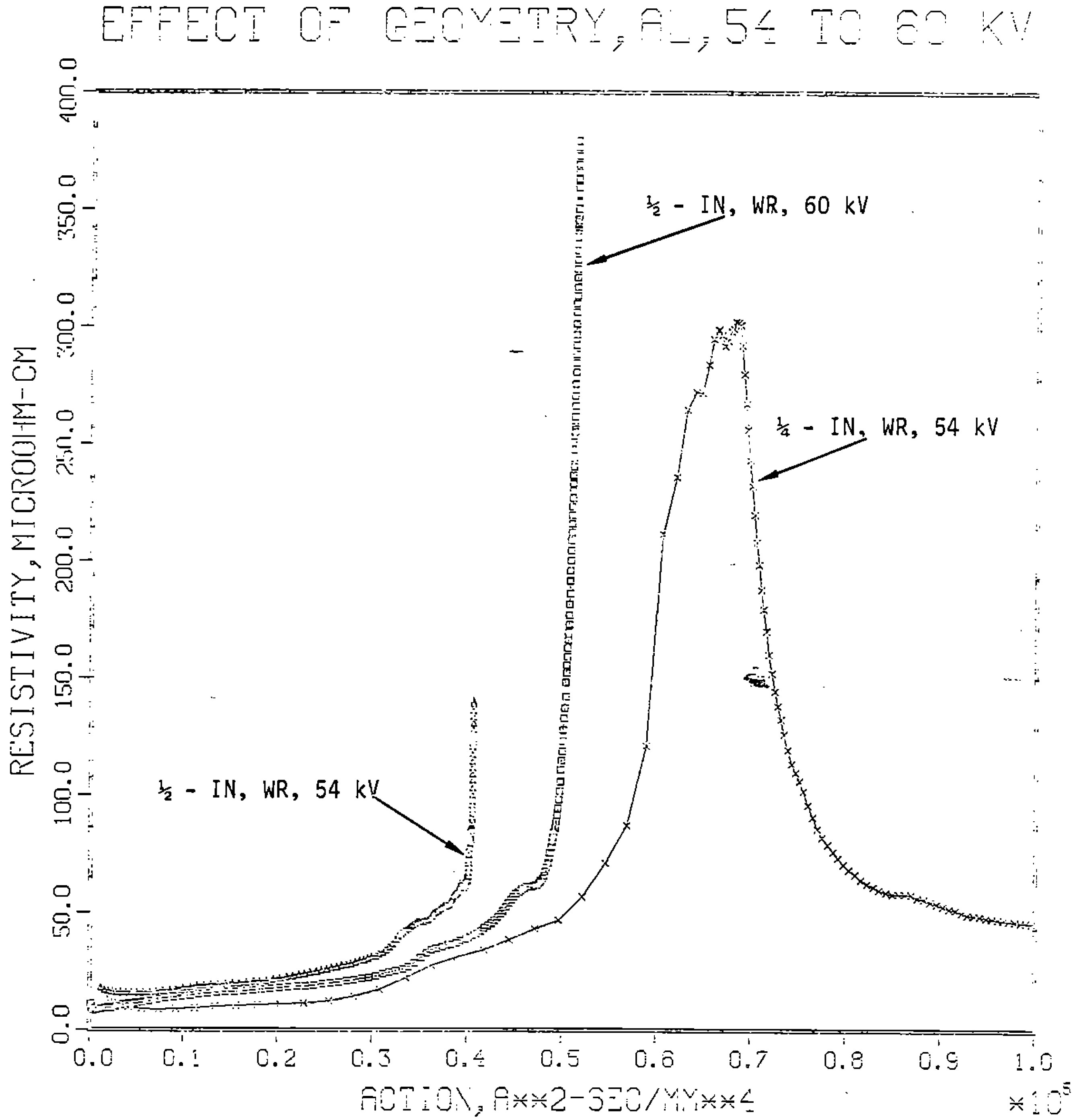
EFFECT OF GEOMETRY, AL, 54 TO 60 KV
RESISTIVITY, MICROOHM-CM
0.0
50.0
100.0
150.0
200.0
250.0
300.0
350.0
400.0
0.0
0.1
0.2
0.3
0.4
0.5
0.6
0.7
0.8
0.9
1.0
ACTION, A**2-SEC/MM**4
*10^5
½ - IN, WR, 60 kV
¼ - IN, WR, 54 kV
½ - IN, WR, 54 kV

Figure 4-30b.

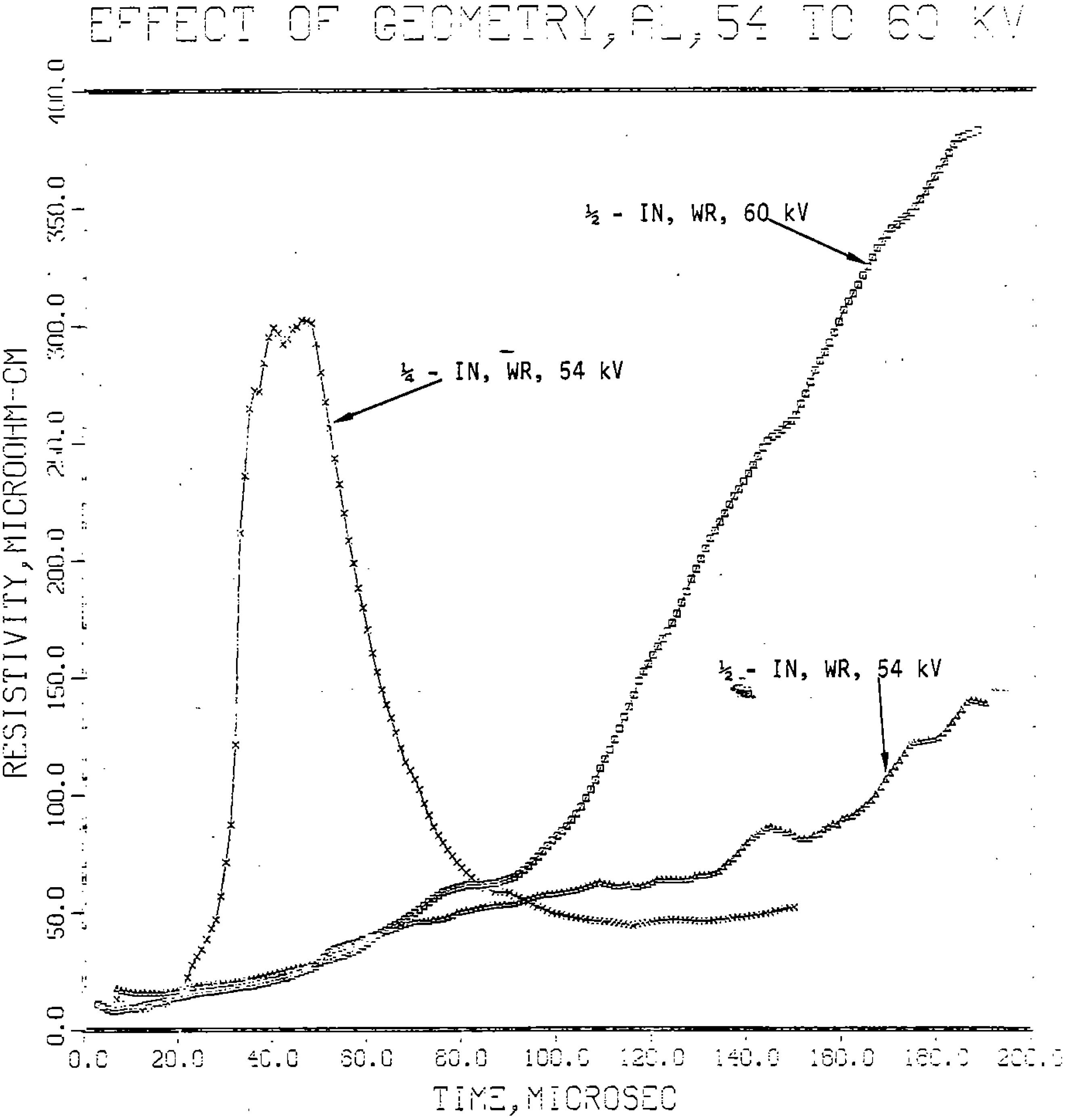

EFFECT OF GEOMETRY, AL, 54 TO 60 KV
RESISTIVITY, MICROOHM-CM
TIME, MICROSEC
0.0
50.0
100.0
150.0
200.0
250.0
300.0
350.0
400.0
0.0
20.0
40.0
60.0
80.0
100.0
120.0
140.0
160.0
180.0
200.0
½ - IN, WR, 60 kV
¼ - IN, WR, 54 kV
½ - IN, WR, 54 kV

Figure 4-31a.

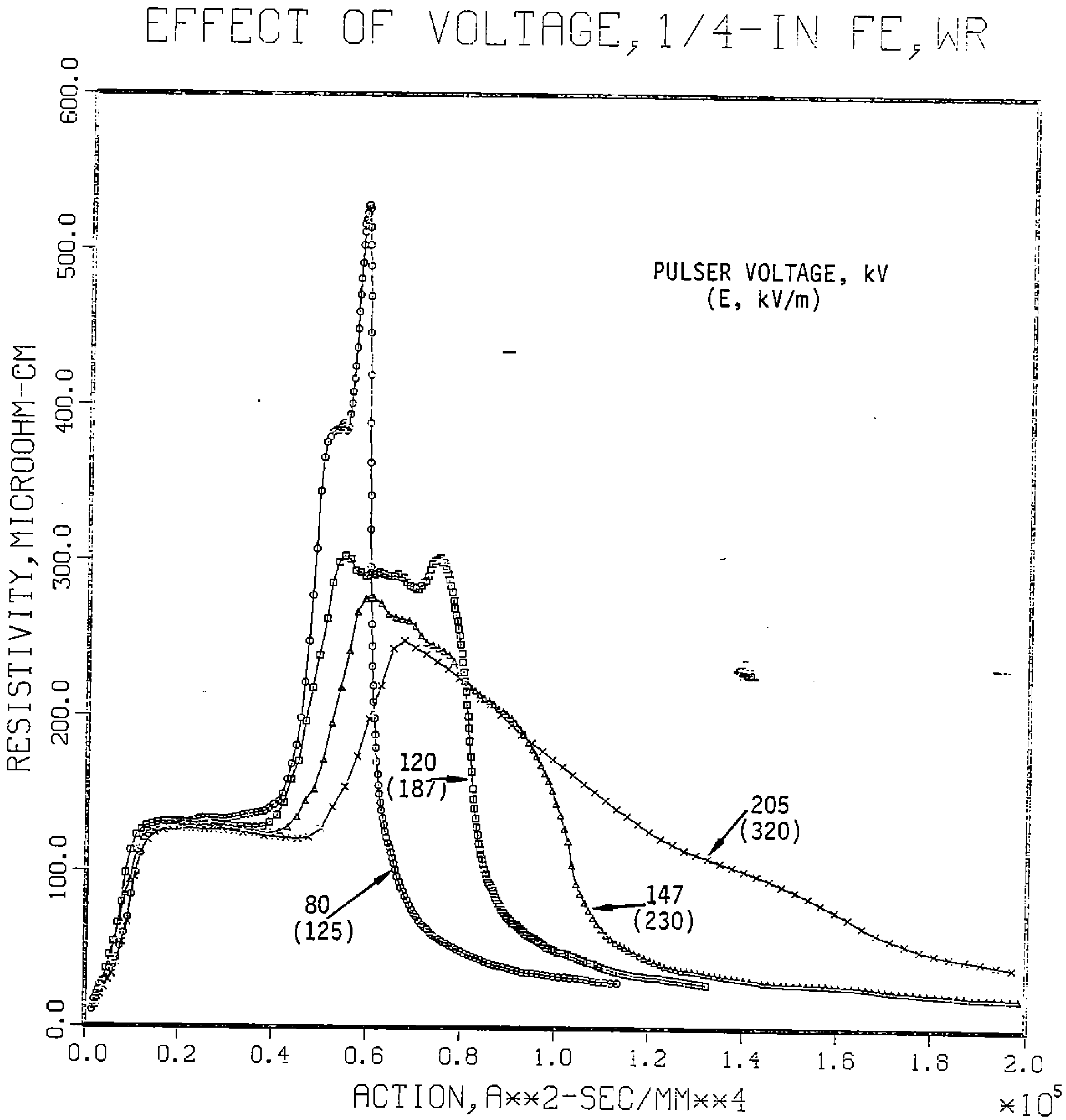
EFFECT OF VOLTAGE, 1/4-IN FE, WR
RESISTIVITY, MICROOHM-CM
0.0
100.0
200.0
300.0
400.0
500.0
600.0
ACTION, A**2-SEC/MM**4
0.0
0.2
0.4
0.6
0.8
1.0
1.2
1.4
1.6
1.8
2.0
$*10^5$
PULSER VOLTAGE, kV
(E, kV/m)
80
(125)
120
(187)
147
(230)
205
(320)

Figure 4-31b.

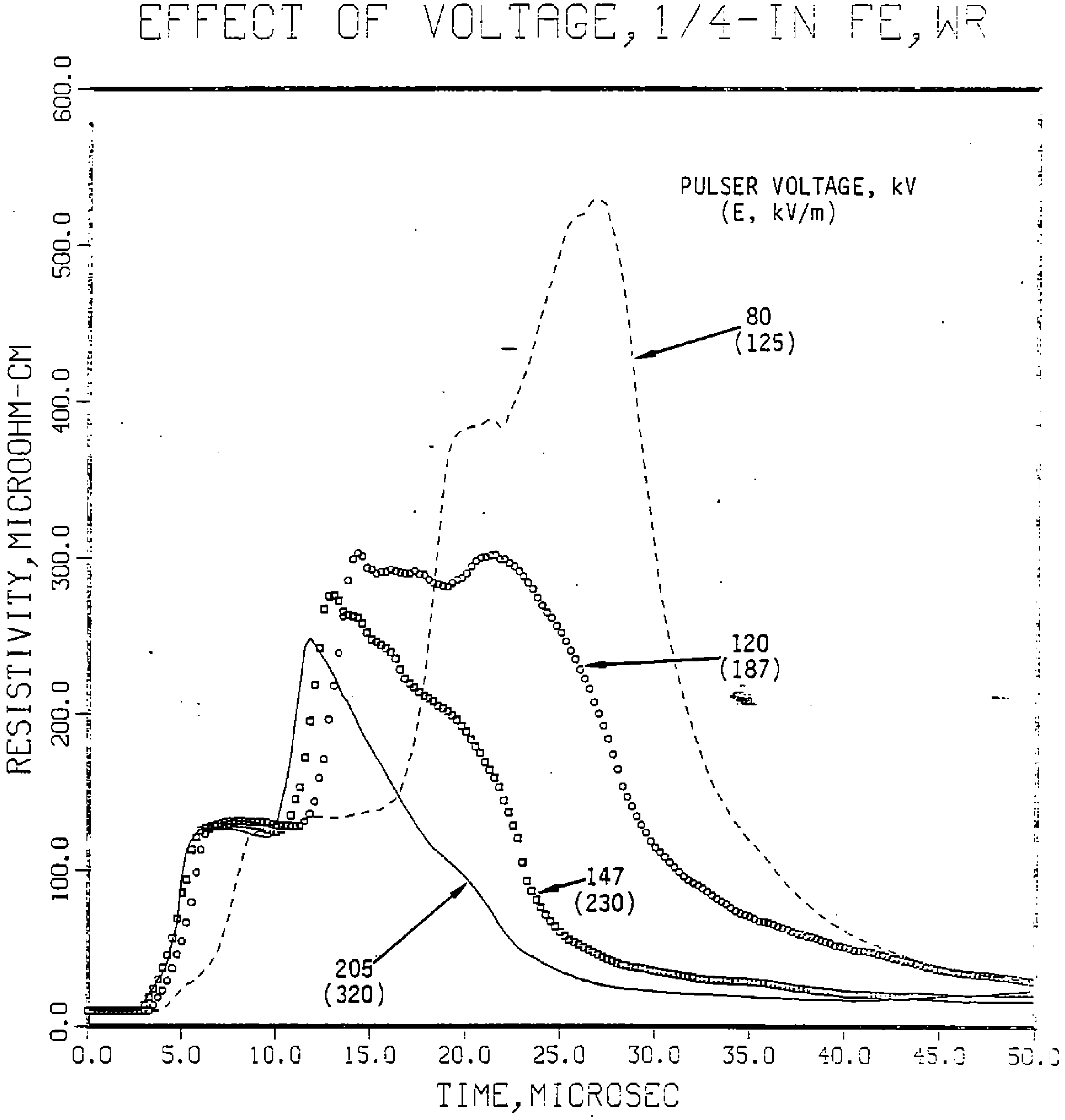
EFFECT OF VOLTAGE, 1/4-IN FE, WR
PULSER VOLTAGE, kV
(E, kV/m)
80
(125)
120
(187)
147
(230)
205
(320)
RESISTIVITY, MICROOHM-CM
0.0
100.0
200.0
300.0
400.0
500.0
600.0
0.0
5.0
10.0
15.0
20.0
25.0
30.0
35.0
40.0
45.0
50.0
TIME, MICROSEC

Figure 4-32a.

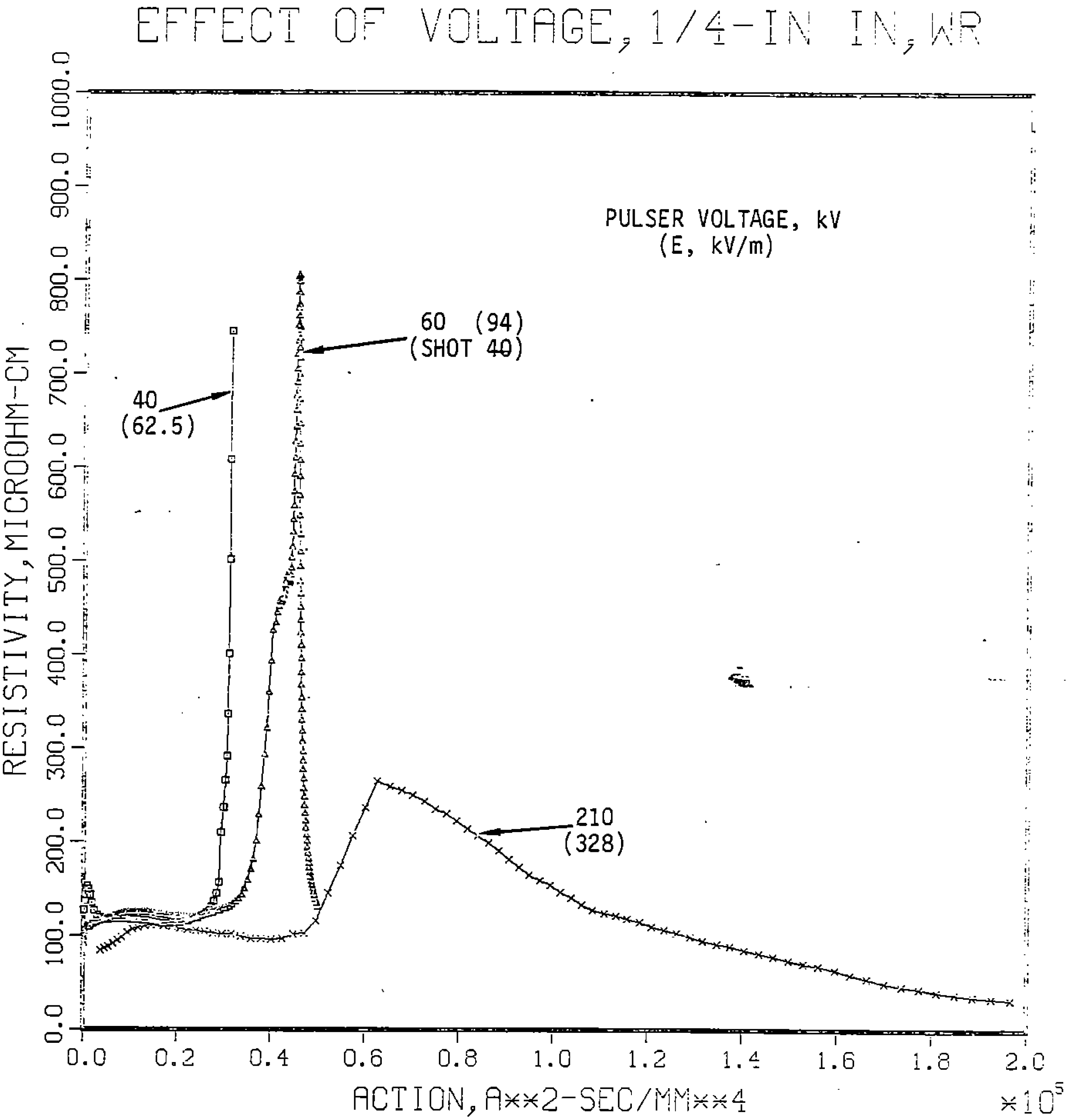
EFFECT OF VOLTAGE, 1/4-IN IN, WR
RESISTIVITY, MICROOHM-CM
0.0
100.0
200.0
300.0
400.0
500.0
600.0
700.0
800.0
900.0
1000.0
ACTION, A**2-SEC/MM**4
0.0
0.2
0.4
0.6
0.8
1.0
1.2
1.4
1.6
1.8
2.0
$\times 10^5$
PULSER VOLTAGE, kV
(E, kV/m)
60 (94)
(SHOT ~~40~~)
40
(62.5)
210
(328)

Figure 4-32b.

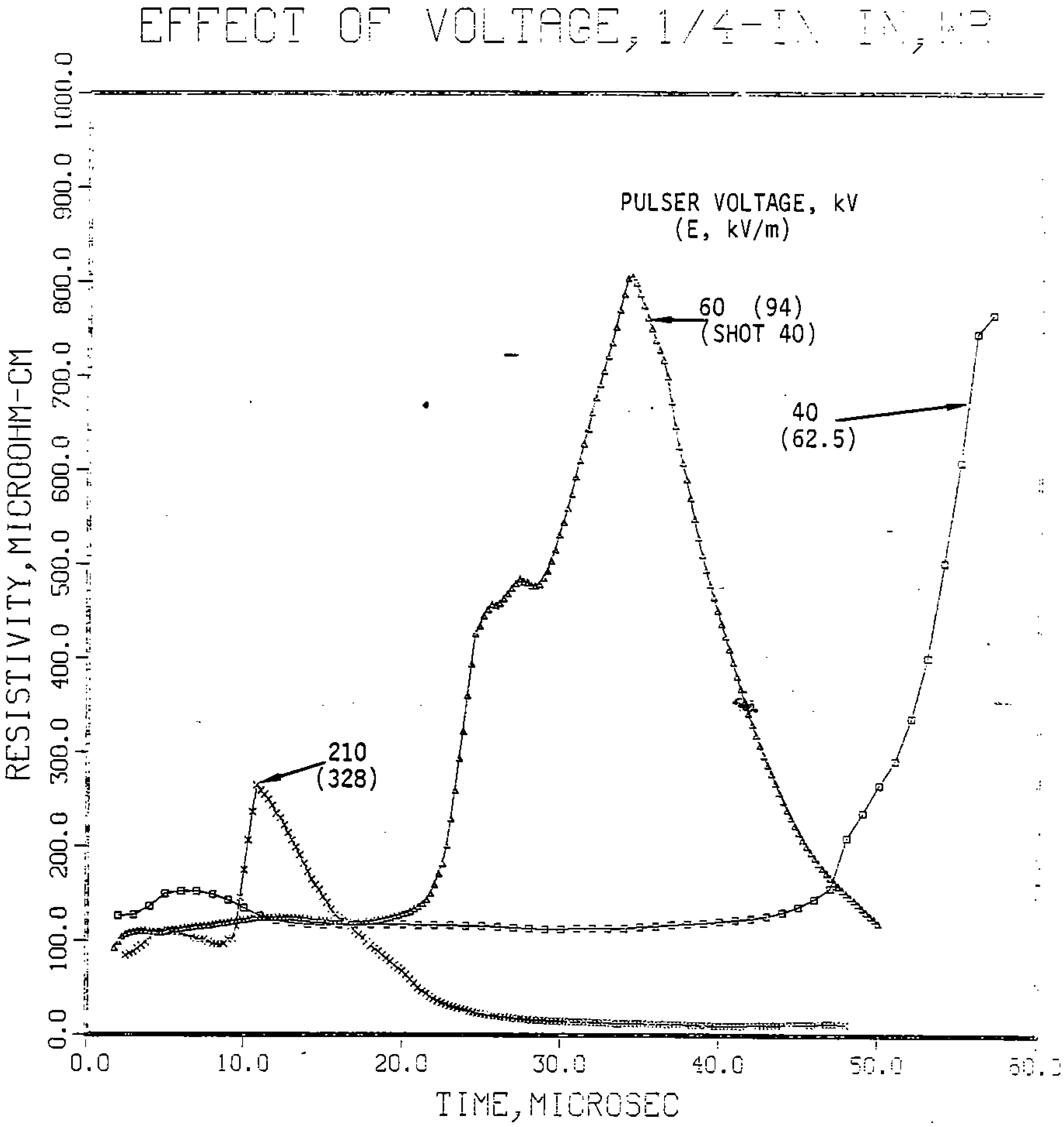
EFFECT OF VOLTAGE,1/4-IN IN,WP
PULSER VOLTAGE, kV
(E, kV/m)
60 (94)
(SHOT 40)
40
(62.5)
210
(328)
RESISTIVITY,MICROOHM-CM
0.0
100.0
200.0
300.0
400.0
500.0
600.0
700.0
800.0
900.0
1000.0
0.0
10.0
20.0
30.0
40.0
50.0
60.0
TIME,MICROSEC

Figure 4-33a.

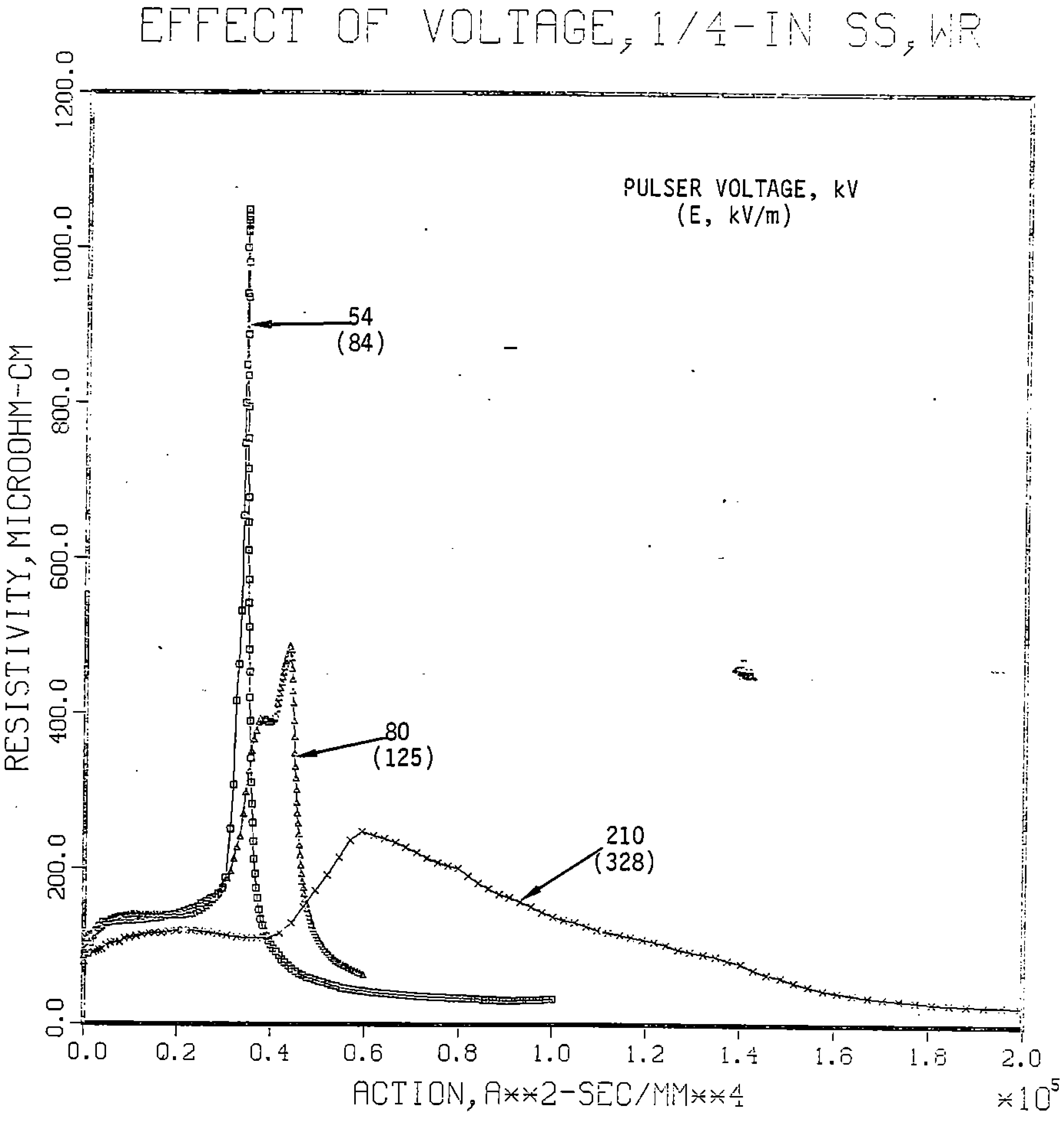
EFFECT OF VOLTAGE, 1/4-IN SS, WR
PULSER VOLTAGE, kV
(E, kV/m)
54
(84)
80
(125)
210
(328)
RESISTIVITY, MICROOHM-CM
0.0
200.0
400.0
600.0
800.0
1000.0
1200.0
ACTION, A**2-SEC/MM**4
0.0
0.2
0.4
0.6
0.8
1.0
1.2
1.4
1.6
1.8
2.0
*10^5

Figure 4-33b.

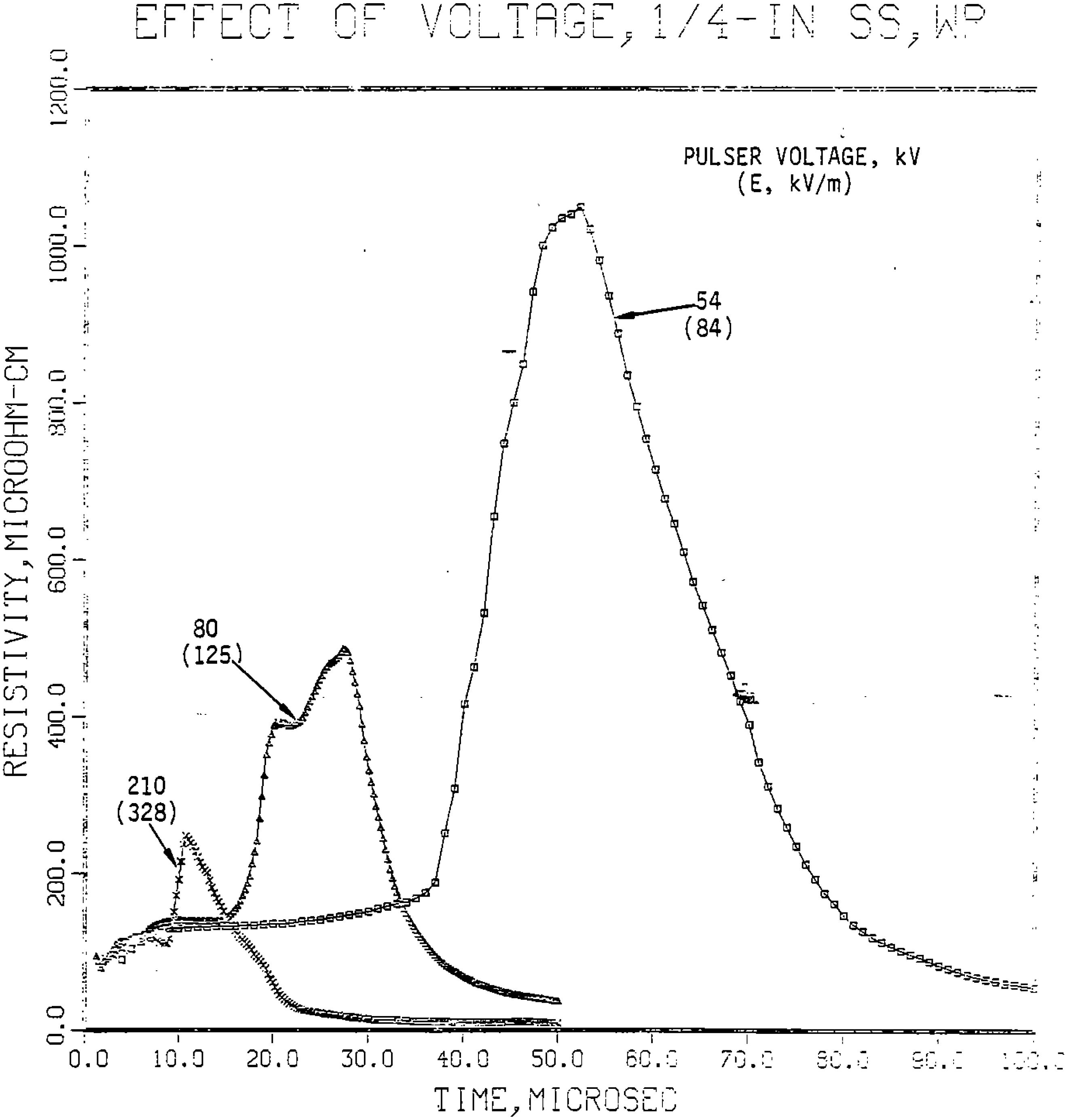
EFFECT OF VOLTAGE, 1/4-IN SS, WP
RESISTIVITY, MICROOHM-CM
TIME, MICROSEC
0.0
200.0
400.0
600.0
800.0
1000.0
1200.0
0.0
10.0
20.0
30.0
40.0
50.0
60.0
70.0
80.0
90.0
100.0
PULSER VOLTAGE, kV
(E, kV/m)
54
(84)
80
(125)
210
(328)

Figure 4-34a.

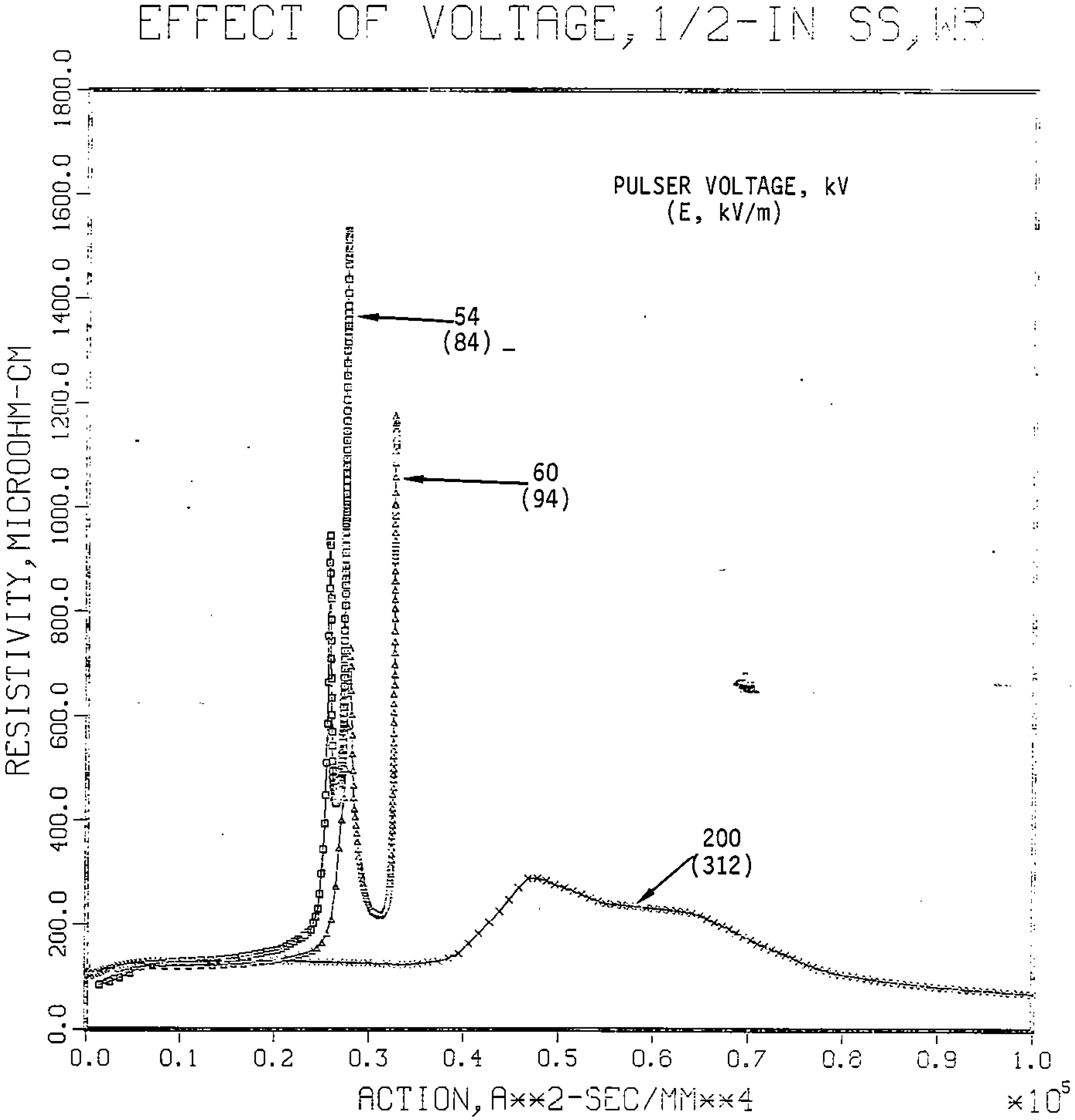
EFFECT OF VOLTAGE, 1/2-IN SS, WR
RESISTIVITY, MICROOHM-CM
0.0
200.0
400.0
600.0
800.0
1000.0
1200.0
1400.0
1600.0
1800.0
ACTION, A**2-SEC/MM**4
*10^5
0.0
0.1
0.2
0.3
0.4
0.5
0.6
0.7
0.8
0.9
1.0
PULSER VOLTAGE, kV
(E, kV/m)
54
(84)
60
(94)
200
(312)

Figure 4-34b.

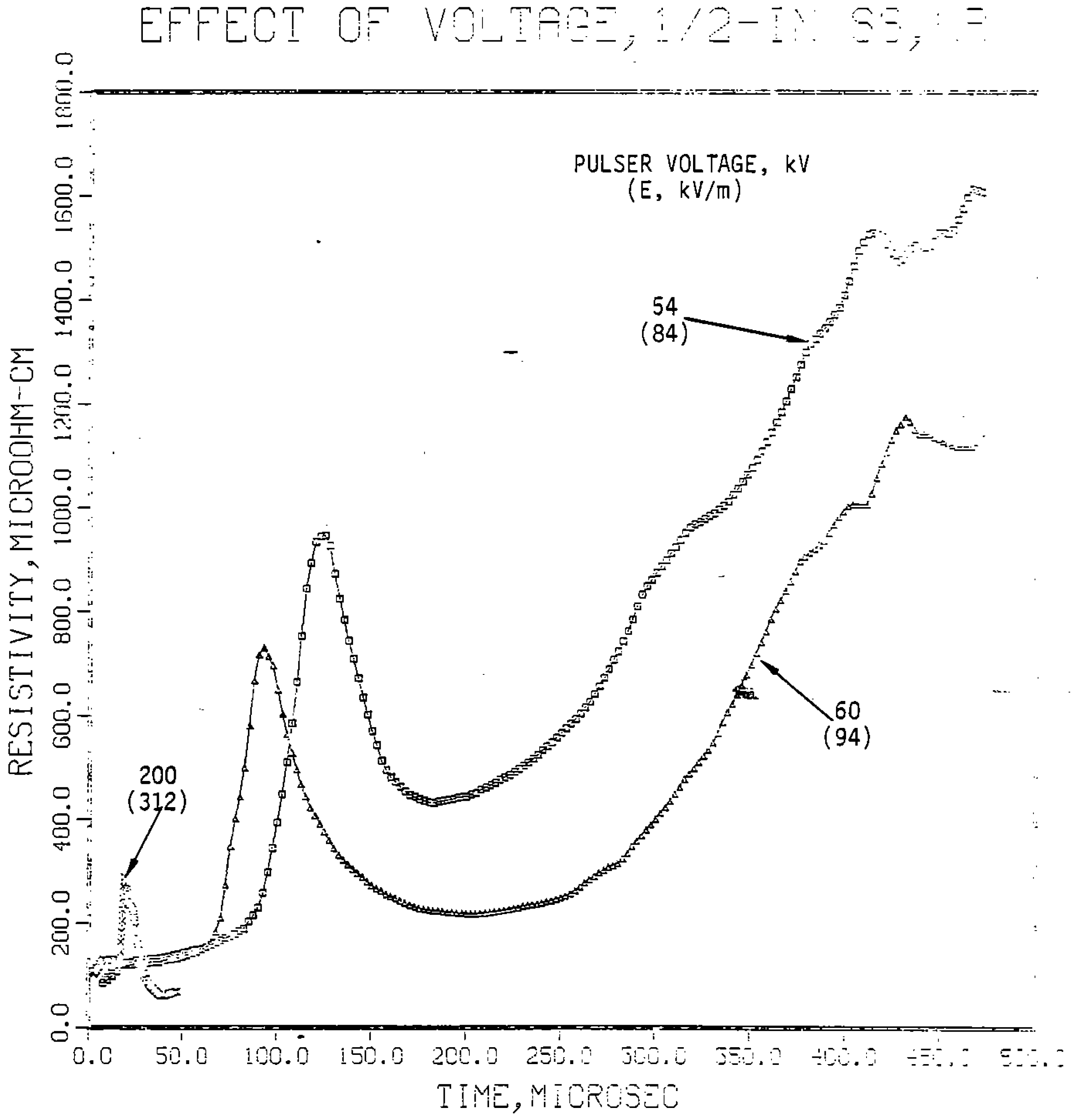

EFFECT OF VOLTAGE,1/2-IN SS,
RESISTIVITY,MICROOHM-CM
0.0
200.0
400.0
600.0
800.0
1000.0
1200.0
1400.0
1600.0
1800.0
TIME,MICROSEC
0.0
50.0
100.0
150.0
200.0
250.0
300.0
350.0
400.0
450.0
500.0
PULSER VOLTAGE, kV
(E, kV/m)
54
(84)
60
(94)
200
(312)

Figure 4-35a.

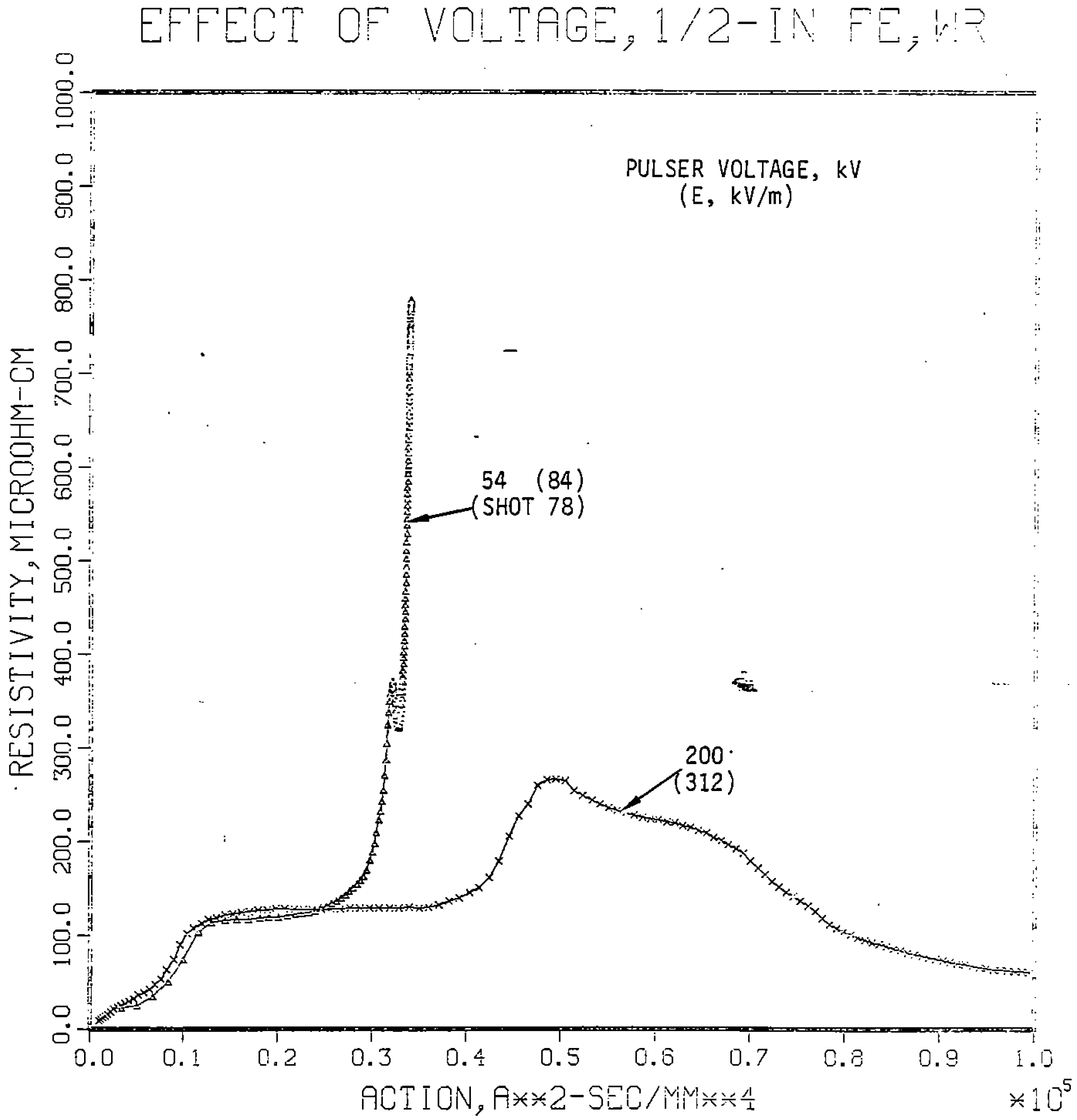
EFFECT OF VOLTAGE, 1/2-IN FE, WR
RESISTIVITY, MICROOHM-CM
0.0
100.0
200.0
300.0
400.0
500.0
600.0
700.0
800.0
900.0
1000.0
PULSER VOLTAGE, kV
(E, kV/m)
54 (84)
(SHOT 78)
200
(312)
0.0
0.1
0.2
0.3
0.4
0.5
0.6
0.7
0.8
0.9
1.0
ACTION, A**2-SEC/MM**4
$\times 10^5$

Figure 4-35b.

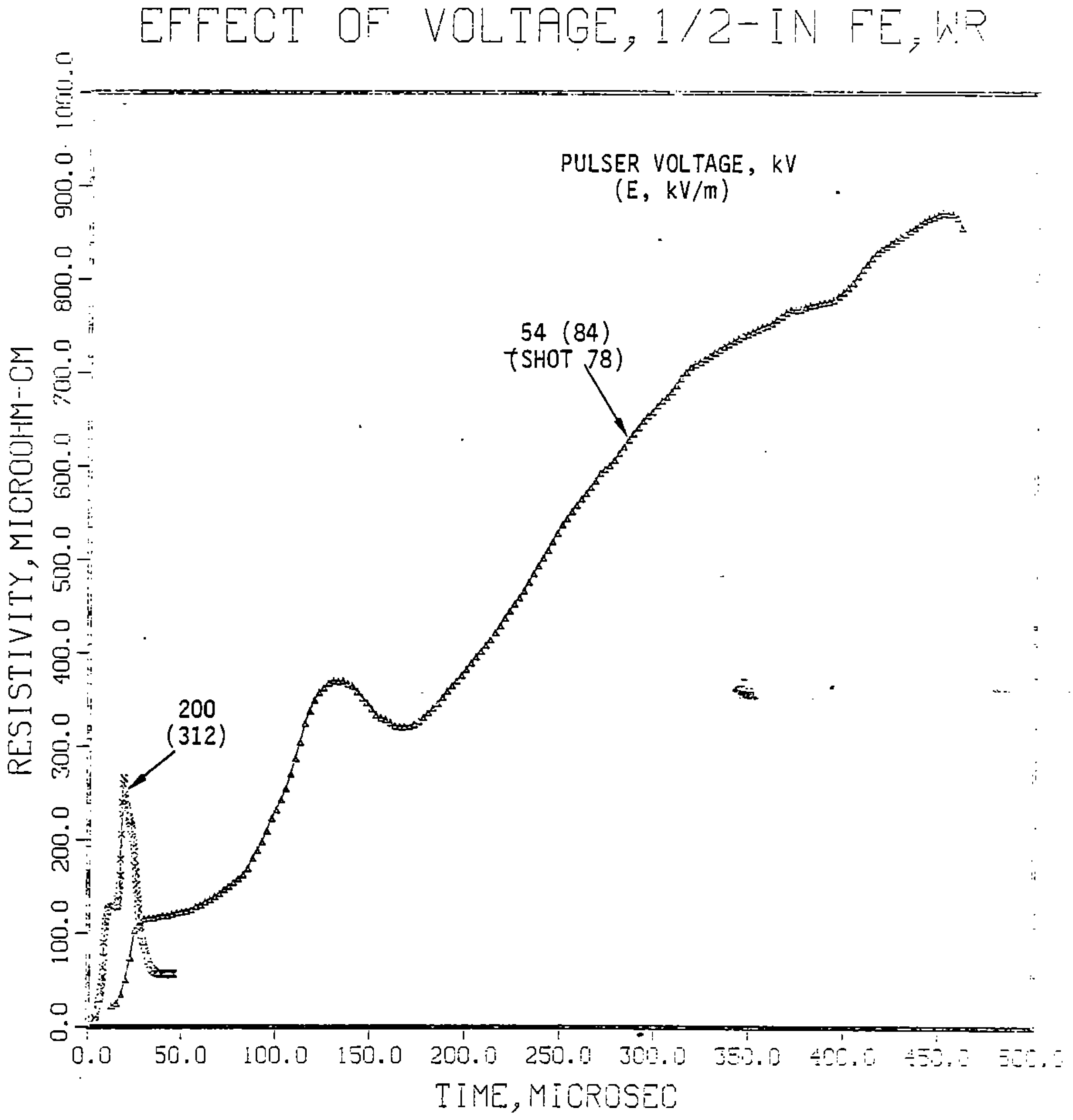
EFFECT OF VOLTAGE, 1/2-IN FE, WR
PULSER VOLTAGE, kV
(E, kV/m)
54 (84)
(SHOT 78)
200
(312)
RESISTIVITY, MICROOHM-CM
0.0
100.0
200.0
300.0
400.0
500.0
600.0
700.0
800.0
900.0
1000.0
TIME, MICROSEC
0.0
50.0
100.0
150.0
200.0
250.0
300.0
350.0
400.0
450.0
500.0

Figure 4-36a.

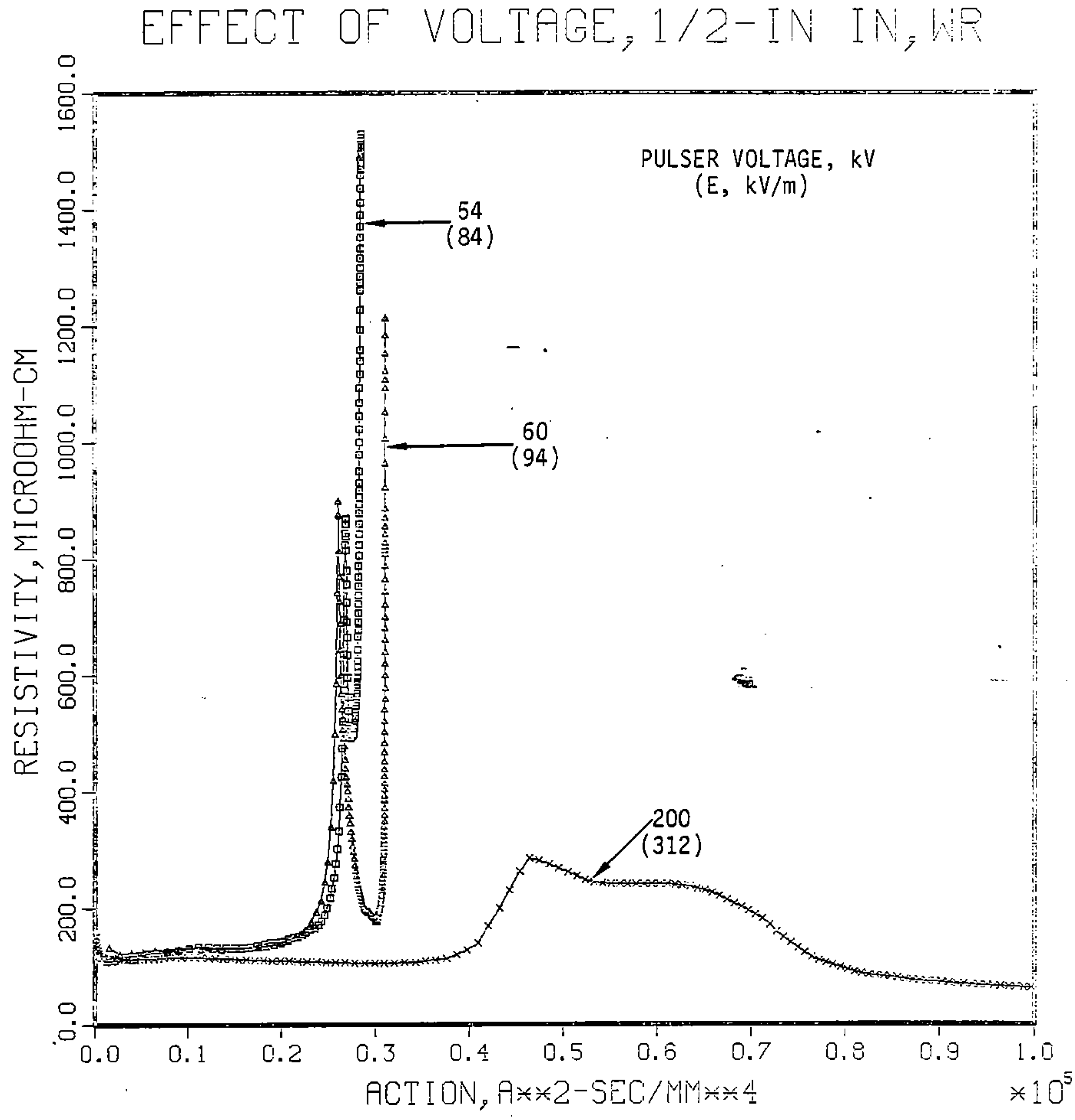
EFFECT OF VOLTAGE, 1/2-IN IN, WR
RESISTIVITY, MICROOHM-CM
0.0
200.0
400.0
600.0
800.0
1000.0
1200.0
1400.0
1600.0
PULSER VOLTAGE, kV
(E, kV/m)
54
(84)
60
(94)
200
(312)
0.0
0.1
0.2
0.3
0.4
0.5
0.6
0.7
0.8
0.9
1.0
ACTION, A**2-SEC/MM**4
×10^5

Figure 4-36b.

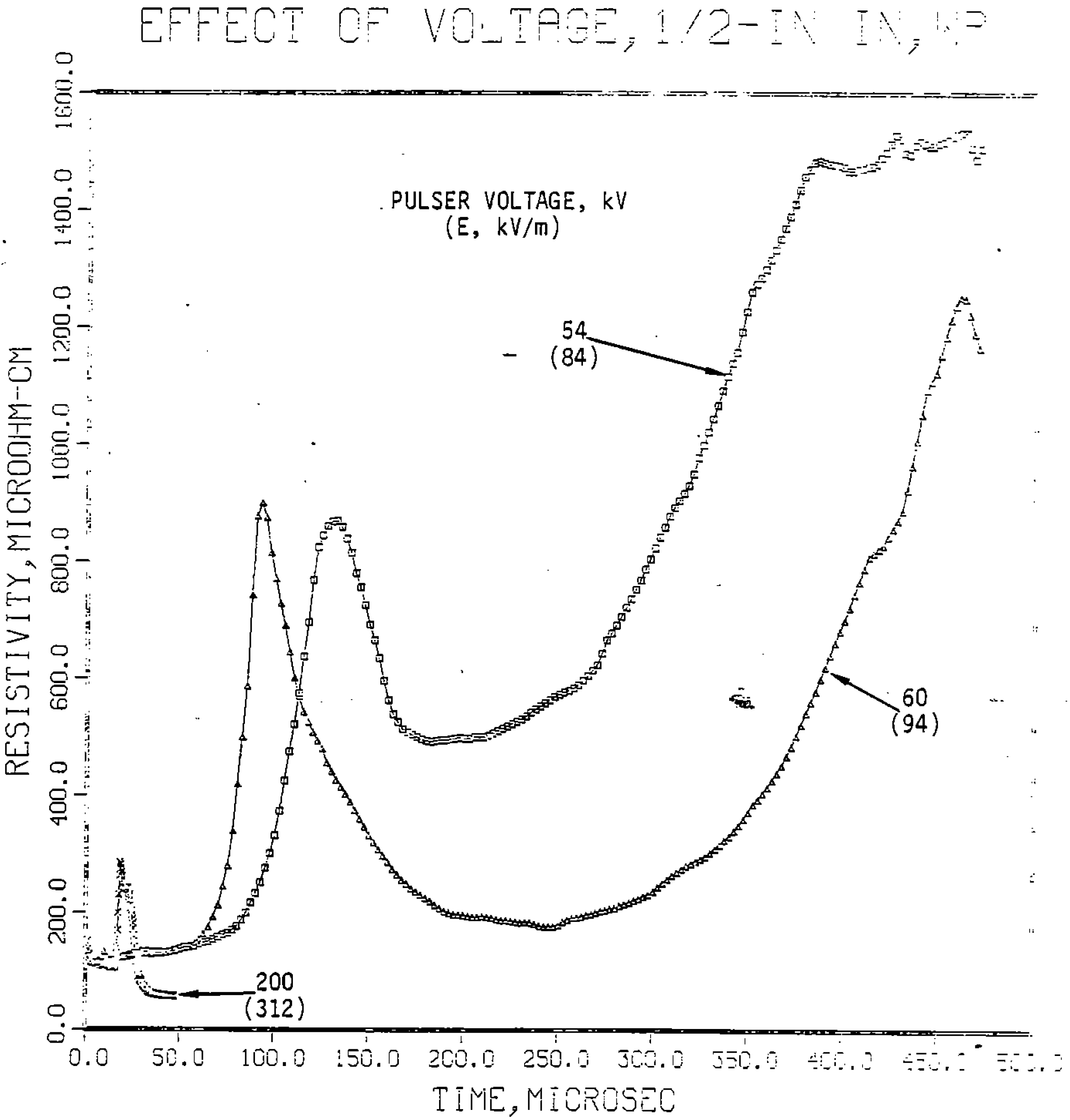
EFFECT OF VOLTAGE, 1/2-IN IN, WP
RESISTIVITY, MICROOHM-CM
TIME, MICROSEC
0.0
200.0
400.0
600.0
800.0
1000.0
1200.0
1400.0
1600.0
0.0
50.0
100.0
150.0
200.0
250.0
300.0
350.0
400.0
450.0
500.0
PULSER VOLTAGE, kV
(E, kV/m)
54
(84)
60
(94)
200
(312)

expect a difference versus time due to voltage (as observed) because the heating rate changes with the pulser voltage. However, once vaporization begins, there is also a considerable difference in the magnitudes of resistivity and the shapes of the curves versus action. In Section IV.6, two qualitative models are proposed to explain the differences in these curves. Briefly, the models assume that the effective resistivity at a given time is a fairly complicated function of the vaporization rate of the metal, the pressure of the vapor that is still contained within the polyethylene wrap, the rate at which the vapor escapes from the polyethylene wrap, and the ionization rate of the vapor inside and outside the wrap, as a function of electric field and vapor pressure. This complicated dependence on time is the reason, as discussed previously, for much of the difference between the curves for the 1/4-inch helical samples and the other three geometries in Figures 4-24 through 4-27. In fact, it is interesting that the change in shape of the curves in Figure 4-31 with decreasing pulser voltage (say, from 205 kV to 147 kV) is similar to the changes in Figures 4-24 through 4-27 in going from the 1/4-inch helical wrapped sample to the other configurations. This similarity is consistent with the speculation that the observed differences are due to the speed at which a certain value of action is achieved.

In Figures 4-37 through 4-40, some of the results in the preceeding figures are replotted to illustrate the effect of the different metals for the same geometry and voltages. The four metals are compared for the 1/4-inch WR and 1/2-inch WR geometries with a pulser voltage of 200 kV and for the 1/2-inch WR geometry with pulser voltages from 54 to 60 kV. For the 1/4-inch WR geometry, Inconel, SS, and Aℓ are compared at pulser voltages from 54 to 60 kV.

For a pulser voltage of 200 kV, there is not a major difference in the resistivity curves for Inconel, SS, and Fe, except at small values of action where the resistivity for Fe is considerably smaller than for Inconel and SS. Because the ambient resistivity of Aℓ is so low, it does not heat up as fast as the other metals. Therefore, its burst point occurs at larger values of action. Although the minimum resistivities after restrike appear to be considerably larger for the 1/2-inch WR geometries than the 1/4-inch WR geometry, a factor of two of this difference is an artifact of using the pre-melt cross-sectional areas for the two geometries to calculate the resistivities, as mentioned earlier. However, even eliminating this factor of two, the arc resistances for the 1/4-inch WR samples appear to be somewhat smaller than for the 1/2-inch WR samples. This difference, if real, could be due to creating a quicker, hotter arc in the sample with the smaller area. The arc resistance for Aℓ appears to be slightly larger than for the other metals.

(Text continues on page 118)

Figure 4-37a.

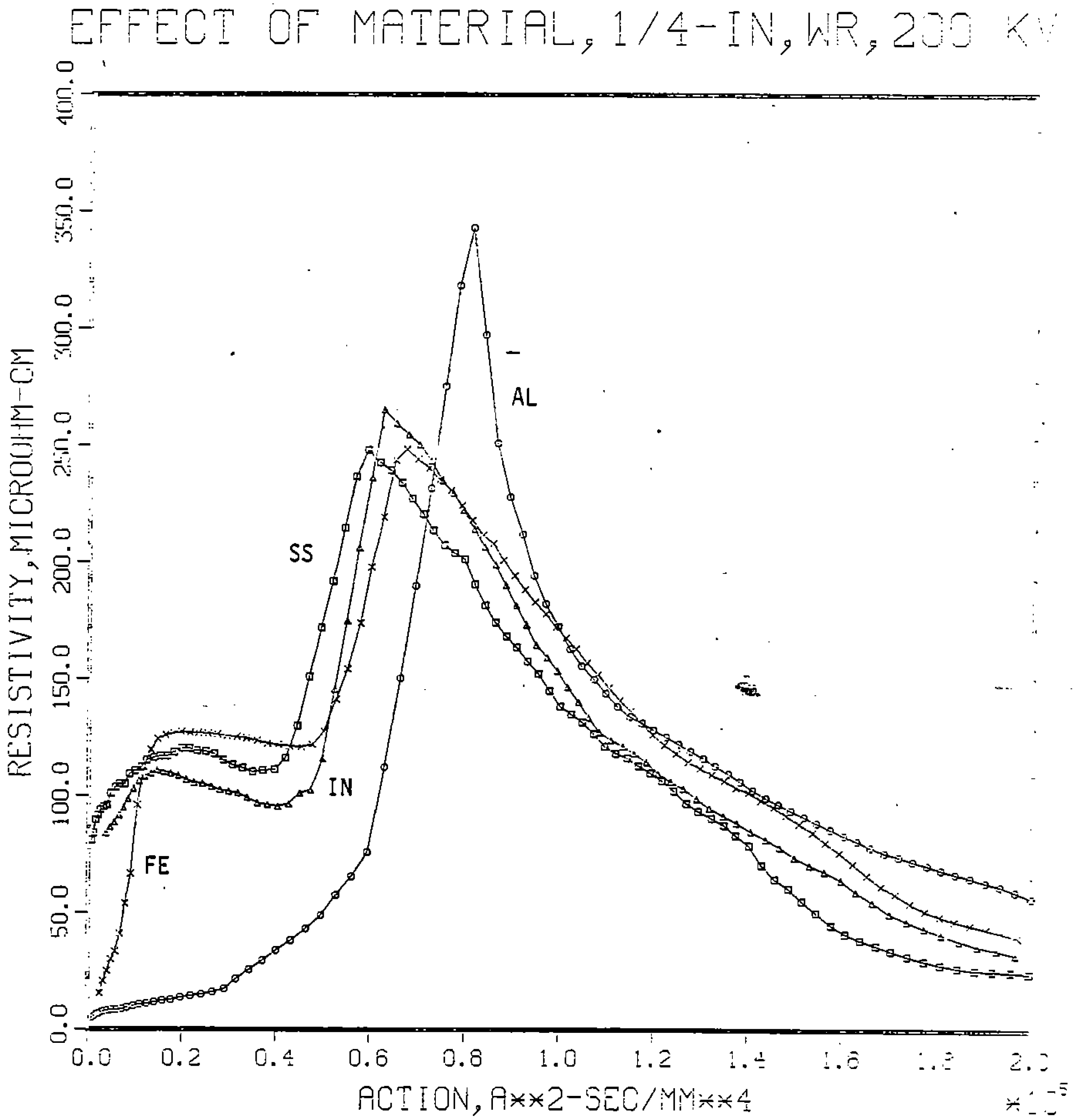
EFFECT OF MATERIAL, 1/4-IN, WR, 200 KV
RESISTIVITY, MICROOHM-CM
0.0
50.0
100.0
150.0
200.0
250.0
300.0
350.0
400.0
ACTION, A**2-SEC/MM**4
0.0
0.2
0.4
0.6
0.8
1.0
1.2
1.4
1.6
1.8
2.0
*10^5
AL
SS
IN
FE

Figure 4-37b.

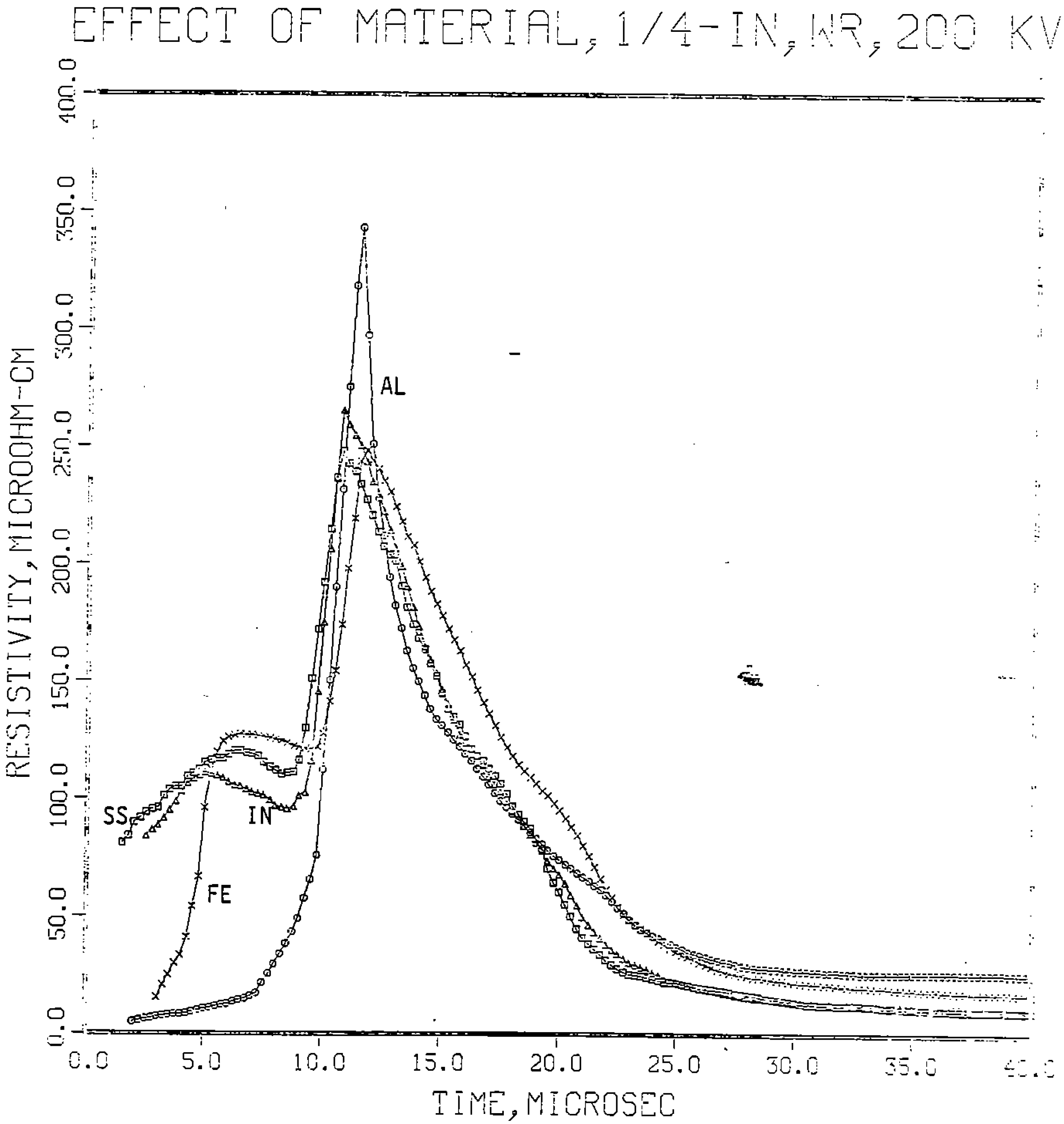
EFFECT OF MATERIAL, 1/4-IN, WR, 200 KV
RESISTIVITY, MICROOHM-CM
0.0
50.0
100.0
150.0
200.0
250.0
300.0
350.0
400.0
TIME, MICROSEC
0.0
5.0
10.0
15.0
20.0
25.0
30.0
35.0
40.0
AL
SS
IN
FE

Figure 4-38a.

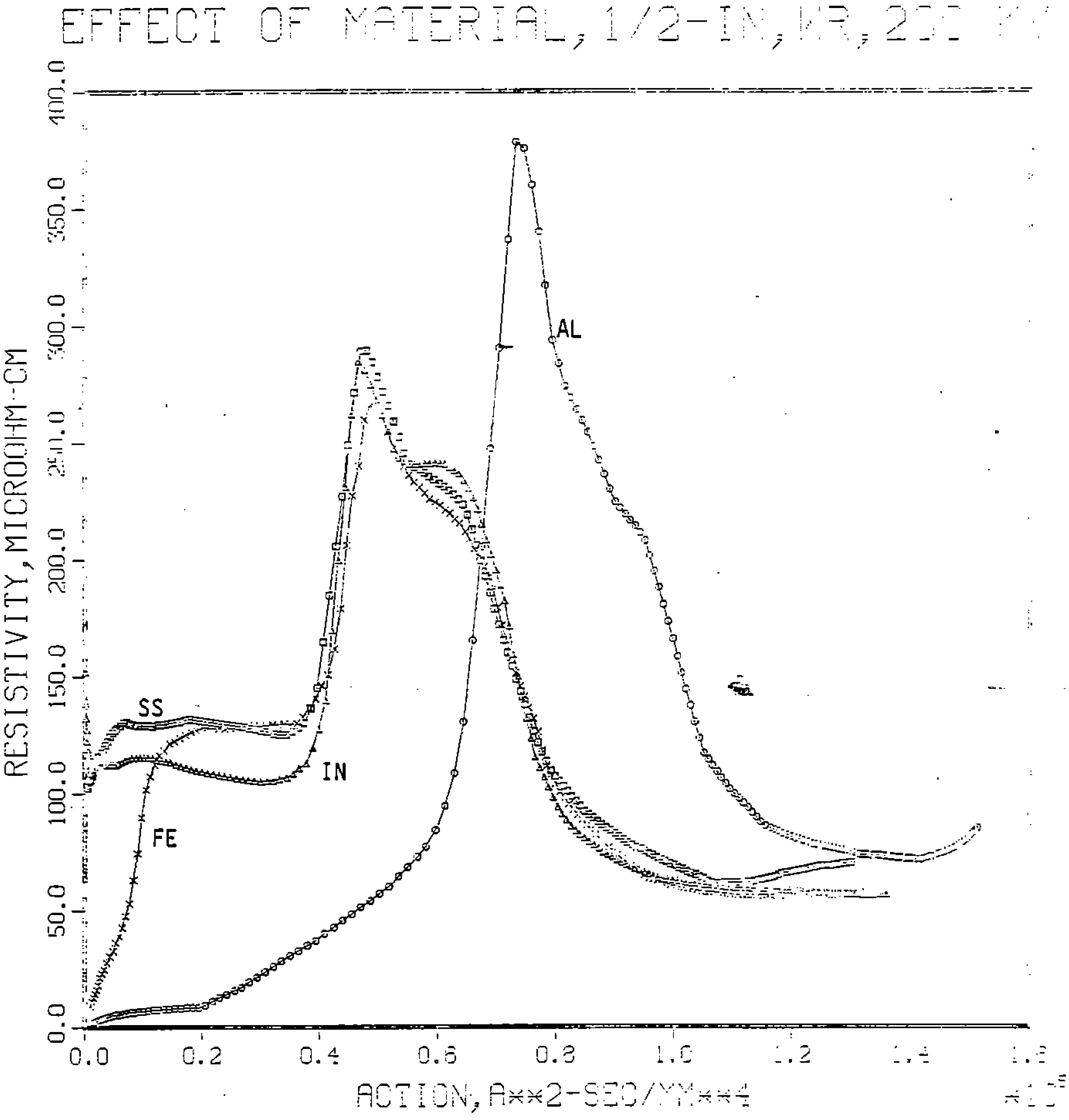
EFFECT OF MATERIAL,1/2-IN,WR,200
RESISTIVITY,MICROOHM-CM
0.0
50.0
100.0
150.0
200.0
250.0
300.0
350.0
400.0
ACTION,A**2-SEC/MM**4
0.0
0.2
0.4
0.6
0.8
1.0
1.2
1.4
1.6
$*10^5$
SS
IN
FE
AL

Figure 4-38b.

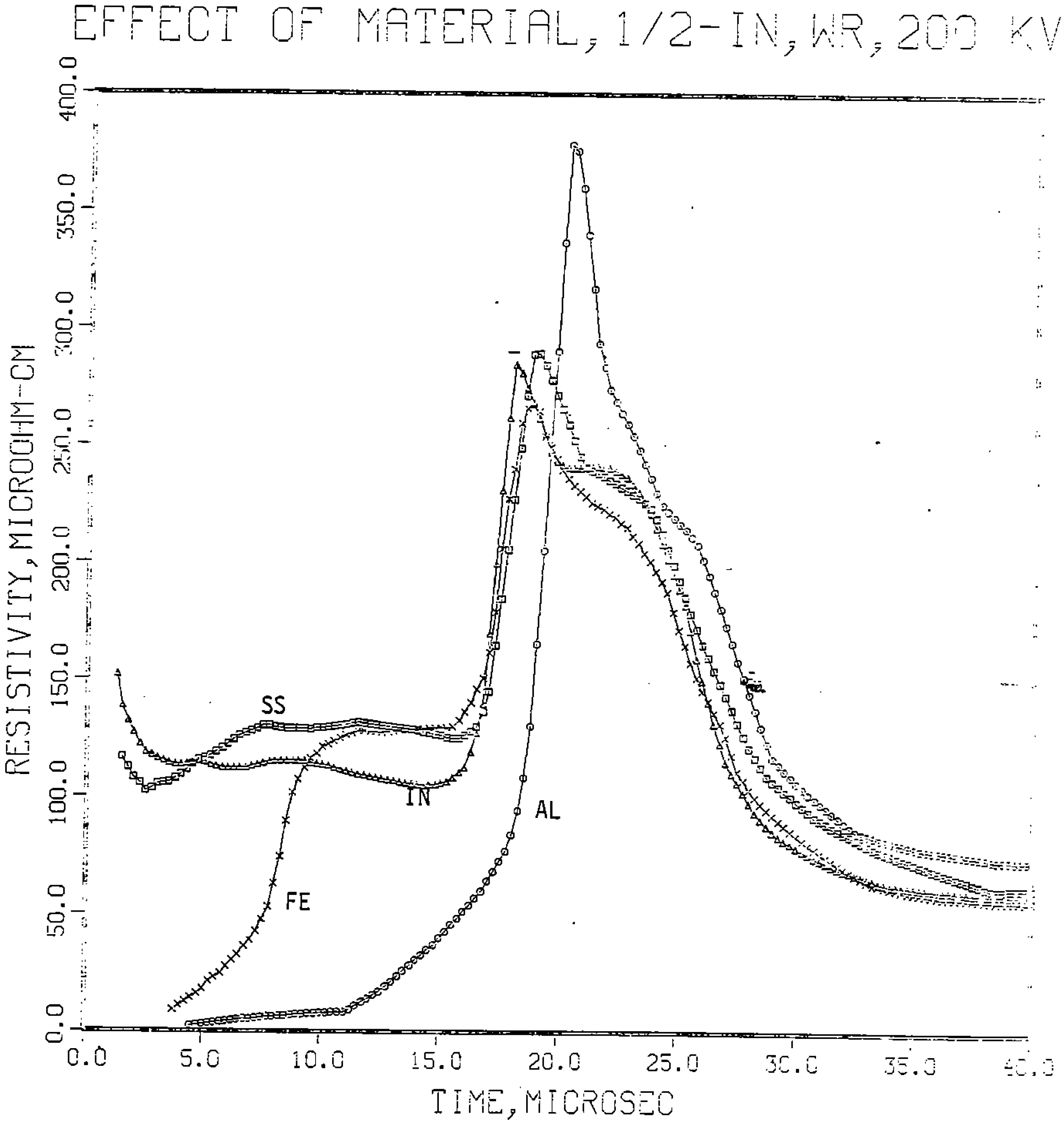
EFFECT OF MATERIAL, 1/2-IN, WR, 200 KV
RESISTIVITY, MICROOHM-CM
0.0
50.0
100.0
150.0
200.0
250.0
300.0
350.0
400.0
TIME, MICROSEC
0.0
5.0
10.0
15.0
20.0
25.0
30.0
35.0
40.0
SS
IN
FE
AL

Figure 4-39a.

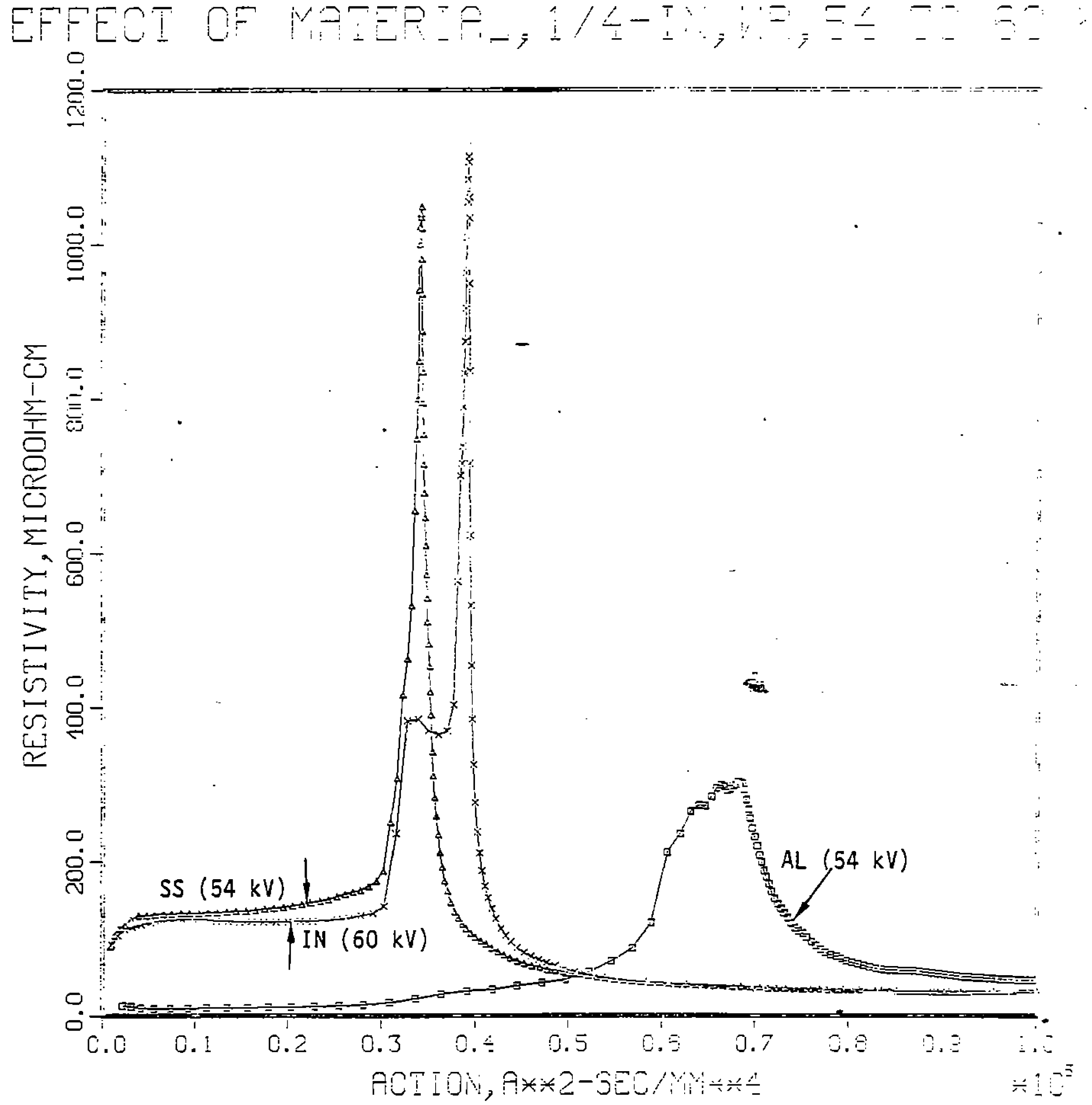
EFFECT OF MATERIAL, 1/4-IN, WP, 54 TO 60 KV
RESISTIVITY, MICROOHM-CM
0.0
200.0
400.0
600.0
800.0
1000.0
1200.0
ACTION, A**2-SEC/MM**4
*10^5
0.0
0.1
0.2
0.3
0.4
0.5
0.6
0.7
0.8
0.9
1.0
SS (54 kV)
IN (60 kV)
AL (54 kV)

Figure 4-39b.

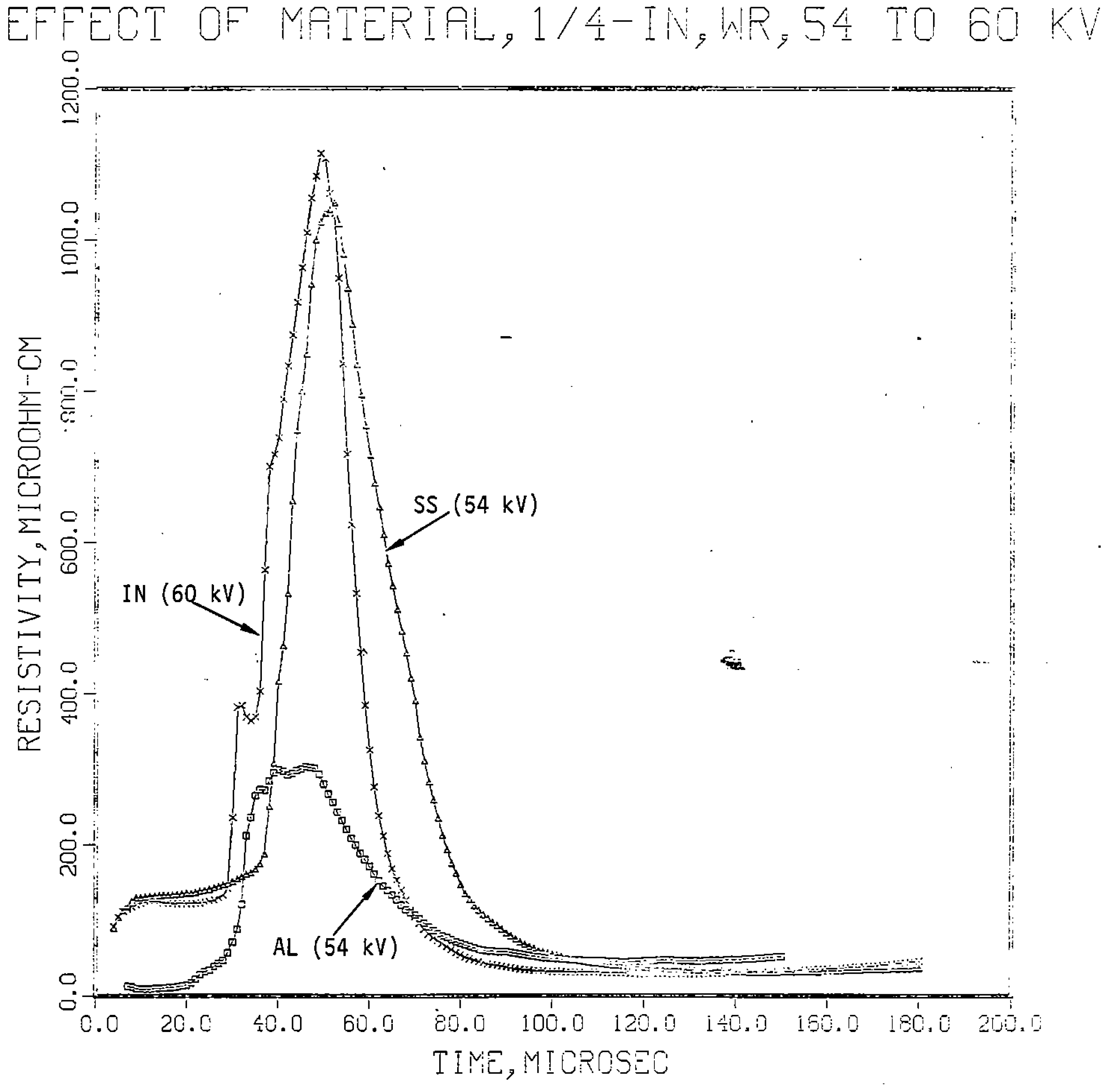
EFFECT OF MATERIAL, 1/4-IN, WR, 54 TO 60 KV
RESISTIVITY, MICROOHM-CM
0.0
200.0
400.0
600.0
800.0
1000.0
1200.0
TIME, MICROSEC
0.0
20.0
40.0
60.0
80.0
100.0
120.0
140.0
160.0
180.0
200.0
IN (60 kV)
SS (54 kV)
AL (54 kV)

Figure 4-40a.

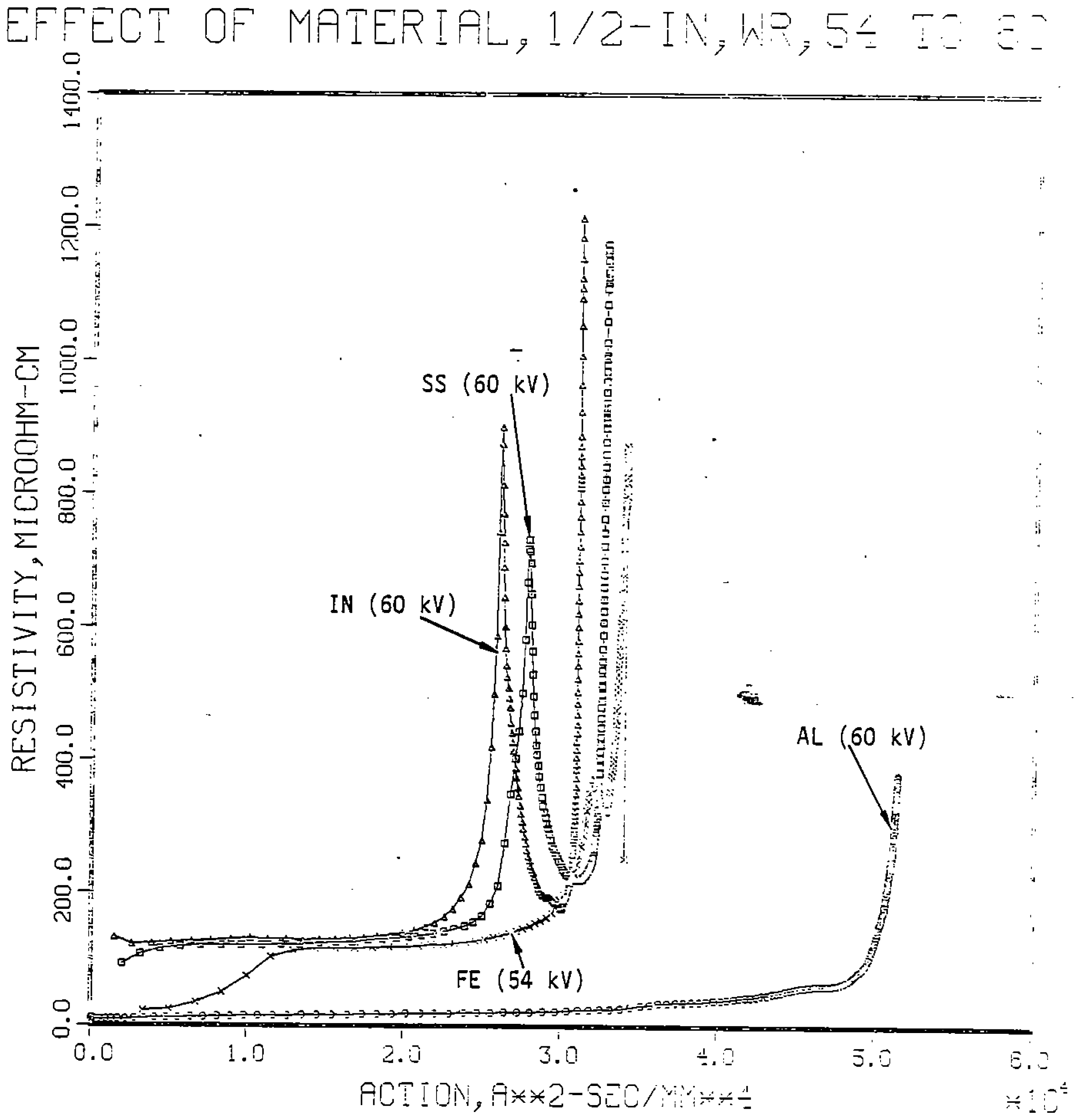
EFFECT OF MATERIAL, 1/2-IN, WR, 54 TO 60
RESISTIVITY, MICROOHM-CM
0.0
200.0
400.0
600.0
800.0
1000.0
1200.0
1400.0
ACTION, A**2-SEC/MM**4
0.0
1.0
2.0
3.0
4.0
5.0
6.0
*10^4
SS (60 kV)
IN (60 kV)
FE (54 kV)
AL (60 kV)

Figure 4-40b.

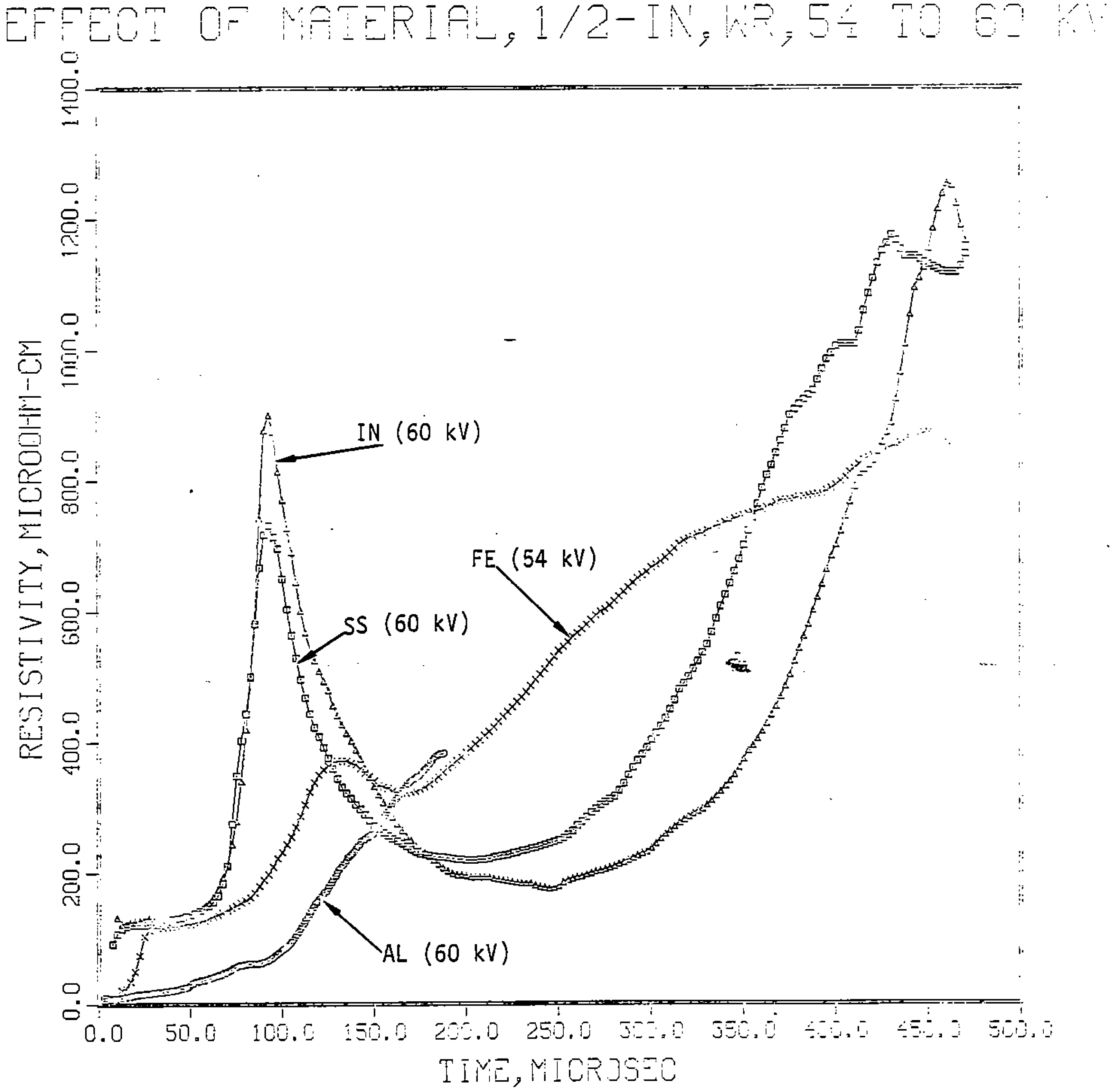
EFFECT OF MATERIAL,1/2-IN,WR,54 TO 60 KV
RESISTIVITY,MICROOHM-CM
0.0
200.0
400.0
600.0
800.0
1000.0
1200.0
1400.0
TIME,MICROSEC
0.0
50.0
100.0
150.0
200.0
250.0
300.0
350.0
400.0
450.0
500.0
IN (60 kV)
FE (54 kV)
SS (60 kV)
AL (60 kV)

Similar effects of material occur at the lower pulser voltages.

In Table 4-5, the energy-to-burst (from Table 4-3) is organized to illustrate the effect of geometry and material at a pulser voltage of 200 kV, while, in Table 4-6, the effect of voltage is illustrated for Fe and SS for the 1/4-inch WR geometry. From Table 4-5, there is not a completely consistent pattern of the dependence of energy-to-burst on geometry although the 1/4-inch WR geometry never has the smallest value and, in three instances, it has the largest. Aluminum has the lowest energy-to-burst, which is probably consistent with its relatively low melting temperature. From Table 4-6, there seems to be a tendency for the energy-to-burst to decrease with decreasing voltage. The inconsistency with this trend for the 80 kV points in that table arise because the resistivity curves have double peaks around 120 kV for this geometry (see Figure 4-31b) and the second peak is used for the 80 kV value and the first peak for the larger voltages.

Table 4-5. Effect of Geometry and Material on Energy to Burst (Pulser Voltage ≡ 200 kV)

Geometry	FE		IN—		SS		Aℓ	
	Shot No.	kJ/cm^3	Shot No.	kJ/cm^3	Shot No.	kJ/cm^3	Shot No.	kJ/cm^3
1/4 - IN, WR	31	85	28	74	29	78	66	61
1/4 - IN, ST	45	76	46	81	47	76	68	35
1/2 - IN, WR	49	61	51	57	50	69	67	44
1/2 - IN, ST	43	74	48	74	44	76	69	45

Figure 4-41 gives curves of ρ versus action and ρ versus time for a 1/4-inch SS straight sample with and without the 280-mil polyethylene jacket. The ρ versus action curve for the bare sample is quite similar to the data from Reference 4-1 for Fe exploding wires (Figure 4-42). The difference in the curves in Figure 4-42 at small values of action are undoubtedly due to the differences between Fe and SS. The smaller peak resistivity for the SS may be due, at least partially, to the difficulties in time-correlating the current and voltage curves in this region where the voltage is changing very rapidly. Nevertheless, the comparison is fairly good. Thus, the effect of the polyethylene jacket appears to be to delay the peak resistivity to a larger value of action and broaden the ρ versus action curve around the peak resistivity. The effect of these changes on the

Figure 4-41a.

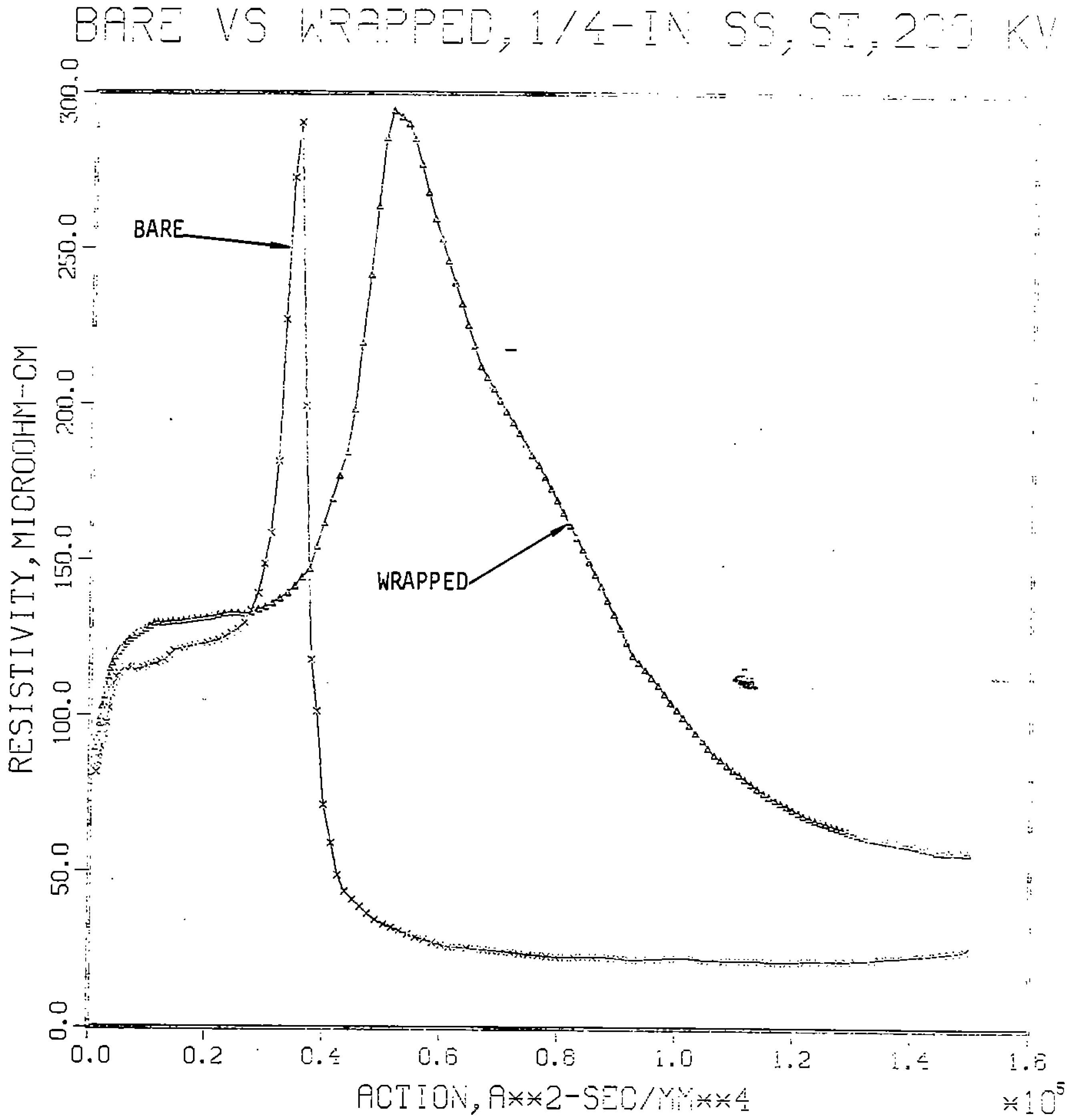
BARE VS WRAPPED,1/4-IN SS,ST,200 KV
RESISTIVITY,MICROOHM-CM
0.0
50.0
100.0
150.0
200.0
250.0
300.0
BARE
WRAPPED
0.0
0.2
0.4
0.6
0.8
1.0
1.2
1.4
1.6
ACTION,A**2-SEC/MM**4
$\times 10^5$

Figure 4-41b.

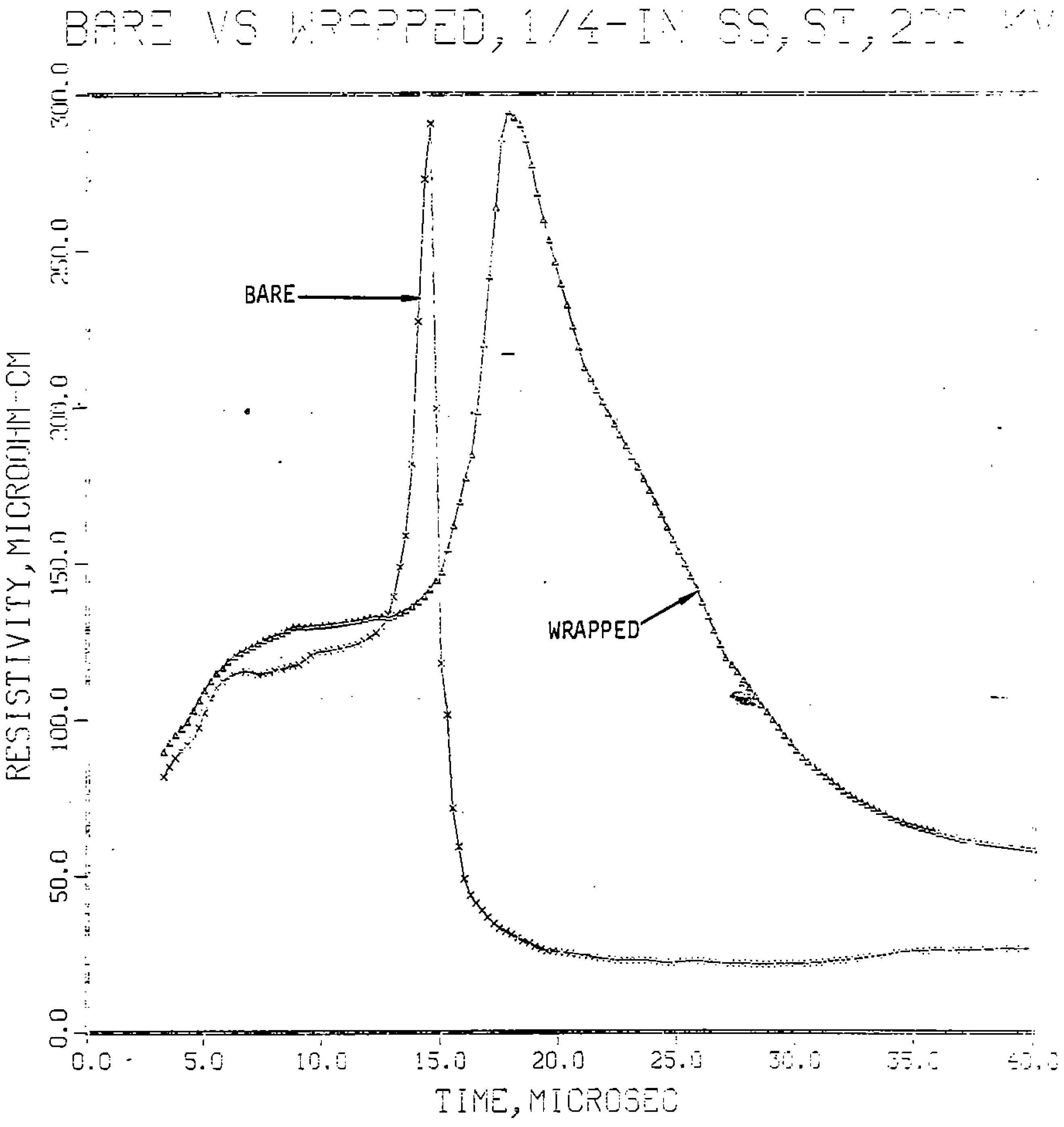

BARE VS WRAPPED,1/4-IN SS,ST,200 KV
RESISTIVITY,MICROOHM-CM
0.0
50.0
100.0
150.0
200.0
250.0
300.0
TIME,MICROSEC
0.0
5.0
10.0
15.0
20.0
25.0
30.0
35.0
40.0
BARE
WRAPPED

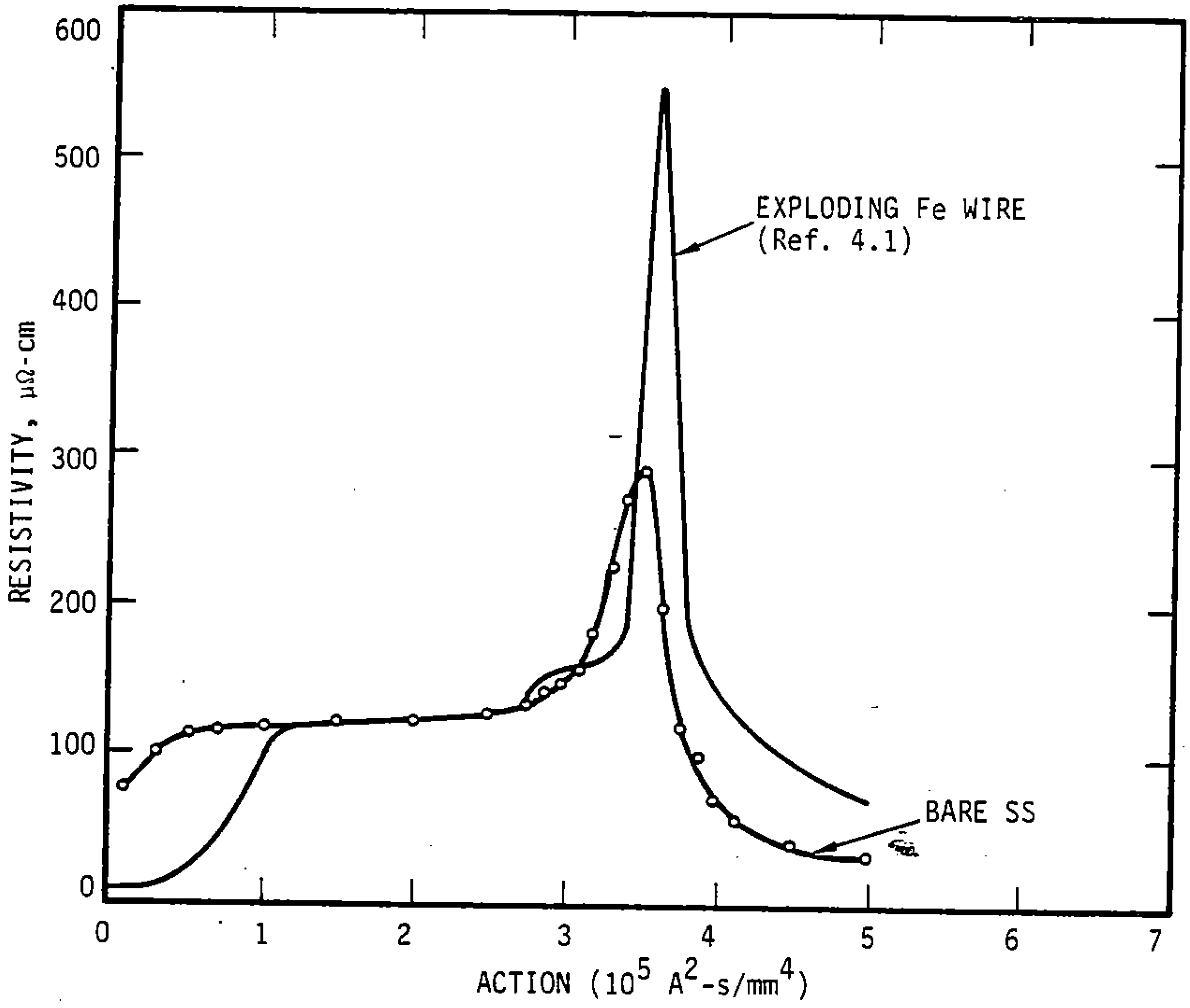

RE-04804

Figure 4-42. Comparison of resistivity curves for bare SS and Fe exploding wire.

current and charge delivered to a structure through an R-wire by a typical EMP pulse is discussed in Section IV.5.

Table 4-6. Effect of Voltage on Energy to Burst

Pulser Voltage (kV)	Shot No.	kJ/cm^3
(1/4 - IN FE, WR)		
205	31	85
147	32	81
120	34	74
80	35	100
(1/4 - IN SS, WR)		
210	29	78
80	36	88
54	82	59

Figure 4-43 gives ρ versus action and ρ versus time curves for the three-strand graphite fiber samples for two pulser voltages. The shapes of these curves are similar to those for the bare SS sample in Figure 4-41, except that the peak resistivity is considerably larger and occurs at a much lower value of action for the graphite fiber. The smaller value of action at the peak resistivity undoubtedly occurs because the ambient-temperature resistivity of graphite is much larger than the corresponding metal resistivities, so the energy deposited per unit volume in the graphite is larger for a given current density. The fact that the ρ versus action curves are not much different for two considerably different voltages indicates that the thin polyethylene (≈1 mm thick) cover over the graphite fibers has little effect on the vaporization/restrike characteristics of these samples. However, since the full-size R-wire graphite cable has a heavy jacket more like the present metal samples, one would expect more of a change in the ρ versus action curves for different voltages for those cables.

As an illustration of the self-consistency of the data, Figure 4-44 shows the data for the graphite fiber with a pulser voltage of 54 kV using three difference oscilloscope sweep speeds, and Figure 4-45 shows the beginning of Figure 4-44b on an expanded time scale. The repeatability of the data over most of the range of the curve is quite good. As might be expected, at early times (Figure 4-45), there is some inaccuracy in the data from one of the slower sweeps. The difference in the peak resistivities around 125 μs is

(Text continues on page 128)

Figure 4-43a.

Effect of voltage

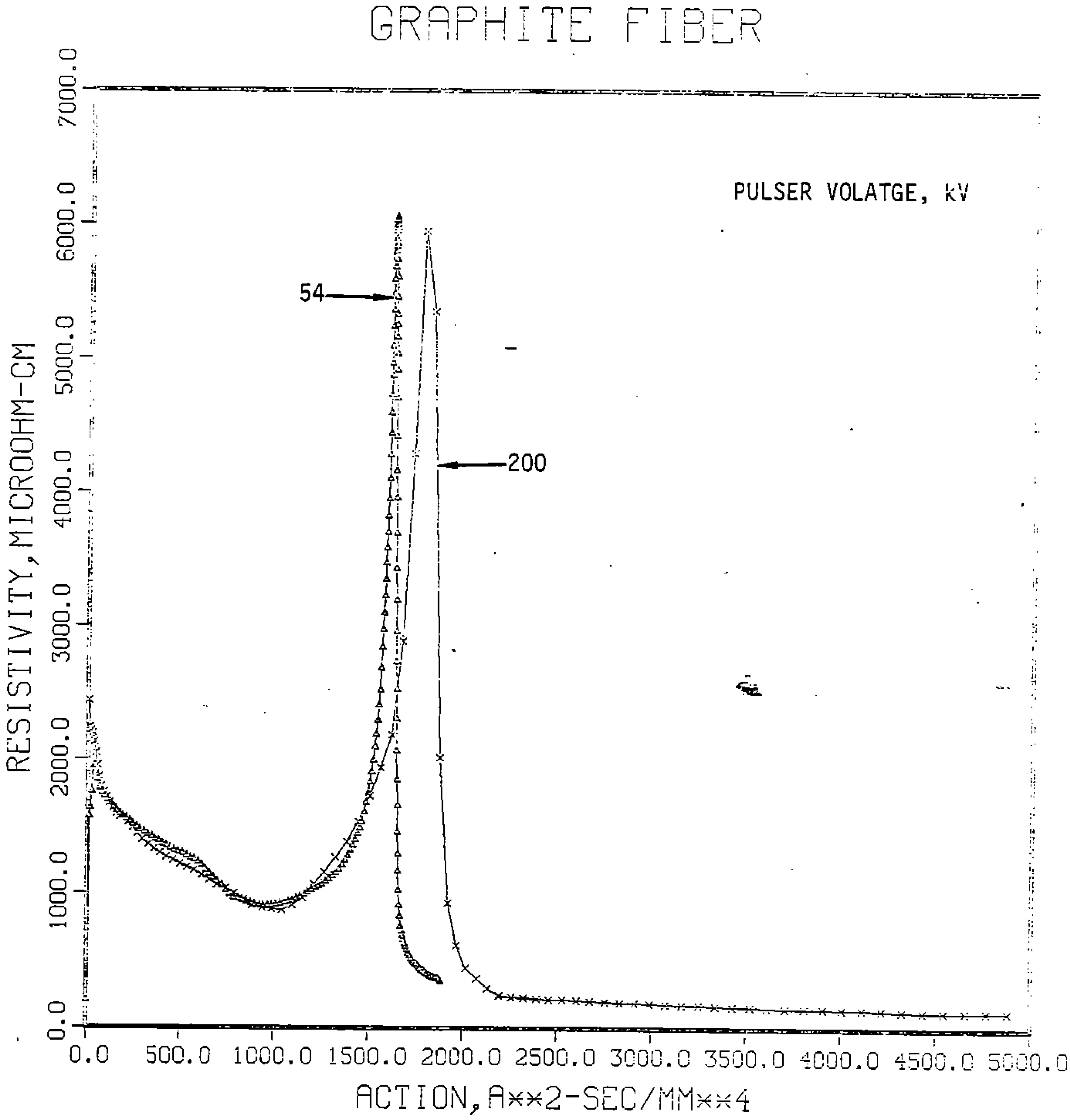

Figure 4-43b.

Effect of voltage

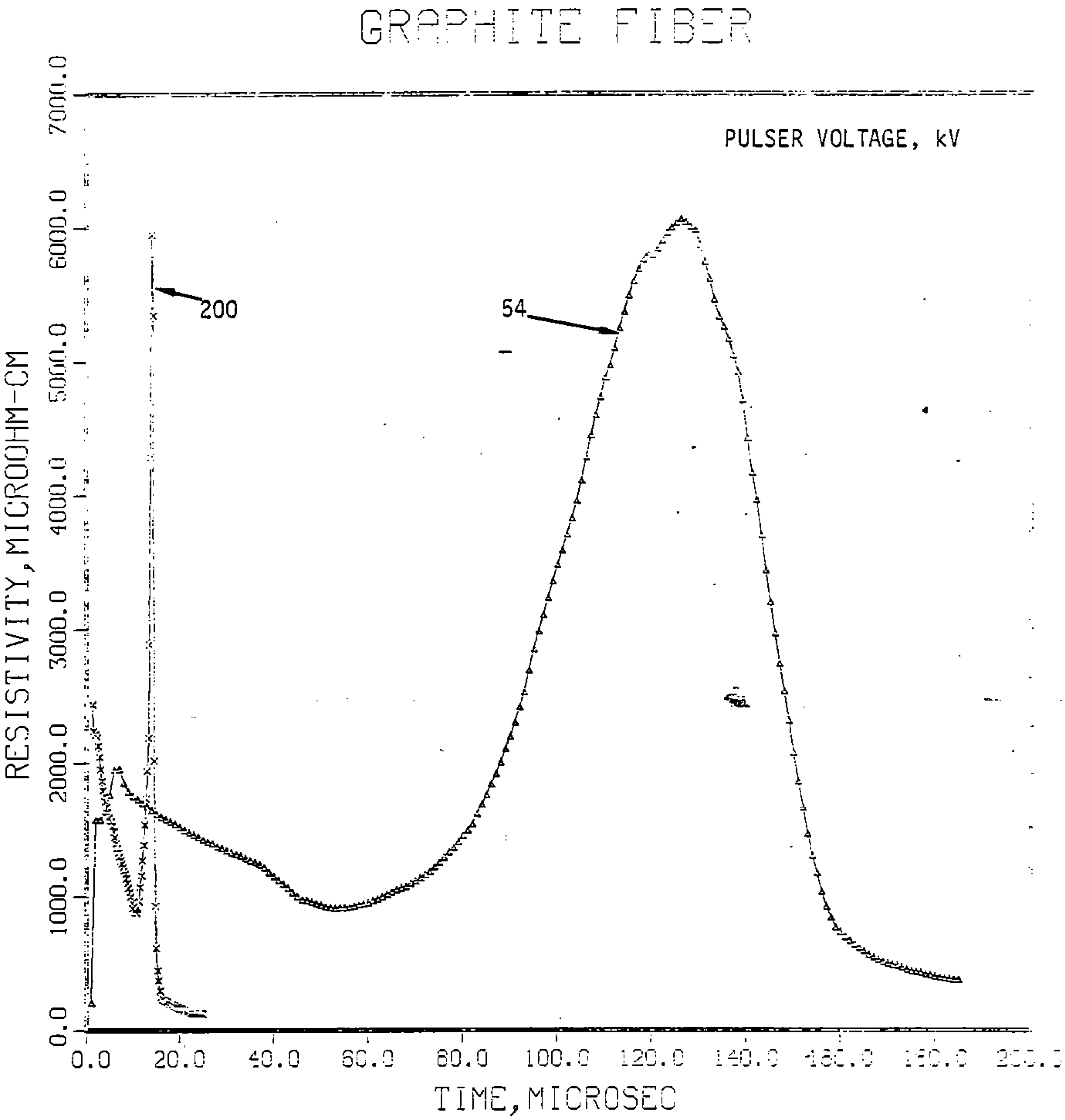

Figure 4-44a.

Comparison of different scope sweep speeds

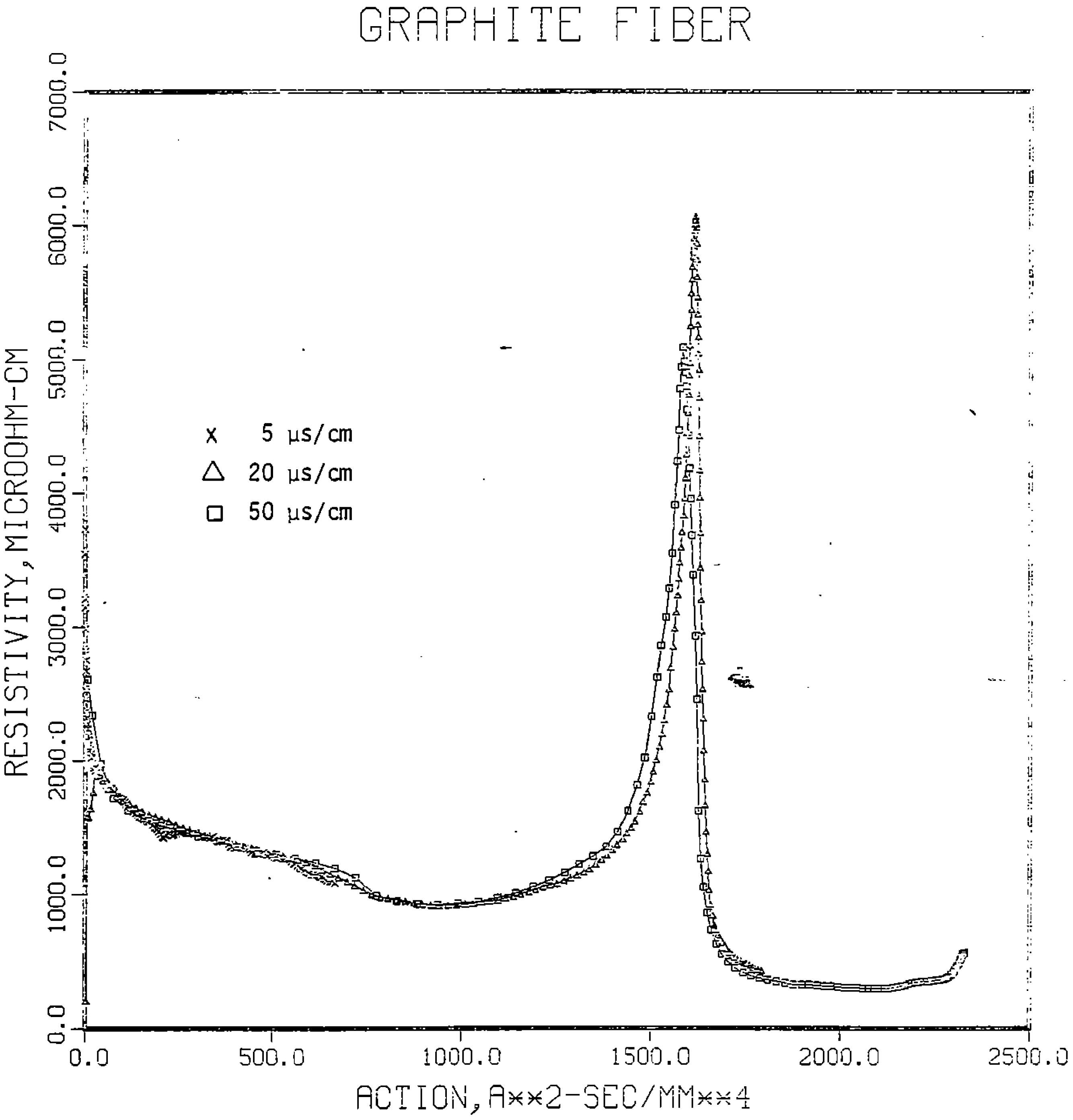

Figure 4-44b.

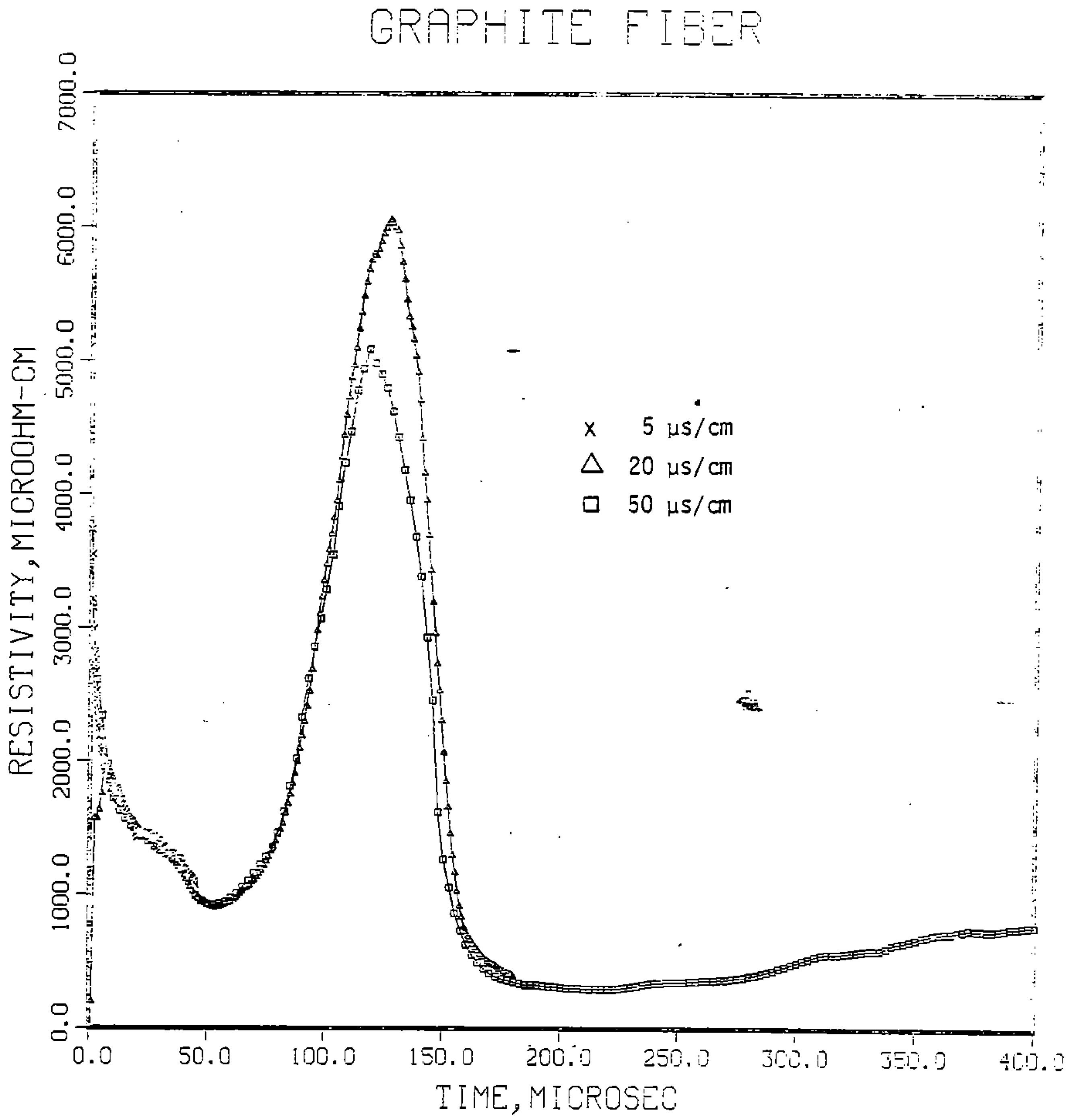
GRAPHITE FIBER
RESISTIVITY, MICROOHM-CM
0.0
1000.0
2000.0
3000.0
4000.0
5000.0
6000.0
7000.0
TIME, MICROSEC
0.0
50.0
100.0
150.0
200.0
250.0
300.0
350.0
400.0
x 5 µs/cm
△ 20 µs/cm
□ 50 µs/cm

Figure 4-45. Comparison of different scope sweep speeds at early times.

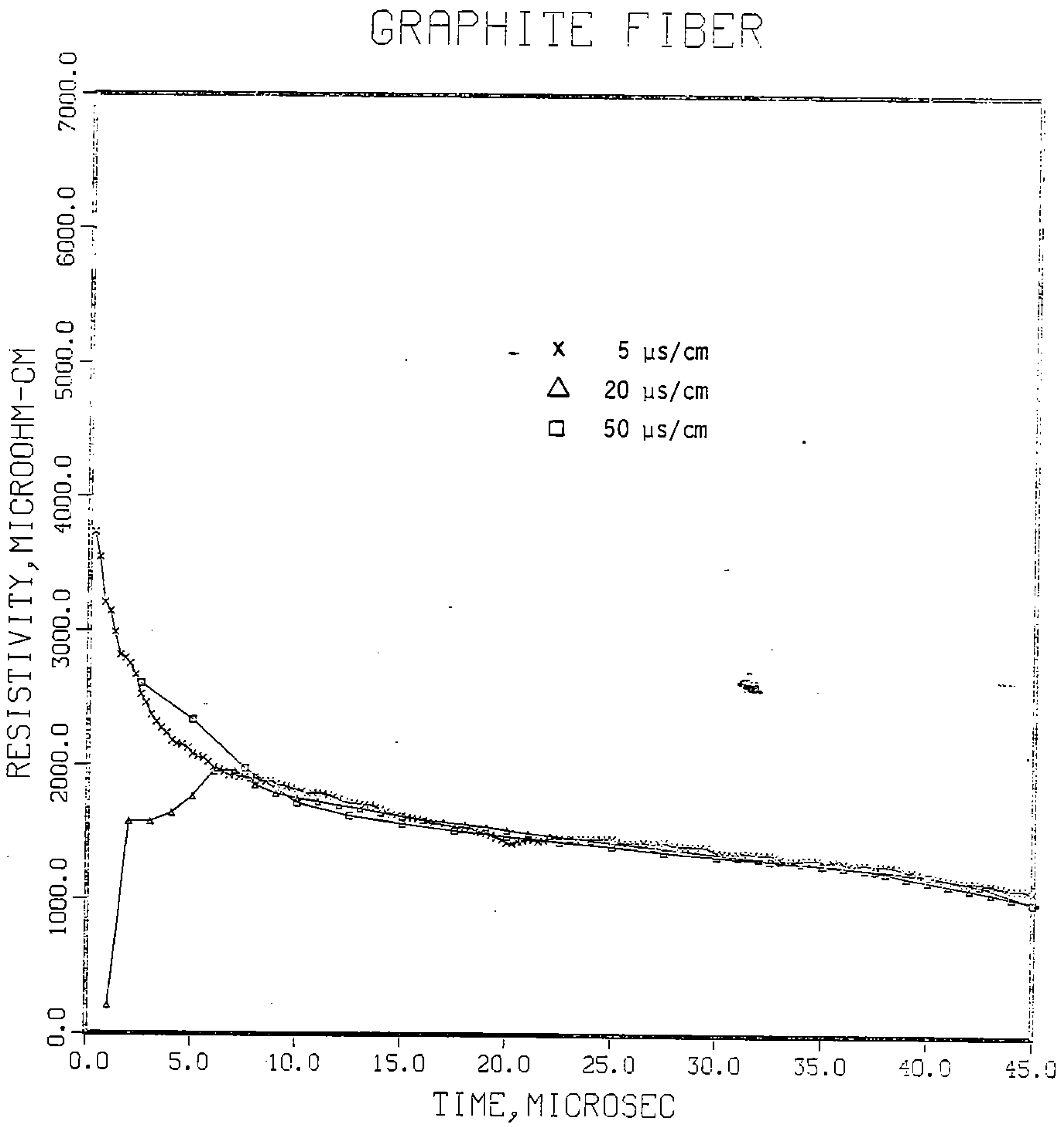

probably caused by the fact that the voltage curve is changing fairly rapidly in that time regime and a slight inaccuracy in the time correlation between the current and voltage traces could result in a significant error in the calculated resistivity. Since this problem is more pronounced for the slower sweep speed (50 μs/cm), the faster sweep speed (20 μs/cm), which indicates the higher resistivity, should be more accurate in this regime.

5. IMPLICATIONS FOR MISSILE GROUND SYSTEMS: A DESIGN APPLICATION

Since wrapping the R-wire in a thick, snug dielectric changes the resistivity-versus-action curve after the start of vaporization, the current and charge that are transmitted to a missile shelter through such an R-wire by a given EMP driver would also be different. To assess the magnitude of this difference, the current and charge driven through a typical R-wire by a representative EMP voltage driver has been calculated using the equivalent-circuit model illustrated in Figure 4-46.

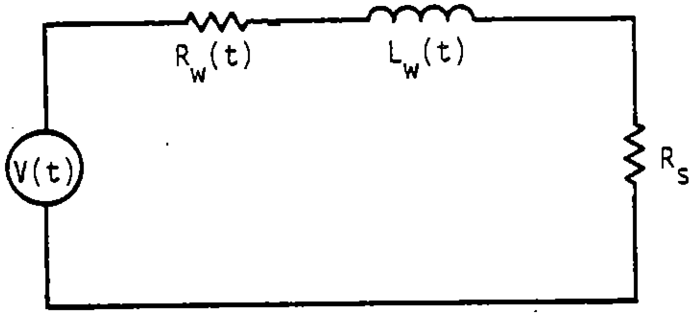

RE-04747

Figure 4-46. Equivalent circuit for R-wire calculations.

The driving voltage V across the R-wire is assumed to be a known function of time which is zero up to time t = 0 and, after t = 0, varies as:

$$V(t) = V_o \, e^{-(t/0.0033)^2} \quad (4\text{-}2)$$

where t is in seconds (Ref. 4-3). The calculations were performed for values of V_o from 1 MV to 3 MV.

4-3 Private communication from T. M. Rynne of TRW.

The inductance $L_w(t)$ in Figure 4-46 is the inductance of the R-wire since V is the voltage across the R-wire. For the present calculations, $L_w(t)$ was obtained from the equation:

$$L_w(t) = \frac{\mu_o \ell_w}{2\pi} \ell n \left(1 + \frac{\delta_g}{r_c}\right), \quad \delta_g < \ell_b \tag{4-3a}$$

$$= \frac{\mu_o \ell_w}{2\pi} \ell n \left(1 + \frac{\ell_b}{r_c}\right), \quad \delta_g > \ell_b \tag{4-3b}$$

where ℓ_w is the length of R-wire (assumed 300 m), μ_o is the permeability of free space, r_c is the radius of the cable (determined from the R-wire cross-sectional area to give the desired resistance), and ℓ_b is the distance from the shelter to the bomb burst (assumed 1000 m). The quantity δ_g is a time-dependent skin depth that is related to the soil resistivity ρ_g (assumed 10^3 Ω-m) by the formula

$$\delta_g = \left(\frac{2\rho_g t}{\mu_o}\right)^{1/2}, \quad t > 0 \tag{4-4}$$

There are obviously many uncertainties in this expression for $L_w(t)$, especially the values for ℓ_b and ρ_g and the fact that Eq. 4-4 for the skin depth must change when δ_g becomes greater than the depth of the R-wire below the surface of the ground. Fortunately, these quantities only have a logarithmic effect on $L_w(t)$ and the actual function used should not have a sensitive influence on the relative magnitudes of the current and charge into the shelter for different curves of ρ versus action.

In the equivalent circuit, R_s is the impedance of the shelter to ground (assumed 8 Ω) and R_w (t) is the time-dependent resistance of the R-wire given by

$$R_w(t) = \frac{\rho_w(t)\ell_w}{a_w} \tag{4-5}$$

where a_w is the cross-sectional area of the wire (assumed circular; $a_w = \pi r_c^2$) and $\rho_w(t)$ is the time-dependent resistivity of the R-wire. For these calculations, ρ_w is assumed to be a known function of the specific action (for each wire configuration) so $\rho_w(t)$ is obtained by calculating the action from time zero up to the desired time t, and then interpolating on the ρ_w-versus-action curve.

The calculations were performed using a simple computer code that integrates the differential equation of the system using a sufficiently small time step so that an explicit integration procedure is adequate.

For this comparison of the effect of different ρ-versus-action curves (due to wrapping the wire in a dielectric), the curves for Fe in Figure 4-31 and the Fe exploding wire in Figure 4-42 were used. To show the greatest effect due to the different wires, the curve in Figure 4-31 for a pulser voltage of 205 kV was used because it is the most different from the Fe exploding wire curve in Figure 4-42. For the calculations, the two ρ-versus-action curves were assumed to be identical up to an action of about 2.5 x 10^4 A^2-s/mm^4. The radius of the Fe R-wire was chosen to give an ambient resistance $R_w(o) = 5\ \Omega$, which corresponds to a resistance on the plateau of the resistance curve before vaporization of about 60 Ω.

Figure 4-47 shows time histories of the current through the bare (Fe exploding wire, Figure 4-42) and wrapped wires for initial voltages $V_0 = 1$, 2, and 3 MV, while Figure 4-48 shows the total charge delivered to the shelter and the maximum specific action versus V_0 for the bare and wrapped wires.

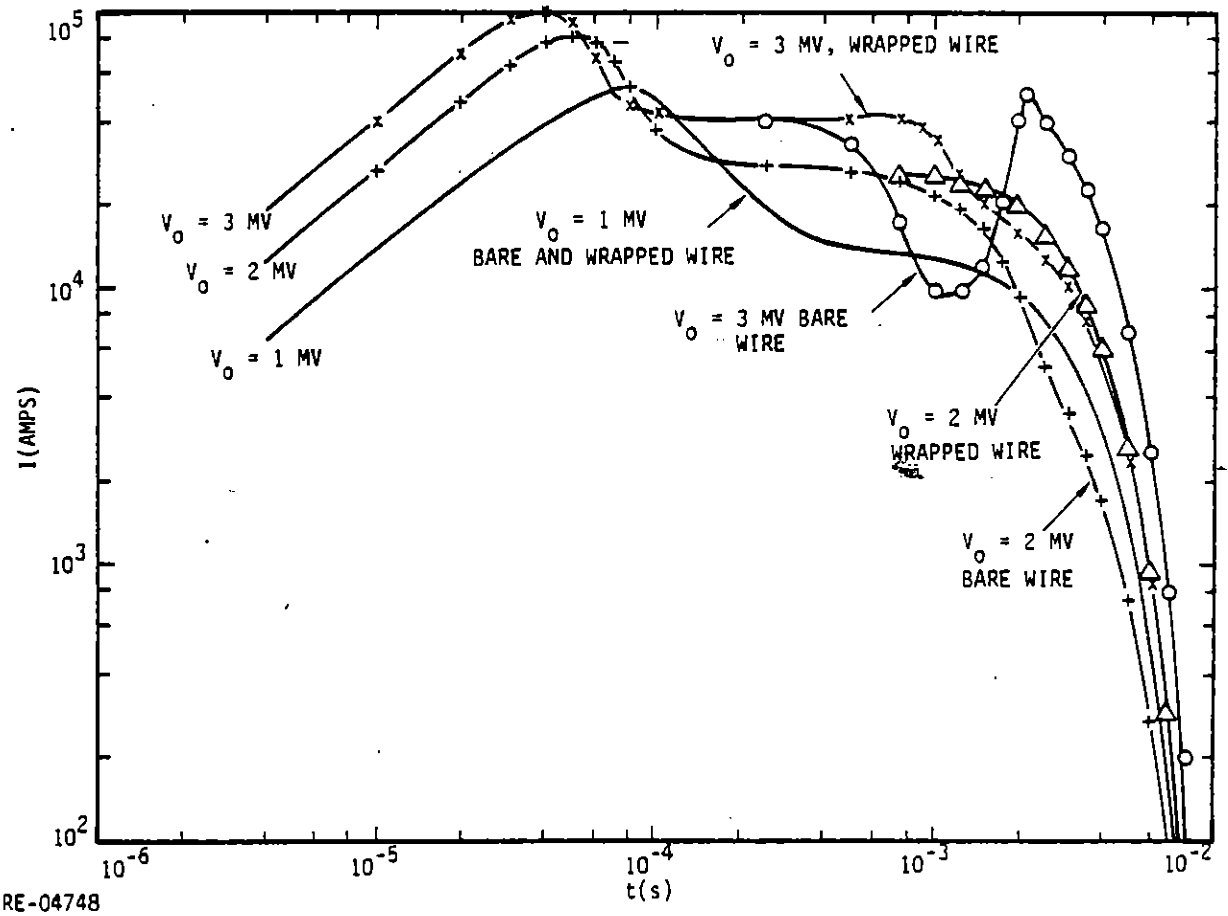

Figure 4-47. Calculated current time histories for bare and wrapped Fe wires for three driver voltages.

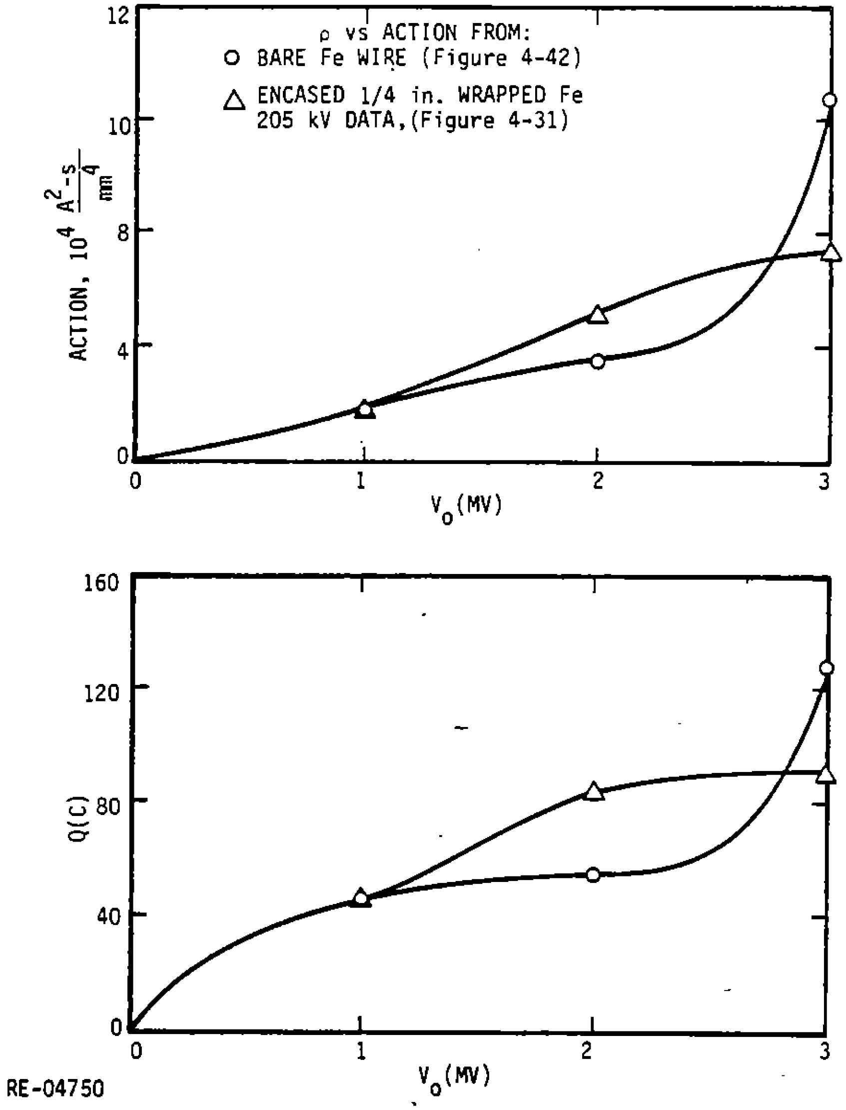

Figure 4-48. Calculated Q into shelter and peak specific action for Fe wire.

Initially the current increases roughly linearly in time due to the inductance in the circuit. The decrease in current from the initial peak around $t \cong 50\ \mu s$ is due to the large increase in resistance at an action between about 5×10^3 and $1 \times 10^4\ A^2\text{-s/mm}^4$, and the subsequent broad plateau is due to the plateau in the resistivity curve before vaporization. The final drop off in the current is due to the decrease in the drive voltage. An interesting feature of these curves is the second peak in the 3 MV curve for the bare wire which occurs when the action exceeds the value for the peak resistivity. For a while thereafter, the wire resistance decreases faster than the driver voltage so the current increases.

For the system assumed for these calculations and the assumed shape of the voltage time history, the maximum action imparted to the Fe R-wire for an initial voltage of 1 MV was only 1.9×10^4 A^2-s/mm^4. Since the resistivity curves for the bare and wrapped Fe wires were assumed to be identical up to 2.5×10^4 A^2-s/mm^4, the current time histories and the total charge are the same for both wires up to an initial voltage slightly greater than 1 MV.

For an initial voltage of 2 MV, the bare Fe wire is pushed close to the peak of its resistivity curve (peak action $\cong 3.6 \times 10^4$ A^2-s/mm^4) but there is not enough energy left to go beyond the peak. However, since the resistivity for the wrapped Fe wire at an action of 3.6×10^4 A^2-s/mm^4 is considerably less than the corresponding resistivity for the bare wire, the peak action for the wrapped wire with $V_o = 2$ MV is larger than for the bare wire, about 5.3×10^4 A^2-s/mm^4, which is just starting up the peak of the resistivity curve for the wrapped wire (curve for 205 kV in Figure 4-31). The result is that the charge delivered to the shelter with $V_o = 2$ MV is about 50 percent larger for the wrapped Fe wire than for the bare Fe wire.

On the other hand, for an initial voltage of 3 MV, there is enough energy available to push the bare Fe wire over the peak of its resistivity curve. When this happens, the current and charge delivered increase rapidly and the peak action exceeds 10^5 A^2-s/mm^4. For the wrapped Fe wire, the peak action for $V_o = 3$ MV (7.4×10^4 A^2-s/mm^4) slightly exceeds the value for the peak resistivity of the wrapped Fe wire. However, since the resistivity curve for the wrapped Fe wire decreases relatively slowly beyond the peak, the total charge delivered for $V_o = 3$ MV is only slightly larger than for $V_o = 2$ MV with the wrapped Fe wire and it is 40 percent less than the charge delivered with a bare Fe wire with $V_o = 3$ MV. Moreover, the curve for the bare Fe wire is increasing much more rapidly above $V_o = 3$ MV than the curve for the wrapped Fe wire. Of course, for considerably larger values of V_o, the wrapped Fe wire would also be pushed well over the peak of its resistivity curve, and the current and charge would increase more rapidly versus initial voltage. However, they would never catch up to the curves for the bare Fe wire with the same initial voltages.

Thus, for the assumed values of length and area for an Fe R-wire and the assumed shape of the voltage curve, there is a range of initial voltages from about 1.2 MV to 2.8 MV where the bare Fe wire is somewhat more advantageous than the wrapped Fe wire. However, above 2.8 MV, the current and charge transmitted by the bare Fe wire increase catastrophically whereas values for the wrapped Fe wire are still increasing at a moderate rate. Thus, if one had high confidence that the initial voltage would never exceed 2.8 MV, it would be advantageous to use a bare Fe wire rather than a wrapped Fe wire. However, if there were some possibility that V_0 would exceed 3 MV, a wrapped Fe wire would provide better protection. Of course, the ideal situation would be to use a bare Fe wire if it could be prevented from restriking. In fact, it would then be better to use a smaller cross-sectional area for the R-wire so that it would vaporize earlier in time [since specific action varies as $1/(\text{area})^2$ for the same currents] and thus the total charge delivered would be less. In Section IV.7 some techniques that might prevent restrike are discussed. However, none of these techniques has been verified as yet.

A similar set of calculations was made for an Aℓ R-wire. Since there is not much difference in the curves in Figure 4-27a, the curve of ρ versus action for 1/4-inch WR Aℓ at 200 kV, was used for these calculations. The cross-sectional area of the sample was chosen to be the same as the Fe used earlier. Thus, from Figure 4-37a, it can be seen that the resistance of this Aℓ wire is considerably smaller than the resistance of the previous Fe wire almost until burst occurs with the Aℓ wire. Figure 4-49 gives the time history of the current for V_0 = 1, 2, and 3 MV and Figure 4-50 shows the charge transferred to the shelter and the specific action through the R-wire as a function of V_0.

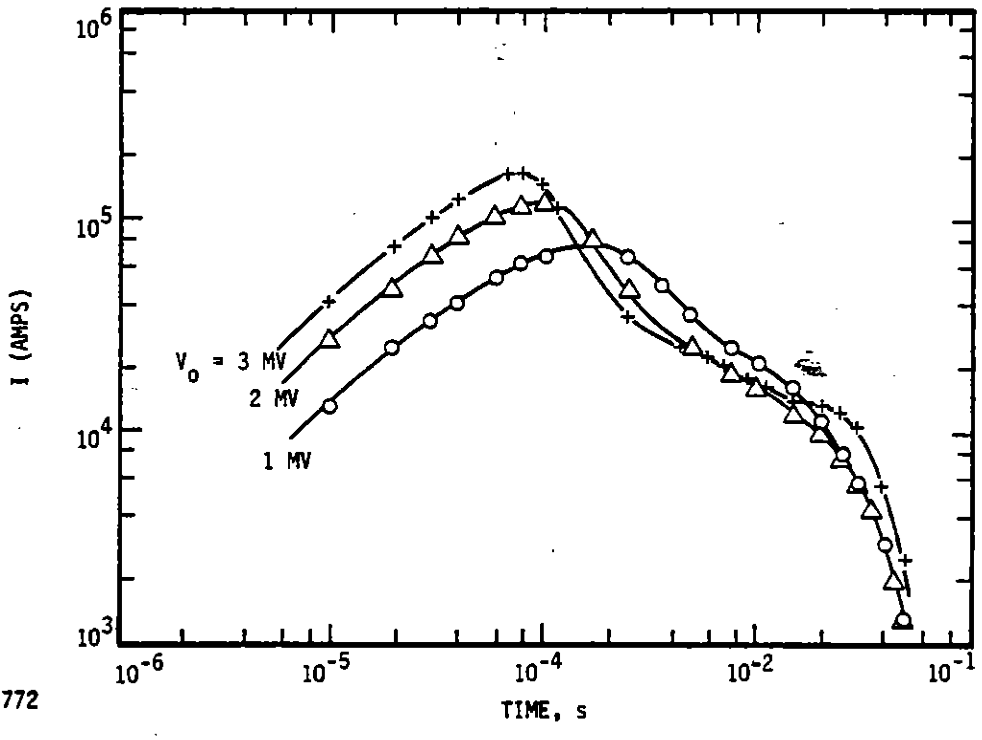

Figure 4-49. Calculated current time histories for wrapped Aℓ wire for three driver voltages.

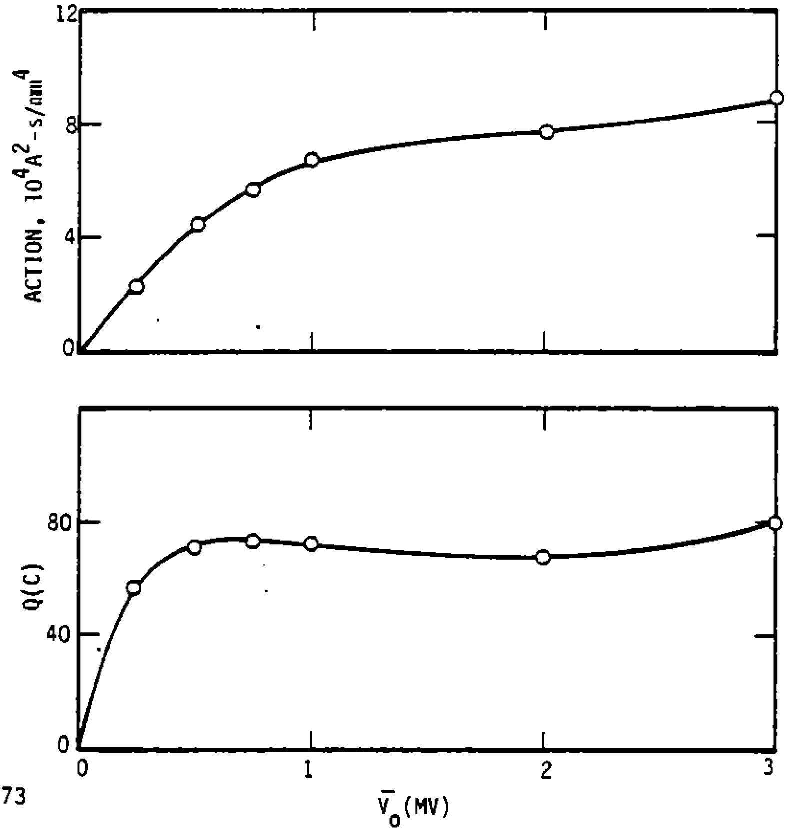

Figure 4-50. Calculated Q into shelter and peak specific action in Aℓ wire.

The curves of Q and maximum specific action are surprisingly flat versus the initial driver voltage, V_0. In fact, the Q delivered with V_0 = 1 MV is slightly larger than the Q with V_0 = 2 MV. This unexpected result occurs because, in the 2 MV case, the action rises fairly high on the ρ versus action curve. As a consequence, the current with V_0 = 2 MV is less than the current with V_0 = 1 MV for a considerable length of time (Figure 4-49). Even for V_0 = 3 MV, the peak specific action is only slightly beyond the resistivity peak so neither Q nor the peak action are starting to increase rapidly versus V_0.

At least for the parameters used in this analysis, the Aℓ wire provides better protection than the Fe wire.

6. POSSIBLE MODELS TO EXPLAIN ρ-VERSUS-ACTION CURVES

In many analyses of results from bare exploding wires, it is assumed or implied that the resistivity of a wire is a unique function of the specific action through the wire, at least up to the burst (peak resistivity), since heat losses from the wire are relatively small on the time scales of interest for most exploding wire experiments ($\lesssim 100\ \mu s$). However, results from the present experiments, such as Figure 4-31, show that enclosing the wire in a thick, snug dielectric jacket changes the resistivity-versus-action curve for a given wire material and geometry, not only after the burst but before as well, and as a function of how hard the wire is pulsed. In this section, some qualitative, speculative models are described which could explain the observed resistivity-versus-action (and versus time) curves. Since these models have not been verified as yet, they are offered merely to simulate thinking and ideas on the subject, and possibly to guide the planning for any future experiments on the vaporization/restrike of wrapped wires.

a. **Bare Wire Model**--To explain the sharp rise and subsequent rapid decrease in the resistivity of a bare wire in the vaporization/restrike regime, it is generally believed that the electrical conduction through the wire consists of two additive processes (Ref. 4-4). The one which occurs earliest in time has a decreasing conductance to explain the rapid rise in the resistance at the beginning of vaporization. It is believed that this initial process is conduction through the melted metal which has not yet been vaporized, and the decreasing conductance is due to the decreasing cross-sectional area of the melted metal as vaporization proceeds. Since this vaporization process would not terminate or reverse itself as long as the current continues to flow through the wire, this conductance should decrease monotonically to zero (when all of the metal is vaporized) and the resistance of the sample would go to infinity if some other conduction process did not intervene.

The second conduction process is believed to be conduction through the ionized metal vapor which has evaporated from the surface of the melted metal. Due to the magnetic pinch effect caused by the current through the wire, the outward diffusion of this metal vapor is somewhat inhibited and the ionized vapor tends to be confined close to the original current path. Since the initial vaporized metal is probably not highly ionized, the initial conductivity of the vapor will be low. However, when the proper conditions of vapor density and electric field across the vapor are achieved, avalanche ionization occurs and the conductivity of the vapor increases dramatically. Because of the confinement of the ionized vapor by the magnetic pinch mentioned previously, this high-conductivity state will continue more or less indefinitely as long as the available

---

4-4 W. C. Chace, 'Exploding Wires,' Vol. 2, edited by W.G. Chace and H. K. Moore, Plenum Press (1962).

voltage exceeds the sustaining voltage for the arc. Of course, eventually, when the applied voltage decreases, the arc will extinguish and the resistance will go to the open-circuit value.

Since there is considerably more structure in the ρ-versus-action (or time) curves for the wrapped wires than the bare wires (see, for example, Figures 4-31 and 4-41), the conduction process for the wrapped wires is apparently more complicated than the model described above for the bare wire. In the following sections, two different models are proposed for the wrapped wires. One will be designated a three-conduction process and the other a two-conduction process. Which of these two models, if either, is correct may be important if attempts are ever made to prevent restrike in wrapped wires.

b. Three-Conduction Model for Wrapped Wires--One possible explanation for the structure (peaks and shoulders) in the resistivity-versus-action (or time) curves (for example Figure 4-31) is three overlapping conduction processes starting at the beginning of vaporization.

The earliest process in time is the same as for the bare wire, namely, conduction through the melted (but unvaporized) metal. The only difference from the bare wire might be a delay in onset, and/or a slowing down, of the vaporization process due to the increased vapor pressure caused by temporarily confining the vapor to the inside of the dielectric. This effect could explain the delay in the rise of the resistivity-versus-action curves and their relatively slower rates of increase for the wrapped wires in Figure 4-31 compared to the bare wire (see Figure 4-41). Actually, one also has to consider resistivity versus time for the different driver voltages because the heat deposition rate (and therefore the vaporization rate) and the rate at which the vapor can escape from the ruptured dielectric are functions of time.

The remaining two conduction processes for the present model are assumed to be through the ionized vapor, similar to the model for the bare wire. The difference from the bare-wire model is that this vapor conduction is assumed to be separated into two processes. One, which occurs first in time, is through the vapor that is still reasonably well confined by the dielectric jacket, and the other is through the vapor that has escaped outside the jacket. These two conduction processes are assumed to be essentially independent of each other, except for the fact that the rate of increase of the amount of vapor outside the jacket is equal to the rate of loss of vapor from inside the jacket.

To explain the valley in the 120 kV curve around 18 μs in Figure 4-31 as well as the shoulder on the left-hand side of the 80 kV curve and the slight bulge on the right-hand side of the two highest-voltage curves around 20 μs, it appears that the second conduction process (first conduction process through the vapor) must start from zero at early times, increase to a peak, and then decrease again, probably to zero.

The third conduction process (through the vapor outside the jacket) is essentially the same as the conduction through the vapor for the bare wire. This last conductivity starts from zero when the first vapor escapes from the jacket, then increases rapidly when avalanche ionization begins, stays large as long as the applied voltage exceeds the sustaining voltage for the arc, and eventually approaches zero when the voltage decreases and the arc extinguishes.

The following is how this model would explain the resistivities versus action and time curves in Figure 4-31.

When vaporization begins, the resistivity starts to increase very rapidly as the liquid metal starts to vaporize. For the 205 kV case, the energy deposition rate, and therefore the vaporization rate, is presumably very fast compared to the rate at which the vapor can escape from the dielectric. Also, because of the large electric field across the confined vapor at this voltage, this vapor is rapidly ionized and the net resistance drops sharply. However, around 20 μs, the resistivity curve appears to be starting to level off. Then, at 20 μs, it starts to decrease more rapidly again when, according to this model, enough vapor has escaped from the dielectric and has finally become ionized to produce a significant conductivity.

For the 147 kV case, similar steps occur. However, the first decrease in the resistance (due to the confined vapor) is less rapid than for the 205 kV case because the vaporization and ionization rates are slower and the vapor can escape relatively faster to the outside. The third phase again becomes dominant around 20 μs.

For 120 kV, the initial rate of decrease in resistivity due to the confined vapor is even slower than for the higher voltages. Moreover, it is so weak an effect that it reaches a peak and starts to decay away (resistance increases) before the exterior vapor becomes sufficiently ionized to dominate the conductivity.

Finally, for 80 kV, the second phase is so weak that it cannot fully compensate for the still decreasing conductivity from the first phase (liquid metal) so the resistivity curve shows only a slight shoulder on its left-hand side and then increases again before the third phase finally takes over.

c. Two-Conduction Model for Wrapped Wires--Although the above three-conduction model seems capable of explaining the observed data for ρ versus action and time, there are some objections to the model.

First, from the standpoint of conciseness and the number of unknown variables, it would be preferrable to postulate only one vapor conduction process, say, through the vapor inside the dielectric, rather than two. Secondly, the fact that there is very little difference between the resistivity-versus-action curves with and without sand around the cable, at least at the two pulser voltages used in this comparison (Figures 4-22 and 4-23), suggests that conduction through the vapor exterior to the dielectric jacket has a minimal effect on the total conduction along the wire. Finally, on the time scales of interest for these experiments ($\lesssim$ 100 μs), there is a serious question whether the metal can become vaporized, rupture the dielectric, diffuse outside the dielectric, and avalanche-ionize to produce the large observed conductivities which are attributed to conduction outside the dielectric jacket in the three-conduction model. For these reasons, the following two-conduction model is offered as an alternative.

The first conduction process in this model is the usual conduction through the melted metal. The second conduction process is through the vaporized metal that is confined within the partially ruptured dielectric jacket. By comparison with the above three-conduction model, conduction through the vapor exterior to the dielectric jacket is assumed to be negligible, either because the vapor diffuses away too rapidly outside the dielectric jacket or because the soil, when it is present, nullifies the ionization of the escaped vapor, and thus reduces its conductivity.

Although this two-conduction model might appear to be simpler, and thus more plausible, than the three-conduction model, the conduction process in the confined vapor for the two-conduction model has to be a fairly complex function of the vaporization rate, the pressure in the confined vapor, the electric field to produce the ionization, the net ionization rate as a function of pressure and field, and the leakage rate of the vapor from the dielectric.

For example, for an applied voltage of 205 kV (Figure 4-31) the vaporization rate will be fairly rapid due to high energy deposition rate, but the avalanche ionization rate at that bias must be even faster because the resistivity decreases monotonically from the peak value once ionization begins. For successively smaller pulser voltages in Figure 4-31, the vaporization rates should become slower, which could explain the slower decrease in resistivity after the first peak in Figure 4-31. However, to explain the second peak in the 120 kV curve and the delayed large peak in the 80 kV curve, the conductivity of the confined vapor has to then decrease for a time, before finally becoming very large. Such a non-monotonic variation in conductivity through the vapor could be explained if the increasing pressure in the confined vapor momentarily quenches or slows down the ionization, until the pressure and electric field again become conducive to rapid ionization.

In Section IV.7, some possible methods for preventing restrike in wires are suggested. For wrapped wires, the techniques for preventing restrike might be different if the restrike occurs only inside the dielectric or also outside.

7. POSSIBLE METHODS FOR PREVENTING RESTRIKE

As discussed in Section IV.5, in order to minimize the amount of charge that is transmitted into a missile shelter, one would like to prevent restrike entirely after the R-wire has been vaporized. In this section, some ideas for possibly preventing restrike are suggested, but none of them has been verified as yet by experimentation.

The following are some possible methods of preventing restrike, shortening its duration, and/or increasing the post-restrike arc impedance.

a. Counteracting the magnetic pinch effect, which stabilizes the restrike arc, by bending the R-wire back on itself, separated by a dielectric, so that the magnetic field from the two legs of the R-wire act to disperse the current in the arc.

b. A snug dielectric collar around the R-wire to try to restrict the current path of the arc and thus increase its impedance.

c. Immerse the R-wire in a medium that tends to make the metal vapor products plate out and thus inhibit the formation or maintenance of a low impedance arc.

d. Spring-loading the R-wire, either axially or laterally so that, when the R-wire starts to melt, the mechanical force might sever the R-wire before vaporization and restrike occur.

In some of the above approaches, there is the problem of withstanding the full driver voltage (1 to 3 MV) across a dielectric for time periods of milliseconds, not a trivial task. This problem is further complicated by the fact that the two ends of the vaporized wire will form a point-to-point geometry which enhances the local electric fields.

V. STUDIES OF THE NONLINEAR AXIAL RESISTANCE OF BURIED CONDUCTORS IN THE PRESENCE OF LARGE RADIAL ELECTRIC FIELDS

1. INTRODUCTION

This section of the report presents the results of a series of experiments designed to measure the extent to which the radial electric field near a buried-resistive conductor will reduce the effective resistance of the conductor by permitting current to flow through soil parallel to the conductor.

2. BACKGROUND

Missile systems may incorporate several buried conductors that extend considerable distances away from the missile shelter. Without some protection system, an incident EMP wave would drive large currents along these conductors into the missile shelter, perhaps causing damage to the missile and/or its support equipment. One proposed method for preventing such excessive currents from reaching the missile shelter is to incorporate resistive links in the conductors which would restrict the amount of current that could flow due to the EMP drive. However, for these resistive links to be effective, it is necessary that the soil near the link not become highly conductive and produce a low-resistance shunt path parallel to the resistor.

From previous work (Refs. 5-1,5-2) it is known that a sufficiently large voltage pulse between two conductors immersed in soil will produce breakdown streamers, and consequently a low-resistance path, through the soil between the two conductors. However, it was not determined how much such streamers would contribute to the soil conductivity transverse to their axial directions. To answer that question, in the present experiments a radial electric field was applied between a small cylindrical, resistive conductor and an outer coaxial conducting cylinder, coincident with an axial field along

---

5.1 C. Mallon, et al., 'Electrical Breakdown Characteristics of Soil Samples,' Theoretical Note 316, 12 January 1981

5.2 C. Mallon, et al., 'Electrical Breakdown Characteristics in 0.8 to 1.0 meter Soil Samples,' Theoretical Note 318, 19 April 1982 the center resistive cylinder. The magnitude of the radial field was large enough to initiate radial streamers in the high-field region adjacent to the inner cylinder but small enough so that the streamers did not propagate all the way to the outer cylinder, at least until the axial conductivity measurement could be made. Plastic sheets were also placed perpendicular to the axis of the cylinders to determine the spatial location of any streamers that carried current through the soil parallel to the cylinder axis.

3. TEST CONFIGURATION

The test configuration for these experiments is illustrated in Figure 5-1. It consisted of two concentric cylinders, both approximately 0.9 m long, with the intervening volume filled with soil. The outer cylinder was metallic with a 0.45 m radius. The bottom of this cylinder was closed with a high resistivity dielectric (plexiglass) to contain the soil. The top of the cylinder was closed with a plastic sheet to maintain the moisture content of the soil during the test.

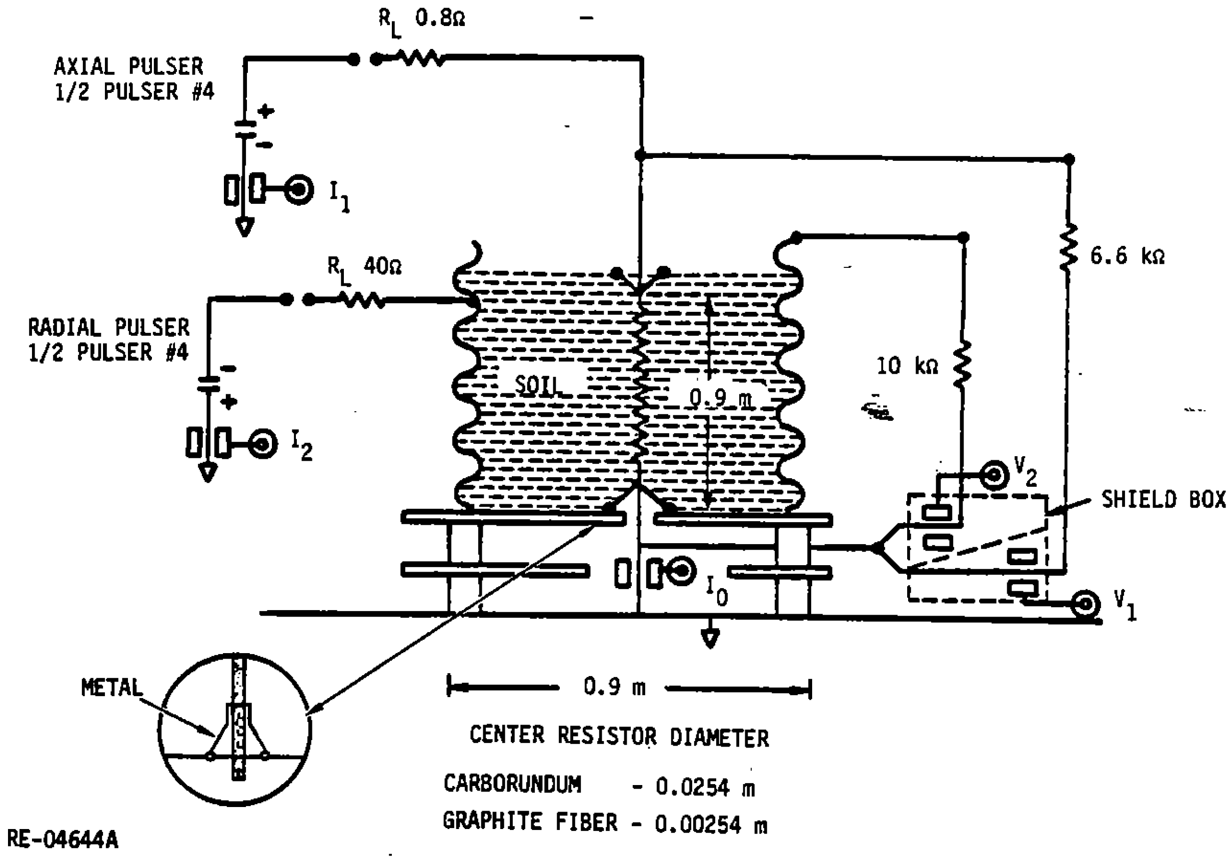

Figure 5-1. Experimental arrangement used for nonlinear studies on buried conductors.

The inner cylinder, a resistive conductor, was either a graphite fiber or a carborundum resistor. The graphite fiber had a radius of 0.00127 m and an ambient resistance of ~ 10 Ω. The carborundum resistor was 0.0127 m in radius and had an ambient resistance of ~ 66 Ω. The basis for selecting these radii and resistances is discussed in Section V.3.a.(2).

The two ends of the central resistive cylinder terminated in flared metal connections, as illustrated in Figure 5-1, to provide field grading to minimize arcing along the air-soil interface. Also, if a surface arc did occur the large current would be carried by the flared metal connections and thus prevent damage to the resistive center cylinder.

The lower end of the center resistive cylinder was connected to ground through a current probe to measure the current flow (I_0) out of the resistive element to ground. The upper end of the center resistive cylinder was connected via a 0.8 Ω stainless steel ribbon resistor, R_L, to a positively charged capacitor bank (1/2 of MCAIR pulser #4) whose voltage could be increased in approximately 10 kV intervals up to 100 kV.

During the series of experiments the outer metallic cylinder was grounded through either 0 or 40 Ω or connected via 40 Ω to a negatively charged capacitor bank to provide a variable radial electric field. The 40 Ω series resistor was used to prevent damage to the center resistive element in the event of a low impedance arc attachment to the outer cylinder.

The configuration used during the test sequence for the axial and radial pulsers is discussed further in Section V.3.b.

The soil used during test series was kiln-dried-20 grit-Missouri river sand. While a seive analysis was not done to determine particle size, a random sampling indicated a particle size of ~ $1.2 \times 10^{-3} \pm 3.5 \times 10^{-4}$ m. The sand as received had a water content of ~ 0.15 percent by weight. For this small water content the electrical conductivity was 8×10^{-5} S/m and the relative dielectric constant was 5.7. Initial attempts to increase the electrical conductivity to ~ 3×10^{-3} S/m by increasing the moisture content of the sand showed that this large of a conductivity could not be obtained for a reasonable distilled water content. For example, at a water content of 2.5 weight percent the electrical conductivity increased to only 6.2×10^{-4} S/m, which was still approximately a factor of 5 lower than the desired value. Also, at this water content the sand appeared quite wet and it was probable that a water content gradient would develop in the 1 meter deep-filled cylinder.

To achieve the desired electrical conductivity of 3×10^{-3} S/m, at an allowable water content, it was necessary to increase the conductivity of the distilled water by the addition of NaCℓ.

Figure 5-2 shows the results of measurements made to determine the resistivity of water required to obtain a sand conductivity of 3×10^{-3} S/m for a water content of 1.5 weight percent. From Figure 5-2, a water resistivity value of 77 Ω-cm was chosen to obtain the desired conductivity. Random samples taken from the 2200 pounds of sand required to fill the cylinder, with a water content of 1.5 weight percent of 77 Ω-cm water, indicated an electrical conductivity of 3.2×10^{-3} S/m.

The frequency dependence of the electrical conductivity and relative dielectric constant for various water contents and water resistivities are shown in Figures 5-3 and 5-4.

a. Pretest Analyses--The major pretest analyses for these experiments were those that led to the decision to use a two-pulser arrangement, and the selection of the radius and resistance for the center cylinder.

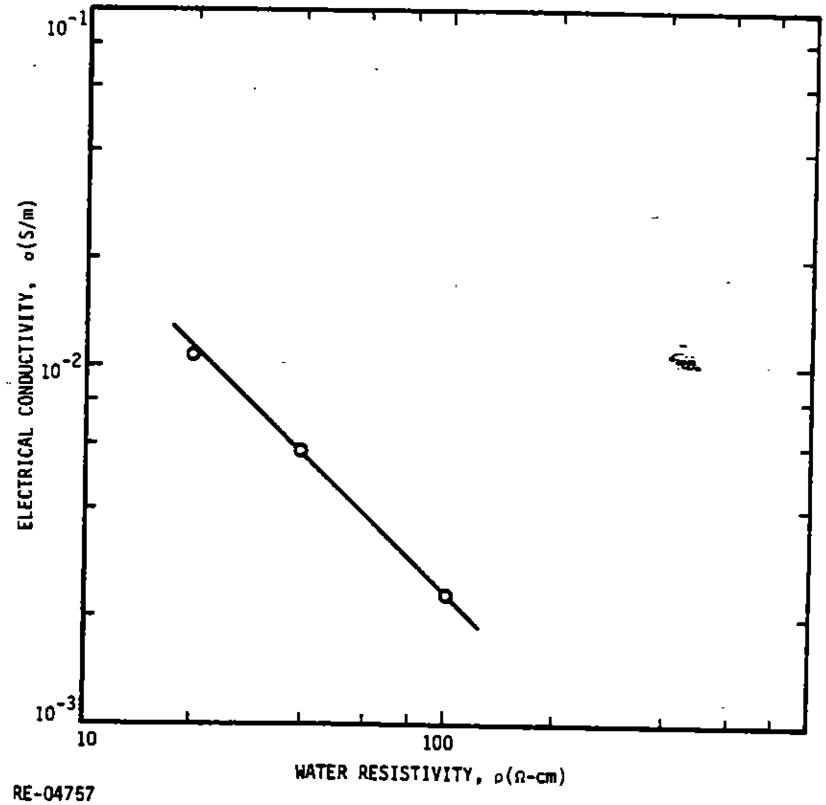

Figure 5-2. Electrical conductivity of sand versus resistivity of water used to give a water content of 1.5 percent by weight. Conductivity values measured at 10^5 Hz.

(1) Selection of Two-Pulser Arrangement--For these experiments, it was necessary to apply both an axial voltage along the center cylinder and a radial voltage between the inner and outer cylinder. These voltages could be generated using just one pulser to drive one end of the center cylinder and connecting the other end of this cylinder to ground via one resistor (R_1) and the outer cylinder to ground via a second resistor (R_2). A wide range of axial and radial voltages could be achieved by a proper choice of the driving voltage and the two grounding resistances. The biasing of the outer cylinder relative to ground results from the radial leakage current through the soil which then has to flow to ground through R_2.

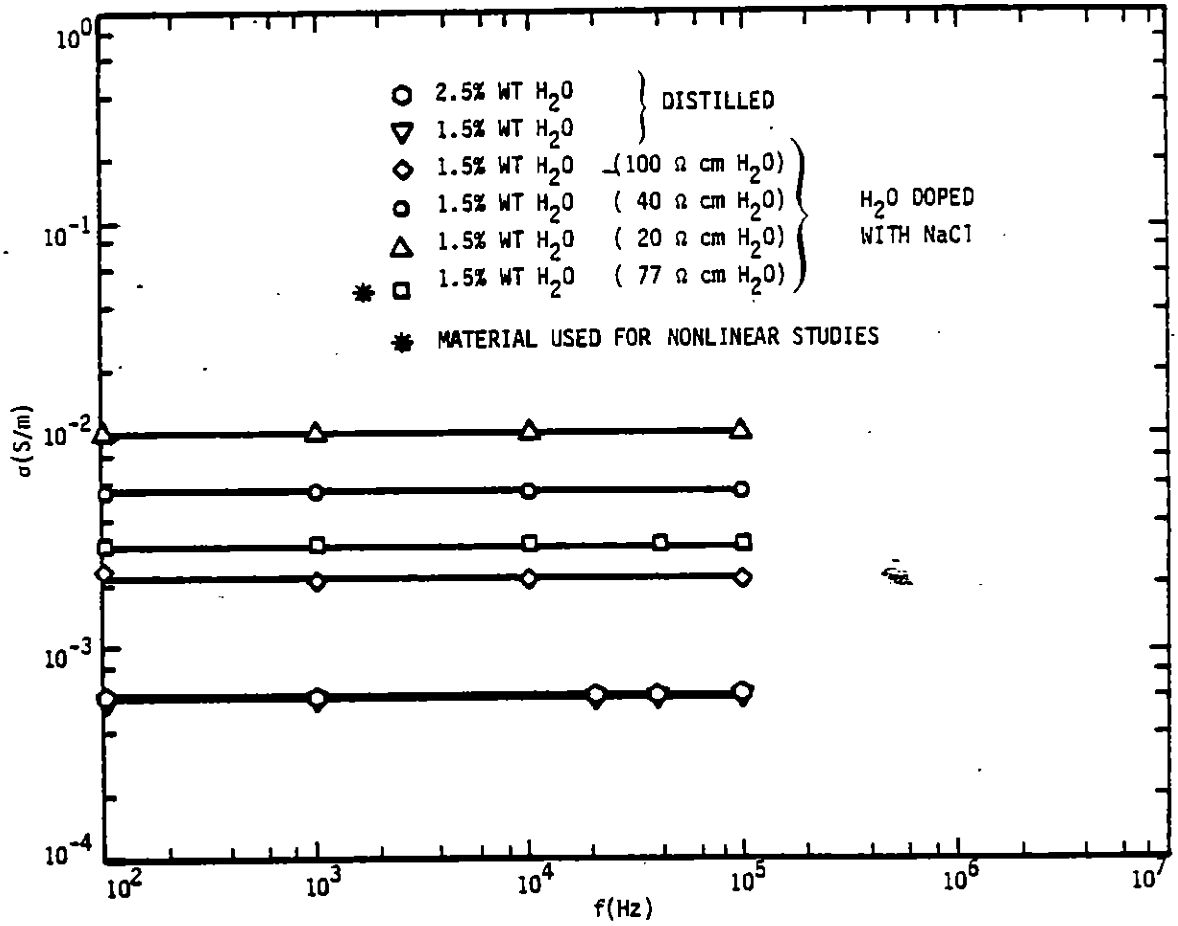

RE-04850

Figure 5-3. Electrical conductivity versus frequency and H_2O content for several values of H_2O resistivity. Soil is 20 grit Missouri river sand.

Although this arrangement was desirable from the standpoint of not having to synchronize the firing of two pulsers within a few microseconds, the magnitudes of R_1 (≈25 to 200 Ω) necessary to obtain the desired ratio of the radial and axial voltages with a center resistance of about 70 Ω could cause a sensitivity problem. From previous work (Ref. 5-2) on meter-size soil samples, it was known that the minimum resistance which a discharge arc in soil achieves is a strong function of the current that the pulser/circuit configuration can drive through the arc. When the peak current through the sample is 50 to 60 kA, the arc resistance can be as low as 0.2 Ω/m. However, for peak currents around 1 kA, the arc resistance is between 2 and 10 Ω/m, and there is some evidence from small-scale samples that the impedance may increase sharply (100 to 1000 Ω/m) for even smaller currents. Hence, in order to produce the largest changes in the total axial resistance of the sample, it is desirable to have the smallest possible exterior resistance in series with an axial arc, if one occurs. As an illustration, for an axial voltage of 100 kV and R_1 = 200 Ω, the largest peak current that could flow would be only 0.5 kA, and the situation would be even worse for smaller axial voltages. Hence, for this reason, the two-pulser arrangement was selected so that the desired ranges of radial and axial voltages could be achieved with a zero value for the resistance R_1.

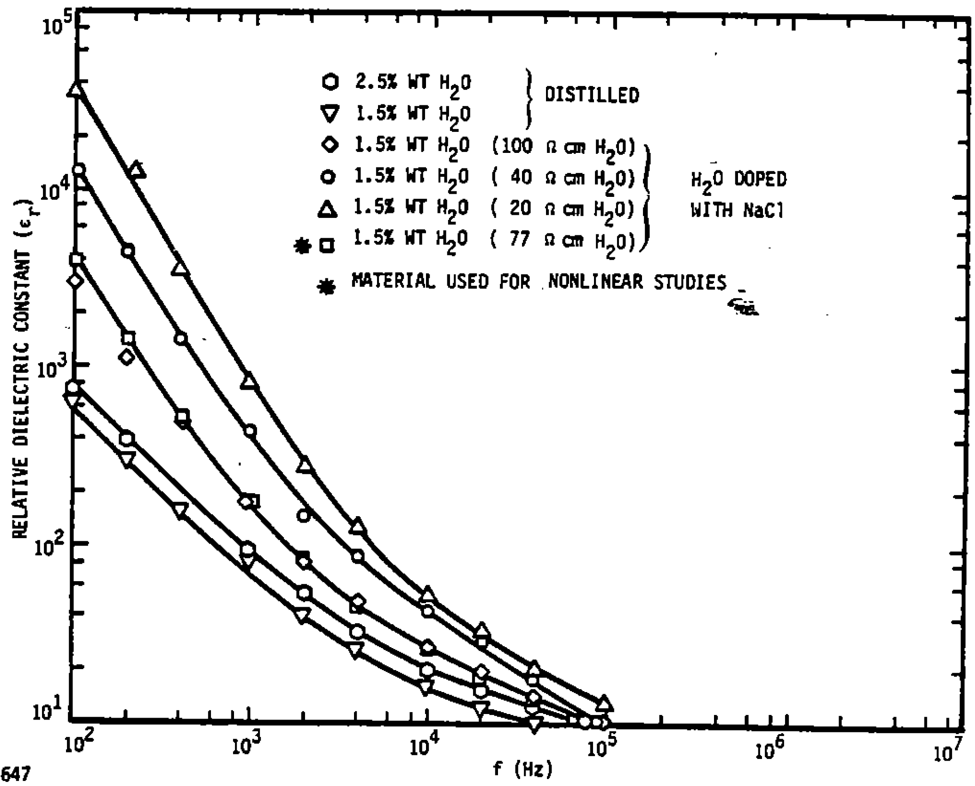

RE-04647

Figure 5-4. Relative dielectric constant versus frequency and H_2O content for several values of H_2O resistivity. Soil is 20 grit Missouri river sand.

(2) Resistance and Radius for Center Cylinder--There were several competing factors that entered into the choice of the resistance and radius of the center cylinder.

First, it was desirable to have the pulser that drives the center cylinder have an RC decay constant of about 1 ms. Therefore, with $R_1 = 0$ and a pulser capacitance of 21 μF, the cylinder resistance should be about 50 Ω. Of course, this decay time could have been obtained using a larger pulser capacitance and a smaller resistance. However, the larger capacitance means that more energy would be dissipated in the resistor, which is also a problem as discussed below. Hence, a nominal resistance of ~50 Ω was selected as the optimum value for the center cylinder. Its actual value was dependent on what resistors were commercially available with the desired radius.

In order to best demonstrate an axial conductivity effect in the present experiments, theoretical arguments and the experimental results of MRC (Ref. 5-3) indicate that the radius of the center cylinder should be as small as practical so that the radial electric field close to the cylinder will be large enough to produce many small radial discharge streamers close to the cylinder. With a large number of streamers, one could expect to see a large axial conductivity in the soil as the neighboring streamers interact more easily with each other. Also, it is felt that a large number of radial streamers should be more stable, that is, less prone to have one streamer punch through to the outer cylinder, than a few, sparsely-spaced streamers. That being the case, larger radial voltages could be used in the experiments to try to enhance the axial conductivity and the time for developing and observing the axial effect should be longer. Finally, if there are a large number of radial streamers at the upper end of the center cylinder (where the radial voltage is largest), it is more likely that there will be enough radial streamers at the lower end of the cylinder (where the radial voltage is smaller due to the IR drop in the center cylinder) to support an enhanced axial current through the soil.

Since the threshold electric field for the breakdown of soil is on the order of 1 MV/m (Ref. 5-2), the radial field near the inner cylinder should be considerably greater than this value (perhaps 3 to 4 MV/m) to produce many small streamers rather than one large streamer which is more apt to be unstable. For a 100 kV radial voltage, an outer radius

---

5.3 V. A. J. van Lint, J. W. Erler, 'Buried Conductor Studies,' Theoretical Note 347, December 1981 of 0.5 m, and a radius for the inner cylinder of 0.01 m, the radial field at the inner cylinder is only 2.56 MV/m. Therefore, it was desirable to have an inner cylinder with a radius significantly less than 0.01 m.

The final considerations in selecting the radius of the inner cylinder were the availability of commercial resistors and their ability to dissipate the energy deposited in them by the axial pulser.

Three sets of resistors were chosen for use in the tests based on availability and conformity to the above analysis. The important properties of the resistor types are given in Table 5-1. The silicon carbide resistors were considered candidates for the tests because of their relatively small diameter (10^{-2} m) and a value of resistance in the desired range. Prior to using these resistors in the soil-filled cylinder, however, a series of 20 kV voltage pulses in air revealed a large dependence of resistance on applied voltage. The resistance of a silicon carbide resistor with a low field resistance of ~40 Ω decreased to ~10 Ω for an applied voltage of 20 kV. Because of the observed resistance-voltage coefficient the silicon carbide resistors were not used for the nonlinear tests.

Table 5-1. Description of Center Resistive Rods Used During Nonlinear Studies on Buried Conductors

Type	Nominal Resistance	Diameter	E (Radial) For $\Delta V = 10$ kV	Remarks
Silicon carbide	40 ohms	1×10^{-2} m	4.4×10^{5} (V/m)	Not used, resistance was a strong function of voltage and not reproducible
Carborundum Resistors (Two In Series)	65 ohms	2.54×10^{-2} m	1.1×10^{5} (V/m)	$\rho(T) \sim -0.075$ %/°C
Graphite Fiber	10 ohms	2.54×10^{-3} m	1.3×10^{6} (V/m)	$\rho(T)$ +, -(See Table 4-4)

The carborundum and graphite fiber resistors described in Table 5-1 were used during the nonlinear tests and the results obtained with these are presented in a later section. Although the resistance of the graphite fiber was lower than desired it was the smallest diameter resistive element available.

b. Experiment Description

(1) Pulser Characteristics--The MCAIR 660 kJ, 240 kV pulser was divided into two separate capacitor banks to provide the axial and radial electric fields for nonlinear studies on buried conductors. In this configuration each bank consisted of five 230 μ F stages capable of producing ~20 kV/stage. The manner in which the banks are constructed, however, allows the output voltage to be extracted at half-stage intervals and thus provides the capability of increasing the output voltage in 10 kV increments.

Each stage consisted of 11 parallel 21 μ F capacitors (two 12 kV, 42 μ F capacitors in series) for a total stage capacitance of 230 μ F. The parallel connections between capacitors, however, can be broken so that the individual stage capacitance can be varied from 21 to 230 μ F. Both of the above flexibilities were used during the series of tests to control the amount of energy deposited in the center resistive cylinders.

Figure 5-5 is a schematic representation of one stage of the axial pulser shown connected to the center resistive rod, R_A. In Figure 5-5, R_C represents the capacitor bank charging resistors which shunt the pulser stage when the bank fires. During this series of tests the value of the charging resistors was approximately 8 Ω. The energy stored for a charge voltage of V_p is

$$E = 1/2\ nC(V_p)^2$$

where n is the number of parallel capacitors (21 μ F each) of the stage being used. The time constant of the pulser was determined by the pulser capacitance (nC) and the parallel combination of the center resistive rod (R_A) and the charging resistors, R_C

$$\tau = nC \times \frac{R_A\ R_C}{R_A + R_C}$$

During the experiments n, the number of parallel capacitors used per stage for the axial pulser, was kept to a minimum such that the pulser decay time constant was approximately equal to the time required for streamer attachment between the center resistive rod and the outer metal cylinder. This resulted in a minimum amount of energy being deposited in the resistive rod.

Generally, an axial pulser capacitance of 42 μ F was sufficient to provide the required decay time constant. As the number of stages was increased to increase the axial drive voltage, the number of parallel capacitors was also increased to maintain a total pulser capacitance of 42 μ F.

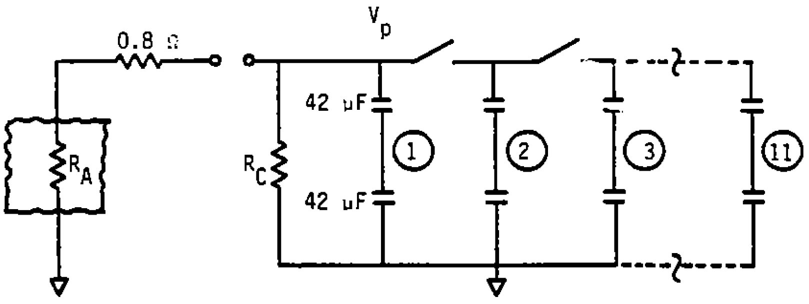

R_C = CHARGING RESISTOR ≈ 8 Ω
R_A = RESISTANCE OF CENTER RESISTIVE ROD

RE-04851

Figure 5-5. Schematic of one stage of axial pulser connected to center resistive rod.

The ratio of energy deposited in the resistive rod to that deposited in the charging resistors is given by

$$E_{rod} = E(\text{stored}) \times \frac{1}{1 + R_A/R_C}$$

For the carbordum resistor ($R_A \sim 60\ \Omega$) only about 10% of the stored energy was deposited in the resistor, while approximately 50% of the stored energy was deposited in the 10 Ω graphite fiber resistors.

The radial pulser was connected to the outer metallic cylinder by a 40 Ω current limiting resistor, which was small compared to the radial resistance between the center resistive rod and the outer cylinder. The use of a limiting resistor in the radial pulser circuit provided protection for the center resistive rod in the event of a low impedance arc attachment. For the radial pulser the total stage capacitance (230 µF) was used which gave a radial pulser decay time constant of $230\ \mu F \times 8\ \Omega = 1.8 \times 10^{-3}$ s.

(2) Instrumentation--Five time dependent measurements were made during the test series to characterize the axial resistance of the center resistive rod and the radial resistance, through the soil, between the center resistive rod and the outer metal cylinder.

(a) V_1, the voltage applied to the top of the center resistive rod by the axial pulser.

(b) I_1, the current flowing into the center resistive rod.

(c) I_0, the current flow to ground out the bottom of the center resistive rod.

(d) V_2, the voltage applied to the outer metal cylinder by the radial pulser.

(e) I_2, the current flow from the outer metal cylinder to ground.

The location of these measurement points was shown in Figure 5-1.

Voltages V_1 and V_2 were calculated from current measurements in calibrated high voltage resistors that connected the measurement points to ground (V_1-6.6 kΩ, V_2-10 kΩ). Pearson 110A current probes, located in shield boxes, were used for these measurements.

Currents I_1 and I_0 were measured by Pearson 1049 current probes and current I_2 was measured by a Pearson 3025. These current probes are described in Table 5-2.

Table 5-2. Pearson Current Probe Characteristics

Measurement	Pearson Model No.	Maximum Peak Current (A)	IT Maximum (A·s)	Rise Time
I_0, I_1	1049	250,000	25	0.25 µs
I_2	3025	20,000	3.2	100 ns
V_1, V_2	110A	10,000	0.49	20 ns

In addition to the above electrical measurements, thin sheets of conductive plastic were used for some shots in an attempt to determine the paths of any breakdown streamers that carry current parallel to the center cylinder. These sheets of plastic were placed normal to the axis of the cylinder. Tests were made with and without the plastic to verify that it did not create any artificial detrimental effects.

(3) **Experimental Approach**--During the test series the following approach was used to investigate the extent of a nonlinear axial resistance for a buried conductor in the presence of radial fields.

(a) Measure the radial resistance as a function of radial voltage with a minimum axial field.

- Bottom of center rod ungrounded
- Outer metal cylinder either grouned or connected via 40 Ω to ground
- Pulse top of center rod with progressively larger voltages.

A typical data set for this configuration is shown in Figures 5-6 and 5-7. Figure 5-6 shows oscilloscope traces for V_1, I_1, and I_2, and Figure 5-7 shows the experimental configuration and an explanation of the current and voltage traces.

(b) Measure axial resistance as a function of axial voltage with a minimum radial field.

- Outer metal cylinder floating
- Bottom of center resistive rod grounded
- Pulse top of center resistive rod with successively larger voltages.

Figure 5-8 shows typical oscilloscope traces for V_1, V_2, I_1, and I_0. Figure 5-9 shows the experimental configuration. Note in Figure 5-9 that I_1 and I_0 are equal and the voltage of the outer metal cylinder, V_2, increases to approximately $V_1/2$ since the bottom of the resistive rod is grounded and the outer cylinder floats.

(c) Combined axial and radial resistance measurements

- Bottom of center resistive rod grounded
- Axial pulser drives top of center resistive rod first in time; 10-20 μs later radial pulser (-) drives outer metal cylinder.

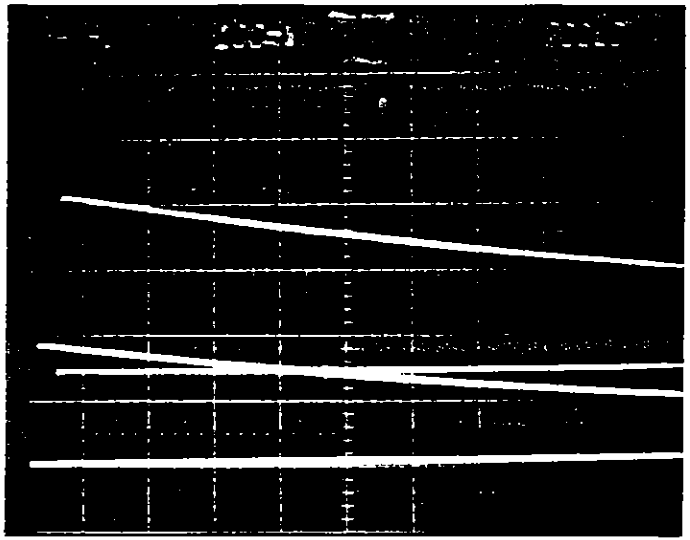

200 µs/cm

V_1 = 6.6 kV/cm
= 17.5 kV

I_1 = 50 A/cm

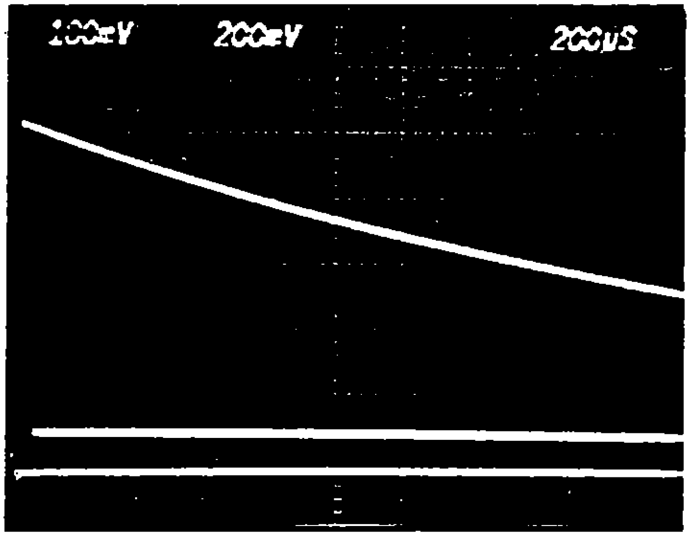

200 µs/cm

V_2 = 0

I_2 = 16 A/cm

RE-04658

Figure 5-6. Current and voltage traces V_1, I_1, and I_2 for carborundum resistor #1, shot 16, and the configuration shown in Figure 5-7.

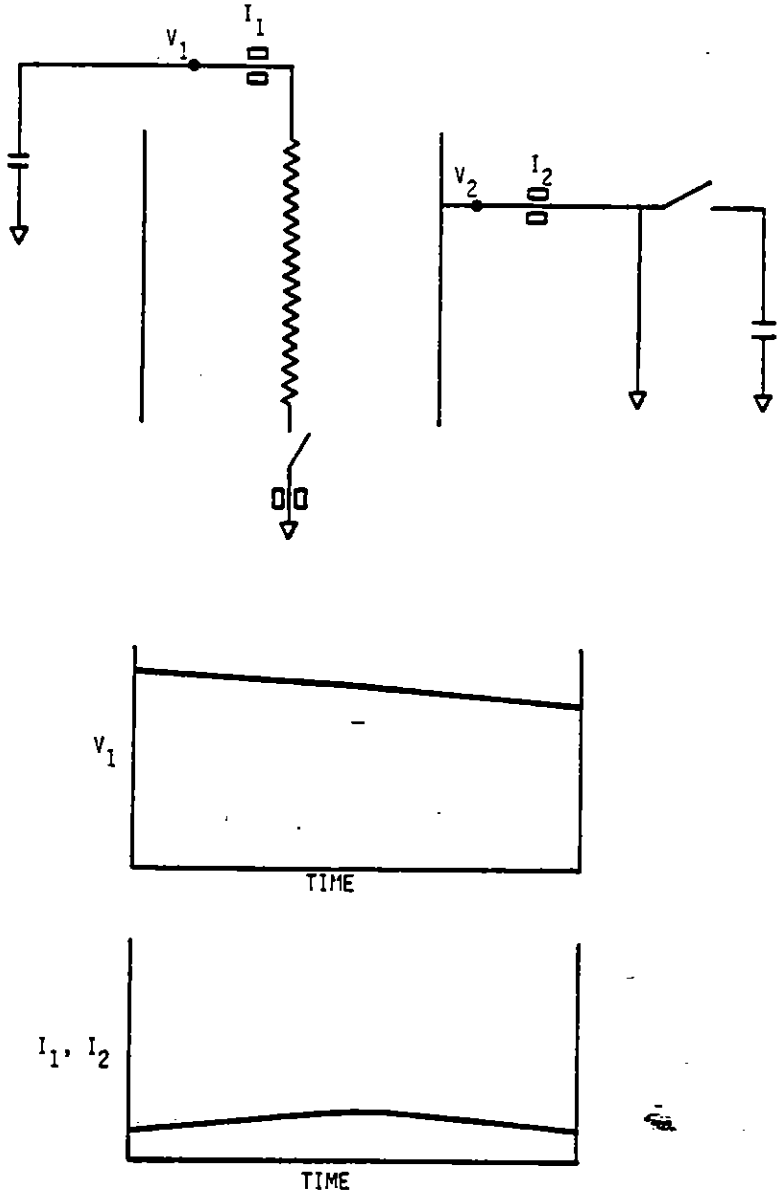

RE-04653

Figure 5-7. Experimental configuration for radial resistance measurements.

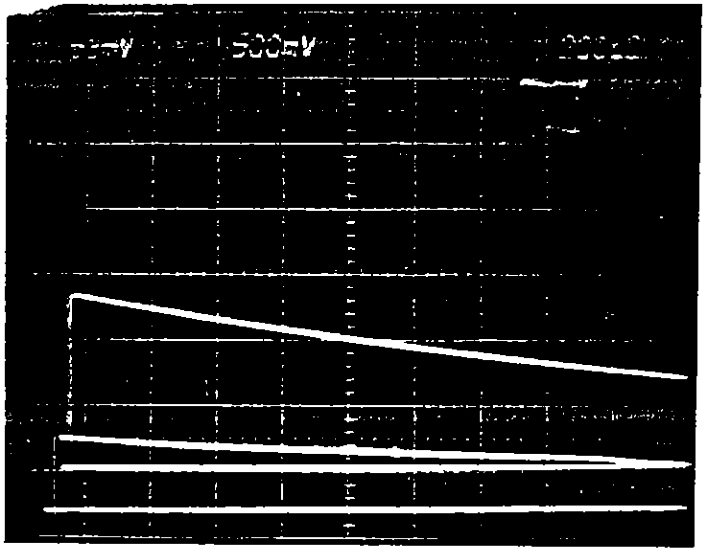

200 µs/cm

V_1 = 6.6 kV/cm

I_1 = 250 A/cm

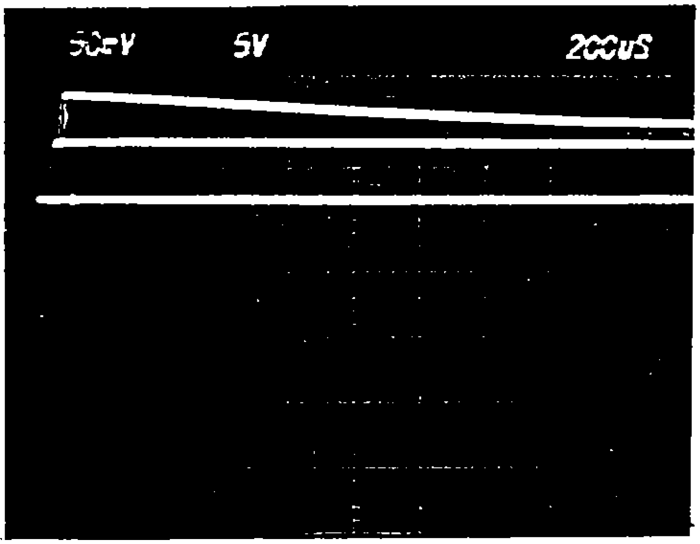

V_2 = 10 kV/cm

I_2 = 0

200 µs/cm

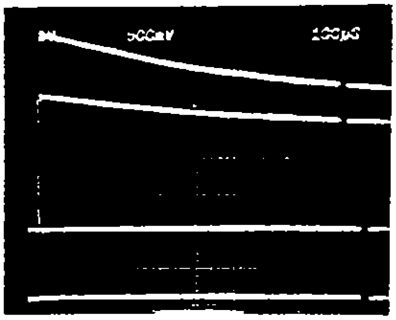

I_a = 80 A/cm

100 µs/cm

RE-04657

Figure 5-8. Typical oscilloscope traces for the experimental configuration shown in Figure 5-9. Carborundum resistor #1, shot 24.

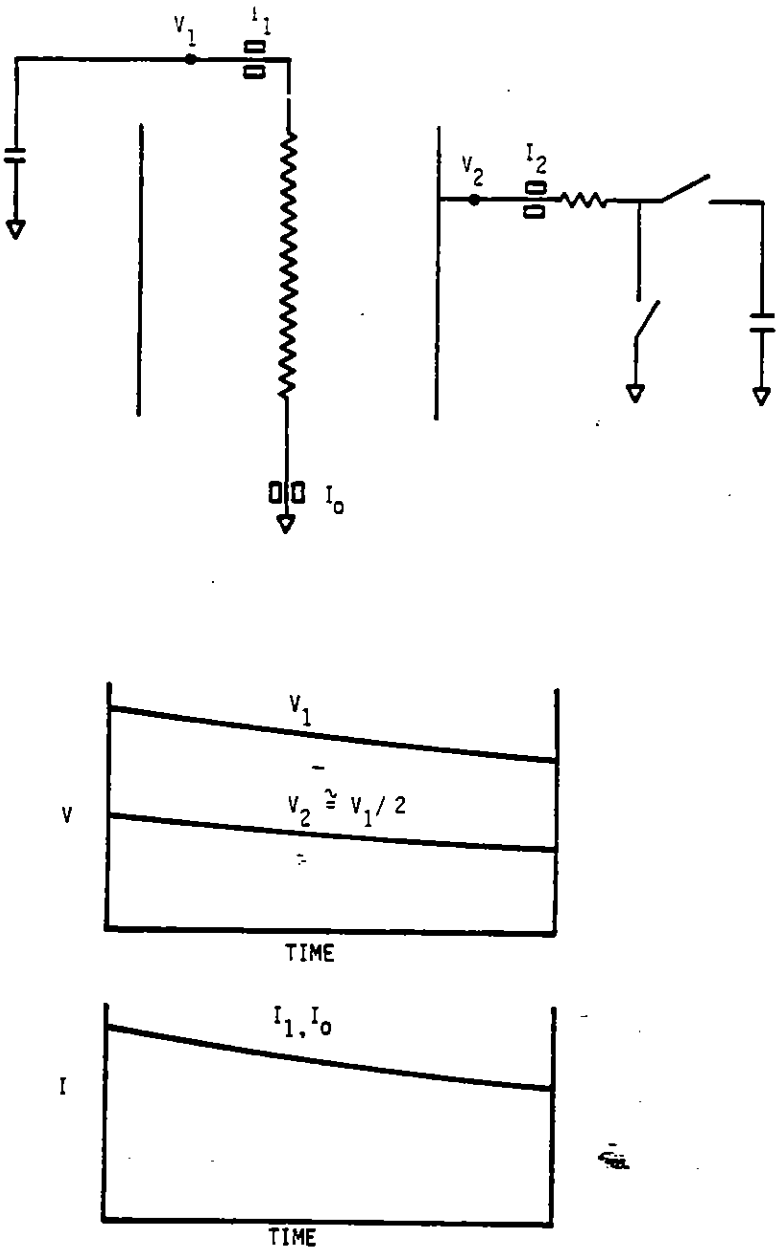

RE-04654

Figure 5-9. Experimental configuration for axial resistance measurements with minimum radial field.

A typical set of oscilloscope traces for this experimental configuration is shown in Figure 5-10. The experimental configuration is shown in Figure 5-11, which also addresses the observed data traces through firing of the radial pulser and the delayed streamer attachment to the outer cylinder.

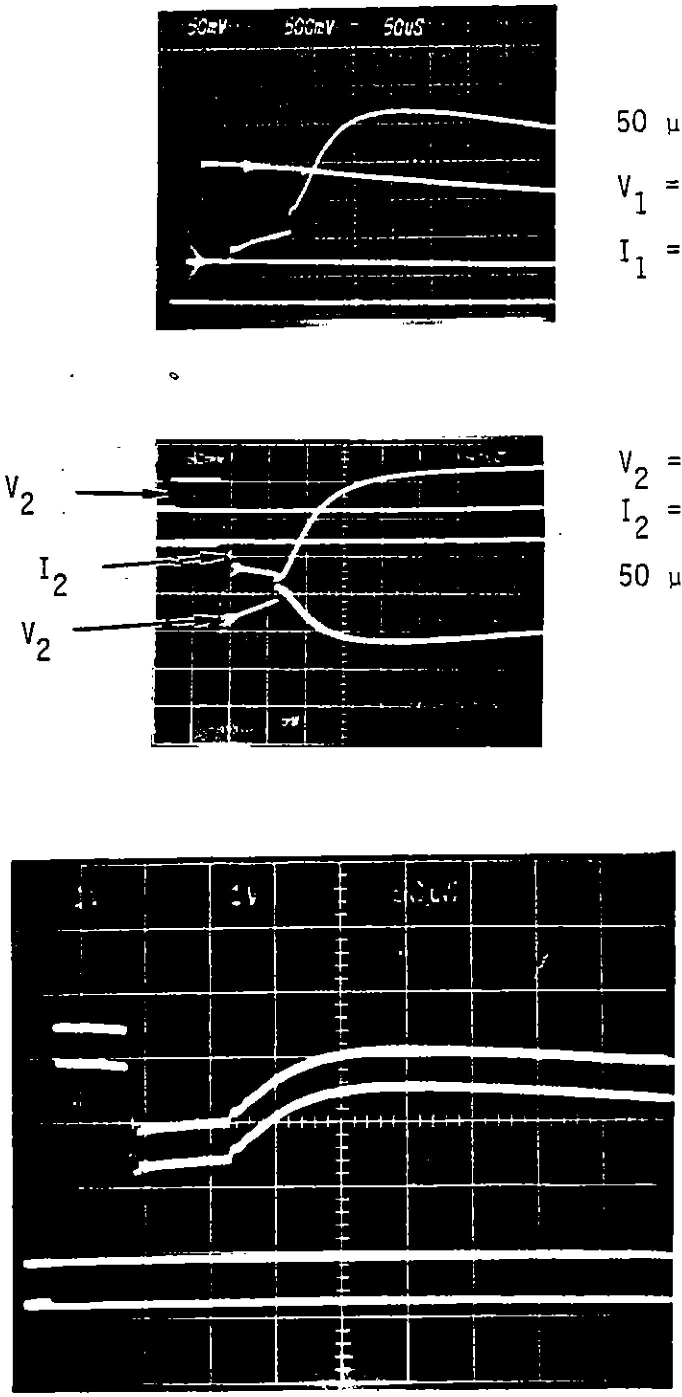

50 µs/cm

V_1 = 6.6 kV/cm

I_1 = 250 A/cm

V_2 = 10 kV/cm

I_2 = 400 A/cm

50 µs/cm

50 µs/cm

I_o = 80 A/cm

RE-04656

Figure 5-10. Voltage and current traces for combined axial and radial drive.

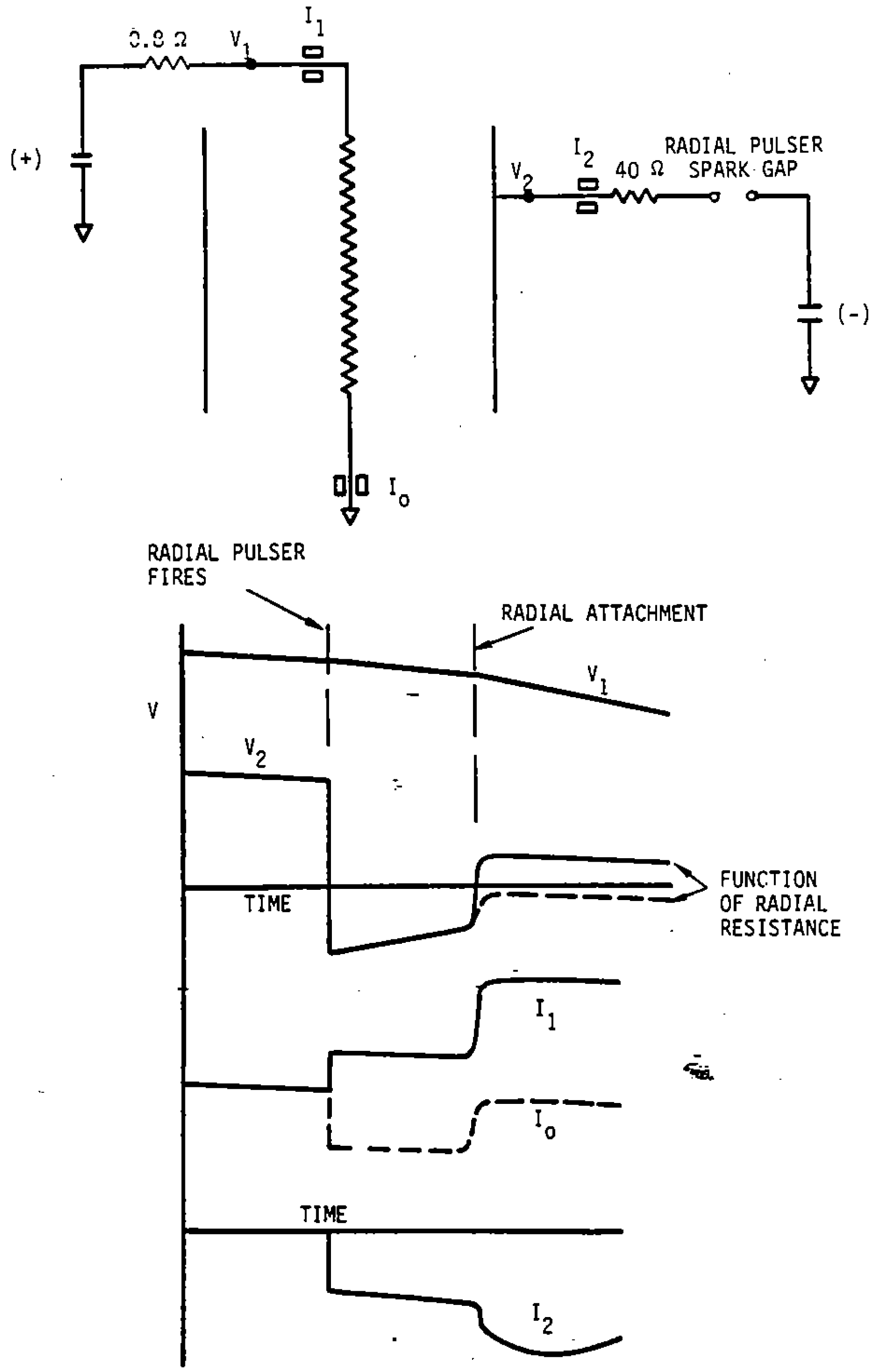

RE-04655

Figure 5-11. Experimental configuration and current-voltage traces for combined axial and radial drive.

The time dependence of voltage V_1 applied to the top of the resistor rod (Figure 5-11) is relatively insensitive to the radial pulser firing or radial streamer attachment since it is connected to the axial pulser by a low impedance (~ 0.8 Ω). Voltage V_2, the potential of the outer cylinder adjusts to approximately 0.5 V_1 before radial pulser fires since the outer cylinder floats until the spark gap of the radial pulser closes. V_2 then goes to a negative value equal to the voltage of the radial pulser minus the IR voltage drop (I_2 x 40 Ω) in the resistor that connects the radial pulser to the outer cylinder. After radial attachment V_2 remains negative, or goes to a positive value, depending on the relative magnitude of the radial streamer resistance and the 40 Ω resistor in series with the radial pulser. The shape of currents I_1 and I_2 are relatively straightforward as both show an increase when the radial pulser fires and also when radial attachment occurs. The decrease in I_0 when the radial pulser fires results from the following.

Before the radial pulser fires the outer cylinder floats and achieves a potential approximately equal to 0.5 V_1 where the voltage V_1 is assumed to be dropped uniformly from top to bottom of the grounded resistive rod. Therefore, the same current that flows outward from the resistive rod to the outer cylinder in the upper-half of the cylinder returns to the resistive rod in the lower-half of the cylinder. For this case I_1 and I_0 are equal. When the radial pulser fires and drives the outer cylinder negative with respect to ground, the electric field is outward over the entire length of the resistive rod and results in a net outward current flow from the resistive rod to the outer cylinder (I_2). The magnitude of I_2 is determined by the net radial electric field and the radial resistance of the soil between the cylinders. The net outward current flow from the center resistive rod results in a division of current I_1 that enters the top of the rod such that $I_0 = I_1 - I_2$ and therefore causes a decrease in I_0.

The increase in current I_0 when radial attachment occurs would result from the following:

Assume that streamer attachment occurs near the top of the resistive rod which is reasonable since this is the region of largest radial electric field. If the streamer resistance is of the order of the 40 Ω resistor in series with the radial (negative) pulser, the potential of the outer cylinder will approach the potential of the resistive rod at the point of attachment. This results in a decrease in the radial electric field while the axial field is relatively unchanged. The decreased radial electric field causes a decrease in the outward current flow from the center resistive rod below streamer attachment thereby increasing current I_0.

c. **Streamer Decoration of Conductive Plastic Films**--Conductive plastic films were placed in the soil-filled cylinder to detect the presence of radial and/or axial streamers during combined axial and radial drive shots. The conductive films were 0.44 m diameter, 1 x 10^{-4} m (4 mils) thick and were placed in the cylinder with their planes normal to the axis of the cylinder. For this geometry, radial streamers produce surface tracking on the film and axial streamers (radial streamers turned downward by the axial field) would produce pinholes in the film. The measured conductivity of the film was ~ 10^{-3} S/m.

(1) **Decoration of Conductive Plastic Film with Graphite Fiber as the Center Resistive Rod**--After shot 69 on graphite fiber #2 sufficient sand was removed, and then replaced, from the cylinder to position the conductive plastic sheet ~ 0.26 meters below the upper end of the graphite fiber sample. During removal of the sand, the graphite fiber sample appeared to be intact. During sand replacement, however, the graphite fiber apparently parted somewhere below the conductive plastic sheet. From the excess length of the fiber after refilling the cylinder it is estimated that the ends of the parted fiber were separated by approximately 0.07 m (~ 3 in.). During shots 70 and 71, current and voltage traces indicate closure of this gap within 5 μs after applying axial voltages of 38 and 46 kV, respectively.

During shot 70, the peak axial voltage was +30 kV and the radial voltage was -15 kV. For shot 71, the axial voltage was increased to 44 kV and the peak radial voltage was -12 kV. Radial attachment to the outer metal cylinder occurred only during shot 71.

Figure 5-12 shows the location and relative length of the observed radial streamers. Inspection of the conductive plastic sheet after shot 71 showed the presence of four radial streamers that extended out to a radius of ~ 0.06 to 0.07 m. One streamer transversed the 0.22 m radius plastic sheet and apparently continued to the outer cylinder. The remaining radial streamer, on the opposite side of the film (dashed line in Figure 5-12), stopped ~ 0.02 m from the outer edge of the film. Note that the streamers that stop at a radius of 0.04 to 0.07 m all exhibit branching, while the longer streamers propagated in a straight line with no side branching. The branching observed for the shorter streamers presumably results from electron flow from the tips of the individual branches to a common channel that terminates on the positive center resistive rod.

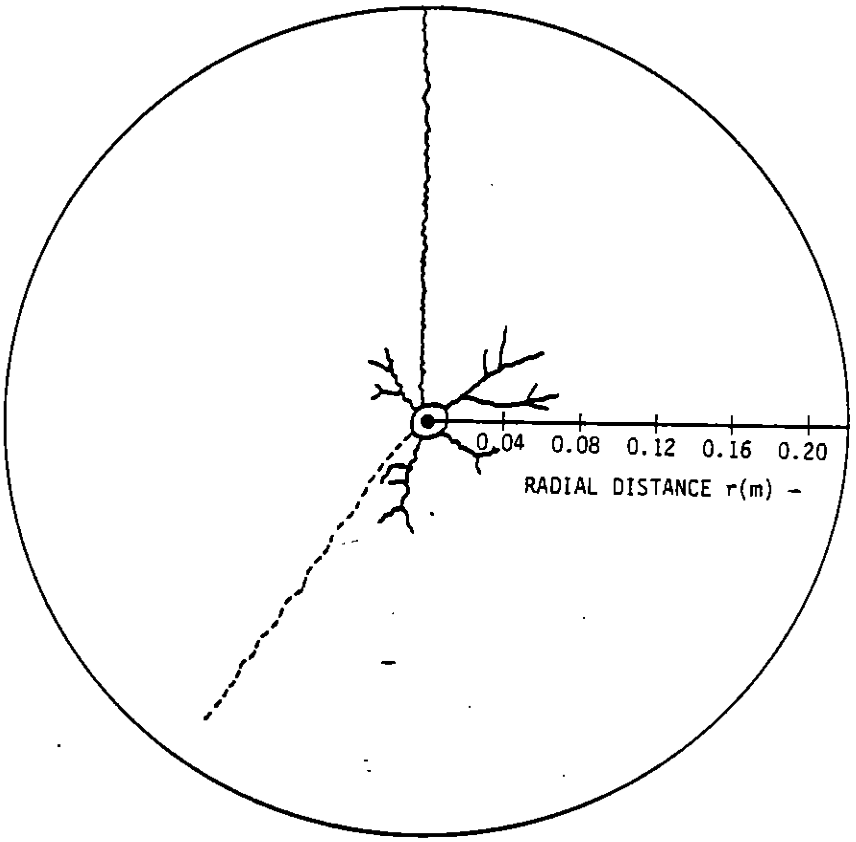

RE-04806

Figure 5-12. Streamer tracks produced in conductive plastic film during shots 70 and 71. Graphite fiber #2.

The electric field versus radial distance from the graphite fiber for shot 71 is shown in Figure 5-13 for the maximum radial voltage of 44 kV at the depth of the conductive sheet. For curve 2, the electric field is calculated by assuming a uniform cylindrical growth of the center rod whereas the electric field shown by curve 1 is the 1/r dependence for a center conductor of constant radius. Both calculations assume no field perturbation due to the conductive plastic sheet or propagation of the streamers. For the streamers that stopped at a radius of ~0.06 m the electric field calculated by the uniform Corona model was $\sim 3.5 \times 10^5$ V/m (curve 2) compared to a value of $\sim 1.1 \times 10^5$ V/m using a 1/r field dependence. The numbers on curve 1 of Figure 5-13 summarize the number of streamers that terminated at the radial distance shown.

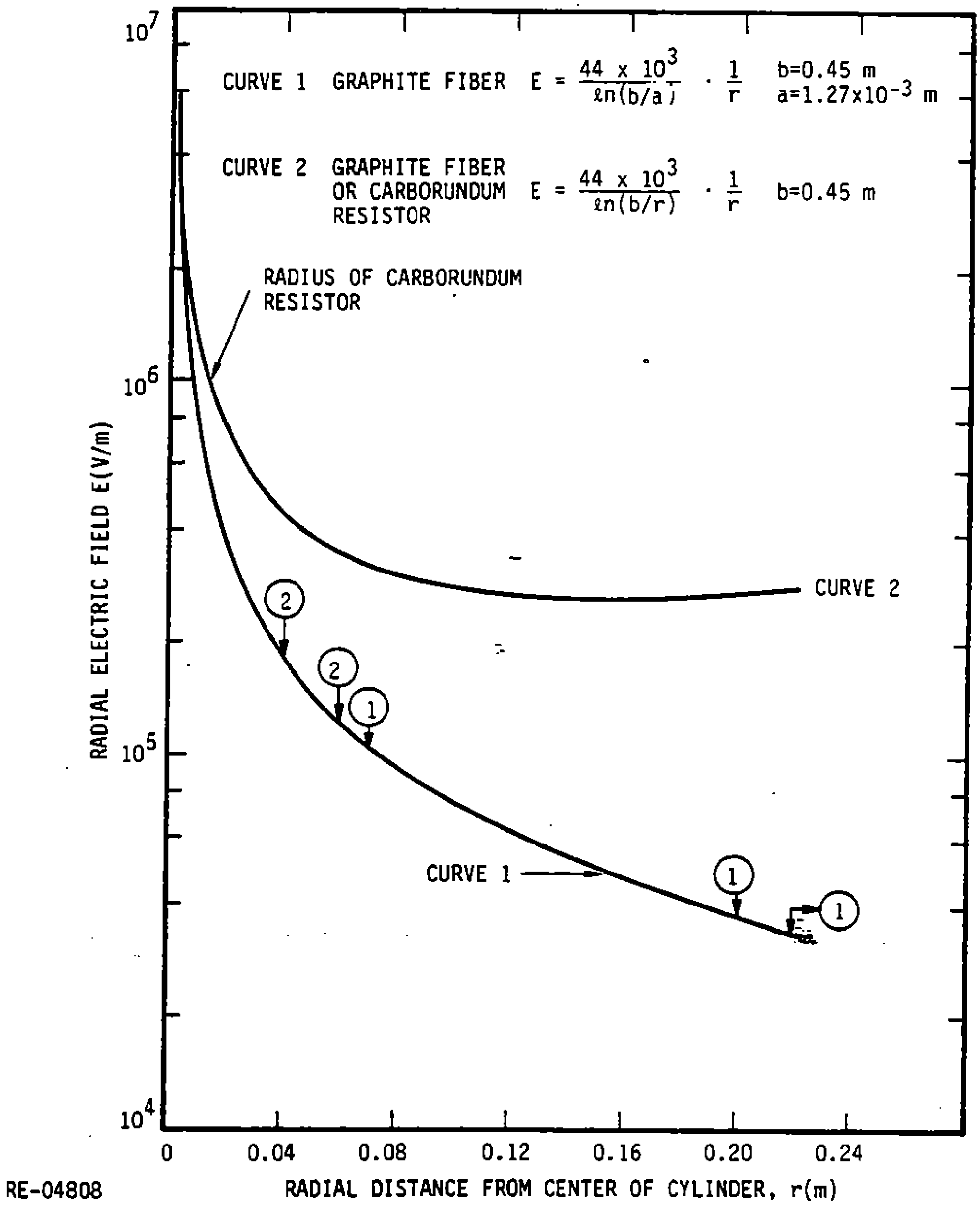

Figure 5-13. Electric field versus radial distance from graphite fiber resistor. Numbers on curve 2 indicate the number of streamers that terminated at the radial distance shown.

(2) Decoration of Conductive Plastic Film with Carborundum Resistor as the Center Resistive Rod--Two conductive plastic films identical to that described in the preceeding section were placed in the soil-filled cylinder during test shots for carborundum resistor #2. The two films were located 0.2 to 0.6 m below the top of the carborundum resistor. These conductive sheets were exposed to multiple shots where the maximum radial electric field experienced by the upper and lower plastic films was 1 x 10^6 V/m and 7.3 x 10^5 V/m, respectively.

The electric field versus radial distance for these peak fields is shown in Figure 5-14. Again, the numbers on the two curves indicate the number of streamers that stopped at the radial distance shown.

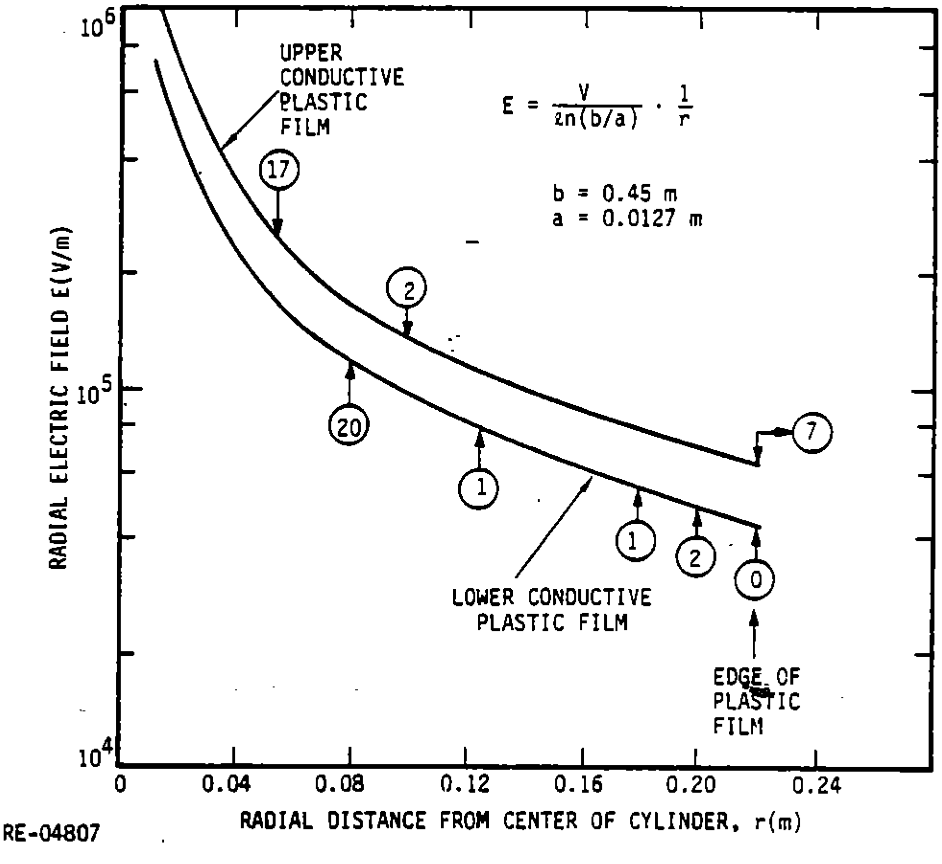

Figure 5-14. Maximum radial electric field for upper and lower conductive plastic films. Carborundum resistor #2. The numbers on the curves indicate the number of streamers that terminated at the radial distance shown.

For the upper conductive film approximately 7 streamers traversed the 0.22 m radius of the film and presumably attached to the outer cylinder. A total of 17 streamers terminated at a radius of ~0.07 m. As with the graphite fiber shots the shorter streamers terminated in branches. The streamers that traversed the conductive film and presumably attached to the outer cylinder had many side branches that were nearly normal to the axis of the streamer. One of these streamers had 8 side branches ~0.02 meters long. The length of the side branches did not decrease with increasing radial distance. Photographs of some of the streamers produced in this conductive film are shown in Figure 5-15. The upper photo shows a side branch streamer 0.02 m long that terminates on a main streamer that extends from the surface of the carborundum resistor to the edge of the conductive film. The width of the main streamer is about 1 to 1.5 mm compared to ~0.5 mm for the side branch. Approximately 1 cm out from the main streamer the side branch streamer disappears for ~4 mm and then reappears.

The middle photograph shows a streamer that propagated to a radius of ~0.07 m and then branched for ~0.013 m before terminating.

The lower photographs shows two main streamers that traversed the 0.22 m radius film. These streamers maintained a nearly constant separation distance of ~0.01 m.

The number of streamers and the radial distance at which they stopped for the lower conductive plastic film is also summarized in Figure 5-14. For this film the majority of the streamers stopped at a radial distance of ~0.08 m and none traversed the entire 0.22 m radius of the conductive film. This lower film also had numerous pinholes out to a radius of 0.04 to 0.05 m. This region, however, exhibited some thermal damage and it is not possible to rule out the possibility that the pinholes may result from thermal effects rather than axial streamers. The thermal damage observed, however, appears greater than expected for the calculated maximum temperature rise of 20°C (Table 5-5) for carborundum resistor #2.

4. PRESENTATION OF DATA

Table 5-3 summarizes the voltage and circuit parameters for the shots with the carborundum resistor #1, graphite fiber #2, and carborundum resistor #2. Also listed in this table are the measurement objectives [i.e., R (radial), or R (radial) plus R (axial)], the target radial electric field close to the resistor, the axial electric field, and comments whether or not attachment of a radial streamer from the resistor to the outer can occurred. For all of the shots in the table, time histories of the measured voltages

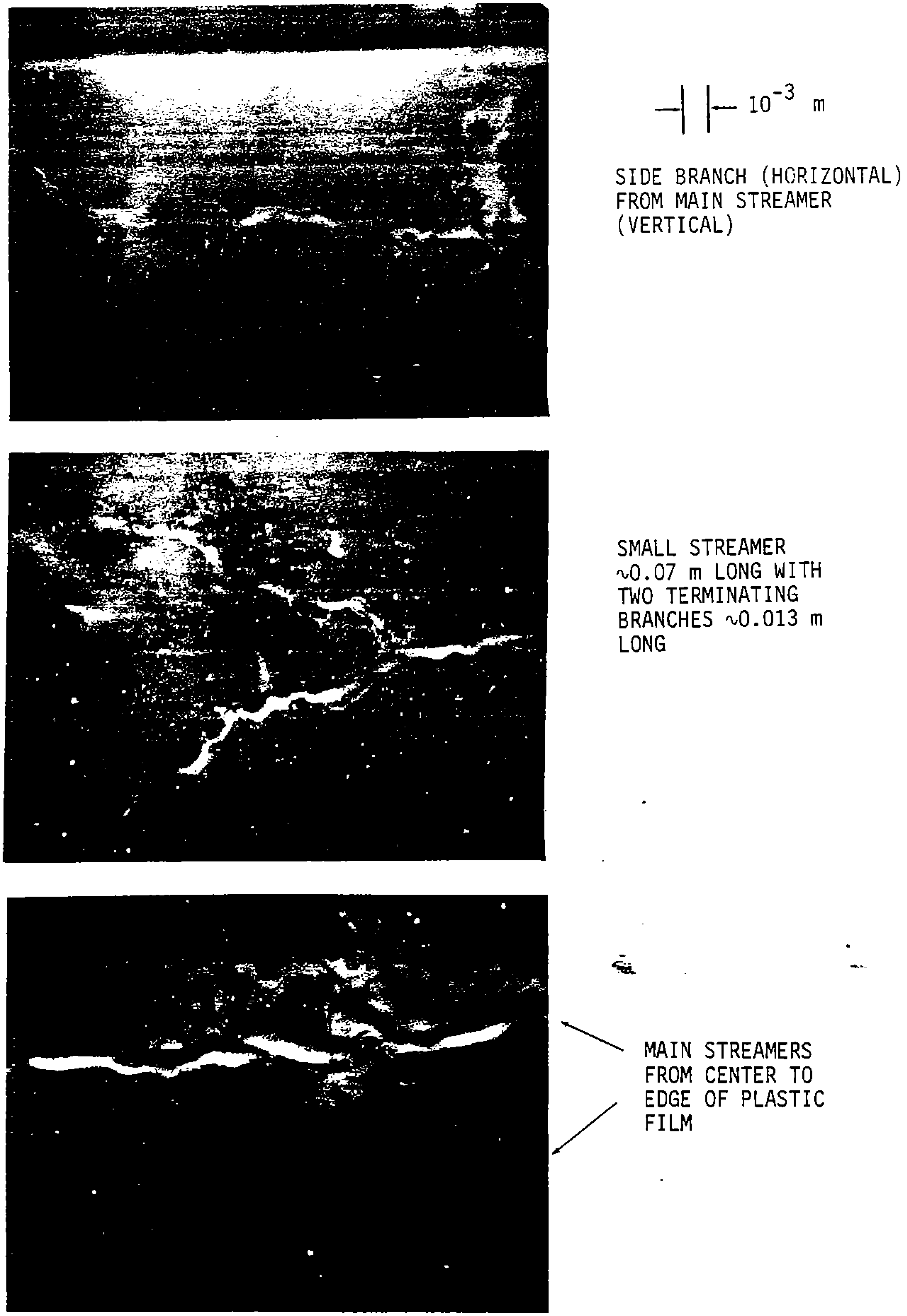

SIDE BRANCH (HORIZONTAL) FROM MAIN STREAMER (VERTICAL)

SMALL STREAMER ~0.07 m LONG WITH TWO TERMINATING BRANCHES ~0.013 m LONG

MAIN STREAMERS FROM CENTER TO EDGE OF PLASTIC FILM

RE-04809

Figure 5-15. Photograph of streamer tracks in conductive plastic film. Carborundum resistor #2.

and currents and calculated radial and axial fields and resistances are given in Appendix A. See Figures 5-6 through 5-11 for the definition of the voltages and currents. The designations A and B on the runs in Appendix A indicate different scope sweep speeds for the same shot. Time zero on the curves corresponds to the scope trigger time, slightly before the first pulser fires. Thus, the time histories for a given shot are time-correlated.

For the radial-only shots (i.e., bottom of center resistor open), time histories are given for the two voltages (V_1 and V_2), one current (I_1, since $I_o = 0$ and I_2 should equal I_1), the maximum radial electric field E_{rad} (assuming no corona effects), and the radial resistance (R_{rad}). The latter two quantities are calculated from the equations:

$$E_{rad} = \frac{(V_1 - V_2)}{a \, \ell n \, (b/a)} \quad , \qquad (5\text{-}1)$$

where b is the radius of the outer can (≈0.45 m) and a is the radius of the center resistor (1.27 cm for the carborundum rod and 0.127 cm for the graphite fiber), and

$$R_{rad} = \frac{(V_1 - V_2)}{I_1} \quad . \qquad (5\text{-}2)$$

The calculated values of E_{rad} probably never actually occur except at very low voltages, due to corona effects, as discussed in Section V.5.a. The axial electric field and impedance cannot be determined from these shots because the bottom of the rod is floating.

For the combined radial and axial shots, time histories are given for the two voltages, all three currents, E_{rad} calculated by Eq. 5-1, and $E_{ax} = V_1/0.8$ m, since the bottom of the center resistor is grounded. Since, in the combined voltage shots, there is a voltage gradient along the center resistor from V_1 at the top to 0 at the bottom, E_{rad} is the theoretical field at the top of the rod, neglecting corona effects.

For these combined shots, four quantities which have the units of resistance are calculated and plotted in Appendix A. One, called R_{rad}, is calculated from the equation:

$$R_{rad} = \frac{0.5 \times V_1 - V_2}{I_2} \qquad (5\text{-}3)$$

Table 5-3(a). Shot Summary--Carborundum Resistor #1 (65 Ω)

Shot	Axial Pulser Positive	Radial Pulser Negative	E (V/m) Measurement	E (V/m) Radial	E (V/m) Axial	Configuration	Attachment to Cylinder
16	20 kV	0	R (radial)	3.8×10^5	~0	Resistor open, cylinder grounded	No
17	20 kV	0	R (radial)	3.2×10^5	~0	Resistor open, cylinder 40 Ω to ground	No
18	40 kV	0	R (radial)	6.3×10^5	~0	Resistor open, cylinder 40 Ω to ground	No
19	40 kV	0	R (radial)	6.3×10^5	~0	Resistor open, cylinder 40 Ω to ground	No
20	~60 kV	0	R (radial)	1×10^6	~0	Resistor open, cylinder 40 Ω to ground	Yes (~ 95 μs)
21	~20 kV	~40 kV	R (radial)	1×10^6	~0	Resistor open, cylinder 40 Ω to ground	Yes (~ 120 μs)
23	20 kV	40 kV	R (radial), R (axial)	1×10^6	1.9×10^4	Resistor grounded, cylinder 40 Ω to (-) pulser	Yes (~ 130 μs)
24	20 kV	Did not fire	-- R (axial)	2×10^5	1.9×10^4	Resistor grounded, cylinder floating	No
25	20 kV	~29 kV	R (radial), R (axial)	8.5×10^6	1.8×10^4	Resistor grounded, cylinder 40 Ω to (-) pulser	Yes (~ 290 μs)
26	20 kV	~20 kV	R (radial), R (axial)	6.5×10^5	1.7×10^4	Resistor grounded, cylinder 40 Ω to (-) pulser	No
27	~40 kV	~20 kV	R (radial), R (axial)	9×10^5	3×10^4	Resistor grounded, cylinder 40 Ω to (-) pulser	Yes (~ 225 μs)

Pulser voltages were target values.

Actual voltages are somewhat smaller due to pulser pre-fire.

E(axial) and E (Radial) are measured values.

Table 5-3(b). Shot Summary--Graphite Fiber #2 (~10 Ω)

Shot	Axial Pulser Positive	Radial Pulser Negative	E (V/m) Measurement	E (V/m) Radial	E (V/m) Axial	Configuration	Attachment to Cylinder
40	20 kV	0	R (radial)	2.7×10^6	~0	Resistor open, cylinder 40 Ω to ground	No
41	40 kV	0	R (radial)	5.4×10^6	~0	Resistor open, cylinder 40 Ω to ground	No
		Pulser Capacitor Failed. Resume Exp. 3/8/82					
48	40 kV	0	R (radial)	5.4×10^6	~0	Resistor open, cylinder 40 Ω to ground	No
50	50 kV	0	R (radial)	6.7×10^6	~0	Resistor open, cylinder 40 Ω to ground	No
53	~50 kV	0	R (radial)	6.7×10^6	~0	Resistor open, cylinder 40 Ω to ground	No
55	~60 kV	0	R (radial)	8×10^6	~0	Resistor open, cylinder 40 Ω to ground	Yes (~50 μs)
62	20 kV	0	R (radial), R (axial)	2.7×10^6	2.2×10^4	Resistor grounded, cylinder 40 Ω to ground	No
63	20 kV	19 kV	R (radial), R (axial)	5.2×10^6	2.2×10^4	Resistor grounded, cylinder 40 Ω to (-) pulser	No
65	20 kV	38 kV	R (radial), R (axial)	7.7×10^6	2.2×10^5	Resistor grounded, cylinder 40 Ω to (-) pulser	Yes (~260 μs)
67	~30 kV	38 kV	R (radial), R (axial)	9×10^6	3.3×10^4	Resistor grounded, cylinder 40 Ω to (-) pulser	Yes (~55 μs)
69	~30 kV	38 kV	R (radial), R (axial)	9×10^6	3.3×10^4	Resistor grounded, cylinder 40 Ω to (-) pulser	Yes (~55 μs)
70	~40 kV	19 kV	R (radial), R (axial)	8×10^6	4.4×10^4	Resistor grounded, cylinder 40 Ω to (-) pulser	?
71*	~60 kV	19 kV	R (radial), R (axial)	$\sim 1 \times 10^7$	$\sim 6 \times 10^4$	Resistor grounded, cylinder 40 Ω to (-) pulser)	Yes (~80 μs)

*Resistor failed during shot 71.

Conductive plastic in place for shots 70 and 71.

Pulser voltages and E (radial) and E (axial) are target values. Actual values may be smaller (10-30%) due to pulser pre-fire and voltage drop across 40 Ω resistor in series with cylinder and ground or radial pulser.

Table 5-3(c). Shot Summary--Carborundum Resistor #2

Shot	Axial Pulser Positive	Radial Pulser Minus	E (V/m) Measurement	Configuration
72	20 kV	0	R (radial)	Resistor open, cylinder 40 Ω to ground
74	40 kV	0	R (radial)	Resistor open, cylinder 40 Ω to ground
77	50 kV	0	R (radial)	Resistor open, cylinder 40 Ω to ground
78	60 kV	0	R (radial)	Resistor open, cylinder 40 Ω to ground
81	60 kV	0	R (radial)	Resistor open, cylinder 40 Ω to ground
82	60 kV	0	R (radial)	Resistor open, cylinder 40 Ω to ground
83	60 kV	0	R (radial)	Resistor open, cylinder 40 Ω to ground
85	20 kV	0	R (radial), R (axial)	Resistor open, cylinder 40 Ω to ground
87	20 kV	19 kV	R (radial), R (axial)	Resistor open, cylinder 40 Ω to radial pulser
88	20 kV	38 kV	R (radial), R (axial)	Resistor open, cylinder 40 Ω to radial pulser
90	40 kV	19 kV	R (radial), R (axial)	Resistor open, cylinder 40 Ω to radial pulser
94	40 kV	19 kV	R (radial), R (axial)	Resistor open, cylinder 40 Ω to radial pulser
95	60 kV	0	R (radial), R (axial)	Resistor open, cylinder 40 Ω to ground

The rationale for Eq. 5-3 is that, before any streamer attachment, the radial resistance of the soil is considerably larger than the axial resistance of the center resistor. Therefore, the radial current is relatively small so the current along the center resistor is fairly constant along its length. Therefore, the average voltage between the center resistor and the can is approximately the numerator of Eq. 5-3. Thus, Eq. 5-3 gives the approximate radial resistance before arc attachments. An analysis which considers the distributed radial current along the center resistor is given in Section V.6. Eq. 5-3 breaks down when arc attachments occur because the radial current is usually no longer small compared to the axial current, and the axial current is not uniform along the length of the center resistor. If one were interested in the impedance of the radial arc after attachment, it would be more accurate to use the equation:

$$R_{arc} = \frac{V_1 - V_2}{I_2} \tag{5-4}$$

since the arc probably occurs near the top of the rod where the radial potential difference is largest.

The other three resistances that are plotted in Appendix A for combined axial-radial pulsers are V_1/I_1, V_1/I_o, and $V_1/[0.5\ (I_1 + I_o)]$. These quantities are three approximations to the axial resistance of the resistor/soil combination. Before arc attachment, when I_2 is much less than I_1 and I_o, these three resistances should be nearly equal. To be consistent with the effective radial resistance given by Eq. 5-3, $V_1/[0.5\ (I_1 + I_o)]$ should give the best representation of the axial resistance, and this quantity is used in subsequent analyses of the variation of the axial resistance with pulser voltages (Section V.5.b). However, after an attachment occurs, a better measure of the axial resistance would be V_1/I_o.

On one shot (#24), the radial pulser did not fire so the outer can was floating for this shot. Therefore, the only time histories that are plotted in Appendix A for this shot are V_1, I_1, and V_1/I_1.

On the final soil shot (#95), some of the scopes failed and a complete set of voltage/current traces was not obtained at any one scope speed. The data that was obtained and the three calculated axial resistances are given in Appendix A.

A word of warning is required in regard to the shots with carborundum resistor rod #2 (shots 72 through 95). Unfortunately, there is a discrepancy between the measured currents and voltages for these shots and the known or estimated resistances of the external loads, the center resistor, and the soil. During the test sequence, this discrepancy was noted but a careful check of all the electrical grounds and current return paths did not disclose any non-standard operation. However, in retrospect, it is possible that one of the measuring instruments, in particular V_2, could have been malfunctioning and not have been detected in the diagnostic check.

To illustrate the problem, consider, for example, the time histories for shot #88A (Figure A-53, Appendix A). Before the radial pulser fires (at t ≅ 0.09 ms), $V_1 \cong 18$ kV, $I_1 \cong I_o$, $I_2 \cong 0$, and $R_{axial} \cong 60\ \Omega$, all of which are reasonable and self-consistent for the particular shot parameters. However, during this time the instrumentation for V_2 indicated a voltage that was increasing from about 21 to 27 kV, that is, greater than V_1. With the circuit setup used in these tests, there is no known way for V_2 to be greater than V_1. Based on Eq. 5-3, since I_2 is 0 before the radial pulser fires (outer can is floating), the numerator of Eq. 5-3 has to be essentially 0, so V_2 should be about one half of V_1. This relationship before the radial pulser fires was verified approximately with carborundum resistor #1 (see, for example, shots 23, 25, 26, while shot 27 gave a smaller value of V_2) and for the graphite fibers (see, for example, shot #70; for the other combined shots with graphite, the two pulsers fired simultaneously).

Another indication of the problem is a lack of consistency for these runs between the measurements of the voltage on the can (V_2), the expected voltage on the radial pulser [$V_R(t)$] and the known resistance between the can and the radial pulser (40 Ω). The details of this check can be explained with the aid of Figure 5-16.

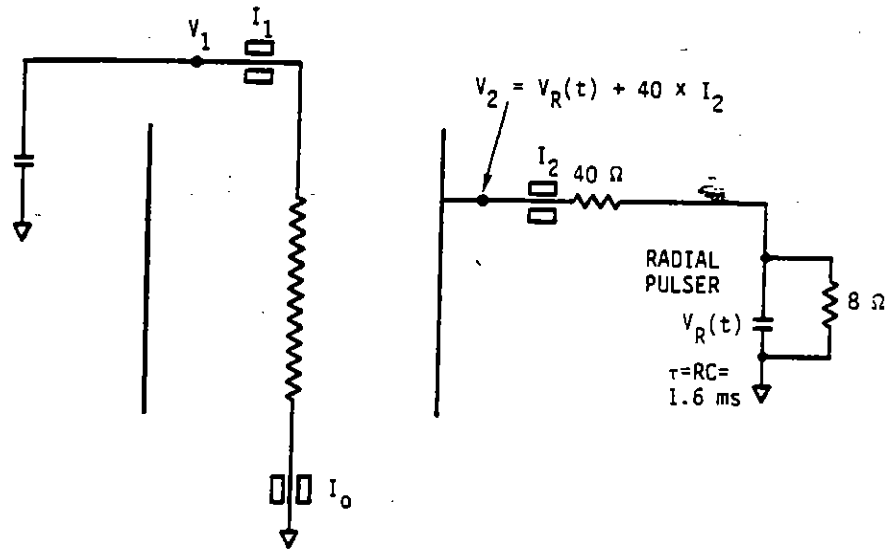

RE-04790

Figure 5-16. Circuit to show discharge path for radial pulser.

The discharge path for the radial pulser is through the 8 Ω charging resistor that shunts the pulser stage(s) and also through the 40 Ω resistor plus the soil resistance (≈ 200 Ω) between the center resistive rod and the outer metal cylinder. The measured time constant for the decay of the radial pulser was 1.6 x 10^{-3} s. The time-dependent pulser voltage [$V_R(t)$] is then

$$V_R(t) = V_o e^{-t/1.6\times10^{-3}} \tag{5-5}$$

where V_o is the charging voltage for the radial pulser and t is the elapsed time after the radial pulser is fired. The voltage of the metal cylinder V_2 (Figure 5-16) is then

$$V_2 = V_o e^{-t/1.6\times10^{-3}} + 40 \times I_2(t) \tag{5-6}$$

The values for V_o are given in Table 5-4 for shots 72 through 92 and the time dependent I_2 values for these shots are given in Appendix A.

Table 5-4. Initial Voltage for Radial Pulser

Shot	Initial V_o Radial Pulser Voltage
72	0
74	0
77	0
78	0
81	0
82	0
85	0
87	-19 kV
88	-38 kV
90	-19 kV
94	-19 kV
95	0

To test the consistency of the above method for calculating V_2, the calculated and measured values of V_2 are compared below for three graphite fiber shots prior to the malfunction of the V_2 voltage monitor. For shot #64,

$$I_2(t = 96\ \mu s) = 240\ \text{A}$$

$$V_{2(\text{measured})} = -26\ \text{kV}$$

The calculated value of V_2 at 96 μs is

$$V_2 = -38 \times 10^3 \, e^{-(96\times10^{-6}/1.6\times10^{-3})} + 40 \times 240$$

$$= -35.8 \times 10^3 + 9.6 \times 10^3$$

$$= -26.2 \text{ kV}$$

in good agreement with the value measured by the voltage monitor V_2. A similar calculation for shot 69 and shot 71, which was the last graphite fiber shot prior to installation of carborundum resistor #2, gave the following comparison:

Shot	V_o	t	I_2	V_2(measured)	V_2(calculated)
69	-38 kV	49 μs	320 A	-24 kV	-25.2 kV
71	-19 kV	80 μs	164 A	-12 kV	-11.5 kV

However, application of this check method to the data for shots 72 through 95 gave poor correlation. For example, on shot #88A just before radial attachment at t ≅ 0.16 ms (= 0.07 ms after the radial pulser fired), $I_2 \cong 280$ A, and $V_2 \cong -14$ kV. For this shot, V_o was -38 kV. Therefore, V_2 should have been $-38 \times 10^3 \exp(-0.07/1.6) + (280 \text{ A})(40\ \Omega) = -25.2$ kV, in significant disagreement with the measured V_2.

As a result of this disagreement, any analysis involving these shots (except for the original calculated time histories in Appendix A) have ignored the measured values of V_2 and have used the calculated values for V_2 [$= V_R(t) + I_2 \times 40$] after the radial pulser fires. Unfortunately this method cannot be used before the radial pulser fires because the 40 Ω is changed to essentially infinity.

5. ANALYSIS OF DATA

The procedure that has been used to look for nonlinear conduction effects through the soil was to first analyze the data for the radial-only pulses for both the carborundum rods and the graphite fibers and then to use those results to try to deduce nonlinear axial effects from the combined-pulser shots. In this latter step, an attempt is made to separate out the change in resistance of the center resistor just due to IR heating.

a. **Radial-Only Shots**--When only a radial voltage is applied between the center resistor (either graphite or carborundum) and the outer can (bottom of resistor open and can grounded), the measured radial resistance often decreases for a time after the application of the pulse. If the radial field is small enough so that a streamer does not propagate from the resistor to the can, the radial resistance goes through a minimum, and then increases again as the pulser voltage decays away. The magnitude of the resistance minimum decreases with increasing radial voltage. In an attempt to quantitatively explain these results, the resistance-voltage time histories have been analyzed using the following model.

In these models it is assumed that the conductivity of the soil is uniform at its low-field value ($\sigma = 3 \times 10^{-3}$ S/m in these experiments) outside a radius r_c around the center resistor. For radii $r > r_c$, the radial electric field varies as 1/r, since the geometry is assumed to be cylindrically symmetric. Thus,

$$E(r) = \frac{r_c E(r_c)}{r} \quad , \tag{5-7}$$

where $E(r_c)$ is the radial electric field at r_c.

For $a < r < r_c$, where a is the radius of the center resistor, it is assumed that the conductivity is increased by some corona/avalanche process so that the radial electric field no longer has to vary as 1/r in this region to provide continuity of radial current. Two different assumptions are made for E(r) in this region. In the first case, it is assumed that the radial conductivity inside r_c is so large that $E(r < r_c)$ is essentially zero. Since there are some valid technical reasons for questioning this assumption (discussed later), a second analysis was also performed using the assumption that, for $a < r < r_c$, the radial electric field E(r) is constant at the value $E(r_c)$ at the edge of the corona region. For both of these models, it should be remembered that an increased radial electrical conductivity does not necessarily imply an increased axial conductivity since the increased radial conductivity could be due to radial streamers which might not noticeably affect the axial conductivity.

Since, for the first model, E(r) is 0 out to r_c and is given by Eq. 5-7 for $r \gtrsim r_c$, the voltage between the center resistor and the outer can (at radius b) is

$$V = r_c \, E(r_c) \, \ln (b/r_c) \tag{5-8}$$

The radial current I_r is constant at every radius and is given by

$$I_r = 2\pi r_c \ell E(r_c)\sigma \tag{5-9}$$

where ℓ is the length of the cylinder (≈ 0.8 m).

The radial resistance is

$$R \equiv \frac{V}{I_r} = \frac{\ell n(b/r_c)}{2\pi\sigma\ell} \tag{5-10}$$

Since everything on the right-hand side of Eq. 5-10 is known except r_c, Eq. 5-10 can be solved for r_c, which can then be calculated for every measured value of R during a shot, up to the time when attachment of a radial streamer occurs from the center resistor to the outer can, at which time this model becomes invalid. Using these values of r_c and the appropriate measured values of V at each time step, the electric field $E(r_c)$ at the edge of the corona region can then be calculated using Eq. 5-8.

All of the experimental data for radial-only pulses with both the carborundum and graphite-fiber center resistors have been analyzed using the above model, and the radii r_c are plotted versus $E(r_c)$ in Figure 5-17. (For shots with carborundum resistor #2, the can voltages were calculated from I_2, as discussed in Section V.4.) To minimize the confusion in this figure, no data points are shown and some of the shots are grouped together as single curves. However, the scatter in the data for averaged shots was less than the distance to the nearest adjacent curve. In the following discussion, a major point to remember is that these curves contain the results for both the carborundum and graphite-fiber center resistors.

Although the curves in Figure 5-17 may appear confusing at first glance, there is a definite trend to the results. Curve 1 is for five carborundum shots (some with two sweep speeds) and one graphite shot, all with a radial voltage of 60 kV. For all of the curves in Figure 5-17, time starts at their right-hand ends and proceeds to the left. All of the shots in curve 1 developed a radial attachment before the radial resistance reached its minimum. When the attachments occurred, the plotting was terminated, at around $r_c \cong 0.07$ m to 0.10 m for this curve.

Curves 2 and 3 are for one carborundum and two graphite-fiber shots, all with a radial voltage of 50 kV. The difference between these shots and those in curve 1 is that these shots did not develop a radial attachment, and the radial resistance went through a minimum and then increased at late times. Shortly after the radial resistance passed its minimum, the calculated values of r_c ceased to increase, and then decreased, sometimes by almost an order of magnitude. For curves 2 and 3, the calculated $E(r_c)$ went to a minimum at around 2×10^5 V/m and then increased slightly as r_c decreased. However, curve 3A, which is just a different sweep speed for one of the shots in curve 3, only went to a minimum of about 3×10^5 V/m. Obviously, the results from the two sweep speeds for the same shot should agree. At the present time, the source of this discrepancy is not known but it could possibly be related to the calculation of V_2 from I_2, which was used for all the shots with carborundum resistor #2, which included shot 77B, which is curve 3A.

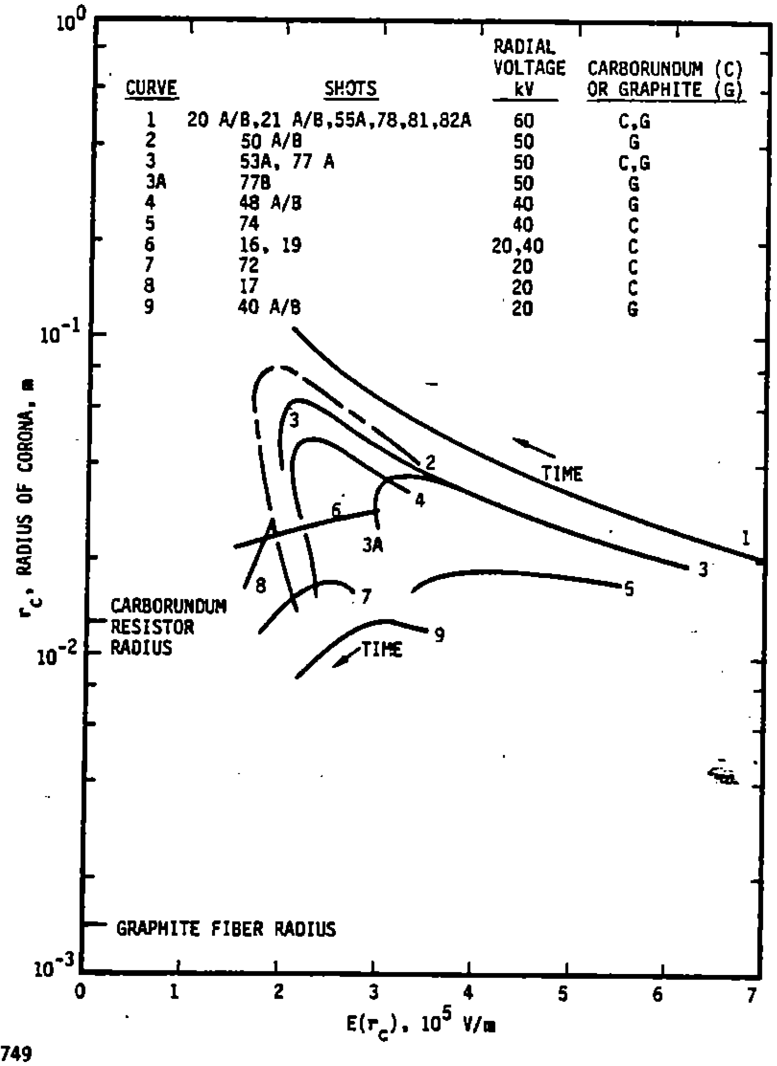

RE-04749

Figure 5-17. Calculated r_c versus $E(r_c)$ for $E(r < r_c) = 0$.

Curve 4 is a graphite-fiber shot with a radial voltage of 40 kV. It is similar to curves 2 and 3, and its minimum $E(r_c)$ is again about 2×10^5 V/m.

Curve 5 is for a shot with carborundum resistor #2 and a pulser voltage of 40 kV. At larger values of $E(r_c)$, curve 5 is in reasonable agreement with the extension of curve 4 to larger electric fields. However, at lower values of $E(r_c)$, curve 5 deviates from the trend of the previous curves. Again, this shot, as well as the one for curve 7, could be subject to the uncertainty of calculating V_2 from the current I_2.

The remaining curves are carborundum and graphite shots at 20 and 40 kV.

The results for one fiber shot (no. 41) are not shown on the figure because the results are somewhat different from the other curves and there is some indication of a significant inconsistency between two scope speeds. At early times, this curve agreed with curve 4, which is reasonable because they are both for 40 kV. The fast scope for this run (shot 41A) went to a minimum $E(r_c) \cong 2 \times 10^5$ V/m before the scope trace ended. However, on the slower sweep speed (no. 41B), the minimum $E(r_c)$ was only about 3×10^5 V/m, and then, after the curve curled over, the values of $E(r_c)$ increased back to about 6×10^5 V/m at $r_c \cong 0.005$ m. The reason that this result is viewed with suspicion is that the minimum radial resistance for shot 41A was about 150 Ω whereas, for shot 41B, it was about 170 Ω. A shift in the resistance curve for shot 41B of 20 Ω would be enough to account for its different behavior in $E(r_c)$ versus r_c.

Another interesting item (not shown in Figure 5-17) is that, on shot 53 (curve 3), part of the capacitor bank prefired to about 18 kV and then it jumped to its normal voltage of about 40 kV. During the period when the voltage was 18 kV, the calculated pairs $[r_c, E(r_c)]$ fell in the region of (0.012 m, $\approx 2.7 \times 10^5$ V/m), that is, almost coincident with curve 9 which was for a graphite fiber shot at 20 kV. When the voltage jumped to 40 kV, the calculated pairs $[r_c, E(r_c)]$ jumped to the right-hand end of curve 3 and then traced out that curve with increasing time.

From the above results, the following appears to be what happens. When the pulser voltage is first applied, the corona radius (r_c) starts to increase, and $E(r_c)$ decreases accordingly, consistent with the applied voltage. When $E(r_c)$ gets to about 2×10^5 V/m, if a radial attachment does not occur, $E(r_c)$ remains about constant while r_c decreases with the decreasing voltage.

The major unexplained feature about the curves in Figure 5-17 is why the early-time portions of the curves appear to shift to smaller values of r_c [for a given $E(r_c)$] for smaller pulser voltages. If this effect is real, it could be a time effect. In other words, it takes time for the electric field to ionize the air or water in the corona region and, for smaller pulser voltages, the corona region might not grow as rapidly.

Although the above model has considerable appeal due to its mathematical simplicity, there are some valid objections to it. First, there is evidence from the radial voltage profiles that were measured by MRC in another set of cylindrical experiments (Ref. 5.3) that the radial electric field in this region is not always zero. Secondly, there probably has to be some electric field in this region to maintain the ionization since the total radial current is not particularly large before radial attachments occur.

Arguments can be given for several different variations for E(r) within this region, and therefore for $\sigma(r)$ to satisfy continuity of radial current. One model that is being pursued by Prof. Robert Carlile of the University of Arizona assumes that the radial conductivity is constant for $r < r_c$, but at a larger value than the low-field value which is assumed for $r > r_c$. With this assumption, E(r) varies as 1/r inside the corona but at a different rate than the 1/r variation outside the corona. Another model, which is the one used below, assumes that E(r) inside the corona radius r_c is constant at the value of the electric field at the corona radius, $E(r_c)$, while outside the corona E(r) goes into the 1/r dependence, given by Eq. 5-7. With this assumption, Eq. 5-8 has to be modified to

$$V = E(r_c)\ [r_c - a + r_c\ \ell n\ (b/r_c)] \qquad (5\text{-}8a)$$

Since Eq. 5-9 is still valid, Eq. 5-10 is modified to

$$R \equiv \frac{V}{I_r} = \frac{[1 - a/r_c + \ell n\ (b/r_c)]}{2\pi\ell\ \sigma} \qquad (5\text{-}10a)$$

Unfortunately, Eq. 5-10a cannot be solved in closed form for r_c as a function of R, as Eq. 5-10 could be. However, it can be solved by a straightforward iteration on a computer. This has been done for the radial-only voltage shots used in Figure 5-17. The resulting values of r_c were then substituted into Eq. 5-8a, along with the appropriate values of V, to obtain $E(r_c)$. The resulting curves of r_c versus $E(r_c)$ are shown in Figure 5-18.

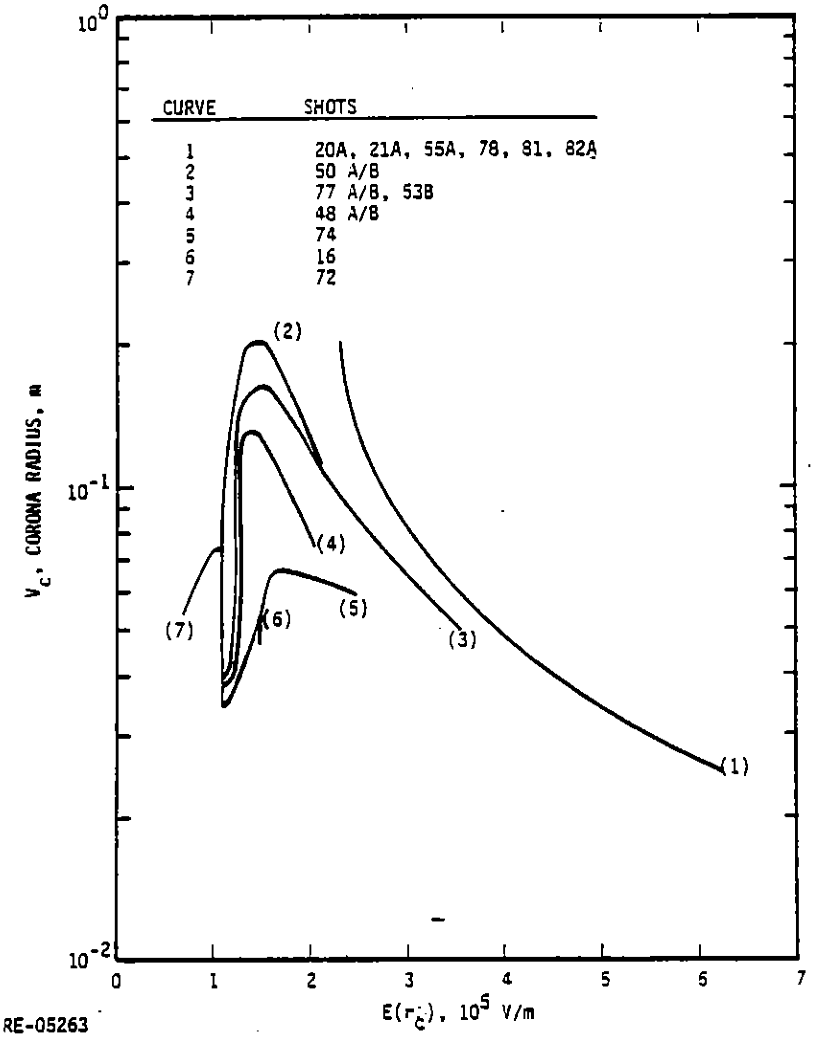

Figure 5-18. Calculated r_c vs. $E(r_c)$ for $E(r < r_c) = E(r_c)$

The curves for the different shots in Figure 5-18 are grouped in the same manner as in Figure 5-17. The scatter between the calculated points for the shots represented by any one curve in Figure 5-18 was again fairly small, although slightly larger for curve 1 than in Figure 5-17. The general characteristics of the curves in Figure 5-18 are similar to those in Figure 5-17 although the portions of the curves to the right of the peaks are steeper in Figure 5-18, the calculated maximum values of r_c are about twice as large, and the minimum value of $E(r_c)$ is about 1 x 10^5 V/m compared to about 2 x 10^5 V/m in Figure 5-17. Without some additional information, none of these three differences provides a conclusive clue as to which model might be more nearly correct. The steepness of the curves is a measure of how rapidly the corona radius grows with time, but we have no independent knowledge of what this rate should be. Since the minimum values of $E(r_c)$ in both Figures 5-17 and 5-18 are considerably less than the nominal breakdown field for atmospheric air ($\approx 3 \times 10^6$ V/m for uniform DC fields, Ref. 5.4), one might be inclined to favor the model with $E(r < r_c) = 0$ since it yields the larger minimum value for $E(r_c)$. However, since it is not definite at this time that air breakdown is the determining factor in producing the radial conductivity and since the degree of field enhancement around the jagged soil particles is unknown, there is little to choose between the two models on the basis of the minimum $E(r_c)$. Similarly, one might question the maximum calculated values of r_c ($\cong$ 0.2 m) in Figure 5-18, since the commonly quoted electrical instability limit for a coaxial cylindrical geometry is $r_c = b/e$ ($\cong$ 0.17 m for these tests). However, this criterion is valid only when the corona is a perfect conductor, that is, $E(r < r_c) = 0$ as in the first model. If one solves Eq. 5-8a for $E(r_c)$ and sets its differential with respect to r_c to zero, with V = constant, the electrical stability limit that is applicable to the model with $E(r < r_c) = E(r_c)$ is $r_c = b$. Therefore, the relatively large values of r_c in Figure 5-18 do not violate the appropriate instability criterion for the model used for that figure.

In summary, at the present time we have no firm basis for choosing one of these models over the other. However, perhaps fortunately, both models yield the same general picture of a corona that grows to a radius consistent with some minimum breakdown field (if a radial attachment does not occur) and then the radius decreases with an approximately constant value of $E(r_c)$ as the pulser voltage decays away.

b. <u>**Combined-Voltage Shots**</u>--If a radial electric field produces a region of high electrical conductivity adjacent to the center resistor, as implied in the models discussed in Section V.a, one would expect a reduced axial, as well as radial, resistance provided that the increased radial conductance is not produced by small radial streamers which do not interact significantly with their adjacent neighbors. To look for an enhanced axial conductance as a function of radial electric field, the time histories of the axial resistance and the maximum radial electric field near the center resistor, assuming no corona effects, are replotted for direct comparison in Figures 5-19 through 5-23 for both the carborundum and graphite fiber combined-pulser shots. To minimize confusion, the curves are terminated when and if radial attachments occur because the models for the

5.4 A. S. Denholm, et al., 'Review of Dielectrics and Switching,' AFWL-TR-72-88, Feb. 1973.

radial and axial resistances break down at that time. The axial resistance that is used is $V_1/[0.5(I_1 + I_0)]$. Although this quantity should be a better estimate of the axial resistance than either V_1/I_1 or V_1/I_0 (at least up to attachment), it is not exact because it does not rigorously account for the variation of the radial and axial currents along the center resistor. In Section V.6, models which attempt to account for these distributed currents in the low-field regime are discussed and applied to some of the data. For the shots with the carborundum resistor #2, the radial electric field is based on calculated values for V_2, as discussed in Section V.4.

Figure 5-19 shows the resistance time histories for three graphite fiber shots, all with a nominal axial voltage of 20 kV and three radial pulser voltages (0, shot 62; -19 kV, shot 63; and -38 kV, shot 65). For all three shots, the axial resistance decreases from the pre-shot resistance ($\approx 10\ \Omega$) to about 7.5 Ω at $t \cong 0.3$ ms. For shots 62 and 63, the resistance then remains roughly constant to the maximum time for the graph. For shot 65, which had the largest radial voltage, attachment of a radial streamer occurred at $t \cong 0.29$ ms, so the curve was terminated at that time. If the decrease in resistance from 10 Ω to 7.5 Ω was due entirely to a parallel conduction path through the soil, the effective resistance of this path when the total resistance was 7.5 Ω would be $R_{soil} = [(7.5)^{-1} - (10)^{-1}]^{-1} = 30\ \Omega$. This value is a lower limit estimate on the parallel resistance through the soil for these conditions, and results for the carborundum resistors indicate a considerably larger parallel soil resistance. However, the fact that the three shots have essentially identical resistance curves in spite of different radial voltages from 0 to -38 kV suggests that the radial electric field is not the main cause of the decrease in resistance. Based on the results of the vaporization/restrike experiments with the same type of graphite fiber in Section IV, a more likely cause of resistance decrease is IR heating.

In Figure 4-43, the resistivity of the graphite fiber at very low values of action is about $2.3 \times 10^{-3}\ \Omega$-cm. Using an area of 0.018 cm^2 and a length of 80 cm, this resistivity corresponds to a resistance of 10.2 Ω, in good agreement with the measured initial resistance. This initial resistivity then decreases by more than a factor of two at an action of 1000 A^2-s/mm^4. In Table 5-5, the calculated energy deposited in the center resistor, the action (A^2-s), and the specific action (A^2-s/mm^4) are listed for both the carborundum and graphite fiber combined-voltage shots for selected times during the shots. For these calculations, the average axial current $[0.5(I_1 + I_0)]$ was used for both the energy and action, even after attachments occur. Thus, the quoted values of energy and action in the resistor after attachments occur are on the high side since not all of I_1

Figure 5-19a.

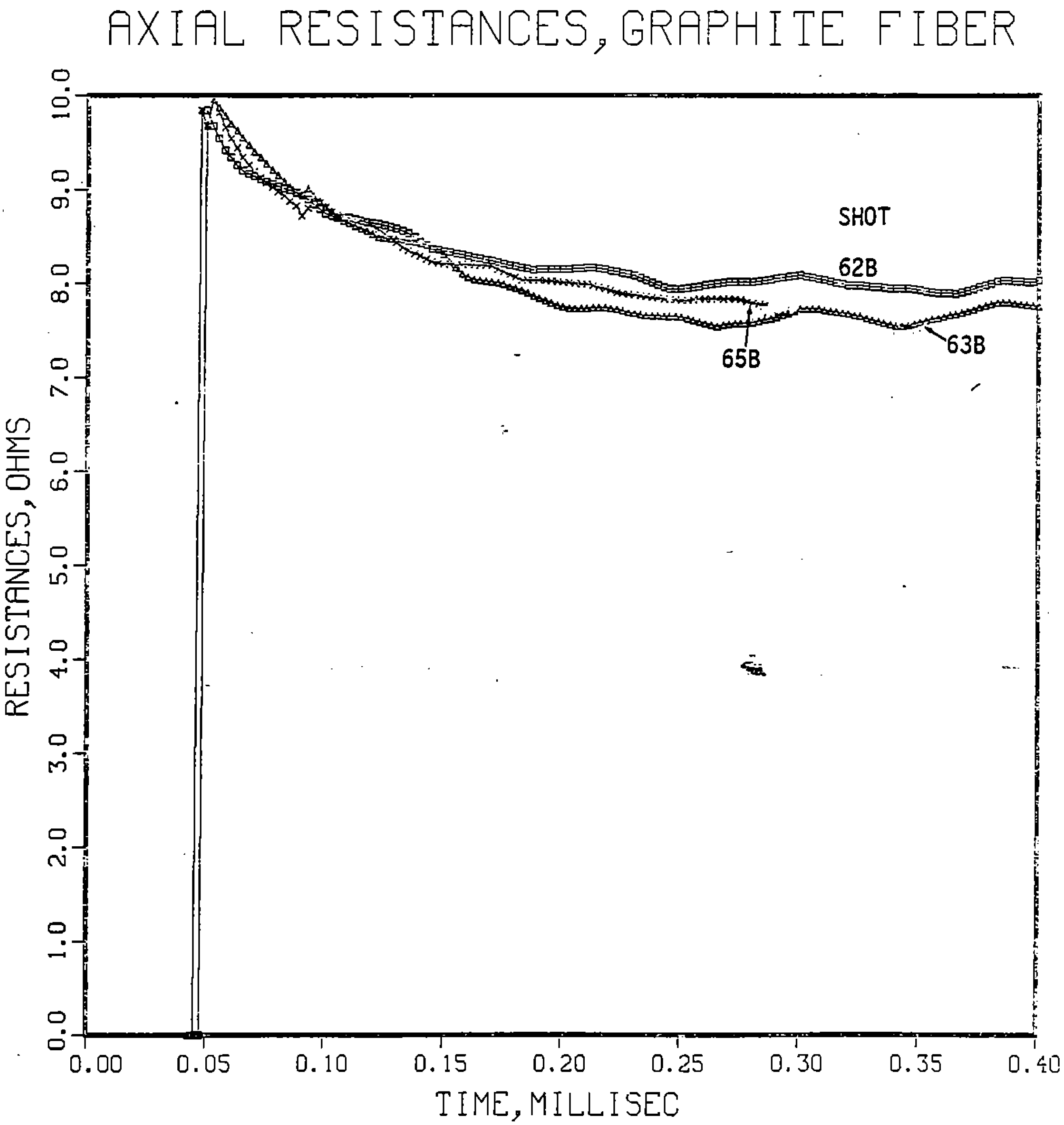
AXIAL RESISTANCES, GRAPHITE FIBER
RESISTANCES, OHMS
0.0
1.0
2.0
3.0
4.0
5.0
6.0
7.0
8.0
9.0
10.0
TIME, MILLISEC
0.00
0.05
0.10
0.15
0.20
0.25
0.30
0.35
0.40
SHOT
62B
65B
63B

Figure 5-19b.

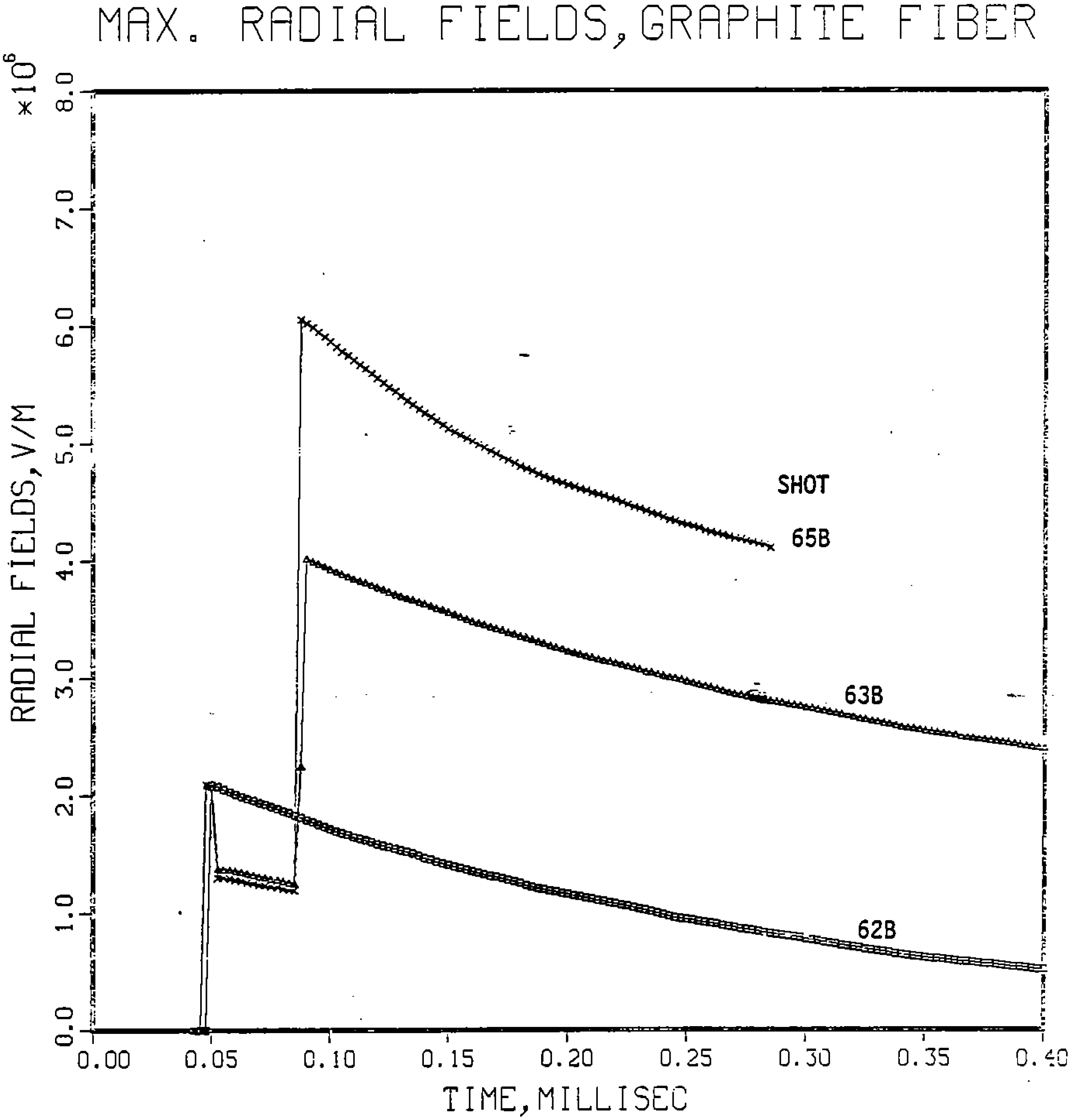
MAX. RADIAL FIELDS, GRAPHITE FIBER
RADIAL FIELDS, V/M
*10^6
0.0
1.0
2.0
3.0
4.0
5.0
6.0
7.0
8.0
TIME, MILLISEC
0.00
0.05
0.10
0.15
0.20
0.25
0.30
0.35
0.40
SHOT
65B
63B
62B

Table 5-5. Calculated Energy and Action for Combined-Voltage Shots

Shot	Time (ms)	Energy (kJ)	Action ($A^2 \cdot s$)	Specific Action* ($A^2 \cdot s/mm^4$)	ΔT† (°C)	Predicted Resistance of Graphite Fiber (Ω)	Comments
Carborundum #1							
23B	0.1	0.25	4.2	8.7×10^{-5}	0.6		Pulser 2 fires
	0.15	0.5	8.7	1.8×10^{-4}	1.2		Attachment
	1.0	7.3	358.0	7.4×10^{-3}	17.5		Maximum scope time
24	2.0	5.4	95.0	2×10^{-3}	13.0		Maximum scope time
25B	0.09	0.23	3.9	8×10^{-5}	0.55		Pulser 2 fires
	0.31	1.2	20.4	4.2×10^{-4}	2.9		Attachment
	1.0	7.8	270	5.6×10^{-3}	18.7		Maximum scope time
26B	0.34	1.3	22.0	4.6×10^{-4}	3.1		Pulser 2 fires
	2.0	5.2	86.0	1.8×10^{-3}	12.5		Maximum scope time
27B	0.1	1.0	17.4	3.6×10^{-4}	2.4		Pulser 2 fires
	0.22	2.5	43.0	8.9×10^{-4}	6.0		Attachment
	2.0	13.6	496.0	1×10^{-2}	32.6		Maximum scope time
Graphite Fiber							
62B	0.3	3.5	407.0	127.0	980.0	7.2	Minimum axial R
	0.45	3.9	453.0	142.0	1090.0	7.0	Maximum scope time
63B	0.09	1.2	126.0	39.4	335.0	9.0	Pulser 2 fires
	0.3	3.6	420.0	131.0	1010.0	7.1	Minimum axial R
	0.5	4.0	467.0	146.0	1120.0	7.0	Maximum scope time
65B	0.09	1.2	127.0	39.6	335.0	9.0	Pulser 2 fires
	0.29	3.5	409.0	128.0	980.0	7.2	Attachment
	0.5	3.8	448.0	140.0	1060.0	7.0	Maximum scope time
67 A/B	0.09	2.8	338.0	106.0	780.0	7.5	Attachment
	0.5	8.1	1275.0	398.0	2270.0	5.5	Maximum scope time
69A/B	0.055	3.6	690.0	216.0	1010.0	6.5	Attachment
	0.5	8.2	2060.0	644.0	2300.0	4.5	Maximum scope time
70A/B	0.09	5.3	870.0	272.0	1480.0	6.1	(Approximate minimum resistance)
	0.5	13.3	2850.0	880.0	377.0	4.0	Maximum scope time
71A/B	0.05	14.4	4200.0	1300.0	402.0	4.0	Minimum Resistance
	0.08	21.7	5980.0	1870.0	6070.0	In Burst Region	Attachment
	0.5	28.2	8620.0	2700.0	7900.0	•	Maximum scope time
Carborundum #2							
85	0.46	1.07	16.5	3.4×10^{-4}	2.6		Maximum scope time
87	0.095	0.25	3.8	7.9×10^{-5}	0.6		Pulser 2 fires
	0.25	0.73	11.2	2.3×10^{-4}	1.7		Minimum resistance
	0.46	1.07	16.3	3.4×10^{-4}	2.6		Maximum scope time
88A/B	0.095	0.25	4.0	8.3×10^{-5}	0.57		Pulser 2 fires
	0.165	0.50	8.7	1.8×10^{-4}	1.2		Attachment
	0.46	1.7	81.0	1.7×10^{-3}	4.1		Maximum scope time
90A/B	0.093	1.5	25.4	5.3×10^{-4}	3.6		Pulser 2 fires
	0.176	2.7	48.0	9.9×10^{-4}	6.5		Attachment
	0.46	6.0	153.0	3.2×10^{-3}	14.4		Maximum scope time
94A/B	0.95	1.1	19.7	4.1×10^{-4}	2.6		Pulser 2 fires
	0.137	1.9	36.0	7.4×10^{-4}	4.6		Attachment
	0.46	6.7	222.0	4.6×10^{-3}	16.1		Maximum scope time
95A	0.082	1.7	32.0	6.6×10^{-4}	4.1		Attachment
	0.178	8.3	268.0	5.5×10^{-3}	20.0		Maximum scope time

*Area = 2.217 cm^2 for carborundum, = 1.8 mm^2 for graphite fiber

†280 °C/kJ for graphite; 2.4 °C/kJ for carborundum.

flows through the resistor. Also shown in the table is the calculated temperature rise, assuming no heat loss from the resistor using average heat capacities of 0.2 and 0.3 cal/gm°C for the carborundum and graphite fiber, respectively, and the predicted resistance of the graphite fiber, ratioed from 10 Ω using Figure 4-43 and the specific action at each time.

From Table 5-5, for shots 62, 63, and 65, the predicted resistance for the graphite fiber at about 0.3 ms (the time of the minimum resistance or attachment in these shots) is about 7.1 Ω, that is, very close to, but slightly less than, the measured minimum resistances for those shots. Thus, the change in resistance in Figure 5-19 could be accounted for by IR heating. And, since these three shots had the same axial voltage (≈ 20 kV), it follows that they should have essentially identical resistivity curves if their shapes are due primarily to IR heating. The fact that the minimum resistances in Figure 5-19 are slightly larger than the predicted values from the specific action could be due to heat loss from the fiber because the time scale of these curves (≈ 0.3 ms) is considerably slower than the time at which the same action was achieved in the vaporization/restrike experiments (≈ 0.02 ms for the smallest pulser voltage, Figure 4-43b). Also, in the present experiments, the graphite fiber was snugly surrounded by moderately damp soil whereas the graphite-fiber vaporization/restrike shots were in air. The heat loss in air is probably less than in the damp soil.

Figure 5-20 shows similar axial resistance time histories for the remaining combined-voltage graphite fiber shots. Their radial/axial voltages were as follows:

Shot	Axial Voltage	Radial Voltage (kV)
67	30	-38
69	30	-38
70	40	-19
71	60	-19

The difference in the timing for these shots in Figure 5-20 is purely a matter of the time delay between scope trigger and the pulser firing so it is not relevant for this discussion. For shots 67, 69, and 71, the radial and axial pulsers fired essentially simultaneously whereas the radial pulser was delayed in shot 70, as can be seen from the curve of radial field in Figure 5-20b.

In addition to the larger axial voltages, which was the intended difference between these shots and shots 62, 63, and 65, there were some unintentional differences also. After shot 69, the sand was removed to insert the plastic sheets, as discussed in Section V.3.c. At that time, the fiber was still intact but it had a decidedly different

Figure 5-20a.

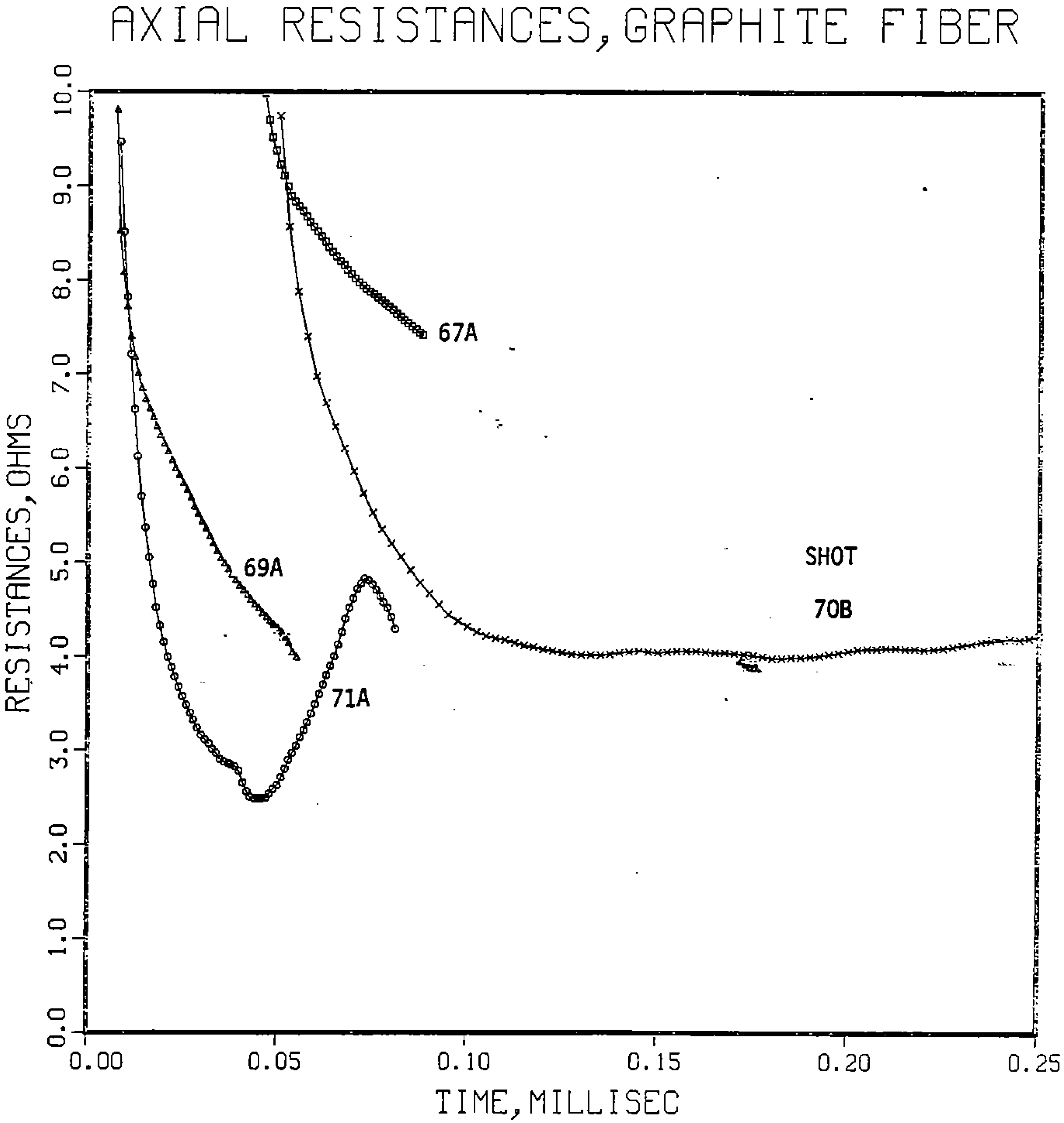
AXIAL RESISTANCES, GRAPHITE FIBER
RESISTANCES, OHMS
10.0
9.0
8.0
7.0
6.0
5.0
4.0
3.0
2.0
1.0
0.0
0.00
0.05
0.10
0.15
0.20
0.25
TIME, MILLISEC
67A
69A
71A
SHOT
70B

Figure 5-20b.

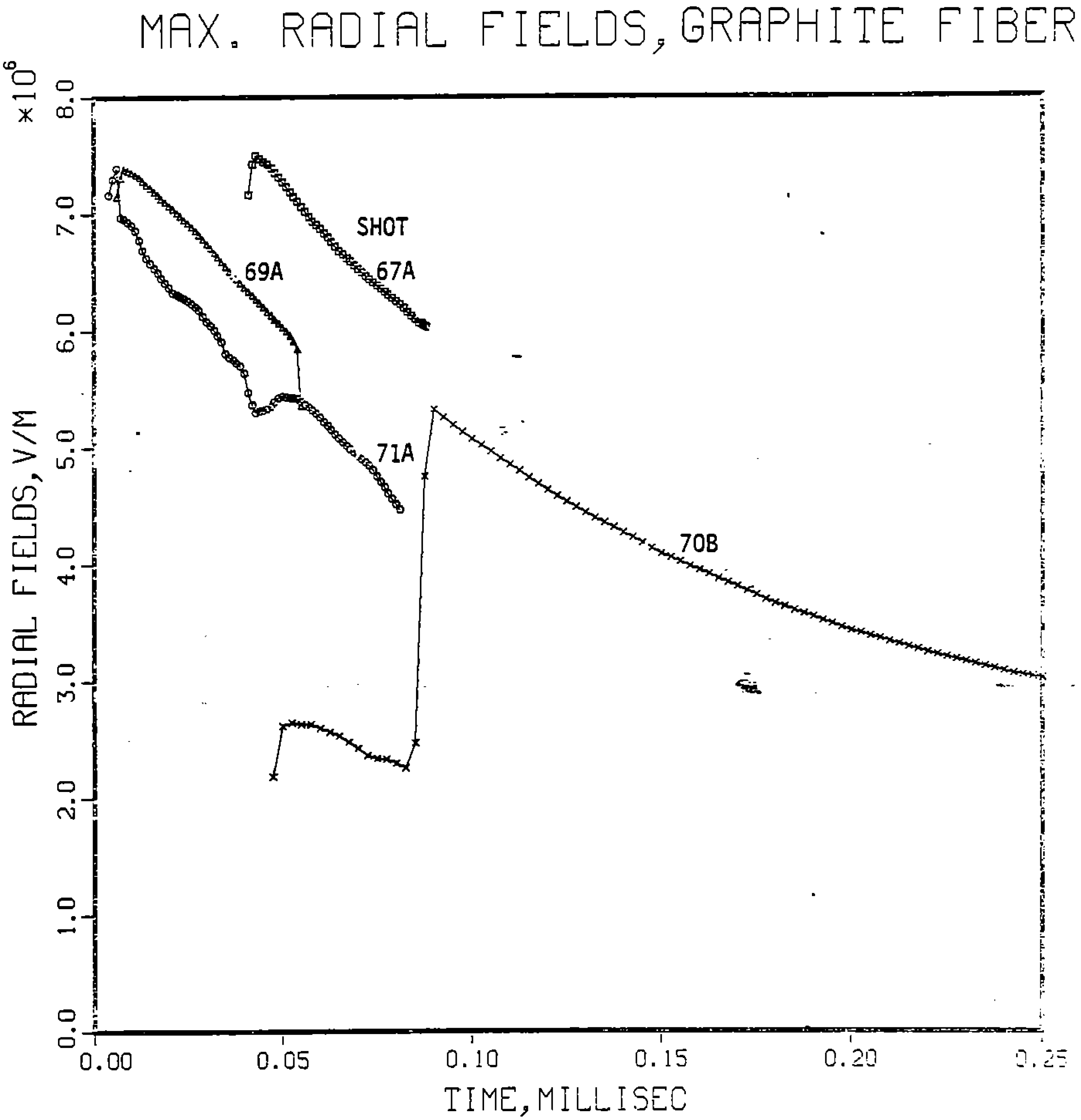
MAX. RADIAL FIELDS, GRAPHITE FIBER
RADIAL FIELDS, V/M
*10^6
0.0
1.0
2.0
3.0
4.0
5.0
6.0
7.0
8.0
TIME, MILLISEC
0.00
0.05
0.10
0.15
0.20
0.25
SHOT
67A
69A
71A
70B

appearance from its pre-installation condition. Specifically, the fibers had puffed out to form a loosely packed cylinder of about 1 cm diameter. Then, while refilling the cylinder with the plastic sheets in place, the fiber apparently broke and the broken ends were inadvertently separated axially by a few inches, as described in Section V.3.c. Although the presence of the plastic sheet probably had little effect on the measured axial resistances, the other configuration changes undoubtedly did affect them. They are probably the cause of the differences between the supposedly identical shots (67 and 69) and could have caused the difference between the measured and predicted resistances, discussed later.

On shot 67, the first shot with more than 20 kV axial voltage, the measured resistance at attachment was in good agreement with the value predicted from the action (≈ 7.5 Ω). On shot 68 with the same axial voltage, the radial pulser did not fire so this shot was not reduced in detail. However, at the same time after the axial pulser fires in shot 68 as attachment in shot 67, the measured resistance was 5.4 Ω, and then the resistance went to a minimum of about 4.0 Ω. It could be only fortuitous that this minimum resistance is very close to the minimum resistance observed on shot 70, when the fiber was known to be severed.

On shot 69, which should have been identical to shot 67, the resistance curve is somewhat steeper than for shot 67, and, at the same time after the pulser fires as attachment in shot 67, the measured resistance was about 4.3 Ω, that is, considerably less than the resistance at the corresponding time in shots 67 and 68. In addition, the resistance in shot 69 at attachment is less than was predicted from the action.

Thus, it appears that the graphite fiber underwent a progressive change as the axial voltage was increased above 20 kV. For shots 62, 63, and 65, the axial resistance was repeatable so it appears that the fiber could withstand that voltage without significant change. Then, with a 30 kV axial voltage, the first shot (#67) follows the predicted resistance as a function of action reasonably well. However, probably later in run 67, something started to happen to the fiber. Although the initial resistances in shots 68 and 69 were close to the usual 10 Ω, the change in resistance with time and action changed progressively from shot 67 to shot 68 to shot 69. This change was probably related to the fluffed-out geometry of the fiber that was noted after shot 69.

Since the graphite fiber was known to be severed for shots 70 and 71, it is perhaps surprising that their axial resistance curves show any similarity, in magnitude or shape, to the resistance curves for the intact fibers. Apparently an air arc is launched between the two severed ends of the graphite so the resistance that is measured is the resistance of the arc plus the resistance of the intact fiber. Of course, there is no way of knowing how much of the intact graphite was shorted out by the arc so the fact that the minimum resistances for these shots are less than the corresponding values predicted from the action is not particularly significant, and these resistances are not too meaningful for our purposes. However, it is fairly clear from shot 70 that these low resistances are not the result primarily of the radial electric field because the minimum resistance on shot 70 is almost reached before the radial pulser fires. Before that happens, the radial differential voltage is relatively small because the can floats to about half of the voltage V_1.

During shot 71, with the 60 kV axial voltage, the graphite fiber was completely destroyed. It is quite possible that the momentary increase and then decrease in the axial resistance for this shot around t = 0.05 ms is due to vaporization and restrike of the graphite fiber, similar to the experiments in Section IV.

An interesting side result from Figures 5-19 and 5-20 is that the threshold radial voltage (radial plus axial voltage) for radial streamer attachment for this configuration is apparently about 60 kV. Shots 65 with 20 kV axial and -38 kV radial developed an attachment whereas shot 70, with 40 kV axial and -19 kV radial, did not. The difference between these shots is probably that, for shot 70, the peak radial electric field was only about 5.3×10^6 V/m whereas the peak field for shot 65 was about 6.1×10^6 V/m. All other shots with peak fields greater than 6×10^6 V/m had attachments while those with smaller fields did not.

In summary for the graphite fibers, any enhanced axial conduction due to radial electric fields is apparently a much smaller effect than the reduction in the resistance of the graphite fiber due to IR heating. However, if one uses the lower-limit value of 30 Ω deduced previously from shots 62, 63, and 65 for the axial resistance through the soil and an average corona radius of 3 cm from curves 4 and 5 of Figure 5-17 (for 40 kV radial voltage), the average axial resistivity in this corona region would have to be greater than

$$\rho_{min} = \frac{(30\ \Omega)\ (\pi 3^2)}{80} = 10.6\ \Omega\text{-cm}$$

where the length of the corona region has been taken to be the length of the sample (≈ 80 cm). As will be seen later from the carborundum shots, the actual resistivity is apparently considerably larger than the above value.

Figures 5-21 through 5-23 give time histories of axial resistance (with very expanded ordinate scales) and maximum radial fields for the combined-pulser shots with carborundum resistors 1 and 2. For shot 24, the radial fields are not shown because the radial pulser did not fire. However, the radial fields for that shot would be quite small ($\lesssim 3 \times 10^5$ V/m) because the axial voltage was only 20 kV and the can floated up to around half that voltage.

It is not known why the resistances based on I_{ave} usually show a sharp jump when the radial pulser fires. Even using a more distributed equivalent circuit model to calculate I_1 and I_2 as functions of V_1 and V_2 (Section V.6), the resulting V_1/I_{ave} should be continuous through the turn-on process for V_2, at least if $V_2 = V_1/2$ before the radial pulser fires. In most cases, this relation is not satisfied exactly, which could account for the discontinuity in the calculated resistance. In any case, for the present discussion, the changes in axial resistance during combined radial/axial pulses is measured from the peak resistance value after the second pulser has fired.

As discussed later, the resistances for the carborundum resistors (Figures 5-21 through 5-23) give indication of enhanced axial conductance through the soil. A lower limit to this axial resistance of the soil, at least up to attachment, can again be obtained from the difference of reciprocal resistances from just after the radial pulser fires to the time of interest. The resistances calculated in this way, either at attachment or at the time of the minimum resistance, are summarized in Table 5-6. Of course, on some of the shots, the axial resistance was still decreasing when attachment occurred. If attachment had not occurred, the soil resistance would have gone to lower values than those listed in Table 5-6, but any estimates of how small they might have gone would be pure speculation.

One indication that these resistance changes may be due to parallel conduction through the soil is the dependence of the resistances on the radial voltage. In Figure 5-21, all of the shots except no. 27 had an axial voltage of 20 kV. Shot 24, during which the outer can was floating so the radial field was relatively low, showed the least change in resistance with time. For progressively larger negative radial voltages (-20 kV, shot 26; -29 kV, shot 25; -40 kV, shot 23), the change in resistance became more rapid with time. Unfortunately, shots 23 and 25 developed radial streamer attachments before the resistance curves reached a minimum. However, the curve for shot 25 gives indications of flattening off between 50 Ω and 55 Ω. If we assume that it would have leveled off at 50 Ω, the corresponding soil axial resistance would be 232 Ω, that is, somewhat less than the lower-limit value given in Table 5-6 for shot 25 at the time of

Figure 5-21a.

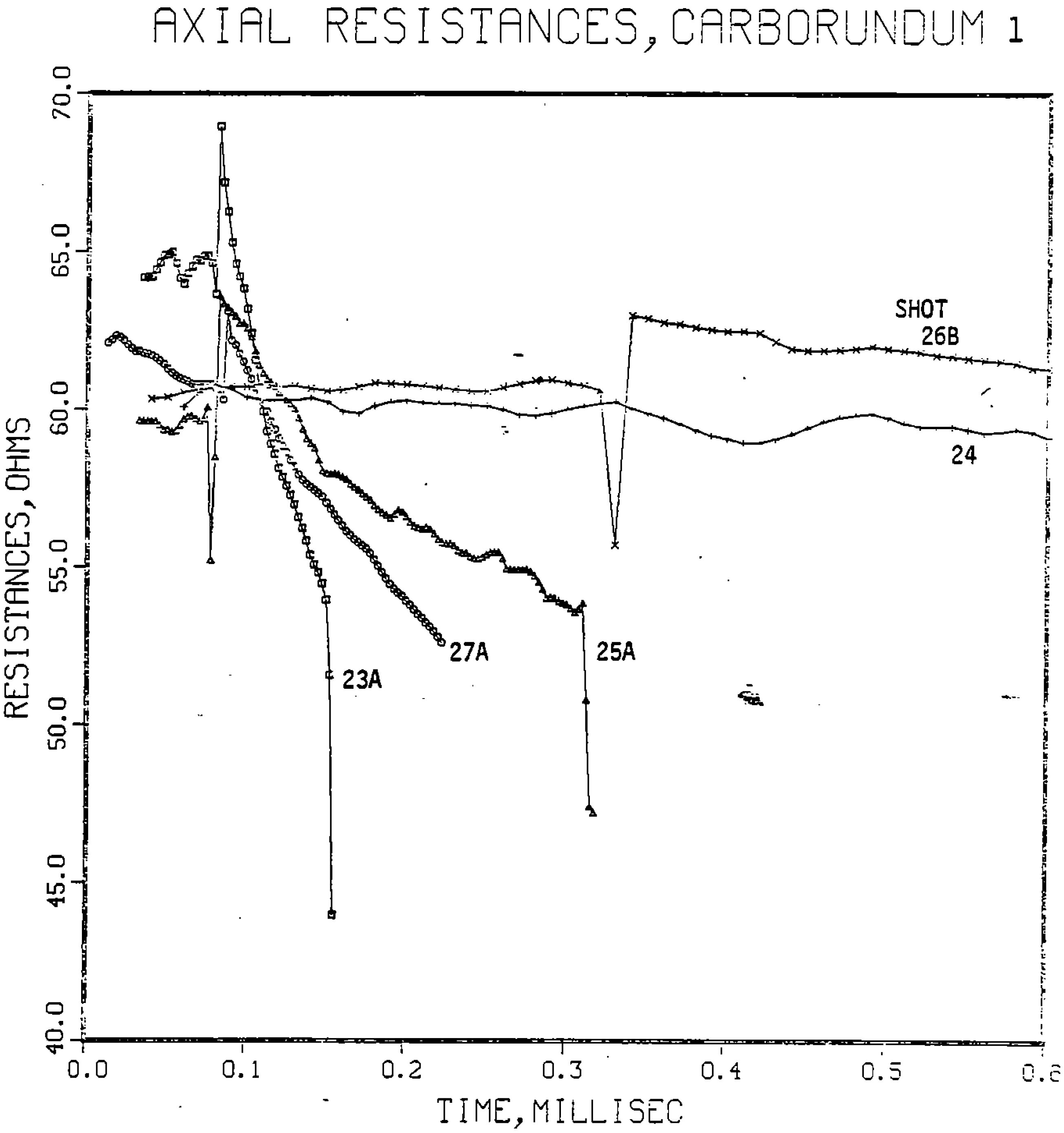
AXIAL RESISTANCES, CARBORUNDUM 1
RESISTANCES, OHMS
TIME, MILLISEC
70.0
65.0
60.0
55.0
50.0
45.0
40.0
0.0
0.1
0.2
0.3
0.4
0.5
0.6
SHOT
26B
24
27A
25A
23A

Figure 5-21b.

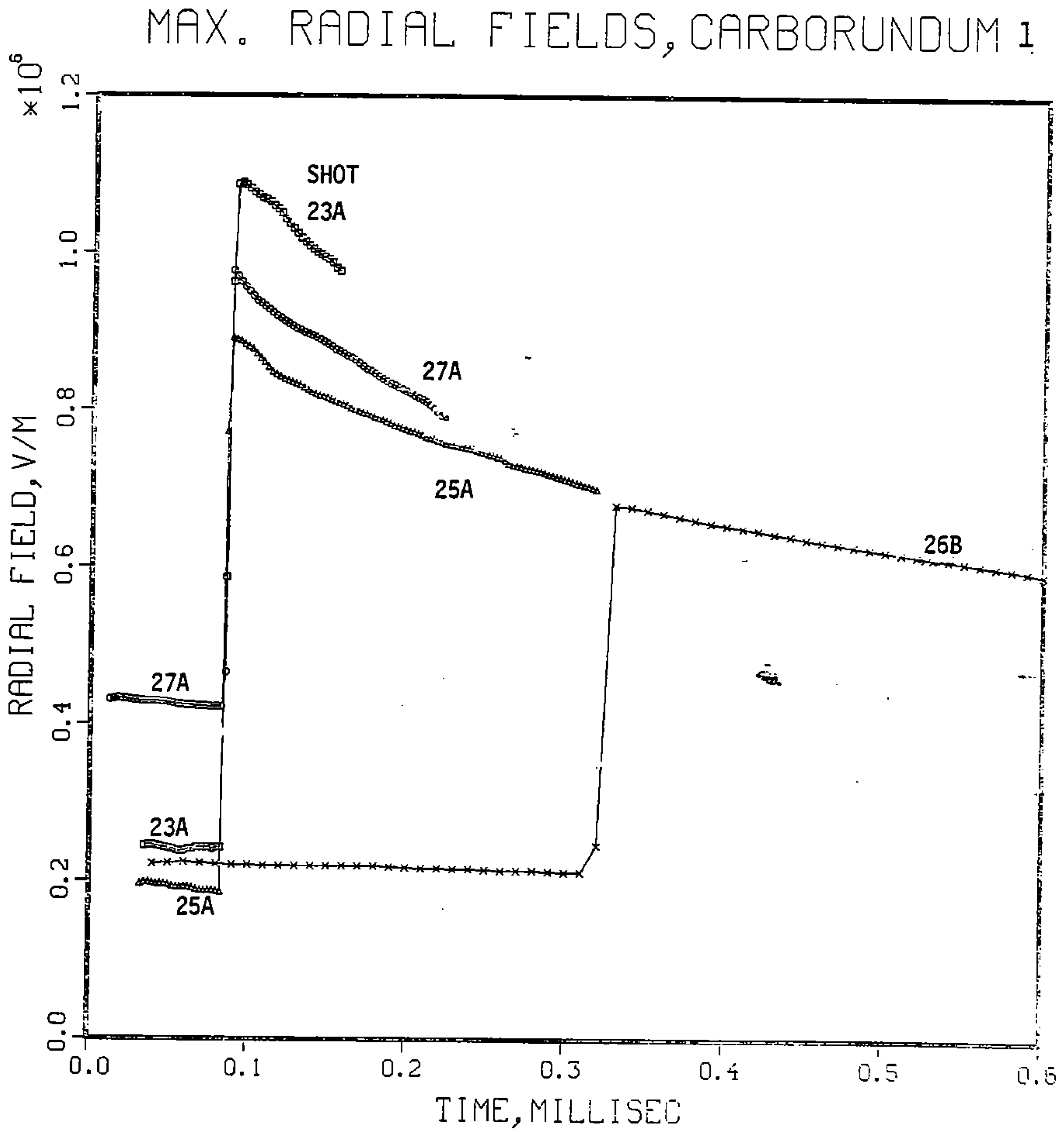

MAX. RADIAL FIELDS, CARBORUNDUM 1
$\times 10^6$
RADIAL FIELD, V/M
TIME, MILLISEC
0.0
0.2
0.4
0.6
0.8
1.0
1.2
0.0
0.1
0.2
0.3
0.4
0.5
0.6
SHOT
23A
27A
25A
26B
27A
23A
25A

Figure 5-22a.

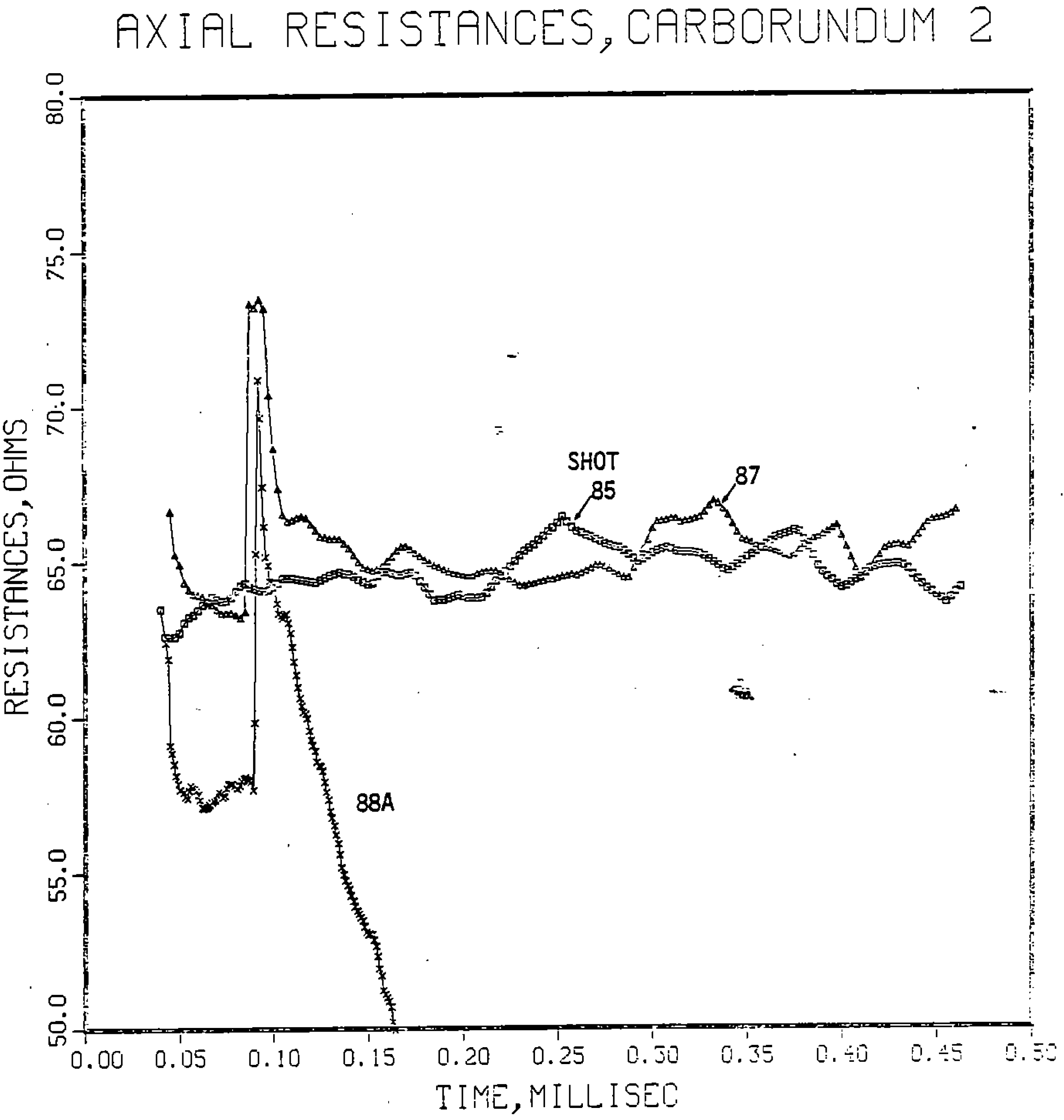

AXIAL RESISTANCES, CARBORUNDUM 2
RESISTANCES, OHMS
80.0
75.0
70.0
65.0
60.0
55.0
50.0
TIME, MILLISEC
0.00
0.05
0.10
0.15
0.20
0.25
0.30
0.35
0.40
0.45
0.50
SHOT
85
87
88A

Figure 5-22b.

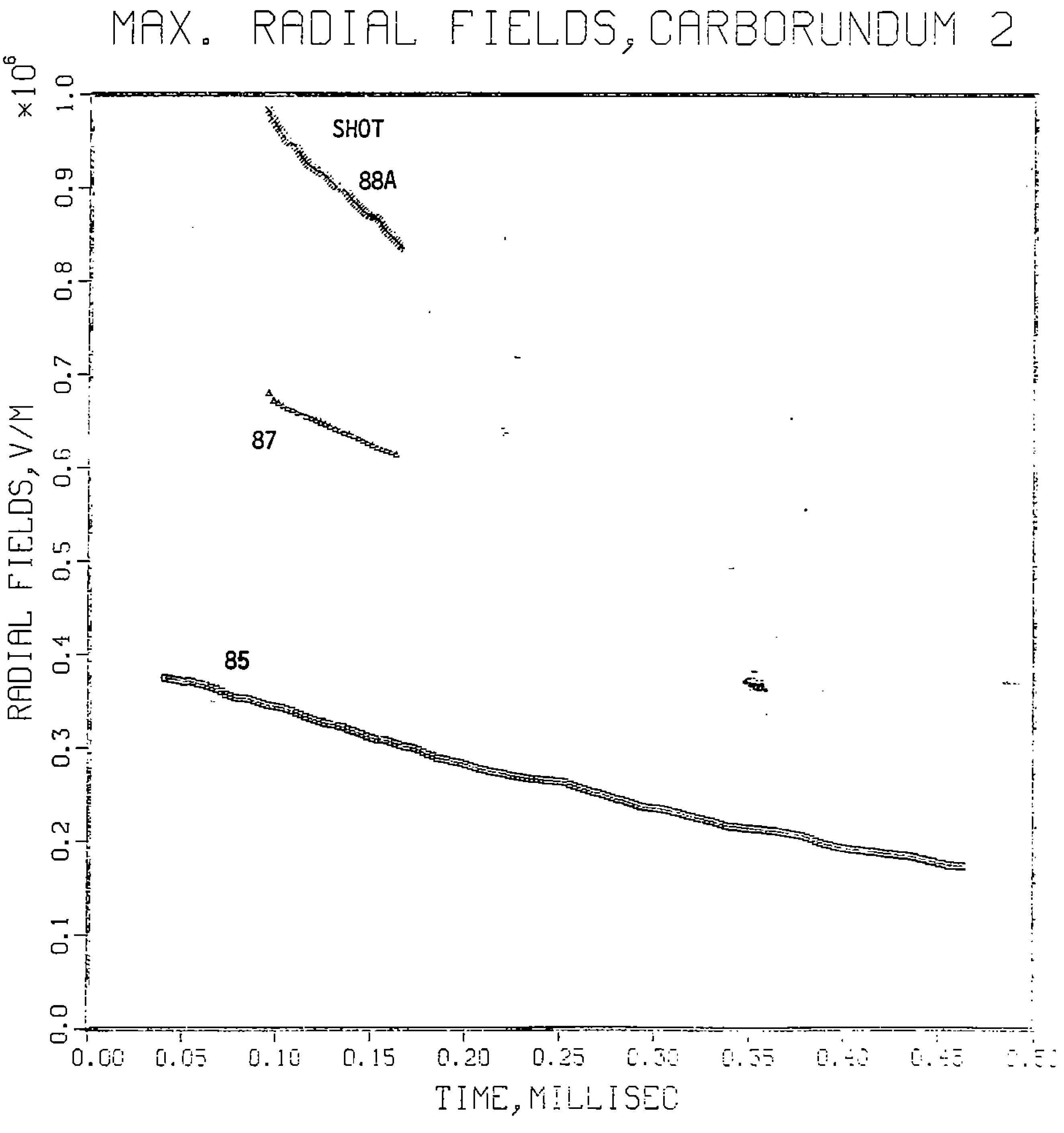
MAX. RADIAL FIELDS, CARBORUNDUM 2
RADIAL FIELDS, V/M
×10⁶
0.0
0.1
0.2
0.3
0.4
0.5
0.6
0.7
0.8
0.9
1.0
TIME, MILLISEC
0.00
0.05
0.10
0.15
0.20
0.25
0.30
0.35
0.40
0.45
0.50
SHOT
88A
87
85

Figure 5-23a.

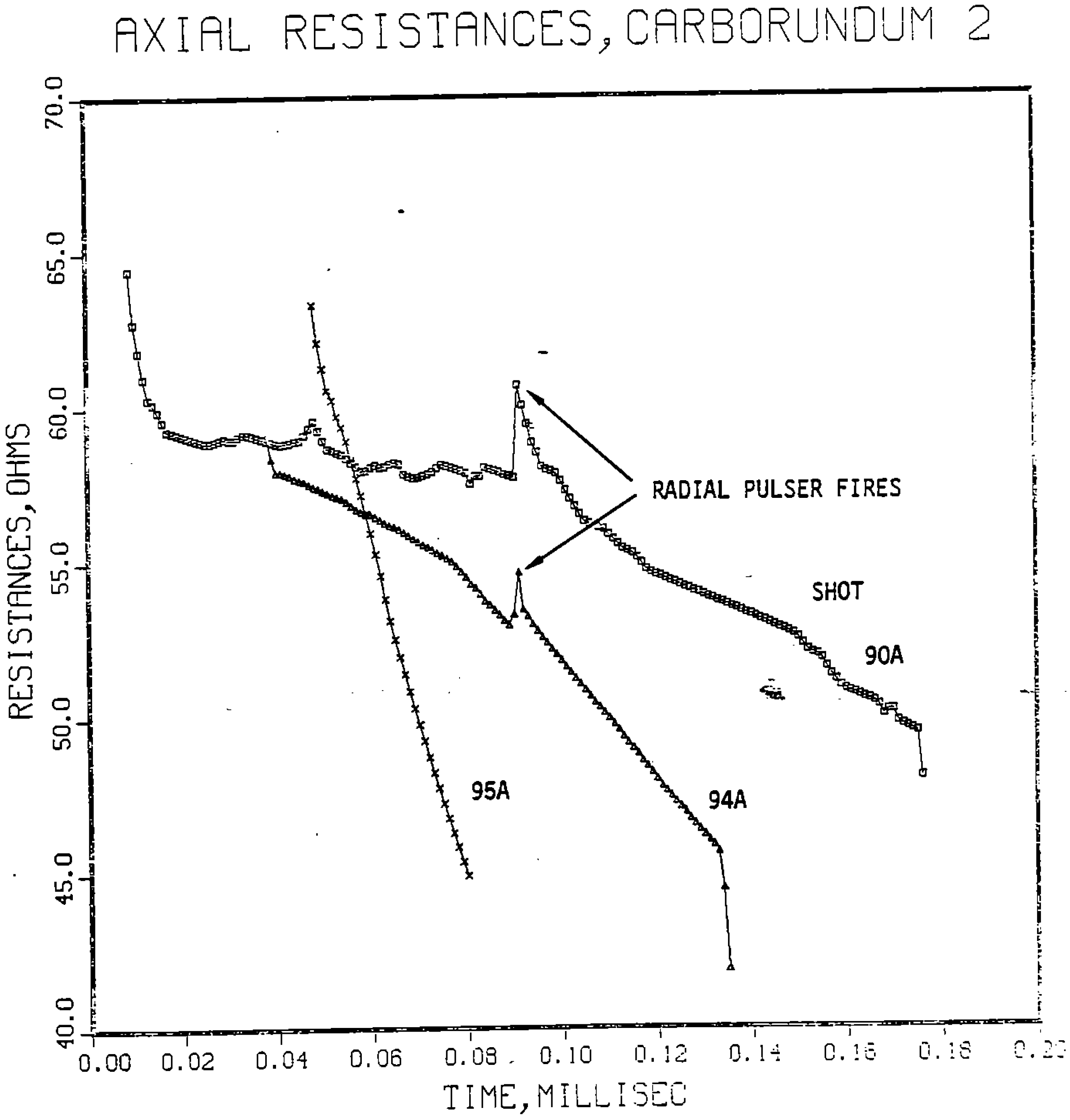
AXIAL RESISTANCES, CARBORUNDUM 2
RESISTANCES, OHMS
70.0
65.0
60.0
55.0
50.0
45.0
40.0
0.00
0.02
0.04
0.06
0.08
0.10
0.12
0.14
0.16
0.18
0.20
TIME, MILLISEC
RADIAL PULSER FIRES
SHOT
90A
95A
94A

Figure 5-23b.

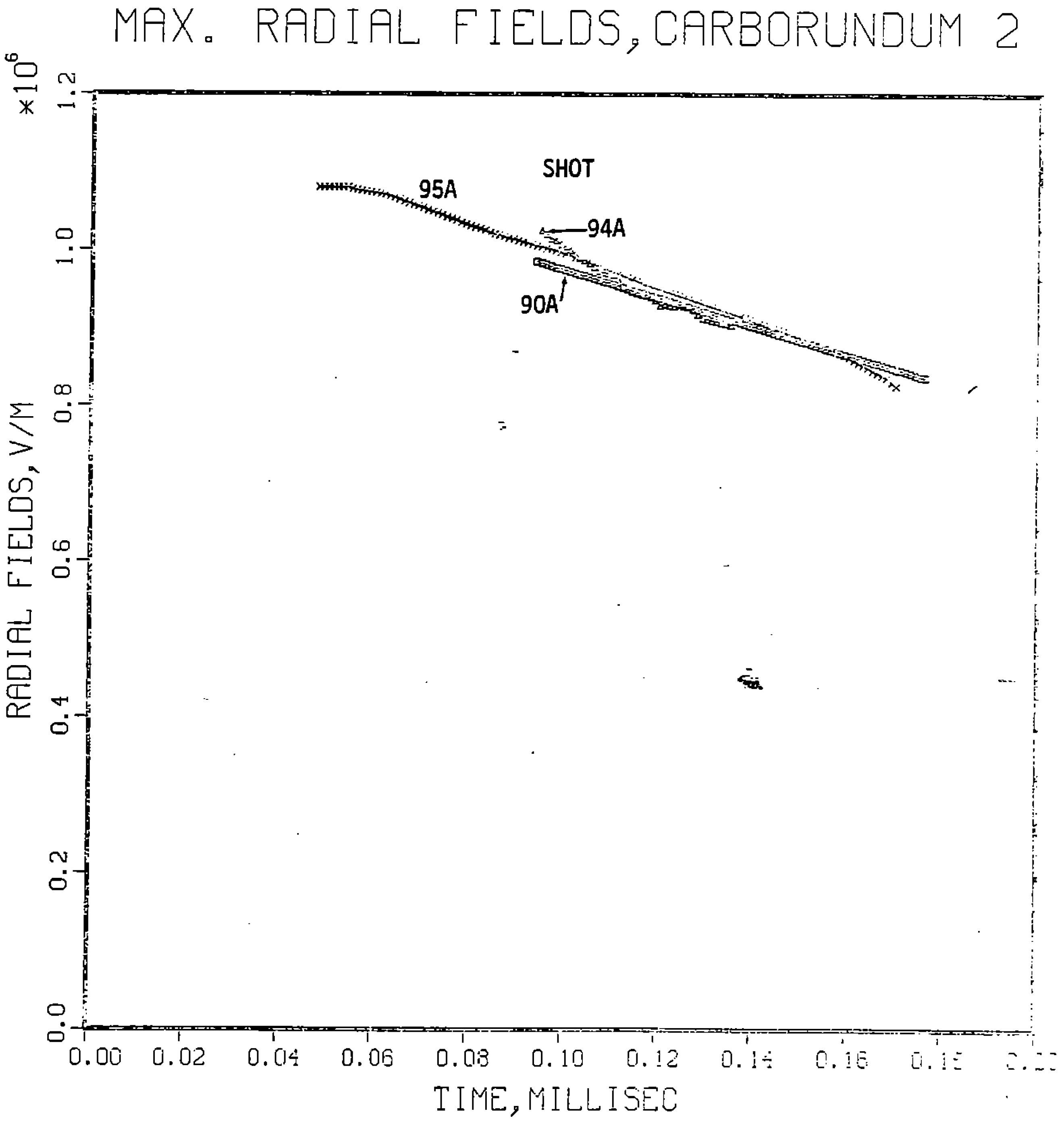
MAX. RADIAL FIELDS, CARBORUNDUM 2
RADIAL FIELDS, V/M
*10^6
0.0
0.2
0.4
0.6
0.8
1.0
1.2
TIME, MILLISEC
0.00
0.02
0.04
0.06
0.08
0.10
0.12
0.14
0.16
0.18
0.20
SHOT
95A
94A
90A

attachment. Shot 27, which had twice as large an axial voltage as shot 23 but only half the radial voltage, showed a less rapid decrease in axial resistance with time than shot 23. This result is consistent with the slightly smaller radial field for shot 27 (Figure 5-21b).

Table 5-6. Lower-Limit for Soil Axial Resistances for Carborundum Resistors

Shot	Resistance (Ω)	at T = (ms)	Resistance (Ω) After Radial Pulser Fires	Lower-Limit Soil Axial Resistance (Ω)
23	54.0	0.15	69.0	250
24	50.0	2.0	60.5	286
25	53.5	0.31	63.5	345
26	56.0	2.0	62.5	526
27	52.5	0.22	62.5	323
85	Resistance appears to increase slightly with time			
87	64.0	0.23	73.0	536
88	50.0	0.16	71.0	170
90	49.5	0.175	60.5	278
94	45.5	0.135	54.0	294
95	44.5	0.08	63.0	152

A similar trend is observed in the curves in Figures 5-22 and 5-23 for carborundum resistor #2. The three shots in Figure 5-22 all had an axial voltage of 20 kV while the radial voltage was 0 for shot 85, -19 kV for shot 87, and -38 kV for shot 88. The resistivity curve for shot 85 shows only a small resistivity increase with time after the axial pulser fires. This increase could be a temperature effect in the carborundum although its resistivity-temperature coefficient is supposed to be negative. However, this increase is probably within the accuracy of the data reduction and one can say that the resistivity for this shot is essentially constant. It is interesting that, in Figure 5-17, the calculated corona radius for shot 72 (curve 7), which had a 20 kV radial voltage, was only slightly greater than the radius of the carborundum rod (0.0127 m). Since, in shot 85, the 20 kV voltage was axial, the average radial voltage was only 10 kV. Thus, for shot 85, it is reasonable that there is only a negligible corona region, if any, around the resistor so there would be little enhanced conduction and the axial resistance should be constant with time.

For shot 87, there is an initial decrease in the resistance when the radial pulser fires and then it remains essentially constant. From Table 5-6, this decrease in axial resistance could be produced by a soil axial resistance of 536 Ω.

For shot 88, which had the largest radial voltage (-38 kV) with 20 kV axial, the axial resistance decreased fairly rapidly until radial attachment occurred. There is no way of knowing how low this resistance would have gone if attachment had not occurred. At attachment, the 50 Ω resistance corresponds to soil axial resistance of 170 Ω (Table 5-6), so, without attachment, it would have been somewhat smaller.

For the shots in Figure 5-23, shots 90 and 94 should theoretically have been identical, with 40 kV axial and -19 kV radial, while shot 95 had 60 kV axial and no radial pulser. It is not clear why shots 90 and 94 were not more nearly the same. One difference could be that the radial pulser fired sooner after the axial pulser fired for shot 94 than for 90. Thus, the combined axial-plus-radial voltage could have been slightly larger for shot 94, although this difference is not especially evident in the radial E fields (Figure 5-23b), which were based on calculated values for V_2 using I_2. However, this difference in firing times should not have affected the axial resistances before the radial pulser fired, and yet, the axial resistance for shot 94 decreases considerably more rapidly than the axial resistance for shot 90, shortly before the radial pulser fires. Since these resistances are calculated from V_1 and the two currents I_1 and I_0, the above effects are also evident in the corresponding current and voltage time histories (Figures A-55 and A-57). For shot 90, I_1 and I_0 are decreasing somewhat before the radial pulser fires (roughly following V_1) whereas, for shot 94, they are more nearly constant even though V_1 is decreasing. Similarly, after the radial pulser fires, I_1 increases fairly rapidly and I_0 is about constant for shot 94 while I_1 increases less rapidly and I_0 decreases for shot 90. One could speculate that the carborundum resistor might have been damaged during shot 90 (perhaps a slight crack) and this caused the observed differences on shot 94.

During shot 95 with the 60 kV axial voltage, the carborundum was completely shattered. We do not know for sure when, during the shot, that this occurred. However, similar to shots 70 and 71 with the graphite fiber, an opening in the resistor apparently does not create an extremely high impedance, except briefly after application of the voltage, probably because air arcs are launched between the jagged pieces of the resistor. Therefore, since the average radial voltage over the length of the resistor for shot 95 was less than for shots 90 and 94, the rapidly decreasing axial resistance in shot 95 is probably not due primarily to the radial electric field.

In summary, there are indications from the shots with the carborundum resistors of an enhanced axial conduction through the soil which increases with increasing radial electric field. At the maximum times of usable data (before radial attachments), the resistance of the parallel (axial) conduction path through the soil was on the order of 100 Ω to 500 Ω, depending on the magnitude of the applied voltages. If radial streamer attachment had not occurred with the larger radial voltages, the resistance of the parallel conduction path would have been less than 100 Ω, but how much less is unknown. Even if the parallel resistance were as low as 50 Ω for voltages corresponding to those in the graphite fiber shots, the effect of this conduction path would have been almost unnoticeable in the shots with the relatively low-resistance graphite fibers.

6. DISTRIBUTED CURRENT MODELS

In the previous sections, an average radial resistance defined by

$$R_{rad} = \frac{0.5\ V_1 - V_2}{I_2} \qquad (5\text{-}11)$$

and an average axial resistance defined by

$$R_{ax} = \frac{V_1}{0.5\ (I_1 + I_0)} = \frac{V_1}{I_{ave}} \qquad (5\text{-}12)$$

were used for reducing and analyzing the data for the combined radial/axial pulses. These resistances are the result of a very simplified equivalent circuit for the system which consists of the center resistive rod divided into two lengths with equal resistances $R_{ax}/2$, and with one resistor, R_{rad}, going from the midpoint of the center resistor to the outer can (see Figure 5-24). As discussed previously, this model should be fairly good when I_2 is small (R_{rad} large compared to R_{ax}) so that there is not much difference between I_1 and I_0 and where the radial resistivity is fairly constant along the length of the cylinder However, as an aid in trying to determine from the experimental data if there is any enhanced axial conduction through the soil, it is useful to consider more complex equivalent circuits which allow for the possibility of radial and axial resistances that vary with distance along the axis of the cylinder.

In the following sections, three different equivalent circuits with different degrees of complexity and applicability are considered. In Section V.6.a, an equivalent circuit with two radial resistances and three axial resistances, as illustrated in Figure 5-25, is utilized. The advantage of this model is its relative simplicity, which makes it easy to see the effect of changes in the different circuit parameters. In Section V.6.b, an analytical model with resistances that are continuously distributed along the axis of the cylinder is used. Although the continuous distributions of resistance more nearly approximate the real situation than the discrete resistances in Figure 5-25, unfortunately this model can be solved in closed form only for the case of uniform radial and axial resistances. In order to consider nonuniform radial and axial resistances on a finer distribution of resistances than illustrated in Figure 5-25, an equivalent-circuit computer model was developed with ten radial resistances and nine axial resistances, each with an arbitrary input value. The results from this model are discussed in Section V.6.c.

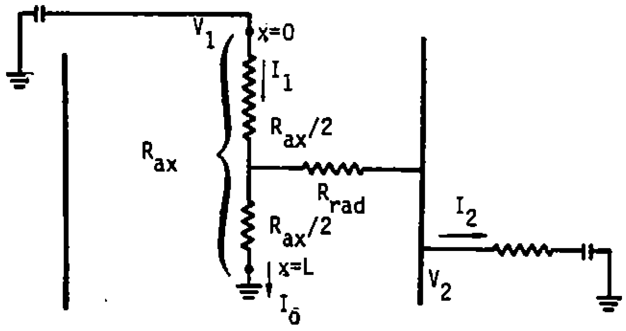

Figure 5-24. Simplified equivalent circuit.

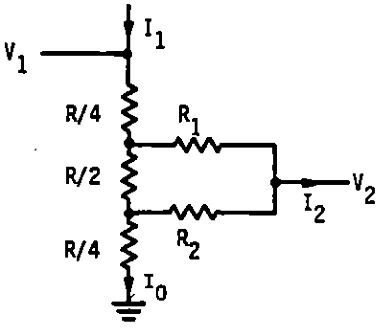

RE-04819

Figure 5-25. Equivalent circuit with two radial resistances.

Each of these three models has been applied to the data from some of the shots with combined radial and axial voltages to try to determine if there is any evidence for enhanced axial conduction through the soil. For each of the models, the general approach was to try to match the observed temporal behavior of the radial and axial currents and voltages with models in which the radial resistance and axial resistance are both allowed to vary (usually decrease) with time. If the actual waveforms can be produced by simply changing the radial conductance in a manner consistent with growth of the effective inner conductor owing to streamer propagation, the conclusion will be that no significant change in axial resistance due to shunting of the resistor by streamers or corona in the soil has been detected. If the actual waveforms can only be reproduced by lowering the axial resistance along with a change in the radial resistance, then there is an inferred change of soil conductivity, and it can be quantified.

6a. MODEL WITH TWO RADIAL RESISTANCES[*]

The equivalent circuit for this model is illustrated in Figure 5-25.

It is expected that, in a combined drive test, the streamers will first develop near the top of the central resistors, where the radial voltage is highest, and that the change of radial conductance would therefore be highest there. The radial conduction in the top and bottom halves of the experiment is represented independently in Figure 5-25 by the two resistors R_1 and R_2 at the midpoints of the top and bottom halves of the central resistor of value R. For any given set of values of V_1, V_2, R_1, R_2, and R, the current values I_1, I_0, and I_2 were calculated by a program written for a TI-59 calculator. The program calculates values of

$$R_{rad} = (0.5\ V_1 - V_2)/I_2$$

and

$$R_{ax} = 2\ V_1/(I_1 + I_0)$$

and compares these with the actual effective radial resistance $(R_1^{-1} + R_2^{-1})^{-1}$ and axial resistance R. The values of V_1/I_1 and V_1/I_0 are also calculated.

---

[*] The analysis in this section is due to Dr. Ian Smith of Pulse Sciences, Inc.

It is instructive to look at some general results obtained in this way using nominal values of resistance and voltage similar to actual circuit values (Table 5-7). Consider the case $R = 60\ \Omega$, $R_1 = R_2 = 400$, $V_1 = 10$ kV, $V_2 = -20$ kV. Before V_2 is turned on (Table 5-7, line 1), the values of V_1/I_1, V_1/I_0 and R_{ax} are all 59 Ω, since $I_1 = I_0$. This value is lower than 60 Ω because the soil shuts the resistor. When V_2 is turned on (Table 5-7, line 2), V_1/I_0 increases and V_1/I_1 decreases, because the presence of V_2 causes more current to be drawn from the V_1 source and at the same time prevents current from reaching ground (i.e., lowers I_0). However, R_{ax} remains 59 Ω. These changes are shown graphically in Figure 5-26.

Table 5-7. Representative Calculations

(Units: kV, A, Ω)

Line	V_1	V_2	R	R_1	R_2	I_1	I_0	I_2	V/I_0	V/I_1	R_{ax}	R_{rad}
1.	10	-5	60	400	400	170	170	0	59	59	58.9	—
2.	10	-20	60	400	400	230	120	109	91	43	58.9	207
3.	10	-20	60	300	300	250	159	91	109	40	58.6	157
4.	10	-20	60	240	400	262	162	99	101	38	55.4	154
5.	10	-15	60	300	300	234	127	107	93	43	58.6	157
6.	10	-15	60	240	400	244	131	113	88	41	56.0	153

Next, suppose that the radial soil resistance falls 25% everywhere because of streamer formation (line 3 and Figure 5-26). The values of V_1/I_0 and V_1/I_1 rise and fall further, while R_{ax} decreases very slightly. (The value of R_{rad} falls about 25%, but not exactly, because of the coarseness of the model.)

Now suppose instead that the same total change of radial soil resistance from 200 to 150 Ω for the parallel combination of R_1 and R_2 occurs by the reduction of R_1 alone, with R_2 remaining at 400 Ω. This corresponds to steamer formation in the top part of the experiment only. In this case (line 4 and Figure 5-26), V_1/I_0 does not increase as much, and V_1/I_1 falls a little more than when conduction is uniform. Also, the inferred R_{ax} falls.

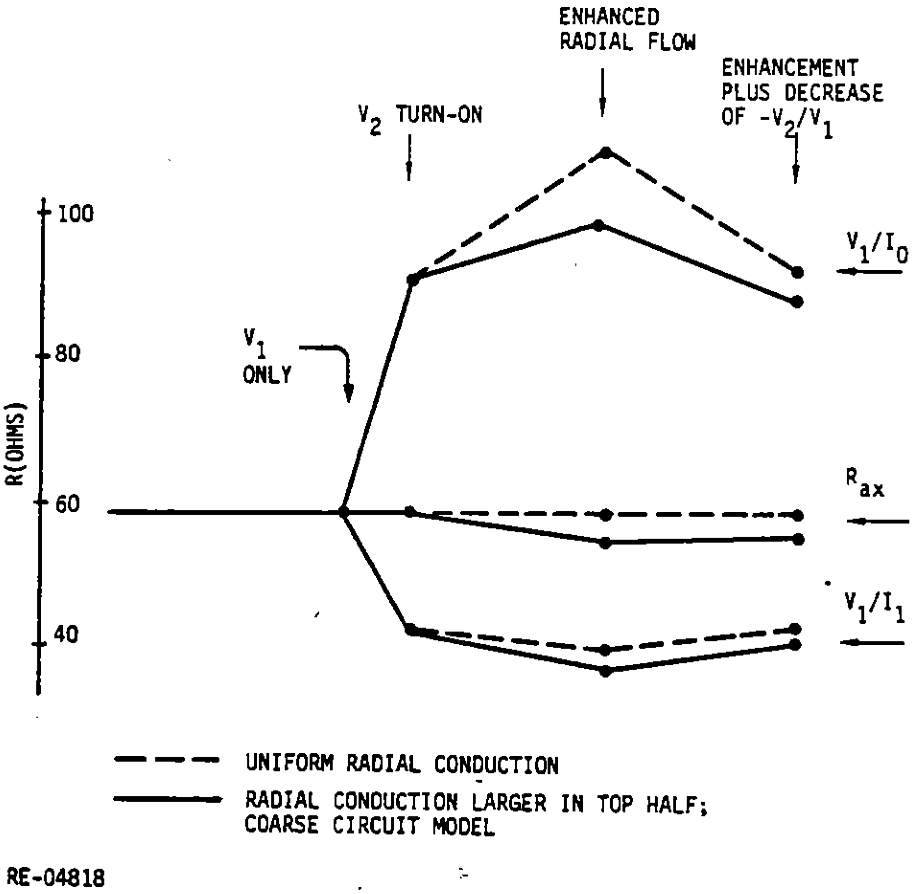

Figure 5-26. Effects of uniformity of radial conduction change on resistance waveforms (illustrating values in Table 5-7).

Finally, lines 5 and 6 show what happens if, at the same time that the streamers grow, the absolute ratio of V_2 to V_1 decreases; the values of V_1/I_0 and V_1/I_1 tend to move back together.

Digitized plots of V_1/I_0, V_1/I_1, and R_{ax} (see, for example, shots 23 to 27, Appendix A) show the kind of behavior illustrated in Figure 5-26. Before V_2 turns on, these three axial resistances are equal, within the accuracy of the data. Then, when V_2 turns on, V_1/I_0 and V_1/I_1 separate and become larger and smaller than R_{ax}, respectively. Subsequently, R_{rad} can be seen falling, showing streamer growth. It is characteristic, however (as illustrated in Figure 5-26), that V_1/I_0 never increases as R_{rad} falls, but rather decreases slightly, though proportionally not as much as V_1/I_1. This suggests that the axial resistance R is decreasing, and indeed the plot of R_{ax} does decrease. However, as the calculations in Table 5-7 and Figure 5-26 show, a non-uniform change of radial conductance can make R_{ax} drop, and can suppress the rise of V_1/I_0.

The case in point in Figure 5-26, which we will now examine in detail, is shot 23A. The value of R appears to be about 65 Ω initially (Figure 5-26 and Table 5-8). When V_2 (= 1.65 V_1) is applied, the values of V_1/I_0 and V_1/I_1 become 110 and 49 Ω (Table 5-8, line 1). It is difficult to match these values exactly by using this coarse circuit model and assuming the simultaneously measured value of 170 Ω for R_{rad}, which corresponds to $R_1 = R_2 = 340$ Ω; line 2 of Table 5-8 illustrates the disagreement.

Before the experiment arcs over, the value of R_{rad} falls to 122 Ω, while the absolute ratio V_2/V_1 falls to 1.5. If the change of R_{rad} is interpreted as a uniform change of radial conductance, V_1/I_0 would be expected to increase 20% (line 4, Table 5-8). Actually V_1/I_0 falls 4-5% (line 3). To explain this, the axial resistance must be assumed to decrease to about 57.5 Ω (line 5). However, if all the radial resistance change is assumed to occur in the top half of the soil, the value of V_1/I_0 would only rise 7% (line 6), and the fall could be explained by R decreasing only to 60.5 Ω (line 7). The latter calculation predicts most of the apparent fall of R_{ax}, which is partly due to the non-uniformity (see line 6). However, R = 58 Ω is needed to predict the full fall of R_{ax} (line 8).

Table 5-8. Analysis of Shot 23A

(Units in Ω)

Line	Description	$-V_2/V_1$	R	R_1	R_2	V_1/I_0	V_1/I_1	R_{ax}
1.	Observed at V_2 turn-on	1.65				110.0	49.0	64.5
2.	Calculation	1.65	65.0	340	340	103.0	40.0	63.5
3.	Observed just before arc	1.5				105.0	36.0	53.0
4.	Calculation (uniform)	1.5	65.0	245	245	122.0	42.5	63.0
5.	Calculation (uniform)	1.5	57.5	245	245	98.0	39.0	56.0
6.	Calculation non-uniform)	1.5	65.0	192	340	111.0	40.0	59.0
7.	Calculation (non-uniform)	1.5	60.5	192	340	98.5	38.5	55.5
8.	Calculation (non-uniform)	1.5	58.0	192	340	97.0	37.5	53.0

In summary, in this coarse model, a decrease in axial resistance is needed to account for the observed waveforms, but if all of the radial conduction change is assumed to occur in the top half of the experiment, the axial resistance change inferred is smaller. Because the model is coarse, it does not accurately represent non-uniform conduction, and moreover the conduction may be still more non-uniform than assumed--perhaps confined to the top quarter of the experiment rather than the top half. Thus, a more detailed model might show that the observations can be accounted for by even smaller changes in axial resistance, possibly within experimental error.

Analysis of several shots with carborundum resistors show similar conclusions. Shots with carbon fiber resistors are difficult to interpret because the resistance of the fibers decreases as they heat up, and because soil resistances are larger compared with the central resistance and so have less effect on waveforms.

If an effect has been found that is indeed due to enhanced axial conduction, it represents a decrease in axial resistances of about 10%. In the example of shot 23A given previously, the decrease from 65 to 60.5 Ω corresponds to the formation of a parallel resistance of about 440 Ω across the top half of the resistor. At the same time, the radial soil resistance in the top half of the cylinder has decreased from 340 to 192 Ω, corresponding to the growth of streamers or corona out to an effective radius of about 6 cm. If the resistance of 440 Ω is assumed to be that of a cylinder of soil 0.5 m long and 6 cm in radius, it follows that the conductivity in the cylinder has risen to about 0.1 S/m. If the resistance is assumed to have decreased to 58 Ω rather than 60.5, this conductivity becomes about 0.15 S/m.

Though the soil conductivity change is more than a factor of 10, according to Curry, et al. (Ref. 5-5), an induced conductivity of less than about 1 S/m still will not affect the operation of the R-wire. However, scaling the present results to the full R-wire is very difficult.

6b. MODEL WITH CONTINUOUSLY DISTRIBUTED RESISTANCES

The equivalent circuit for this model is illustrated in Figure 5-27 where the single radial resistor in Figure 5-24 has been replaced by several radial resistors.

This model is not exact because it does not allow for current flow between the parallel resistors at positions between the center resistor and the outer can. As an

---

5-5 IEEE Trans. Nucl. Sci. NS-28, No. 6, December 1981.

approximation to this inter-resistor flow due to enhanced conduction close to the center resistor, the resistance per unit length of the center resistor will be allowed to vary.

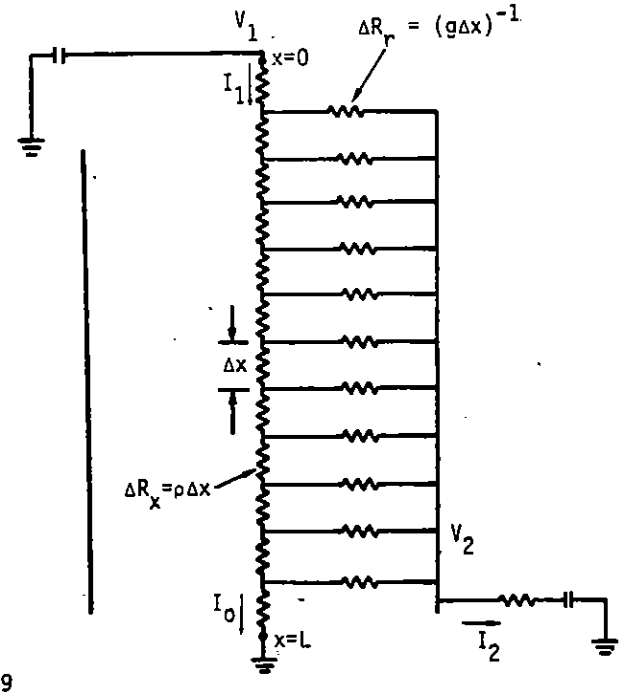

RE-04789

Figure 5-27. Distributed model.

In the limit of an infinite number of closely spaced radial resistors, the discrete resistor network in Figure 5-27 can be replaced with differential equations. Let ρ be the resistance per unit length of the center resistor, including the effect of any enhanced axial conduction through the soil, and assume ρ is constant along the length of the rod. Similarly, let g be the radial conductance, including any enhanced conduction, from the center resistor to the outer can for an infinitesimal length of the center resistor, and assume g is also constant along the length of the center resistor. Then the quasi-static coupled equations for the voltage V(x) and the axial current I(x) at a point x along the center resistor at any instant of time are

$$\frac{dV}{dx} = I\rho \tag{5-13}$$

$$\frac{dI}{dx} = -g(V-V_2) \tag{5-14}$$

where V_2 is the potential of the outer can at that time. These equations have the general solution

$$V(x) = A_1 \sinh kx + A_2 \cosh kx + V_2 \tag{5-15}$$

where $k = \sqrt{g\rho}$.

Using the boundary conditions that $V = V_1$ at $x = 0$ and $V = 0$ at $x = L$, the current into the top of the resistor is

$$I_1 = \frac{k}{\rho} \left[(V_1 - V_2) \operatorname{ctnh} kL + V_2 \operatorname{csch} kL \right] \tag{5-16}$$

and the current out the bottom of the resistor is

$$I_0 = \frac{k}{\rho} \left[(V_1 - V_2) \operatorname{csch} kL + V_2 \operatorname{ctnh} kL \right] \tag{5-17}$$

The current to ground from the outer can is

$$I_2 = I_1 - I_0 = \frac{k}{\rho} (V_1 - 2V_2) \left[\operatorname{ctnh} kL - \operatorname{csch} kL \right] \tag{5-18}$$

Note that, when $V_2 = V_1/2$, $I_2 = 0$ as one would expect. This means that, when the can is floating and $V_2 = V_1/2$, current flows radially from the rod to the can over the top half of the rod and an equal current flows from the can to the rod over the bottom half of the rod.

This model has been applied to the combined-voltage shot #27 for carborundum resistor 1. Before that shot, the radial resistance was measured with the bottom of the resistor open and the can grounded, and a value of 200 Ω was obtained. Ignoring the small voltage drop along the center resistor during this measurement, the 200 Ω resistance corresponds to a radial conductance of 0.00625 S/m for an 0.8-m long cylinder. For radii of 0.462 m and 0.0127 m for the outer and inner cylinders, the soil conductivity corresponding to this conductance is 0.003575 S/m, which is in reasonable agreement with the measured conductivity for this soil (0.003 S/m).

Figure 5-28 shows the time histories of the three measured and calculated axial resistances V_1/I_1, V_1/I_o, and V_1/I_{ave}. In Table 5-9 the measured voltages at different times during the shot are given. Before the radial pulser fires, the can is floating, so $I_2 = 0$, and the measured value of V_1/I_1 ($= V_1/I_o$) is 61.5 Ω. When the can is floating, V_2 should equal $V_1/2$ according to this model. Although the experimental data for V_2 doesn't agree with this assumption exactly, for this calculation we use $V_2 = V_1/2$ before the radial pulser fires. Using this relation for V_2 along with $g = 0.00625$ S/m and Eq. 5-16 or Eq. 5-17 for I_1 or I_o, since they are equal when $V_2 = V_1/2$ the value of ρ required to produce $V_1/I_1 = 61.5$ Ω was found by trial and error. The resulting value for ρ is 79.0 Ω/m. If the center resistor with this ρ were the only current path, the axial resistance for the 0.8 m rod would be (0.8) (79.0) = 63.2 Ω. The fact that the measured axial resistance (61.5 Ω) is less than this value is due to the parallel current path from the center resistor through the soil to the outer can and then back again to the resistor.

If one assumes that it takes a finite length of time for a radial electric field to produce a region of enhanced conductivity, the values of ρ and g calculated above should also apply immediately after the radial pulser fires. Therefore, using these values for ρ and g and the experimental values for V_1 and V_2 immediately after the radial pulser fires (reaches its full voltage, Table 5-9), Eq. 5-16 and Eq. 5-17 were solved for I_1 and I_o. The resulting values of V_1/I_1, V_1,I_1, and V_1/I_{ave} are indicated by the triangle points in Figure 5-28. The good agreement between the experimentally determined resistances and those calculated from this model gives some confidence that the model is reasonably correct and tends to confirm that the radial and axial conductances (g and ρ^{-1}) do not change instantly upon application of the radial voltage.

If the radial and axial conductances do not change with time after application of the radial voltage, the same model should apply up to radial attachment using the previously determined values for ρ and g. However, using these values of ρ and g and the measured values of V_1 and V_2 just before the radial attachment, the resulting values of the axial resistances (not shown in Figure 5-28) were in poor agreement with the experimental curves. In fact, if only ρ or g was varied to fit one curve, say, V_1/I_1, just before radial attachment, the other resistances (V_1/I_o and V_1/I_{ave}) were not in agreement with experiment. In other words, it was necessary to vary both ρ and g simultaneously to obtain agreement with the three resistance curves just before attachment with one set of values for ρ and g.

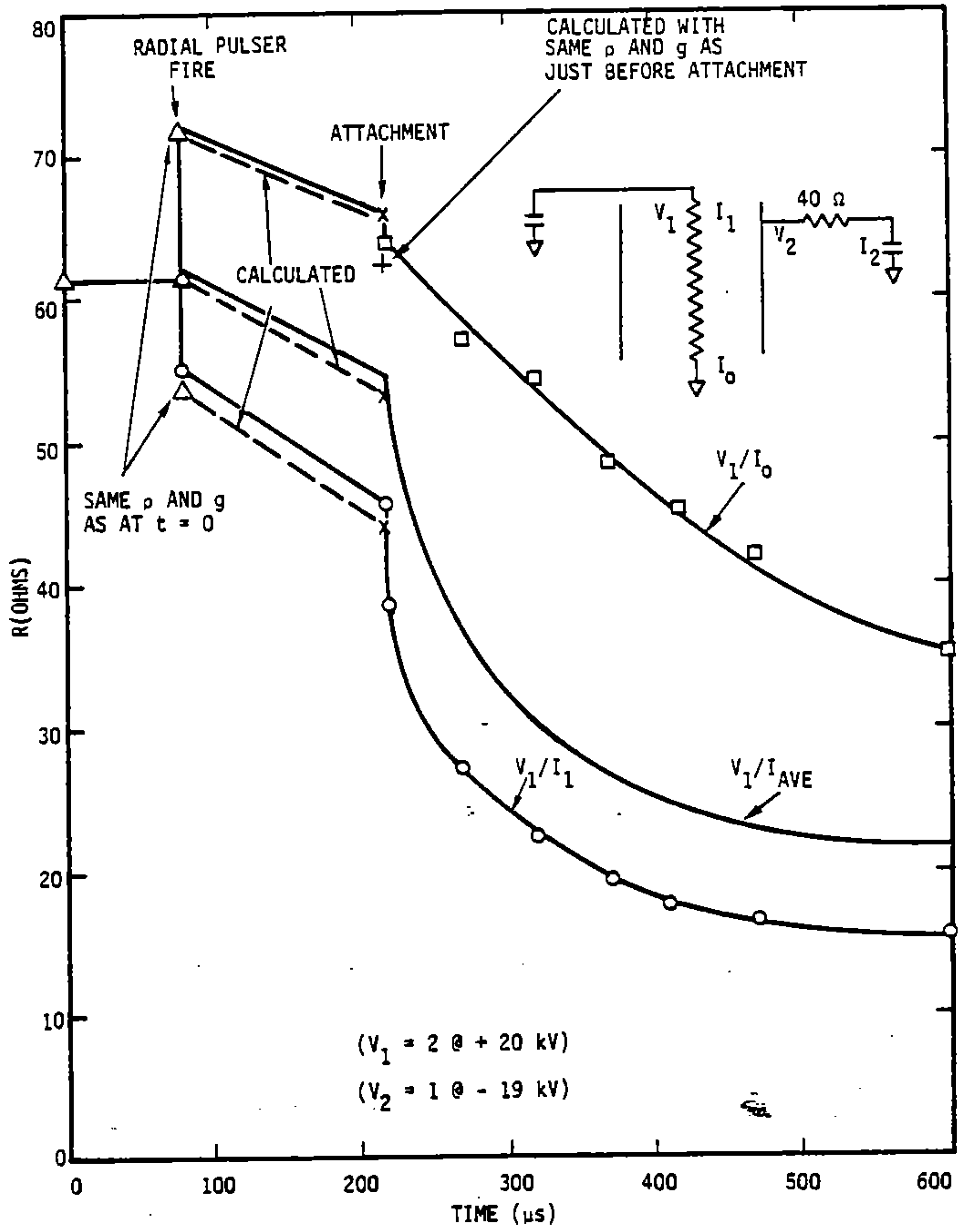

RE-04649

Figure 5-28. Comparison of calculated and experimental effective resistances for carborundum rod.

Table 5-9. Measured Voltages for Shot 27

Time	V_1 (kV)	V_2 (kV)
80 μs (after radial pulser fires)	27.7	-12.0
220 μs (before attachment)	25.1	-8.8
220 μs (just after attachment)	25.1	-4.0

By trial and error, a fairly good fit to the data just before attachment (x symbols in Figure 5-28) was obtained using $\rho = 70\ \Omega/m$ and $g = 0.01$ S/m. The smaller value for ρ and the larger value for g are both in the right direction for an enhanced conduction region through the soil.

This model can also be applied to V_1/I_0 immediately after attachment if one makes the reasonable assumption that the radial arc connects essentially the top of the center resistor to the outer can (where the differential radial voltage is largest) and that ρ and g do not change from their values just before attachment. The resulting point (+ symbol in Figure 5-28) is again in good agreement with experiment. This model cannot be applied to V_1/I_1 or V_1/I_{ave} after attachment because the large radial current (I_2) affects I_1 and the model assumption of a smooth distribution of current from I_1 to I_0 is violated.

It is of interest to see if the changes in ρ and g from the time that the radial pulser is fired to attachment are reasonably compatible with the estimated radii for the corona region in Figure 5-19 as a function of radial electric field.

For shot 27 just before attachment, the <u>average</u> radial differential voltage from the resistor to the can is about $0.5\ V_1 - V_2 \cong 21.3$ kV (see Table 5-9). From Figure 5-17, using an average of curves 6, 7, and 8, an approximate value of the enhanced-conductivity radius is $r_c = 2.2$ cm. Using that radius and the ambient soil conductivity of 3.57×10^{-3} S/m calculated previously in this section from the measured preshot radial resistance, the radial conductance per unit length is

$$g = \frac{2\pi\sigma}{\ln(0.462/0.022)} = 7.4 \times 10^{-3}\ \text{S/m}$$

That value is reasonably close to the one deduced with the present model just before attachment (0.01 S/m). Unfortunately, this conductance is not very sensitive to the magnitude of r_c, so this calculation cannot be considered a significant confirmation of the magnitude of r_c.

To reduce the axial resistance per unit length from 79 Ω/m to 70 Ω/m (as apparently occurs between the first application of the voltage and arc attachment) requires a parallel conduction path with a resistance per unit length of 614 Ω/m. For L = 0.8 m, this gives a parallel resistance of 491 Ω. By comparison, from Table 5-6, the minimum soil axial resistance for shot 27 based on the change in V_1/I_{ave} from just after the radial pulser fires to attachment is 323 Ω. Thus, these two numbers are reasonably consistent (since the 323 Ω value is a lower limit) as they should be, since they are derived from the same set of data. However, the calculation that gave a resistance of 491 Ω uses a more detailed circuit model than the other.

Using a radius $r_c = 0.022$ m for the enhanced conductivity region and the resistance per unit length of 614 Ω/m, the average resistivity in the enhanced region is $\rho_s = 614\,\pi(r_c^2 - a^2) = 0.622$ Ω-m, where a = 0.0127 m is the outer radius of the carborundum rod. By comparison, in Section V.5.b, a lower-limit value of 0.106 Ω-m was deduced from the combined-voltage shots with the graphite fiber if the total change in resistance during the shot had been due to conduction through soil. However, in those shots, there appeared to be little dependence of the axial resistance on radial field, and the resistance change appeared to be due to heating in the graphite fiber. If the resistivity of the enhanced region is as high as 0.622 Ω-m, the resulting resistance would be hard to detect in parallel with the relatively low-resistance graphite fibers.

In summary, application of this distributed-resistance model to one combined-voltage shot (#27) indicates a small enhancement of the axial conductance through the soil, corresponding to a parallel resistance of 491 Ω over the 0.8 m length of the cylinder. This value is comparable in magnitude to the parallel resistance deduced for shot #23 in Section V.6.a, namely 440 Ω across only the top half of the resistor.

6.c MODEL WITH TEN RADIAL RESISTANCES

The equivalent circuit for this model is illustrated in Figure 5-29. A minor difference between the equivalent circuit in Figure 5-29 and those in Figures 5-25 and 5-27 is that the equivalent circuit in Figure 5-29 has a resistor at the very top of the axial resistor to allow for the possibility of simulating a low-impedance arc from the top of the center resistor to the outer can without the arc current going through a portion of

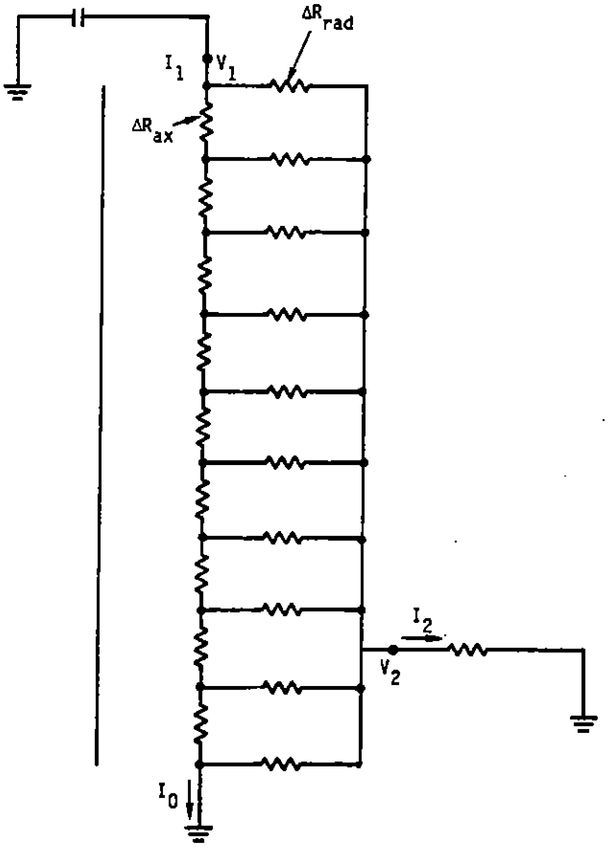

RE-05273

Figure 5-29. Equivalent circuit for model with ten radial resistances

the center resistor. Of course, these circuits could be made equivalent by setting the magnitude of the top resistor in Figure 5-29 to a very large number.

This model has been used in a further attempt to determine if some axial variation of the radial conductance could explain the observed temporal variation of the effective radial and axial resistances without also invoking an enhancement of the axial conductance through the soil. This model does essentially the same thing as the model with two radial resistances (Section V.6.a) except with a finer distribution of resistances. The difference between the present model and the continuous-resistance model in Section V.6.b is that the radial conductance does not have to be constant along the length of the cylinder in this model.

This model has again been applied to the combined-voltage shot #27 that was used in Section V.6.b and whose characteristics are illustrated in Figure 5-28 and Table 5-9. Specifically, starting from the results with the linear model, and using a trial and error procedure, constant values for the nine axial resistances and the ten radial resistances were found to give a reasonable fit to the measured low-field radial impedance (200 Ω) and the measured axial resistance (V_1/I_1 or $V_1/I_0 \cong 61.5\ \Omega$) before pulser 2 fires. (See Section V.6.b.) Before pulser 2 fires, the radial fields are relatively small since the can floats to about $V_1/2$, so there should be little corona effect and it is reasonable that the radial and axial resistances should be constant along the cylinder length. The best-fit values were $\Delta R_{rad} = 7.1\ \Omega$ and $\Delta R_{rad} = 1900\ \Omega$. Note that $9 \times 7.1 = 63.9\ \Omega$, in good agreement with the value of 63.2 Ω deduced for the center resistor in Section V.6.b. The 10 radial resistors by themselves, in parallel, would give a radial resistance of 190 Ω. The difference between this value and 200 Ω is due to the voltage loss in the center resistor for the current that has to flow down the center resistor to the lower radial resistors.

If we again assume, as in Section V.6.b, that it takes a finite length of time for the corona radius to grow, the 7.1 Ω and 1900 Ω resistances should apply immediately after pulser 2 fires. Applying the model with the values of V_1 and V_2 at that time gives acceptable agreement with the measured V_1/I_1, V_1/I_0, and $R_{rad} \equiv (0.5\ V_1 - V_2)/I_2$ (see Table 5-10, line 1). Again, this result is equivalent to the one from the continuous model.

The model was then applied using the voltages just before attachment with the same constant values of $\Delta R_{ax} = 7.1\ \Omega$ and $\Delta R_{rad} = 1900\ \Omega$. The resulting calculated resistances are in poor agreement with experiment (Table 5-10, line 2).

Table 5-10. Results from 10-Resistance Model

Condition	V_1/I_1 (Ω)	V_1/I_0 (Ω)	R_{rad} (Ω)
1. Just after pulser 2 fires			
$\Delta R_{ax} = 7.1\ \Omega$, $\Delta R_{rad} = 1900\ \Omega$			
Experiment	55.7	72.7	196
Calculation	53.3	73.5	194
All of the following are just before attachment			
Experiment	44.3	64.8	134
Calculations			
2. Same resistances as in (1.)	54.2	71.9	194
3. $\Delta R_{rad} = 1300\ \Omega$	50.7	76.2	134
4. ΔR_{rad} linear from 1150 Ω at top to 1600 Ω at bottom	50.3	75.0	135
5. ΔR_{rad} linear from 1000 Ω at top to 1900 Ω at bottom	49.7	74.2	133.3
6. $\Delta R_{rad} = 1900\ \Omega$ except top resistance = 500 Ω	48.8	71.9	134

In order to determine if an acceptable fit to experiment just before attachment could be obtained just be varying the magnitude of the ΔR_{rad} resistances along the cylinder axis, but keeping $\Delta R_{ax} = 7.1\ \Omega$, the model was applied using several different distributions of ΔR_{rad}, each of which was selected by trial and error to give a good fit to the experimental $R_{rad} = 134\ \Omega$ at that time in the shot. The variations that were used are:

a. ΔR_{rad} uniform at 1300 Ω.

b. ΔR_{rad} varies linearly from 1150 Ω at top to 1600 Ω at bottom.

c. ΔR_{rad} varies linearly from 1000 Ω at top to its original value 1900 Ω at bottom.

d. $\Delta R_{rad} = 500\ \Omega$ for top resistor and 1900 Ω for other nine.

The resulting values of V_1/I_1 and V_1/I_0 are compared to experiment in Table 5-10, lines 3 to 6. The agreement with experiment for none of the above variations was as good as was obtained with the continuous model (Section V.6.b) when both the radial and axial resistances were changed from their low-field values. (The present model was not applied with both the radial and axial resistances changed to new constant values, but essentially identical results to those from the continuous model would be expected).

In summary, all three of the models in Sections V.6.a, V.6.b, and V.6.c indicate that there is apparently some enhancement of the axial conductance for combined radial and axial voltages. However, the amount of enhancement is relatively small, for the voltages used in these experiments, corresponding to a parallel resistance of about 500 Ω through the soil.

VI. BREAKDOWN CHARACTERISTICS*

It was previously suggested that the breakdown of soil in an enhanced field geometry might be represented by an equation of the form $Ft^{3/8}d^n = k$, a constant where F is the peak voltage (kV) divided by the spacing d (cm), and t is the effective stress time in microseconds. The exponent n is uncertain, but possible values are $n = 1/6$, in which case the results of previous experiments suggest k is in the range 8-16, and $n = 3/8$, for which k is between 20 and 40.

The results of 7 shots with the carborundum resistor give a relatively narrow spread of k from 9 to 12, assuming $n = 1/6$. The mean value is 11. The range of times to breakdown is 50-220 μs; all tests have the same spacing d.

Four shots with the graphite fiber central resistor give k-values from 10 to 13, again assuming $n = 1/6$. Mean value is again 11. The breakdown time varies from 50 to 200 μs.

Thus, the breakdown times are consistent with previous results and hypothesized scaling laws. Note that the field on the central initiating electrode is very different in the two cases here, being about 1 MV/m on the carborundum and 7 MV/m on the graphite fiber; in spite of this, the k-values agree well.

In these experiments, the 40 Ω resistor in series with the outer can limits the soil arc current to about 1000 A. The typical e-folding fall time of the arc voltage was of order 100 μs. The calculated resistive phase is roughly 20 μs. A discrepancy of roughly this magnitude was noted in the 1 kA current range in previous tests; agreement between the resistive phase and the observed voltage fall time in soil has been observed at currents of about 10 kA and above.

---

*This section is due to Dr. Ian Smith of Pulse Sciences, Inc.

APPENDIX A

TIME HISTORIES FROM CYLINDRICAL SOIL EXPERIMENTS

Appendix A contains time histories of various measured and calculated quantities from the cylindrical soil experiments. The measured variables (I_1, I_2, I_o, V_1, and V_2) are defined in Figures 5-6 through 5-11. The quantities that have been calculated are (1) three approximate axial resistances, V_1/I_1, V_1/I_o, and $V_1/[0.5(I_1 + I_o)]$, (2) an approximate radial resistance $R(rad) \equiv V_1 - V_2/I_1$ when the center rod is open at the bottom, and $R(rad) \equiv (0.5 \times V_1 - V_2)/I_2$ when the bottom of the center rod is grounded, (3) the average axial E field, EAX (V/m) = $1.2 \times V_1$, and (4) the maximum radial E field adjacent to the center rod, ERAD = $C \times (V_1 - V_2)$. For the carborundum rod, $C = 22.7\ m^{-1}$ and for the graphite fiber, $C = 134\ m^{-1}$.

All of the above quantities are plotted versus time, when appropriate. As an example of a quantity that is not plotted, when the can is floating, the radial current is negligible and the calculated R(rad) would be very inaccurate, so it is omitted. Similarly, when the bottom of the center rod is open, the axial E field is not well defined so it is omitted.

Note on the plots that I_1, I_2, I_o are written as I1, I2, I0, respectively; V_1, V_2 are written as V1 and V2, respectively.

Shots 16 through 27 are for carborundom rod #1 and shots 40 through 71 are for the graphite fiber. Shots 72 through 95 are for carborundum resistor #2. Shots 16 through 21, shots 40 through 55, and shots 72 through 82 have the bottom of the center rod open so current flow is essentially only radial. Shots 23 through 27 (except shot 24), shots 62 through 71, and shots 85 through 95 are for combined axial and radial pulses. On shot 24, the radial pulser did not fire so the outer can was floating and current flow is essentially only axial. The same shot number with an 'A' or 'B' designates different scope sweep speeds on the same shot. The initial pulser voltages for the different shots can be found in Table 5-3.